Etude de l’effet des imperfections optiques sur un faisceau de rayons X partiellement cohérent en combinant des simulations optiques avec des expériences de détection de front d’onde

Rafael Celestre

To cite this version:

Rafael Celestre. Etude de l’effet des imperfections optiques sur un faisceau de rayons X partiellement cohérent en combinant des simulations optiques avec des expériences de détection de front d’onde. Optics [physics.optics]. Université Grenoble Alpes [2020-..], 2021. English. NNT : 2021GRALY002 . tel-03237428

HAL Id: tel-03237428

https://theses.hal.science/tel-03237428v1

Submitted on 26 May 2021

Université
Grenoble Alpes

THÈSE pour obtenir le grade de:

DOCTEUR DE L'UNIVERSITÉ GRENOBLE ALPES
Spécialité: **Physique de la Matière Condensée et du Rayonnement**
Arrêté ministériel: 25 mai 2016

Présentée par

RAFAEL CELESTRE

Investigations of the effect of optical imperfections on partially coherent X-ray beam by combining optical simulations with wavefront sensing experiments

- ou -

Étude de l'effet des imperfections optiques sur un faisceau de rayons X partiellement cohérent en combinant des simulations optiques avec des expériences de détection de front d'onde.

Thèse de doctorat dirigée par:

Dr. Manuel SANCHÉZ DEL RÍO, physicien HDR ESRF - the European Synchrotron	Directeur de thèse
Dr. Thomas ROTH, physicien ESRF - the European Synchrotron	Co-encadrant de thèse

préparée à Installation Européenne de Rayonnement Synchrotron (ESRF - the European Synchrotron) dans École Doctorale de Physique (n° 47).

Thèse présentée et soutenue publiquement à Grenoble, le 1er février, 2021 devant le jury composé de :

Dr. Jose Emilio LORENZO DIAZ, directeur de recherche Institut Néel CNRS, Université Grenoble Alpes	Président
Dr. Chris JACOBSEN, professeur Dept. of Physics & Astronomy, Northwestern University, Advanced Photon Source, Argonne National Lab., États-Unis	Rapporteur
Dr. David PAGANIN, professeur adjoint School of Physics and Astronomy, Monash University, Australie	Rapporteur
Dr. Christian SCHROER, professeur Inst. für Nanostruktur- und Festkörperphysik, Universität Hamburg, Deutsches Elektronen-Synchrotron DESY, Allemagne	Examinateur
Dr. Lucia ALIANELLI, chercheuse senior Diamond Light Source Ltd, Royaume-Uni	Examinatrice
Dr. Vincent FAVRE-NICOLIN, maître de conférences HDR ESRF - the European Synchrotron, Université Grenoble Alpes	Examinateur
Dr. Raymond BARRETT, chef du groupe d'optique des rayons X ESRF - the European Synchrotron	Invité

Thèse de doctorat

Self-assertion

I hereby declare that I have produced the present work independently and using no more than the mentioned literature and auxiliary means. The parts taken directly or indirectly from outside sources are identified as such. The work has so far not been presented or published in the same or similar form to any other examination body.

Grenoble, France, 01/02/2021

Rafael Celestre

Acknowledgements

Working on my PhD project and bringing it to a conclusion would not have been possible without the help of several people. I would like to take a moment to thank them while having in mind that when naming so many people, there is always the risk of missing a name or two. To that end, if your name is missing, I apologise.

I start this long list by thanking my PhD supervisors Manuel Sanchez del Rio - whom I met way back in 2015: long before my PhD project started - and Thomas Roth. While *Manolo* helped me getting started with my simulations and introduced me to prominent researchers in my field, Thomas was a great company during several beamtimes - more often than not, until very early in the morning - in Grenoble and Chicago. Both Manolo and Thomas were always open for discussions at every stage of the research project while allowing this PhD thesis to be my work. Similarly, I would like to extend my sincere thanks to Ray Barrett, who helped to steer this work in the right direction whenever he thought I needed it.

I also want to express my gratitude to the members of my jury: Lucia Alianelli, Vincent Favre-Nicolin, Chris Jacobsen, Jose Emilio Lorenzo Dias, David Paganin and Christian Schroer for accepting reviewing and reporting on my work. Our exchanges were very rich and it was a pleasure to expose my work to them.

This work made extensive use of experimental data and I must thank the staff of the BM05 and ID06 beamlines at the ESRF. Special thanks to Sebastien Berujon (BM05) and Carsten Detlefs (ID06). Always very attentive, *Seb* introduced me to wavefront sensing with speckles and helped me gain proficiency at the beamline. Carsten is an early enthusiast of the project - always keen on providing insightful feedback and accommodating Thomas and me on the tight beamline schedule. I would be remiss if I didn't thank our colleagues from the 1-BM/X-ray Optics Group from the Advanced Photon Source - Argonne National Laboratory (APS/ANL), who hosted our experiments during the long ESRF shutdown for the ESRF-EBS upgrade: Lahsen Assoufid, Xianbo Shi, Zhi Qiao, Michal Wojcik and their great technical staff. Also, thanks to Carsten Detlefs; Terence Manning; Sergey Antipov; Arndt Last & Elisa Konnermann; Christian David & Frieder Koch; and Paw Kristiansen for providing samples for the beamtimes.

I would like to acknowledge Oleg Chubar, whom I met while still working on my master's thesis in 2017. Oleg has often made himself available for our numerous discussions - always very patient when explaining the ins and outs of simulations with SRW, physical optics or accelerator physics. This good synergy can be exemplified by the two visits to the National Synchrotron Light Source-II/Brookhaven National Laboratory, where Oleg and I could work closely together. We acknowledge the ”DOE BES Field Work Proposal PS-017 funding” for partially financing these two stays. I should also thank Luca Rebuffi for, among other things, showing interest in my work and for creating a *pip-installable* version of my python libraries to be distributed with OASYS.

A general shout out to all the people I have had fruitful discussions with, E-mails exchanges or (watered down) coffees during conference breaks: Sajid Ali, Ruxandra Cojocaru, Vincent Favre-Nicolin, Wallan Grizolli, Herbert Gross, Chris Jacobsen, Michael Krisch, Arndt Last, Sérgio Lordano, Virendra Mahajan, Bernd Meyer, Peter Munro, Boaz Nash, David Paganin, Maksim Rakitin, Claudio Romero, Andreas Schropp, Frank Seiboth, Irina Snigireva, Pedro Tavares (. . .)

My research was conducted within the X-ray Optics Group (XOG) from the Instrumentation Services & Development Division (ISDD) at the European Synchrotron (ESRF) and I would like to thank my colleagues, especially the XOG, for providing a very nice work environment. Amparo Vivo merits a special thanks for proof-reading the French parts of my thesis.

I do not know when I realised I wanted to have a career in science, but for as long as I can remember, *I wanted to be a lumberjack*, I mean, a scientist. Following that dream would not have been possible without the support and incentive of my parents, grandparents & my family. A special mention to my friends from República Beijos me Liga and Coloc la Flemme - too many to mention by name; to Baptiste Belescot, Gaetan *PC* Girard, Edoardo Zatterin, Luca Capasso, Rafael Vescovi, Jan Sandner, Maik Rosenberger and the Konnermanns. These are the people who have been there for me since I left Brazil and I am thankful.

Finally, there is a quotation by Joe Walsh that sums up very well how writing this PhD thesis was like to me: "*I can't complain, but sometimes I still do. Life's been good to me so far*".

Muito obrigado,
Rafael Celestre

Résumé

Le déploiement des installations synchrotron à haute énergie de 4e génération (ESRF-EBS et les projets APS-U, HEPS, PETRA-IV et SPring-8 II) et des lasers à électrons libres (Eu-XFEL, SLAC) allié aux récents développements d'optiques réfractives « free-form » de haute qualité visant à conditionner le faisceau de rayons X, a ravivé l'intérêt pour les lentilles réfractives composées (CRL) permettant la propagation du faisceau, ou son conditionnement pour la micro et la nano-analyse, ou encore pour les applications d'imagerie. Dans ce contexte, l'ESRF a repris en 2018 la fabrication et les tests de lentilles bi-concaves en aluminium à focalisation 2D. Les optiques réfractives actuelles, commerciales ou non, présentent des aberrations qui détériorent leurs performances finales. Aussi, une modélisation précise incluant des données de métrologie est nécessaire pour évaluer la dégradation du front d'onde afin de proposer des stratégies d'amélioration.

En optique physique, les éléments faiblement focalisant sont généralement simulés comme un seul élément mince dans l'approximation de projection. Alors qu'une seule lentille rayons X dans des conditions de fonctionnement typique peut souvent être représentée de cette manière, la simulation d'une CRL entière avec une approche similaire conduit à un modèle idéalisé qui manque de polyvalence. Ce travail propose de décomposer une CRL en ses lentilles élémentaires séparées par une propagation en espace libre, comme dans la technique dite de multi-coupes (multi-slicing - MS) déjà utilisées dans les simulations optiques. L'attention est portée sur la modélisation de la lentille élémentaire en lui ajoutant des degrés de liberté supplémentaires permettant de simuler des désalignements typiques ou des erreurs de fabrication. Des polynômes orthonormaux décrivant les aberrations optiques ainsi que des données de métrologie obtenues avec les rayons X sont également utilisés pour obtenir des résultats de simulation réalistes, qui sont présentés dans plusieurs simulations cohérentes et partiellement cohérentes tout au long de ce travail. Les résultats ainsi obtenus se comparant qualitativement bien avec les données expérimentales, sont utilisés pour évaluer l'effet des imperfections optiques sur la dégradation du faisceau de rayons X partiellement cohérent ainsi que la pertinence de facteurs de mérite communs. Contrairement à d'autres travaux, la modélisation présentée ici peut être utilisée de façon transparente avec l'un des codes les plus populaires pour la conception de lignes de faisceaux de rayons X, "Synchrotron Radiation Workshop" (SRW), et est disponible sur GitLab.

Les imperfections optiques mesurées avec une haute résolution spatiale peuvent être ajoutées à la représentation MS d'une CRL pour simuler avec précision de vraies lentilles rayons X. Le suivi vectoriel du speckle des rayons X (XSVT) est une technique polyvalente qui permet d'obtenir facilement les erreurs de forme des lentilles rayons X dans l'approximation de projection avec une haute résolution spatiale. Elle a été utilisée pour caractériser les lentilles 2D-beryllium qui sont ensuite utilisées dans les modélisations présentées ici. Cette thèse présente une revue des concepts les plus pertinents de l'imagerie basée sur le speckle des rayons X appliquée à la métrologie des lentilles.

La mise en œuvre du modèle MS d'une CRL incluant des données de métrologie permet d'extraire les erreurs cumulées résultantes de l'empilement des lentilles ainsi que le calcul des corrections de phase. Cette thèse se termine par la présentation d'une méthodologie de calcul du profil des correcteurs de réfraction, qui est appliquée pour produire des plaques de phase ablatées en diamant. Les premiers résultats expérimentaux montrent une amélioration du profil du faisceau, mais l'alignement transversal de la plaque est un facteur limitant. Des améliorations concernant la métrologie des lentilles et des plaques de correction, ainsi que les protocoles d'alignement seront nécessaires optimiser les performances de ces correcteurs optiques.

Abstract

The advent of the 4th generation high-energy synchrotron facilities (ESRF-EBS and the planned APS-U, HEPS, PETRA-IV and SPring-8 II) and free-electron lasers (Eu-XFEL, SLAC) allied with the recent demonstration of high-quality free-form refractive optics for beam shaping and optical correction has reinforced interest in compound refractive lenses (CRLs) as optics for beam transport, probe formation in X-ray micro- and nano-analysis as well as for imaging applications. Within this context, in 2016, the ESRF resumed the fabrication and tests of 2D focusing bi-concave aluminium X-ray lenses. Current refractive optics, commercial or otherwise, have non-negligible aberrations which deteriorate their final performance and accurate modelling with input from metrology is necessary to evaluate the wavefront degradation and in order to propose mitigation strategies.

In physical optics, weakly focusing elements are usually simulated as a single thin element in the projection approximation. While a single X-ray lens at typical operation conditions can often be represented in this way, simulating a full CRL with a similar approach leads to an idealised model that lacks versatility. This work proposes decomposing a CRL into its lenslets separated by a free-space propagation, which resembles the multi-slicing techniques (MS) already used for optical simulations. Attention is given to modelling the single lens element by adding additional degrees of freedom allowing the modelling of typical misalignments and fabrication errors. Orthonormal polynomials for optical aberrations as well as at-wavelength metrology data are also used to obtain realistic simulation results, which are presented in several coherent- and partially-coherent simulations throughout this work. They compare qualitatively well with the experimental data and are used to evaluate the effect of optical imperfections on partially coherent X-ray beam and the suitability of common figures of merit. Unlike other works, the modelling presented here can be used transparently with one of the most popular codes for X-ray beamline design, "Synchrotron Radiation Workshop" (SRW), and is publicly available on GitLab.

Optical imperfections measured with high spatial resolution can be added to the MS representation of a CRL to accurately represent real X-ray lenses. X-ray speckle vector tracking (XSVT) is a versatile technique that conveniently obtains the figure errors of X-ray lenses in the projection approximation with high spatial resolution and is used in this work for characterising lenses to be used in the modelling presented here. This thesis presents a review of most relevant concepts of X-ray speckle based imaging applied to lens metrology.

Implementing the MS model of a CRL using metrology data allows extraction of the accumulated figure errors of stacked lenses and enables the calculation of phase corrections. Finally, this thesis presents a methodology for calculating the profile of refractive correctors, which is applied to produce phase plates ablated from diamond. Early experimental results

show an improvement on the beam profile, but the transverse alignment of the phase-plate is a limiting factor. Further improvements to the metrology of lenses and correction plates and alignment protocols are necessary to optimise the performance of these optical correctors.

Contents

List of Figures

List of Tables

Préface

L'amélioration de la qualité des sources de rayons X modernes impose des optiques pour rayons X de qualité considérablement accrue, permettant de conserver la brillance de la source même focalisée. Pour cela, il faut réduire au minimum la perturbation du front d'onde des rayons X, les effets néfastes sur les points focaux et les pertes d'intensité. Pour y parvenir avec des lentilles rayons X, elles doivent présenter une fidélité de forme, des surfaces lisses et une structure interne homogène et pure.

Ce projet de doctorat visait à déterminer l'effet des erreurs de forme des lentilles réfractives, de la rugosité de surface et des impuretés sur un faisceau de rayons X partiellement cohérent ayant des caractéristiques similaires à celles d'une ligne de lumière avec onduleur après la mise à niveau de l'ESRF-EBS. Sur la base de développements récents, l'atténuation des erreurs de forme des lentilles à l'aide d'optiques correctives a également été étudiée. Pour atteindre les objectifs proposés, ce projet reposait sur deux piliers : théorique et expérimental, avec des aspects techniques liés aux deux. Ce projet a abordé des aspects importants du programme de R&D en optique des rayons X de l'ESRF-EBS, tel qu'il est défini dans le plan stratégique de mise à niveau (*Orange book*).

Le volet théorique du travail a consisté à étudier les limites de la modélisation actuelle et les approximations utilisées dans la plupart des codes de simulation pour traiter les éléments optiques. Après avoir évalué la validité des outils existants, des propositions d'extension et de nouveaux développements ont été proposés. Les objectifs étaient également, d'une part, d'ajouter aux simulations la capacité de traiter les données de métrologie et de développer un cadre pour la conception d'optiques réfractives correctives, et d'autre part, d'intégrer les modèles de simulation à des simulations cohérentes et partiellement cohérentes pour obtenir de manière réaliste l'effet des imperfections optiques sur un faisceau de rayons X et de comparer les résultats avec la littérature et les données expérimentales. Les objectifs techniques liés à cette partie théorique comprenaient le développement de bibliothèques Python permettant d'utiliser facilement la modélisation nouvellement développée avec le code "Synchrotron Radiation Workshop" (SRW) pour la conception des lignes de faisceaux. Une partie de ce développement a été mené en collaboration avec O. Chubar (auteur du SRW) au cours de deux visites scientifiques au Brookhaven National Lab. aux États-Unis. Cette nouvelle bibliothèque Python est disponible pour une intégration dans des interfaces graphiques utilisateur telles que OrAnge SYnchrotron Suit (OASYS).

Afin d'obtenir des résultats de simulation réalistes, des techniques de détection de front d'onde en champ proche basées sur le speckle des rayons X ont été utilisées pour caractériser les lentilles produites en interne, les lentilles et optiques de type « free-form » dans le cadre de collaborations scientifiques, et les lentilles commerciales récemment acquises. La métrologie dite « en longueur d'onde » a été effectuée sur la ligne de lumière BM05 de l'ESRF jusqu'à son arrêt début décembre 2018, puis sur la ligne 1-BM de l'APS à Chicago en 2019 et enfin sur la ligne ID06 pendant la période de mise en service de l'ESRF-EBS. Outre la mesure de composants optiques pour rayons X et la création d'une base de données de métrologie pour les lentilles rayons X, les objectifs techniques de cette partie expérimentale étaient de former le doctorant pour le rendre autonome et compétant dans la mise en œuvre du dispositif expérimental sur une ligne de lumière, mais aussi dans l'acquisition et le traitement des données. Le développement de protocoles d'alignement, de standardisation des mesures et d'analyse des données étaient également attendus.

Par la suite, l'étude de récents développements concernant les techniques de fabrication additive et soustractive pour la réalisation d'éléments de correction optique s'est avérée nécessaire. C'est donc naturellement que cette formation doctorale s'est achevée par la conception d'un premier correcteur de phase suivi d'expériences pour évaluer ses performances sur le faisceau de rayons X à l'ESRF.

Aperçu

Ce travail est divisé en six chapitres, une conclusion et une annexe résumant les publications pertinentes de l'auteur au cours de ce projet de doctorat :

Chapitre 1 - On a new kind of rays est le premier de deux chapitres essentiellement théoriques. Le titre est un clin d'œil au titre de la publication qui relate la découverte des rayons X en 1895. Il commence par introduire les concepts de brillance et les relie aux sources de rayons X basées sur les accélérateurs. Les sources de rayons X à haute brillance sont ensuite présentées et le concept de rayons X latéralement cohérents est illustré. L'optique physique est ensuite présentée comme la description la plus appropriée des champs (partiellement) cohérents. La propagation en espace libre et l'approximation paraxiale sont expliquées et la propagation des rayons X à travers la matière est modélisée par l'introduction de l'élément de transmission. Une brève discussion sur la cohérence optique et la présentation de quelques concepts de base sont faites à la fin de cette section. Ce chapitre se termine par une discussion sur les simulations, méthodes et approches pour optiques des rayons X.

Chapitre 2 - X-rays as a branch of optics, en référence au discours de A. Compton lauréat du prix Nobel. Ce chapitre s'ouvre sur un récit historique des débuts de la science des rayons X montrant les étapes qui ont conduit à la compréhension des rayons X comme branche de l'optique. Un bref examen des développements de l'optique de focalisation des rayons X en fonction des phénomènes optiques est donné pour contextualiser l'évolution récente de l'optique réfractive. La modélisation d'une lentille rayons X idéale et celle d'un empilement idéal, basé sur des techniques de type multi-coupes, sont présentés. Avec peu de modifications, ce modèle peut accepter des cartographies d'erreurs arbitraires pour tenir compte des imperfections optiques. Des mesures déterminantes pour l'évaluation des performances de CRL sont introduites et les conditions de tolérance des aberrations sont présentées. Ce chapitre conclut la présentation des aspects théoriques nécessaires à cette thèse.

Chapitre 3 - Modelling optical imperfections in refractive lenses se concentre sur la modélisation d'une lentille rayons X. En ajoutant des degrés de liberté latéraux et angulaires aux faces avant et arrière des éléments focalisants, il est possible d'imiter les désalignements et les erreurs de fabrication typiques rencontrés dans les lentilles réelles. Dans les cas où ces degrés de liberté paramétrés ne suffisent pas, une modélisation d'erreurs de forme plus complexe est possible en utilisant les polynômes orthonormaux Zernike ou 2D Legendre, ou encore des données de métrologie. Ce chapitre se termine par le détail des bibliothèques Python implémentées pour la modélisation des imperfections de phase pour les lentilles rayons X.

Chapitre 4 - Measuring optical imperfections in refractive lenses présente une description complète de la technique de suivi des vecteurs de speckle en champ proche par rayons X (XSVT) employée pour inspecter les lentilles utilisées dans cette thèse. Il commence par décrire la diversité des techniques de métrologie en longueur d'onde et explique pourquoi la technique XSVT est la plus appropriée pour ce travail. Un examen des principaux aspects du dispositif expérimental, de l'acquisition, du traitement et de l'analyse des données est présenté et une discussion sur la métrologie des lentilles rayons X par rapport aux empilements de lentilles clôt ce chapitre.

Chapitre 5 - Effect of optical imperfections on an X-ray beam traite les effets induits par les imperfections optiques sur la dégradation du faisceau de rayons X en présentant de nombreuses simulations des caustiques du faisceau, de la fonction d'étalement du point et du profil du faisceau à des positions déterminées le long de l'axe optique pour différentes configurations optiques. Une étude comparative des simulations de la métrologie des lentilles individuelles par rapport aux lentilles empilées est présentée, suivie d'une discussion sur l'effet des imperfections optiques et la pertinence du rapport de Strehl pour les lentilles rayons X. Quelques commentaires sur les temps de simulation concluent le chapitre.

Chapitre 6 - Correcting optical imperfections in refractive lenses est le dernier chapitre et conclut ce voyage qui a commencé dans le **Chapitre 2** par la modélisation des lentilles idéales, en passant par la modélisation des lentilles aberrantes dans le **Chapitre 3**, en mesurant leurs imperfections dans le **Chapitre 4** et en comprenant leurs effets sur un faisceau de rayons X dans le **Chapitre 5**. Ce chapitre commence par énumérer les étapes importantes des techniques extrêmement précises de fabrication additive et soustractive qui ont permis de produire des optiques « free-form » très précises pour la correction des aberrations optiques. Un récapitulatif des stratégies de correction des imperfections optiques pour les rayons X est donné et une approche méthodique du calcul de la plaque réfractive de correction de phase est présentée. Les outils de simulation développés pour cette thèse ont permis d'évaluer la performance attendue de la plaque corrective ainsi que les tolérances d'alignement. Un prototype en diamant est présenté et une première expérience sur une ligne de lumière démontre une amélioration qualitative du profil du faisceau de rayons X. Une longue discussion sur la conception et les performances attendues confrontées aux résultats expérimentaux obtenus avec la plaque corrective sur le faisceau de rayons X est présentée à la fin de ce chapitre.

Chapitre 7.fr - Conclusion résumant la signification, les implications, les contributions et les limites de cette thèse et exposant les orientations futures.

Annexe A - Publication list liste les publications réalisées par le doctorant au cours de ce projet.

Prelude

Improvements in the quality of modern X-ray sources place increasingly stringent demands upon the quality of X-ray optics, which ideally when interacting with X-ray beams should not degrade the X-ray source brilliance. To achieve this, the perturbation of the X-ray wavefront, adverse effects on the focal spots, and intensity losses all need to be minimised. To achieve that with refractive optics, X-ray lenses shape fidelity, smooth surfaces and a homogeneous internal structure are of particular importance.

This PhD project aimed at determining the effect of refractive lens shape errors, surface roughness and impurities on a partially coherent X-ray beam the characteristics of a typical undulator beamline after the ESRF-EBS upgrade. Based on recent developments, the mitigation of lens shape error employing corrective optics was also investigated. To achieve the proposed goals, this project was based on two pillars: a theoretical one and an experimental one, with technical aspects related to both. This project addressed important aspects of the ESRF-EBS X-ray optics R&D programme as laid out in the strategic upgrade plan (Orange book).

The theoretical facet of the work involved studying the limitations of current modelling and approximations used in most simulation codes for dealing with the optical elements. After evaluating the validity of the existing tools, extensions and new developments were proposed. Adding to such simulations the capability of handling metrology data and developing a framework for the design of refractive corrective optics was also targeted. A subsequent aim was to incorporate such modelling into coherent- and partially-coherent X-ray beam propagation simulations to predict the effect of optical imperfections on an X-ray beam and compare the results with the literature and experimental data. The technical goals related to this theoretical part included the development of Python libraries for straightforward use of the newly developed modelling with "Synchrotron Radiation Workshop" (SRW) code for beamline design. Part of this implementation was developed in collaboration with O. Chubar (SRW author) during two scientific visits to the Brookhaven National Lab. in the U.S.A. This newly-developed Python library was the base for further integration in user graphical interfaces like OrAnge SYnchrotron Suit (OASYS).

To obtain realistic results for the simulations, near-field X-ray speckle-based wavefront sensing techniques were used to characterise in-house produced lenses; lenses and free-form optics in the context of scientific collaborations; and newly-acquired commercial lenses. Measurement campaigns for at-wavelength metrology were routinely conducted at the BM05 beamline at the ESRF before its shutdown in early December 2018, the 1-BM beamline at the APS in Chicago during the year of 2019 and at the ID06 beamline, during the ESRF-EBS commissioning period in 2020. Besides the measurement of X-ray optics and curation of a metrology database for X-ray lenses, the technical goals of this experimental part were training the PhD candidate to be able to conduct X-ray experiments with understanding, proficiency and autonomy: the setting up the experimental setup at the beamline, data acquisition and data processing. Developing internal measurement protocols in terms of probe alignment and standardising the measurements and data analysis were also expected.

At a later stage, investigating recent developments in additive and subtractive manufacturing techniques for the manufacturing of optical correction was also required. Designing and testing the performance on an X-ray beam of the first phase correctors at the ESRF was performed as a natural way of concluding the PhD.

Outline

This work is divided into six chapters, a conclusion and one appendix summarizing the author's relevant publications during this PhD project:

Chapter 1 - On a new kind of rays is the first of two predominantly theoretical chapters. The title is a reference to the title of the publication reporting the discovery of X-rays in 1895. It begins by introducing the concepts of brilliance and connecting it to accelerator-based X-ray sources. High-brilliance X-ray sources are then presented and the concept of laterally coherent X-rays are explained. Physical optics is then presented as the most appropriate description of (partially-) coherent fields. Free-space propagation and the paraxial approximation are explained and the propagation of X-ray though matter is modelled through the introduction of the transmission element. A short discussion on optical coherence with the presentation of some basic concepts is done at the end of this section. This chapter concludes with a discussion on X-ray optical simulations, methods and approaches.

Chapter 2 - X-rays as a branch of optics, a reference to A. Compton's Nobel lecture, opens with a historical recount of the early days of X-ray science showing the milestones that led to the understanding of X-rays as a branch of optics. A short review of the developments in X-ray focusing optics divided by optical phenomena is given for contextualising the relative novelty of refractive optics. The modelling of the ideal X-ray lenses and the ideal lens stacks based on multi-slicing-like techniques are presented. With little modification, this model can accept arbitrary 2D figure error maps to account for optical imperfections. Important metrics for evaluating the CRL performance are introduced and tolerance conditions for aberrations are presented. This chapter concludes the presentation of the theoretical aspects necessary for this dissertation.

Chapter 3 - Modelling optical imperfections in refractive lenses focuses on modelling the X-ray lenslet. By adding to the front- and back- focusing surfaces lateral- and angular- degrees of freedom, it is possible to mimic typical misalignments and fabrication errors encountered in real lenses. For the cases where the newly parametrised degrees of freedom are not enough, the modelling of more intricate shape errors is enabled by employing the Zernike or 2D Legendre orthonormal polynomials or metrology data. This chapter finishes with the details of the Python libraries implemented for modelling phase imperfections in X-ray lenses.

Chapter 4 - Measuring optical imperfections in refractive lenses presents a complete description of the X-ray near field speckle vector tracking (XSVT) technique used to inspect the lenses used in this thesis. It begins by describing the wide variety of at-wavelength metrology techniques which have been demonstrated in the X-ray regime and indicates why XSVT is the most appropriate technique to be used in this work. A review of the main aspects of the experimental setup, data acquisition, processing and analysis is presented and a discussion on the metrology of X-ray lenses vs. lens stacks closes this chapter.

Chapter 5 - Effect of optical imperfections on an X-ray beam discusses the effect of optical imperfections on the X-ray beam degradation by presenting an extensive collection of simulations of beam-caustics, the point-spread function and the beam profile at selected positions along the optical axis for several optical setups. A discussion on the metrology of individual lenses vs. stacked lenses from the point of view of the simulations are presented, followed by a discussion on the effect of optical imperfections and the adequacy of the Strehl ratio for X-ray lenses. Some comments on the simulation time conclude the chapter.

Chapter 6 - Correcting optical imperfections in refractive lenses is the last chapter and concludes the journey that began in **Chapter 2** with the modelling of ideal lenses, passing through the modelling of aberrated lenses in **Chapter 3**, measuring the very same imperfections in **Chapter 4** and understanding the their effects on an X-ray beam in **Chapter 5**. This chapter begins by listing important milestones in extremely accurate additive and subtractive manufacturing techniques that enabled producing very accurate free-form optics for the correction of optical aberrations. A review on strategies for correcting optical imperfections in X-ray optics is given and a methodical method for the refractive correction phase plate calculation is given. Using the simulations tools developed for this thesis, the expected performance of the correction plate can be calculated and alignment tolerances can be drawn. A prototype diamond correction plate is presented and an early test on an aberrated X-ray beam is shown to demonstrate a qualitative improvement on the beam profile. A discussion on the design and expected performance versus the early phase plate tests on an X-ray beam is presented at the end of this chapter.

Chapter 7.en - Conclusion summarising the significance, implications, contributions and limitations of this thesis and laying out future directions.

Appendix A - Publication list of the works produced by the PhD candidate during this project.

1

On a new kind of rays

Hard X-rays are electromagnetic radiation with wavelength below[1] 2 Å. From their discovery in 1895 by W. C. Röntgen [Röntgen, 1896b], the first observation of synchrotron radiation (SR) in 1947 [Elder et al., 1947], the first (late 1950s and early 1960s), second (late 1970s and early 1980s), third (end of 1980s and early 1990s) and the fourth generation (late 2000s and early 2010s) of accelerator-based X-ray sources, the brilliance and consequently, the coherent fraction has increased out-passing Moore's law [Robinson, 2015]. This chapter is divided into three main parts. The first part introduces the concept of brilliance and relates it to the coherent fraction of synchrotron radiation emission, presenting undulators as the mains source of coherent X-rays in synchrotron radiation facilities. In the second part of this chapter, the scalar wave theory is presented as a framework for modelling X-ray propagation through free-space and optical elements. Some definitions regarding optical coherence are also presented. The last part of this chapter deals with simulation strategies based on the degree of spatial coherence of the radiation.

1.1 From the Crookes-Hittorf tube to the ESRF-EBS

Since the discovery[2] of X-rays in late November 1895 by W. C. Röntgen [Röntgen, 1896b] up to the concept and implementation of the fourth generation high-energy synchrotron light sources in the second half of the 2010s [Eriksson, 2016], there has been an Herculean amount of effort directed towards increasing a key energy-dependent quality parameter of x-ray sources, called brilliance[3]:

$$\mathcal{B}_0 = \frac{\varphi}{4\pi^2\epsilon_\mathrm{h}\epsilon_\mathrm{v}}, \tag{1.1}$$

where φ is the X-ray photon flux for a given bandwidth $\Delta\mathrm{E}/\mathrm{E} = 0.001$ centred at energy E, given in $(\mathrm{photons/s/0.1\%bw.})$. Both ϵ_h and ϵ_v refer to the photon-beam emittances in the horizontal and vertical planes, respectively. The photon beam emittance is defined as:

$$\epsilon_\mathrm{h,v} \equiv \Sigma_\mathrm{h,v} \cdot \Sigma'_\mathrm{h,v}. \tag{1.2}$$

Here $\Sigma_\mathrm{h,v}$ stands for the beam size and $\Sigma'_\mathrm{h,v}$ is the photon-beam divergence. The usual unit used for the beam size is (mm) and for beam divergence is (mrad), hence brilliance is commonly given in $(\mathrm{ph/s/0.1\%bw./mm^2/mrad^2})$ [Kim, 1986]. It is clear from Eq. 1.1 that increasing

---

[1] The choice of wavelength or energy to limit soft-, tender- and hard- X-rays is rather arbitrary. The conversion of energy to wavelength in practical unit is given by $\mathrm{E(keV)} = 12.3984/\lambda(\mathrm{Å})$.

[2] W. C. Röntgen has published his first notes on the discovery of X-rays in January 1896 [Röntgen, 1896b]. In March the same year, Röntgen went on to publish some additional notes on his discovery [Röntgen, 1896a]. Further observations of the X-ray properties were later published [Röntgen, 1897].

[3] Although a common jargon in X-ray science and technology, the term brilliance is not unanimously agreed upon. For an insightful discussion on the terminology, please refer to the discussion in [Mills et al., 2005] and to the Chapter 3.9 and Table 3.1 in [Talman, 2006]. Eq. 1.1 is an approximate result. For an accurate calculation of the brilliance, please, refer to [Walker, 2019].

the brilliance means increasing the spectral photon flux φ and/or reducing the photon-beam emittance in both horizontal and vertical directions (ϵ_{h} and ϵ_{v}), i.e. having a smaller and more collimated X-ray source.

1.1.1 X-ray sources

Two main processes are responsible for generating X-rays: acceleration of charged particles, for example, electrons; and the change of an electron state from a higher atomic or ionic energy level to a lower one.

In the very early X-ray sources[4] such as the Crookes-Hittorf tube used by Röntgen[5] or any modern X-ray tube (electron-impact X-ray sources) both processes generate X-rays: Bremsstrahlung by rapid deceleration of fast electrons, generating a broad-band smooth spectrum; and characteristic radiation (X-ray fluorescence), responsible for narrow spikes in the spectrum. Although modern sources can focus the electron-beam into the target (anode), reducing the source size considerably, the emission of X-rays happens in a large solid angle, 4π (steradians). The emission angle, in conjunction with the fact that the X-ray flux is limited by the low current of electrons due to target heating, makes X-ray tubes relatively low brilliance sources [Michette and Buckley, 1993, *§1.6* & *§2*].

In accelerator-based X-ray sources, more specifically, storage-ring-like facilities[6], (ultra-relativistic[7]) electrons are usually chosen for generating X-rays as they are simple to generate using a thermionic source and their low rest mass means that they emit by far the most radiation for given particle energy. Charged particles in storage rings are subjected to a magnetic field perpendicular to the direction of motion and this causes the particle to move in a circular trajectory (centripetal acceleration). If the particle is non-relativistically accelerated, the emitted radiation is described by the Larmor pattern (torus-shaped profile), which shows no radiation in the direction of acceleration as the radiation goes out transverse to the direction of motion. However, for a particle in the ultra-relativistic regime, the Lorentz-transformed radiation pattern shows that the (synchrotron) radiation pattern is very peaked in the forward direction with a narrow angular divergence (cf. Fig. 1.1[8]) [Jackson, 1998].

---

[4] This works focuses only on artificial X-ray sources, most specifically storage-rings. X-rays and synchrotron radiation also occur in nature with astrophysical sources of synchrotron radiation, which exist across the full electromagnetic spectrum, being of extremely scientific relevance [Ginzburg and Syrovatskii, 1965; Wielebinski, 2006].

[5] On the opening sentence of his most important work "*On a new kind of rays*", Röntgen mentions that X-rays can be produced by [sic.] "*an electric discharge passing through a Hittorf's tube or a well-exhausted Lenard's or Crook's tube*" [Röntgen, 1896b].

[6] Linear accelerators are also used as a source of intense X-rays, in particular in free-electron lasers (XFELs) [Huang and Kim, 2007].

[7] At an energy of ~11.43 MeV, the electron reaches $v/c = 99.9\%$ and at roughly 36.13 MeV the ratio is $v/c = 99.99\%$, where v is the particle velocity and c is the speed of light. Storage rings dedicated to synchrotron radiation operate at least above a few hundred MeV.

[8] This illustration, Fig. 1.1, is an oversimplification of the real spectra and emission profiles, showing general trends. Depending on strength of the magnetic field applied to the electron beam and the magnetic period, the spectrum of a wiggler can be spiky. The increase in flux relative to bending magnet radiation is partly due to field strength, and partly due to having a number of dipole-like sources adding up along the line of sight. In an undulator, odd harmonics involve transverse motion and thus forward radiation, while even harmonics involve longitudinal motion and thus sideways radiation that is relativistically contracted to a hollow ring in the forward direction. The even harmonics are weak on axis with moderately low emittance, and zero with diffraction-limited emittance, but their angle integrated flux is much stronger than shown.

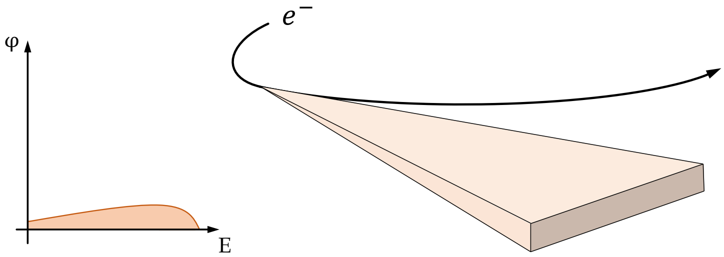

(i) spectrum (ii) emission profile

(a) bending magnet radiation

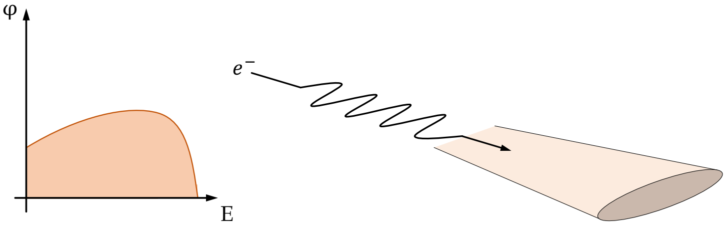

(i) spectrum (ii) emission profile

(b) wiggler radiation

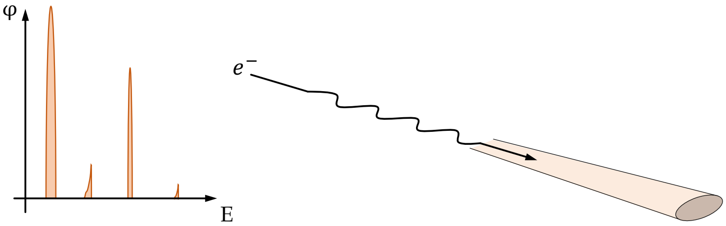

(i) spectrum (ii) emission profile

(c) undulator radiation

Fig. 1.1.: Sketch of the three main sources of synchrotron radiation. On the left-hand side the photon-flux φ as a function of energy E is shown. The right-hand side shows the electron (e^-) trajectory and the accompanying emission profile. Figure adapted from Figs. 5.1-5.3 in [Attwood, 1999] and Fig. 1.2 from [Clarke, 2004].

There are two main families of X-ray sources in a synchrotron facility: bending magnets (BM's) and insertion devices (IDs). Bending magnets are necessary magnetic structures in the storage ring to deflect the electron-beam transversely to its motion direction and keep it in a closed trajectory by applying a constant magnetic field or gradient. They produce a smooth broad-band spectrum and the photon-beam footprint is very large as both the source and divergence sizes are very large. Historically, BMs have been used as the primary source of X-rays in first- and second-generation light-sources[9]. The bending magnet radiation spectrum and profile are shown in Fig. 1.1(a). Storage rings generally a multi-edge polygon where at each vertex sits a bending magnet gently deflecting the electron-beam keeping the electrons in a closed loop. The distance between two adjacent dipole magnets is called a straight section and is where insertion devices can be placed.

---

[9] The first generation of synchrotron light sources is usually attributed to the parasitic use of high-energy physics accelerators. The second-generation marks the beginning of fully-dedicated machines for synchrotron radiation.

Insertion devices (IDs) are generally periodic magnetic structures that sinusoidally deflect the electron-beam transversely to its direction of motion[10]. IDs can be sub-grouped into two categories based on the amplitude of the electron motion inside them and their magnetic period: wigglers have a higher magnetic field applied to the electron-beam causing the amplitude of electron motion to be large. This generates a broad-band spectrum several times more intense than that of a bending magnet (higher flux) - wigglers are also called wavelength shifters. The beam footprint is also very large: in the transverse direction the source size is enlarged and the beam has a high divergence. Figure 1.1(b) shows the spectrum and emission profile of a wiggler insertion device. The second member of the ID family is the undulator. In it, the amplitude of the transverse electron oscillations is much smaller than inside a wiggler. This is because in the undulators a less intense magnetic field is applied to the electrons and because the magnetic period is usually smaller than the one of a wiggler. The small excursion of the electrons inside the undulator accounts for a small photon source size with low divergence. Due to the low electron-motion amplitude, constructive interference between the emitted radiation occurs and the spectrum of an undulator is composed of narrow-band peaks called undulator harmonics[11]. This is possible because, in an undulator, the electron excursion is smaller than the X-ray cone emission. Figure 1.1(c) shows the spectrum and emission profile of an undulator. A very useful metric used for summarising the effects of the and ultimately classifying an ID as a wiggler or an undulator is the dimensionless deflection parameter K given by

$$K = \frac{B_0 e}{m_0 c}\frac{\Lambda}{2\pi}, \tag{1.3}$$

where B_0 is the magnetic field, e is the electron charge, m_0 is the electron rest mass, c is the light speed in vacuum and Λ is the magnetic period. It is generally accepted that IDs with $K >> 1$ are classified as wigglers, while undulators have a $K < 1$ leaving a grey area where K is in the range of 1 to 10 and the radiation may exhibit some features of the wiggler or the undulator [Clarke, 2004, §3.1].

The advent of storage rings especially designed to accommodate ID's marks the third generation of synchrotron light sources, from which the ESRF - European Synchrotron Research Facility (1994) in France is the pioneering machine, followed by the APS - Advanced Photon Source (1996) in the USA and the SPring-8 - Super Photon ring-8 GeV (1999) in Japan.

1.1.2 High brilliance X-ray sources

The small photon source size and low divergence of the X-rays emitted by an undulator make it a great candidate for generating high-brilliance X-ray beams. As Eq. 1.1 suggests, increasing the brilliance for a given storage ring energy can be done by two different strategies: increasing the photon flux, which is done by increasing the electron current in the storage ring; and/or by reducing the photon-beam emittance.

---

[10] It is important to acknowledge the existence of exotic ID designs that are not strictly periodic magnetic structures, namely the quasi-periodic undulator family [Onuki and Elleaume, 2013, *§7.2*].

[11] For diffraction-limited photon-beam emittances, if the observer is on-axis with the electron motion, only odd harmonics are observed. Away from the emission axis, even harmonics start being observed [Clarke, 2004, *§4.2*].

The radiation profile (beam sizes and divergences) emitted by an undulator is given by the convolution between the electron-beam profile and the radiation pattern specific to the X-ray source[12]:

$$\Sigma_{\mathrm{h,v}} = \sigma_{e_{\mathrm{h,v}}} * \sigma_{u_{\mathrm{h,v}}}, \tag{1.4a}$$
$$\Sigma'_{\mathrm{h,v}} = \sigma'_{e_{\mathrm{h,v}}} * \sigma'_{u_{\mathrm{h,v}}}. \tag{1.4b}$$

Here $\Sigma_{\mathrm{h,v}}$ and $\Sigma'_{\mathrm{h,v}}$ are the already defined photon-beam size and divergence. The $\sigma_{e_{\mathrm{h,v}}}$ and $\sigma'_{e_{\mathrm{h,v}}}$ represent the electron-beam size and divergence. Lastly, $\sigma_{u_{\mathrm{h,v}}}$ and $\sigma'_{u_{\mathrm{h,v}}}$ are the specific radiation pattern size and divergence of the insertion device - these are then obtained by calculating the emission of a single-electron or a filament electron-beam (negligible dimension and divergence) passing through the magnetic field of the insertion device. Once designed, the specific radiation pattern of an undulator[13] is considered to be a fundamental wavelength-dependent property of the insertion device[14].

A closer look into Eqs. 1.4 allows one to suppose three distinct regimes for the photon-beam characteristics: a) $\epsilon_{e_{\mathrm{h,v}}} \gg \epsilon_{u_{\mathrm{h,v}}}$ in this regime, the photon-beam characteristics are dominated by the electron-beam, which is well approximated by a Gaussian distribution. This is usually the case for horizontal emittance in third-generation synchrotrons; b) an intermediate state where the electron-beam emittance $\epsilon_{e_{\mathrm{h,v}}}$ is comparable to $\epsilon_{u_{\mathrm{h,v}}}$ leading to a photon-beam profile with clear contributions from both the electron-beam and specific radiation pattern of the undulator; c) the electron-beam emittance can be further reduced so that $\epsilon_{e_{\mathrm{h,v}}} \ll \epsilon_{u_{\mathrm{h,v}}}$ and the photon-beam profile is dominated by the undulator's specific radiation pattern. Since $\epsilon_{u_{\mathrm{h,v}}}$ is a fundamental limit, efforts to reducing the electron-beam beyond that limit will not have any impact in the photon-beam profile. Mathematically, the three emittance regimes can be expressed as:

$$\epsilon_{\mathrm{h,v}}\Big|_{\epsilon_{e_{\mathrm{h,v}}} \gg \epsilon_{u_{\mathrm{h,v}}}} \simeq \left(\sigma_{e_{\mathrm{h,v}}} * \delta_{u_{\mathrm{h,v}}}\right)\left(\sigma'_{e_{\mathrm{h,v}}} * \delta_{u_{\mathrm{h,v}}}\right) = \sigma_{e_{\mathrm{h,v}}}\sigma'_{e_{\mathrm{h,v}}}, \tag{1.5a}$$
$$\epsilon_{\mathrm{h,v}}\Big|_{\epsilon_{e_{\mathrm{h,v}}} \sim \epsilon_{u_{\mathrm{h,v}}}} \simeq \left(\sigma_{e_{\mathrm{h,v}}} * \sigma_{u_{\mathrm{h,v}}}\right)\left(\sigma'_{e_{\mathrm{h,v}}} * \sigma'_{u_{\mathrm{h,v}}}\right) = \Sigma_{\mathrm{h,v}}\Sigma'_{\mathrm{h,v}}, \tag{1.5b}$$
$$\epsilon_{\mathrm{h,v}}\Big|_{\epsilon_{e_{\mathrm{h,v}}} \ll \epsilon_{u_{\mathrm{h,v}}}} \simeq \left(\delta_{e_{\mathrm{h,v}}} * \sigma_{u_{\mathrm{h,v}}}\right)\left(\delta_{e_{\mathrm{h,v}}} * \sigma'_{u_{\mathrm{h,v}}}\right) = \sigma_{u_{\mathrm{h,v}}}\sigma'_{u_{\mathrm{h,v}}}. \tag{1.5c}$$

Where δ represents the Dirac function. The electron-beam emittance matching to the undulator's specific radiation pattern is shown in Fig. 1.2. Fourth-generation synchrotron storage-ring-based

---

[12] This is true for any accelerator-based X-ray source - cf. chapter "3.10 - Photon beam features inherited from the electron beam" in [Talman, 2006].

[13] The specific radiation pattern of an undulator is a function of its magnetic period, number of periods, magnetic field, storage ring energy and X-ray emission-wavelength.

[14] In the literature, there is a variety of formulae for calculating the specific radiation pattern size and divergence [Kim, 1986, 1989; Tanaka and Kitamura, 2009; Onuki and Elleaume, 2013]. Different assumptions, approximations and fits are done on their derivation. It is important to state that those are approximations and should not be regarded as fundamental results - please, refer to the discussion in [Walker, 2019]. The exact calculation of the radiation pattern can be done by computing the electric field of an electron subjected to an arbitrary magnetic field - cf. [Chubar, 1995, 2001] or by calculating the Wigner-function for synchrotron radiation [Bazarov, 2012] as in [Tanaka, 2014].

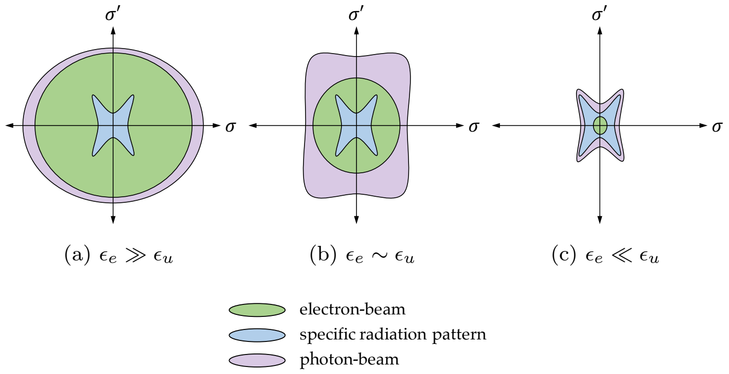

(a) $\epsilon_e \gg \epsilon_u$ (b) $\epsilon_e \sim \epsilon_u$ (c) $\epsilon_e \ll \epsilon_u$

Fig. 1.2.: Matching of the electron-beam emittance to the undulator specific radiation pattern to increase the photon-beam brilliance, where σ stands for beam size and σ' for beam divergence. Adapted from Fig. 21.20 in [Wiedemann, 2015].

light-sources[15] use emittance-matching - Eq. 1.5(b) mainly, but ideally Eq. 1.5(c) - as the main source of increasing the X-ray brilliance[16] [Wiedemann, 2015, *§21.8.1*].

1.1.3 Undulators as a primary source of coherent X-rays

Let's consider the case of a filament electron-beam passing through a planar undulator. The associated emission at a resonant photon energy is almost symmetric and $\sigma_{u_\mathrm{h}} \approx \sigma_{u_\mathrm{v}} = \sigma_u$ and $\sigma'_{u_\mathrm{h}} = \sigma'_{u_\mathrm{v}} = \sigma'_u$ [Kim, 1989]. Because the electron bunch has negligible emittance ϵ_e in both horizontal and vertical directions, the photon-beam emittance is given by $\epsilon_{\mathrm{h,v}} = \sigma_u \sigma'_u = \epsilon_\mathrm{u}$. The associated brilliance of such a filament beam is given by:

$$\mathcal{B}_0 = \frac{\varphi}{4\pi^2\epsilon_u^2} \tag{1.6}$$

Since the emission of a filament electron-beam is fully-coherent, it makes sense to define a coherent photon flux of a zero-electron-emittance-beam:

$$\varphi_{\mathrm{coh.}} = 4\pi^2\epsilon_u^2\mathcal{B}_0 = \left(\frac{\lambda}{2}\right)^2\mathcal{B}_0. \tag{1.7}$$

---

[15] The fourth-generation synchrotron light sources or ultra-low emittance machines have been proposed as early as the 1990s [Einfeld et al., 1996, 2014], but were deemed to be technologically unfeasible for high-energy storage rings [Ropert et al., 2000; Elleaume and Ropert, 2003]. Overcoming the technological barriers [Borland et al., 2014] was essential in paving the way for high energy storage rings with ultra-low emittance [Bei et al., 2010; Eriksson, 2016]. The first machines to come online using the multi-bend-achromat design (MBA) are the MAX-IV in Sweden (2016) and the SIRIUS in Brazil (2019) - the former operating with two storage rings: 1.5 GeV and 3 GeV and the latter operating at 3 GeV. The ESRF upgrade programme has opted for a hybrid-multi-bend-achromat (HMBA) magnetic lattice for its new storage ring [Biasci et al., 2014] and it is the first of its kind to operate at high-energies (6 GeV). The lattice concept behind the Extremely Brilliant Source (ESRF-EBS) has its origins in 2006 with the SuperB project for an electron-positron collider [P. Raimondi, 2017] and in early 2020 has produced the first X-rays.

[16] This is because, with the new storage-ring designs (multi-bend-achromat and its variations), the electron-beam emittance can be routinely reduced by one to two orders of magnitude, when compared to current third-generation light sources. To obtain equivalent gain in brilliance by just increasing the electron-beam current is very challenging in function of collective effects (coherent and incoherent). On top of that, there are thermal load issues on the vacuum system and on the beamline optics, that is, the X-ray transport system to the sample. This footnote is the result of discussions with Pedro F. Tavares (MAX-IV, Sweden) and Boaz Nash (RadiaSoft LLC, USA).

Although Eq. 1.7 implies that $\epsilon_u = \sigma_u\sigma'_u = \lambda/4\pi$, it has been demonstrated that the non-Gaussian behaviour of the undulator emission makes the photon-beam emittance approach asymptotically $\lambda/2\pi$ instead [Onuki and Elleaume, 2013; Tanaka and Kitamura, 2009]. However, it is important to mention that the right-hand side of Eq. 1.7 is valid for any symmetric electric field distribution at any value of undulator detuning and it does not depend on a Gaussian approximation of the undulator specific radiation pattern [Walker, 2019]. One can define the coherent fraction as the ratio between the coherent flux $\varphi_{\text{coh.}}$ (Eq. 1.7) and the nominal photon-flux $\varphi = 4\pi^2\epsilon_{\text{h}}\epsilon_{\text{v}}\mathcal{B}_0$ (Eq. 1.1):

$$\zeta = \frac{\varphi_{\text{coh.}}}{\varphi} = \frac{\epsilon_u^2}{\epsilon_{\text{h}}\epsilon_{\text{v}}}. \tag{1.8}$$

Eq. 1.8 allows to deduce that by reducing the electron-beam emittance, the coherence fraction is increased (cf. Eqs. 1.5). An important conclusion to be drawn is that emittance-matching as a form of increasing the photon-beam brilliance in fourth-generation synchrotrons increases the X-ray beam transverse (spatial) coherence[17].

Temporal Coherence

Lastly, the temporal coherence[18] of the synchrotron radiation emitted by storage rings should be addressed. Without further conditioning, the radiation emitted on the X-ray region exhibits low temporal coherence for high energies. Spectral filtering with monochromators increases the temporal coherence at the expense of photon-flux reduction. Compressing the electron bunch length also offers an increased temporal coherence for X-rays, as coherent synchrotron radiation (CSR) naturally appears when the electron-beam bunch length is comparable to the observed radiation wavelength - cf. [Chubar, 2006], [Talman, 2006, *§3.8* & *§13*] and [Wiedemann, 2015, *§21.7*].

Recommended literature

The correct description of the electron-beam inside each different source of X-rays in a storage ring is of primary importance for accurate modelling of the radiation spectrum and photon spatial distribution, with consequences for X-ray optical design. An extensive review on particle accelerator physics is given by [Duke, 2000] and by [Wiedemann, 2015]. An in-depth look into X-rays from accelerator sources can be found in [Clarke, 2004], in [Talman, 2006] and in [Onuki and Elleaume, 2013].

The accurate calculation of the brilliance from undulators in low-emittance accelerators and the coherence properties of the emitted X-rays is an active area of research topic and a deeper look into it is offered by [Bazarov, 2012; Tanaka, 2014; Geloni et al., 2015, 2008; Walker, 2019; Khubbutdinov et al., 2019]. See also [Singer and Vartanyants, 2014].

---

[17] Please, refer to §1.2.3 - *Optical coherence* for a definition of spatial and temporal coherence.

[18] See footnote 17.

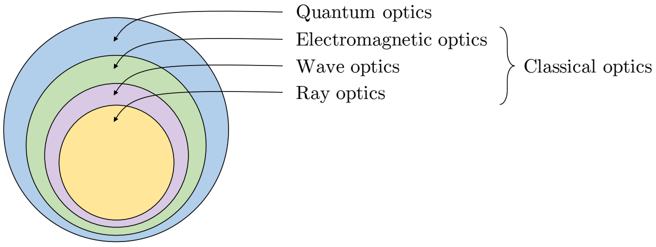

Fig. 1.3.: Hierarchical optical theories. Optical modelling in the X-ray regime can be accurately represented in the realms of wave optics for most cases where coherence effects are present. Adapted from Fig. 1.0-1 in [Saleh and Teich, 2019].

1.2 Physical optics

The increasing coherent fraction of X-rays from fourth-generation storage rings requires an appropriate framework for their representation. Light can be described by an electromagnetic wave phenomenon governed by the Maxwell equations - cf. [Born et al., 1999, *§1.1*]:

$$\nabla \cdot \mathbf{E} = \frac{\rho}{\varepsilon} \qquad \text{(Gauß's law)}, \tag{1.9a}$$

$$\nabla \cdot \mathbf{B} = 0 \qquad \text{(Gauß's law for magnetism)}, \tag{1.9b}$$

$$\nabla \times \mathbf{E} = -\frac{\partial}{\partial t}\mathbf{B} \qquad \text{(Faraday's law)}, \tag{1.9c}$$

$$\nabla \times \mathbf{B} = \mu\left(\mathbf{J} + \varepsilon\frac{\partial}{\partial t}\mathbf{E}\right) \qquad \text{(Ampère's law modified by Maxwell)}. \tag{1.9d}$$

Where $\mathbf{E} \equiv \mathbf{E}(x, y, z, t)$ is the electric field, $\mathbf{B} \equiv \mathbf{B}(x, y, z, t)$ is the magnetic induction, $\varepsilon \equiv \varepsilon(x, y, z, t)$ and $\mu \equiv \mu(x, y, z, t)$ are the electric permittivity and magnetic permeability, $\rho \equiv \rho(x, y, z, t)$ is the charge density and $\mathbf{J} \equiv \mathbf{J}(x, y, z, t)$ is the current density. The operator $\nabla \cdot \bullet$ denotes the divergence of a vectorial field (scalar function) and $\nabla \times \bullet$ is the curl operator (vectorial function), where $\bullet$ is a generic vectorial field. The Cartesian coordinates (x, y, z) and time t have been omitted in favour of a more compact notation. Although electromagnetic optics provides the most complete framework for classical optical phenomena, it is possible to move away from the vectorial treatment of light towards a scalar wave theory in order treat a large variety of relevant optical phenomena. This simplified treatment of light is commonly referred to scalar wave optics or physical optics (cf. Fig. 1.3 for the hierarchical representaion of optical theories). X-ray wave-fields in free-space are discussed in §1.2.1 - *Free-space propagation* and their transmission through generic refractive optical elements is discussed in §1.2.2 - *Transmission elements*.

1.2.1 Free-space propagation

In order to describe wave-fields in free-space under the scalar theory, one usually starts[19] by obtaining the Maxwell equations for free-space (vacuum). This is done considering that the

---

[19] The developments in §1.2.1 - *Free-space propagation* are inspired by the derivations from [Paganin, 2006, *§1*] and [Goodman, 2017, *§3* & *§4*].

medium where the wave-fields exist are uncharged and non-conducting, which is done by letting $\rho = 0$ and $\mathbf{J} = \mathbf{0}$ in Eqs. 1.9a and 1.9d:

$$\nabla \cdot \mathbf{E} = \mathbf{0}, \tag{1.10a}$$

$$\nabla \times \mathbf{B} = \mu_0 \varepsilon_0 \frac{\partial}{\partial t} \mathbf{E}. \tag{1.10b}$$

Where ε_0 and μ_0 are the vacuum electric permittivity and magnetic permeability. Direct consequences of deriving the scalar theory for waves in vacuum is that the medium is assumed to be linear (permittivity is linear), isotropic (permittivity is independent of polarisation direction), homogeneous (permittivity is constant within the region of propagation), nondispersive (permittivity is independent of wavelength throughout the region of interest) and, finally, nonmagnetic (the magnetic permeability constant and equal to μ_0) [Goodman, 2017, *§3.2*].

The wave-equation

The d'Alembert wave-equation for the electric field can be obtained by applying the curl operator $\nabla \times \bullet$ to both sides of Faraday's law, using the vector calculus identity $\nabla \times (\nabla \times \bullet) = \nabla(\nabla \cdot \bullet) - \nabla^2 \bullet$ to the electric field $\mathbf{E}$, and making use of the Maxwell equations for free-space (Eqs. 1.9 and 1.10):

$$\left(\varepsilon_0 \mu_0 \frac{\partial^2}{\partial t^2} - \nabla^2 \right) \mathbf{E} = \mathbf{0}. \tag{1.11}$$

The same reasoning can be applied to the magnetic induction $\mathbf{B}$:

$$\left(\varepsilon_0 \mu_0 \frac{\partial^2}{\partial t^2} - \nabla^2 \right) \mathbf{B} = \mathbf{0}. \tag{1.12}$$

Each vectorial component of **E** and **B** satisfies individually a scalar form of the wave-equation and each of the individual components are uncoupled from each other - cf. [Paganin, 2006, *§1.1*]. It is possible to define a (complex) scalar field $u(x, y, z, t)$ representing any of the components of **E** or **B** such that:

$$\left(\frac{1}{c^2} \frac{\partial^2}{\partial t^2} - \nabla^2 \right) u = 0. \tag{1.13}$$

with $c = 1/\sqrt{\varepsilon_0 \mu_0}$ (speed of light in vacuum). This complex scalar solution of the d'Alembert equation can be spectrally decomposed as a superposition of monochromatic fields using the Fourier transform:

$$u(x, y, z, t) = \frac{1}{\sqrt{2\pi}} \int_{-\infty}^{\infty} U(x, y, z) \exp\left(-i\omega t\right) \mathrm{d}\omega \tag{1.14}$$

The argument of the integral in Eq. 1.14 implies that the monochromatic field can be written down as a product of a spatial dependent function and a time dependent function (separation of variables) [Paganin, 2006, *§1.2*]. Plugging Eq. 1.14 in Eq. 1.13:

$$(\nabla^2 + k^2) U(x, y, z) = 0, \tag{1.15}$$

where $k = \omega/c = 2\pi/\lambda$ is the wavevenumber and λ, the associated wavelength. Eq. 1.15 is know as the Helmholtz equation. Given a volume in space and boundary conditions, the scalar diffraction theory consists in finding the solutions to q. 1.15 [Paganin, 2006, *§1.2*]. One of the simplest solutions to the Helmholtz equation in free-space is the so-called plane-wave:

$$U(\mathbf{r}) = A\exp(-i\mathbf{k}\cdot\mathbf{r}) = A\exp[-i(k_x x + k_y y + k_z z)], \tag{1.16}$$

where A is a complex constant (complex envelope), $\mathbf{k} = (k_x, k_y, k_z)$ is the wavevector such as $|\mathbf{k}| = k$ and $\mathbf{r} = (x, y, z)$. A second solution is a spherical wave:

$$U(\mathbf{r}) = \frac{A}{r}\exp(-ikr), \tag{1.17}$$

here $|\mathbf{r}| = r = \sqrt{x^2+y^2+z^2}$ is the distance from the origin of the wavefront. Defining henceforth the $z-$axis as the optical axis, the paraboloidal wave is given by:

$$U(\mathbf{r}) = \frac{A}{z}\exp(-ikz)\exp\left(-ik\frac{x^2+y^2}{2z}\right), \tag{1.18}$$

Eq. 1.18 is a paraxial[20] approximation of the spherical wave defined by Eq. 1.17. The paraboloidal wave does not, however, formally satisfy the Helmholtz equation as defined by Eq. 1.15. It does obey a paraxial form of the Helmholtz wave-equation[21]. This assumes a plane wave as defined in Eq. 1.16 can be modulated by a complex envelope $A(\mathbf{r})$ that slowly varies along a distance $\lambda = 2\pi/k$ along the optical axis z. It can be shown[22] that plugging this modulated plane-wave in the Helmholtz equation (Eq. 1.15) leads to:

$$\left(i2k\frac{\partial}{\partial z} - \nabla_T^2\right)A = 0. \tag{1.19}$$

where $\nabla_T^2 \equiv \partial^2/\partial x^2 + \partial^2/\partial y^2$ is the transverse Laplace operator. Eq. 1.19 is the paraxial Helmholtz equation [Saleh and Teich, 2019, *§2.2*]. Determining the evolution in space of the solutions to the Helmholtz equation (Eq. 1.15) or the paraxial Helmholtz equation (Eq. 1.19) is the core of what is called scalar diffraction theory.

Fresnel diffraction

Consider a Cartesian coordinate system where the $z-$axis is the optical axis (cf. Fig 1.4), suppose a transverse component of a wave-field complying with Eq. 1.15 can be completely described at a position z_0, that is, $U(x, y, z_0)$ is known for all the $xy-$plane. The wave-field

---

[20] Consider a spherical wave with $\mathbf{r} = (x, y, z)$ and that $|\mathbf{r}| = r = \sqrt{x^2+y^2+z^2}$ and take a sufficiently large coordinate along the $z-$axis (optical axis). The paraxial approximation of the spherical wave can be obtained by choosing points in the $xy-$plane near enough to the $z-$axis so that $\sqrt{x^2+y^2} \ll z$ holds. It follows that $r = z\sqrt{1+(x^2+y^2)/z^2}$ can be expanded in a Taylor series: $r \approx z + (x^2+y^2)/2z$ and directly plugged into the exponent in Eq. 1.17 leading to Eq. 1.18 [Saleh and Teich, 2019, *§2.2*]. The paraxial approximation of the spherical wave is also called the Fresnel approximation.

[21] The Gaussian beam is another very common solution of the paraxial Helmholtz equation. Consider the paraboloidal wave as defined by Eq. 1.18. Evaluating it along the optical axis at a position $z^+ = z + \Delta z$ also yields a solution to the paraxial Helmholtz equation (cf. Eq. 1.19) even if Δz is a purely imaginary number [Saleh and Teich, 2019, *Exercise 2.2-2*]. The Gaussian beam can be obtained from the paraboloidal wave by substituting z in Eq. 1.18 by $z - iz_0$, for a real z_0 [Saleh and Teich, 2019, *§3.1*]

[22] The complete derivation of the paraxial wave-equation can be found in [Saleh and Teich, 2019, *§2.2.C*].

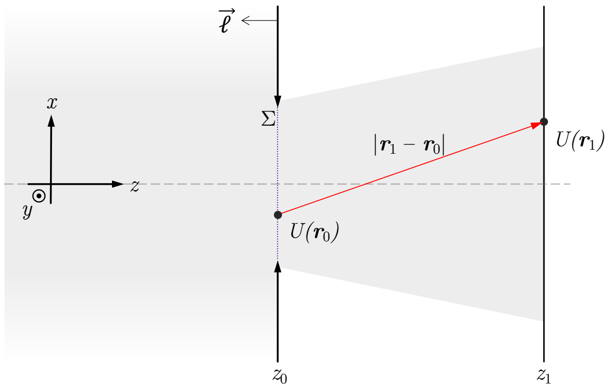

Fig. 1.4.: Scalar diffraction problem geometry. Σ represents the input plane, where the electric field is completely defined, that is, $U(x_0, y_0, z_0)$ is known for all (x_0, y_0, z_0), ℓ is a orthonormal vector to Σ. Scalar diffraction theory concerns the calculation of an electric field $U(x_1, y_1, z_1)$ in the output plane with the knowledge of it in the input plane.

distribution in a parallel plane at a position z_1 of the optical axis can be calculated using the first Rayleigh-Sommerfeld diffraction equation [Goodman, 2017, *Eq. 3-42*]:

$$U(\mathbf{r}_1) = \frac{k}{i2\pi} \iint\limits_{\Sigma} U(\mathbf{r}_0) \frac{\exp\left(ik|\mathbf{r}_1 - \mathbf{r}_0|\right)}{|\mathbf{r}_1 - \mathbf{r}_0|} \cos\left(\theta\right) \, \mathrm{d}s, \tag{1.20}$$

where $\mathbf{r}_0 = (x_0, y_0, z_0)$, $\mathbf{r}_1 = (x_1, y_1, z_1)$, $\vec{\ell}$ is a normal vector parallel to the optical axis, θ is the angle between $-\vec{\ell}$ and the vector $\mathbf{r}_1 - \mathbf{r}_0$; and Σ is the $xy-$plane in z_0 where the integration takes place - cf. Fig 1.4. Eq. 1.20 assumes that $|\mathbf{r}_1 - \mathbf{r}_0| \gg \lambda$ and is often referred to as the Huygens-Fresnel principle[23] [Goodman, 2017, *§3.7*]. In the paraxial approximation $\cos\left(\theta\right) \approx 1$ and $|\mathbf{r}_1 - \mathbf{r}_0| = \sqrt{(x_1 - x_0)^2 + (y_1 - y_0)^2 + L^2} \approx L + [(x_1 - x_0)^2 + (y_1 - y_0)^2]/2L$, where $L = z_1 - z_0$ with $L \gg |x_1 - x_0|$ and $L \gg |y_1 - y_0|$. The latter is know as the Fresnel approximation. Using this, Eq. 1.20 can be expressed as:

$$U(x_1, y_1, z_1) = \frac{k \exp\left(ikL\right)}{2\pi i L} \iint\limits_{-\infty}^{\infty} U(x_0, y_0, z_0) \exp\left\{ \frac{ik}{2L} \left[(x_1 - x_0)^2 + (y_1 - y_0)^2\right] \right\} \mathrm{d}x_0 \mathrm{d}y_0, \tag{1.21}$$

which is know as the Fresnel diffraction integral [Goodman, 2017, *§4.2*]. The accuracy of Eq. 1.21 is limited by the Taylor expansion of $|\mathbf{r}_1 - \mathbf{r}_0| = L\sqrt{1 + \rho^2/L^2}$, where $\rho = \sqrt{(x_1 - x_0)^2 + (y_1 - y_0)^2}$, which is usually usually truncated on the linear term[24], provided that the phase induced by the quadratic term of the expansion is much less than the Rayleigh's quarter-wave criterion, which limits the maximum phase error to $\pi/4$ radians [Born et al., 1999, *§9.3*]. Neglecting high-order terms in the approximation of the square-root in Eq. 1.21 can be done if:

$$\sqrt[3]{\frac{\rho^4}{\lambda}} \ll z. \tag{1.22}$$

---

[23] Eq. 1.20 expresses the wave-field evaluated in $\mathbf{r}_1$, that is, $U(\mathbf{r}_1)$ as a sum of spherical wave-fronts originating from a secondary sources modulated by $U(x_0, y_0, z_0)$ at each point $\mathbf{r}_0$ within the aperture Σ.

[24] The Taylor series expansion in teh vicinity of $v = 0$ is $\sqrt{1+v} = 1 + \frac{v}{2} - \frac{v^2}{8} + \frac{v^3}{16} + \mathcal{O}(v^4)$ and it converges for $|v| < 1$.

Fraunhofer diffraction

Still analysing Eq. 1.21, the quadratic term in the exponential part of the integrand can be expanded and rearranged:

$$\begin{aligned} U(x_1, y_1, z_1) = \frac{k \exp{(ikL)}}{2\pi i L} \exp\left[\frac{ik}{2L}(x_1^2 + y_1^2)\right] \cdot \\ \cdot \iint\limits_{-\infty}^{\infty} U(x_0, y_0, z_0) \exp\left[\frac{ik}{2L}(x_0^2 + y_0^2 - 2x_1x_0 - 2y_1y_0)\right] \mathrm{d}x_0\mathrm{d}y_0. \end{aligned} \quad (1.23)$$

Applying the Rayleigh's quarter-wave criterion to the $k(x_0^2 + y_0^2)/2L$ term in Eq. 1.23:

$$4\frac{x_0^2 + y_0^2}{\lambda} \ll z, \quad (1.24)$$

which allows to further simplify Eq. 1.21 into:

$$\begin{aligned} U(x_1, y_1, z_1) = \frac{k \exp{(ikL)}}{2\pi i L} \exp\left[\frac{ik}{2L}(x_1^2 + y_1^2)\right] \cdot \\ \cdot \iint\limits_{-\infty}^{\infty} U(x_0, y_0, z_0) \exp\left[-\frac{ik}{L}(x_1x_0 + y_1y_0)\right] \mathrm{d}x_0\mathrm{d}y_0, \end{aligned} \quad (1.25)$$

Eq. 1.25 is known as the Fraunhofer diffraction integral.

Numerical computation of the Fresnel and Fraunhofer diffraction

The numerical calculation of the diffraction integrals is a vast subject and has been addressed by many authors [D'Arcio et al., 1994], [Kelly, 2014], [Goodman, 2017, *§5*], [Buitrago-Duque and Garcia-Sucerquia, 2019] and [Chubar and Celestre, 2019], among others. This arises from the fact that unless the resulting field $U(x_1, y_1, z_1)$ has an analytical representation, numerically calculating the integrals in Eq. 1.21 and Eq. 1.25 will forcefully result in tackling issues like replicas and aliasing. This comes from the fact that the diffraction integrals are intimately connected with the Fourier analysis.

Upon closer inspection, it is apparent that the Fresnel diffraction integral (Eq. 1.21) is a two-dimensional convolution type integral [Goodman, 2017, *§2.1*]:

$$g(x, y) * h(x, y) = \iint\limits_{-\infty}^{\infty} g(u, v)h(x - u, y - u)\, \mathrm{d}u\mathrm{d}v, \quad (1.26)$$

which can be computed by invoking the convolution theorem:

$$g(x, y) * h(x, y) = \mathcal{F}^{-1}\{\mathcal{F}\{g(x, y)\} \cdot \mathcal{F}\{h(x, y)\}\}, \quad (1.27)$$

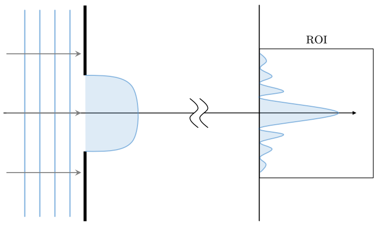

(a) analytical solution

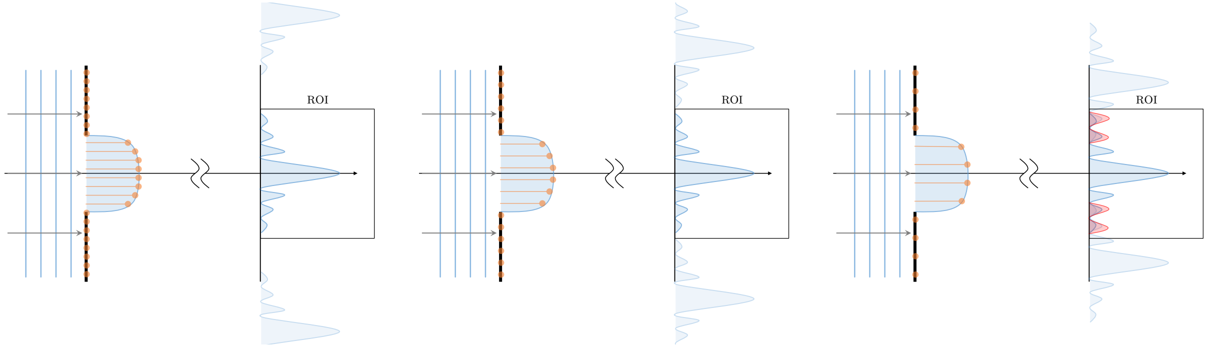

(b) (c) (d)

Fig. 1.5.: Replicas and aliasing from numeric calculations of the diffraction integrals. (a) analytical solution of the integrals have no signal replicas. Sampling the input plane signal will introduce replicas in the output plane [Kelly, 2014]. (b) appropriate sampling - cf. Eq. 5 in [Chubar and Celestre, 2019] - makes the unavoidable replicas appear far enough so that cross-talk between them is negligible within the region of interest (ROI). (c) coarser sampling brings replicas closer together to a point that (d) replicas are so close that aliasing is apparent (red signal).

where $\mathcal{F}\{\bullet\}$ is the two-dimensional Fourier transform and $\mathcal{F}^{-1}\{\bullet\}$ denotes inverse Fourier transform:

$$\mathcal{F}\{g(x,y)\} = \iint\limits_{-\infty}^{\infty} g(x,y)\exp\big[-i2\pi(f_x x + f_y y)\big]\,\mathrm{d}x\mathrm{d}y \tag{1.28a}$$

$$\mathcal{F}^{-1}\{G(f_x,f_y)\} = \iint\limits_{-\infty}^{\infty} G(f_x,f_y)\exp\big[i2\pi(f_x x + f_y y)\big]\,\mathrm{d}f_x\mathrm{d}f_y. \tag{1.28b}$$

It is common to represent the Fourier analysis and syntheses as $\mathcal{F}\{g(x,y)\} \equiv G(f_x,f_y)$ and $\mathcal{F}^{-1}\{G(f_x,f_y)\} \equiv g(x,y)$, where (f_x,f_y) are generally referred to as frequencies. The Fresnel diffraction integral in Eq. 1.21 can be rewritten as a convolution (Eq. 1.27) where the kernel, that is $\mathcal{F}\{h(x,y)\}$, has an analytical solution:

$$\frac{k}{2\pi iL}\mathcal{F}\{h(x,y)\} = \frac{k}{2\pi iL}\mathcal{F}\bigg\{\exp\bigg[\frac{ik}{2L}(x^2+y^2)\bigg]\bigg\} = \exp\bigg[-\frac{i2L\pi^2}{k}(f_x^2+f_y^2)\bigg], \tag{1.29}$$

This formulation allows to calculate the Fresnel diffraction integral (Eq. 1.21) by means of the convolution theorem (Eq. 1.27) by applying a Fourier transform to the input field, multiplying it by an analytical kernel and applying an inverse Fourier transform to the result. It is also evident that the Fraunhofer diffraction integral (Eq. 1.25) is a Fourier type integral, differing from Eq. 1.28a by a multiplicative factor outside the integrand.

It should be clear, then, that the paraxial diffraction equations are intertwined with Fourier analysis. Numerically computation of the Fresnel or Fraunhofer diffraction implies *a*-) sampling the input plane $U(x_0, y_0, z_0)$ and *b*-) limiting its extent by either defining an aperture of finite extent or simply by cropping (truncating) the input field. It follows from sampling theory and the discrete Fourier transform (DFT) [Bracewell, 2000, *§10* & *§11*] that sampling the input field causes replicas of the main signal to appear (cf. Fig. 1.5). Generally, the finer the sampling in the input plane, the further apart the replicas. Consequently, the coarser the mesh, the closer they become until the replicas are close enough to each other that they start cross-talking. The interaction between the main signal and its replicas is called aliasing. Due to the finite extent of the input plane (either by limiting the signal with an aperture or by simply truncating it), it is inevitable that power from neighbouring replicas leaks into each other. Sampling should be sufficiently high to make this inevitable cross-talk negligible [Kelly, 2014]. On the other hand, a very dense sampling leads to very inefficient calculations largely because of the size of the input and output planes - cf. considerations in [Goodman, 2015, *§5*]. Efforts towards memory and CPU efficient computation of the Fresnel free-space propagator in Fourier optics have been reported in [Chubar and Celestre, 2019].

1.2.2 Transmission elements

The propagation of X-rays in the presence of matter can also be modelled with the Maxwell equations (Eqs. 1.9). It is possible to derive a Helmholtz equation in the presence of scatterers with a similar treatment given in the previous section, albeit considerably more algebraic - a detailed account of the derivation is given by [Paganin, 2006, *§2.1*]. Restricting the analysis to linear isotropic non-magnetic materials where both the electric permittivity and magnetic permeability are independent of time (static medium) and considering again that the waves exist in a uncharged and non-conducting material, that is, $\rho = 0$ and $\mathbf{J} = \mathbf{0}$:

$$\left[\varepsilon(x,y,z)\mu_0\frac{\partial^2}{\partial t^2} - \nabla^2\right]\mathbf{E}(x,y,z,t) = \mathbf{0}, \tag{1.30a}$$

$$\left[\varepsilon(x,y,z)\mu_0\frac{\partial^2}{\partial t^2} - \nabla^2\right]\mathbf{B}(x,y,z,t) = \mathbf{0}. \tag{1.30b}$$

considering that the scatterers are sufficiently slowly varying when compared to the radiation wavelength - cf. Eqs. 2.18-2.21 in [Paganin, 2006]. Eqs. 1.30 resemble the vectorial wave-equations 1.11 and 1.12. This enables application of the same scalar treatment used for deriving the Helmholtz equation in free-space, that is, to propose a scalar field $u(x,y,z,t)$ such as:

$$\left[\varepsilon(x,y,z)\mu_0\frac{\partial^2}{\partial t^2} - \nabla^2\right]u = 0, \tag{1.31}$$

and spectrally decompose u in its monochromatic Fourier components $U(x,y,z)\exp(-i\omega t)$ (cf. Eq. 1.14):

$$u(x,y,z,t) = \frac{1}{\sqrt{2\pi}}\int\limits_{-\infty}^{\infty} U(x,y,z)\exp(-i\omega t)\,\mathrm{d}\omega$$

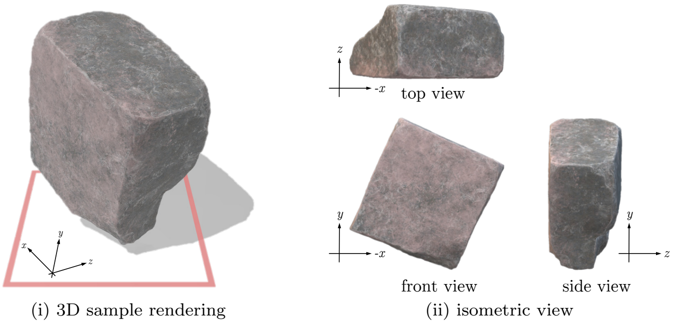

(i) 3D sample rendering (ii) isometric view

(a) sample description

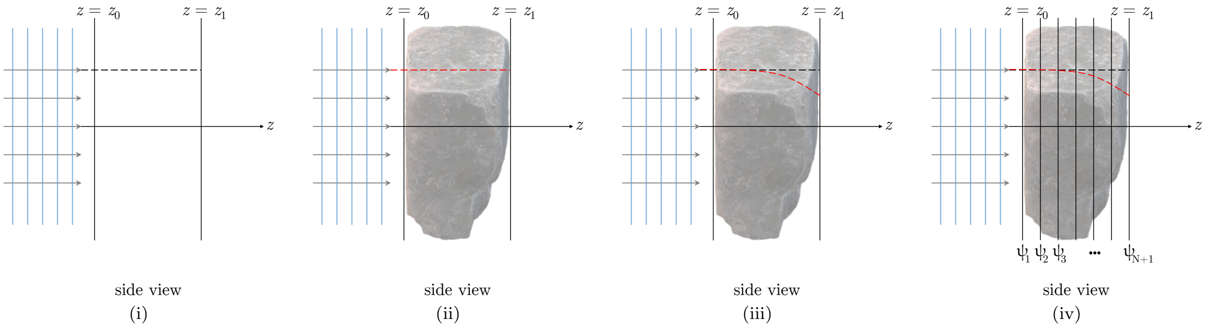

(b) transmission element representation

Fig. 1.6.: (a) arbitrary-shaped scattering volume in free-space. (b) transmission element representation of said scatterer. The 3D model was taken from the *3D shapes* library in the Paint 3D software from the Microsoft Corporation.

This Fourier integral can be substituted into Eq. 1.31, giving the Helmholtz equation in the presence of scatterers[25]:

$$[\nabla^2 + k^2 n^2(x,y,z)]U(x,y,z) = 0, \tag{1.32}$$

where n is the wavelength-dependent refractive index such that $n(x,y,z)^2 \equiv \varepsilon(x,y,z)/\varepsilon_0$. This version of the Helmholtz equation for a inhomogeneous medium can rarely be solved exactly and approximations are necessary to handle it [Paganin, 2006, *§2.1*]. The same argument used to derive the paraxial Helmholtz equation (Eq. 1.19) can be applied here. Assuming a plane wave (Eq. 1.16) modulated by a complex envelope $A(\mathbf{r})$ slowly varying along a distance λ and substituting it into Eq. 1.32 yields:

$$\left\{2ik\frac{\partial}{\partial z} - \nabla_T^2 + k^2\left[n^2(x,y,z) - 1\right]\right\}A = 0. \tag{1.33}$$

which is known as the paraxial Helmholtz equation in matter. Eq. 1.33 is compatible to the treatment used for propagating the wave-fields in free-space - cf. [Paganin, 2006, *Eq. 2.33*]. Notice that Eq. 1.33 reduces to Eq. 1.19 for $n = 1$.

The projection approximation

Consider an arbitrary-shaped scattering volume as shown in Fig. 1.6(a). Suppose that such scatterer is completely confined within a region $z_0 \leq z \leq z_1$ and outside that there is vacuum. Let this sample be illuminated by a plane-wave moving along the positive direction of the optical

---

[25] cf. [Paganin, 2006, *Eq. 2.28*].

axis ($z-$axis). In the absence of the scatterer, the gradient between the $z = z_0$ and $z = z_1$ planes is very well defined and parallel to the optical axis, as shown in Fig. 1.6(b-i). It follows from [Paganin, 2006, *§2.2*] that if the scatterer is sufficiently weak as to minimally disturb the path that the wave-field would have taken in its absence, cf. Fig. 1.6(b-ii), the transmission of a wave-field through this sample is given by:

$$U(x,y,z_1) \approx \exp\left\{ -\frac{ik}{2} \int\limits_{z=z_0}^{z=z_1} \left[1 - n^2(x,y,z)\right] \,\mathrm{d}z \right\} U(x,y,z_0). \tag{1.34}$$

Eq. 1.34 shows that the effect of a weak scatterer can be accounted by a multiplicative complex transmission element represented by the complex exponential. In the X-ray regime the index of refraction is typically very close to unity and often expressed as $n = 1 - \delta + i \cdot \beta$ [Als-Nielsen and McMorrow, 2011, *§1.6*], which allows for the approximation $1 - n(x,y,z)^2 \approx 2\left[\delta(x,y,z) + i \cdot \beta(x,y,z)\right]$ that can be substituted in Eq. 1.34. The $z-$dependence of δ and β is abandoned in the projection approximation, hence the complex transmission element in Eq. 1.34 can be reduced to:

$$\begin{aligned} \mathrm{T}(x,y,z) &= \exp\left\{ -ik \int\limits_{z=z_0}^{z=z_1} \left[\delta(x,y) + i \cdot \beta(x,y)\right] \,\mathrm{d}z \right\} \\ &= \exp\left\{ -ik\left[\delta(x,y) + i \cdot \beta(x,y)\right]\Delta_z(x,y) \right\}, \\ \mathrm{T}\left[\Delta_z(x,y)\right] &= \sqrt{\mathrm{T}_{\mathrm{BL}}(x,y)} \exp\left[i\phi(x,y)\right]. \end{aligned} \tag{1.35}$$

and:

$$\begin{aligned} \mathrm{T}_{\mathrm{BL}}(x,y) &= \exp\left[-2k\beta(x,y)\Delta_z(x,y)\right] \qquad (1.36a) \\ &= \exp\left[-\mu(x,y)\Delta_z(x,y)\right], \\ \phi(x,y) &= -k\delta(x,y)\Delta_z(x,y). \qquad (1.36b) \end{aligned}$$

Δ_z is the projected thickness along the $z-$axis and it depends on the transverse coordinates (x,y), which can be dropped out for a more concise representation.

Because of the multiplicative nature of the transmission element, Eq. 1.35 can be put in operator[26] form:

$$\mathrm{T}(\Delta_z) \bullet = \sqrt{\mathrm{T}_{\mathrm{BL}}(\Delta_z)} \exp\left[i\phi(\Delta_z)\right] \ \bullet . \tag{1.37}$$

Eq. 1.36a shows the absorption experienced by the wave-field when passing through matter (Beer-Lambert law) and Eq. 1.36b shows the phase-shift experienced by the wave-field. The coefficient μ multiplying Δ_z in T_{BL} (Eq. 1.36a) is known as the linear attenuation coefficient μ [Als-Nielsen and McMorrow, 2011, *§1.6*].

---

[26] Using the operator formulation was inspired by discussions with David Paganin (Monash University, Australia) and Vincent Favre-Nicolin (ESRF, France).

The multi-slice approximation

For the cases where the projection approximation may not be adequate to correctly represent the scattering volume in question, multi-slicing techniques[27] (MS) can be used for describing the wave-field propagation inside an arbitrary-shaped scattering volume - cf. discussion in [Paganin, 2006, *§2.7*], [Li et al., 2017] and [Munro, 2019].

Consider the scatterer depicted in Fig. 1.6(a). If its presence considerably disturbs the path that the wave-field would have taken in its absence, cf. Fig. 1.6(b-iii), it is possible to section the sample into a number N of parallel slabs until the projection approximation is valid between two adjacent slices - Fig. 1.6(b-iv). The projected thickness Δ_z to be used in Eq. 1.35 is the one in between slices, which are $\Delta_S = (z_1 - z_0)/N$ apart from each other. Each slice represented as a thin element in projection approximation is separated by vacuum. The propagation of a wave-field propagation through this sample is done step-wise, where each step is composed of a multiplication by a complex transmission element in projection approximation (cf. Eq. 1.35) and a Fresnel free-space propagation (Eq. 1.21) over a distance Δ_S. The output field from this operation is again multiplied by complex transmission element in projection approximation followed by a free-space propagation from the plane ψ_j to the ψ_{j+1} - refer to Fig. 1.6(b-iv). This operation is done recursively N times until the wave-field emerges from the sample. The multi-slicing transmission operator can be written in operator form as:

$$\mathrm{T_{MS}} = \prod_{j=1}^{N} \mathcal{D}(\Delta_S)\left[\mathrm{T}_j(\Delta_z) \;\bullet\right] \tag{1.38}$$

where $\prod$ indicates concatenation of operators to be performed from right to left, $\mathcal{D}(\Delta_S)$ is the operator formulation of the Fresnel free-space propagation over a distance Δ_S:

$$\mathcal{D}(\Delta_S) \bullet = \frac{k \exp\left(ik\Delta_S\right)}{2\pi i \Delta_S} \iint_{-\infty}^{\infty} \bullet \; \exp\left\{ \frac{ik}{2\Delta_S}\left[(x_1 - x)^2 + (y_1 - y)^2\right] \right\} \mathrm{d}x\mathrm{d}y, \tag{1.39}$$

and $\mathrm{T}_j(\Delta_z)$ is the $j-$th complex transmission element operator in projection approximation associated with the $j-$th slice given by Eq. 1.37.

– On the validity of the Fresnel approximation for short propagation distances[28]

A case of particular importance for X-ray optical design is the application of the Fresnel propagators in real or reciprocal space to very short propagation distances (from millimetres to hundreds of micrometres) at hard X-ray energies (wavelength of the order of the Ångstrom) with physical apertures of the order of the millimetre. For situations of practical interest such as the one just described, Eq. 1.22 is generally very restrictive. This section presents conditions under which this constraint can be relaxed and even overlooked.

---

[27] This technique was first described in the context of the scattering of electrons by atoms and crystals [Cowley and Moodie, 1957].

[28] The author acknowledges the fruitful discussions with David Paganin (Monash University, Australia), Peter Munro (University College London, England), Oleg Chubar (Brookhaven National Lab., USA) and Chris Jacobsen (Northwestern University/Argonne National Lab., USA) when investigating the application of the Fresnel approximation for short propagation distances.

Consider an X-ray wavefield with wavelength $\lambda = 1$ Å fully illuminating an aperture $A = 500\ \mu$m situated at $z = z_0$ along the optical axis as shown in Fig. 1.4. The X-rays passing through such an aperture will illuminate an identical aperture A at a distance $z_1 - z_0 = L$. Suppose one wants to place the second aperture at a distance L such that it is possible to calculate the field distribution in z_1 using the Fresnel diffraction integral in Eq. 1.21. Using Eq. 1.22 with the extreme points[29] given by $(x_0 = -A/2, y_0 = 0)$ and $(x_1 = A/2, y_1 = 0)$, one concludes that $L \gg 86$ mm. However, if one wants to place the second aperture at a distance of $L = 1$ mm and still be able to safely apply Eq. 1.21 to calculate the field distribution in z_0, the apertures should be reduced to $A \ll 18\ \mu$m according to Eq. 1.22. The situation just described is at odds with the employment of the Fresnel propagator for very short propagation distances at hard X-ray energies with physical apertures of the order of the millimetre. Yet, with the exception of [Ali and Jacobsen, 2020], that explicitly uses the Huygens-Fresnel principle [Goodman, 2017, *§3.7*] in its reciprocal form for the wavefield propagation[30], authors make extensive use of the Fresnel propagator for multi-slicing applications under these conflicting conditions [Li et al., 2017; Munro, 2019; Celestre et al., 2020]. Possibly one of the few explicit mentions of the propagation distance relation to the transverse plane size applied to multi-slicing techniques is given by Eq. 15 in [Ishizuka and Uyeda, 1977]. It turns out that, indeed, Eq. 1.22, when applied to a collimated beam (either a plane-wave or a slowly diverging/converging wave), is too restrictive and can be overlooked when applied to MS modelling of weak scatterers.

In [Southwell, 1981] the Fresnel diffraction integral (Eq. 1.21) is directly compared with the Huygens-Fresnel integral (Eq. 1.20) in terms of amplitude and phase, it was shown that the Fresnel approximation has good accuracy: within 2% in amplitude and 0.02 rad in phase, when compared to the Huygens-Fresnel integral. The findings hold even for very high Fresnel numbers[31] along the optical axis within the projected aperture, that is, $\forall\ (x, y) \in A$ - [cf. Figs. 1–4 ibid.]. However, for points outside that region ($\forall\ (x, y) \notin A$) at very high Fresnel numbers (shadow region), the approximation breaks down: although the amplitude calculation retains good agreement, the phase errors become unacceptably high [cf. Fig. 10 ibid.].

Another study that confirms the validity of the Fresnel approximation for a collimated beam being propagated over a very short distance is presented by [Rees, 1987]. This work not only confirms the numerical findings in [Southwell, 1981] but also provides physical explanations, some analytical formulations and derives quantitatively the shape of the region where the Fresnel approximation is valid. By applying directly Eq. 1.22 and Eq. 1.24, one obtains the the regions of validity for both Fresnel and Fraunhofer integrals as shown in Fig. 1.7(a), in which case, $z_{Fresnel}$ is given by Eq. 1.22 - cf. Eq. 7 in [Rees, 1987]. The relaxing of such constraints is done by invoking the concept of Fresnel zones[32] and how much contribution they have to the total amplitude and phase of the propagated beam. Considering that the first zone is unobstructed by

---

[29] For simplicity, the 1D case is analysed, but the conclusions are easily translated to a 2D system if $U(x, y) = U(x)U(y)$.

[30] cf. Eq. 22 or procedure *PropShort* in Algorithm 1 from [Ali and Jacobsen, 2020].

[31] The Fresnel number is defined as $N_F = a^2/\lambda L$, where a is the half aperture, λ is the wavelength and L is the propagation distance. A high Fresnel number indicates the region known as near-field, while the far-field region is known for its low Fresnel numbers. In [Southwell, 1981], it is reported that even for $L < a$ good agreement between the Fresnel approximation and the Huygens-Fresnel integral is found for a point within the projected aperture.

[32] cf. [Hetch, 2017, *§10.3.1*]

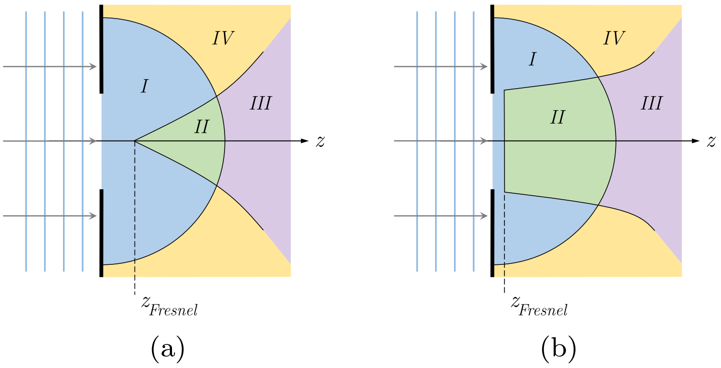

(a) (b)

Fig. 1.7.: The Fresnel and Fraunhofer approximations region of validity according to the (a) Eqs. 1.22 and 1.24. For a gently divergent, convergent or plane wavefield the constraints can be relaxed, increasing the region o applicability of said approximations. Region *I* represents the shadow zone, where neither approximations are valid. Region *II* is where only the Fresnel approximation is valid. In region *III*, both approximations coexist, the Fraunhofer being advantageous computationally. Region *IV* illustrates an area where only the Fraunhofer approximation is valid - this counter-intuitive result is discussed in [Rees, 1987], but is out of the scope here. The boundaries between regions *I* and *II* have been exaggerated for clarity. This figure is adapted from Fig. 4 and Fig. 5 in [Rees, 1987].

the aperture A, which is the case for all points not within the shadow region, the distance where the Fresnel diffraction integral starts to be accurate can be as low as $z_{Fresnel} = 2\lambda$ - cf. Eq. 9 in [Rees, 1987]. This more relaxed regime is represented in Fig. 1.7(b).

Based on the results from [Southwell, 1981] and [Rees, 1987], it is possible to affirm that provided the object is illuminated with a plane wave and the output field is calculated in the vicinity of the projected aperture, the application of the Fresnel diffraction integral to very short propagation distances for hard X-ray optics modelling with MS techniques is not limited to the constraints imposed by Eq. 1.22. Cases of interest often have non-plane-wave illumination and require special handling to ensure MS with the Fresnel diffraction integral yields accurate results. Approaches that rely on spherical-to-plane-wave conversion are often employed to avoid such accuracy issues: the angular spectrum of plane waves decomposition [Paganin, 2006, *§1.3*][33], the Fresnel-scaling theorem [Paganin, 2006, *§A*], the divergent-beam-to-plane-wave transformation from [Munro, 2019] and the analytical treatment of the quadratic phase term [Chubar and Celestre, 2019], which is of particular interest within the context of this work, as it is the chosen method for the free-space wavefront propagation simulations presented here.

– Real and reciprocal space Fresnel propagators at short propagation distances

Because of the equivalency of the Fresnel diffraction integral (Eq. 1.21) and the convolution integral (Eq. 1.26), one can define the kernel of the Fresnel transform in real-space as:

$$h(x,y) = \exp\left[\frac{i\pi}{\lambda L}(x^2+y^2)\right], \tag{1.40}$$

---

[33] Also in [Goodman, 2017, *§3.10* & *§4.2.4*].

while the kernel of the Fresnel transform in reciprocal-space is given by:

$$H(f_x, f_y) = \exp\left[-i\pi\lambda L(f_x^2 + f_y^2)\right]. \tag{1.41}$$

The Eqs. 1.40 and 1.41 are related by: $H(f_x, f_y) = i/(\lambda L) \cdot \mathcal{F}\{h(x, y)\}$ (cf. Eq. 1.29). When propagating a wave-field over a very small distance L with the Fresnel diffraction integral, the argument of the exponential function in the transformation kernel in real-space becomes very large and the kernel becomes less well-behaved due to fast oscillations, consequently small propagation distances are better represented in the reciprocal space. This hints to the fact that when numerically evaluating the Fresnel transform for short propagation distances, methods using the reciprocal-space are more advantageous than in real-space and constrains like the Eq. 1.22 can be overlooked provided the non-paraxial components of the Fourier spectrum of the input wavefield is negligible.

– The analytical treatment of the of the quadratic radiation phase term[34]

Consider an uncollimated wave-field $U(x_0, y_0, z_0)$ in free-space (eg. Eq. 1.17). The phase term of such wave has quadratic terms with radii of curvature in the horizontal and vertical planes R_x and R_y and the transverse coordinates of the centre point $(x_\mathrm{c}, y_\mathrm{c})$. It is possible to rewrite $U(x_0, y_0, z_0)$ as:

$$U(x_0, y_0, z_0) = F(x_0, y_0, z_0)\exp\left\{\frac{ik}{2}\left[\frac{(x_0 - x_c)^2}{R_y} + \frac{(y_0 - y_c)^2}{R_y}\right]\right\}, \tag{1.42}$$

where $F(x_0, y_0, z_0)$ is the residual wavefront after the quadratic phase term is factorised. This residual wave-field satisfies the necessary conditions for the compliance with the Fresnel propagation of collimated beams through very short propagation distances as required by [Southwell, 1981] and [Rees, 1987]. Substituting Eq. 1.42 in the Fresnel diffraction integral (Eq. 1.21):

$$\begin{aligned} U(x_1, y_1, z_1) = \frac{k\exp(ikL)}{2\pi iL} \iint\limits_{-\infty}^{\infty} F(x_0, y_0, z_0) \cdot \\ \cdot \exp\left\{\frac{ik}{2}\left[\frac{(x_1 - x_0)^2 + (y_1 - y_0)^2}{L} + \frac{(x_0 - x_c)^2}{R_y} + \frac{(y_0 - y_c)^2}{R_y}\right]\right\} \mathrm{d}x_0 \mathrm{d}y_0, \end{aligned} \tag{1.43}$$

which can be conveniently expressed as:

$$U(x_1, y_1, z_1) = F(x_1, y_1, z_1)\exp\left\{\frac{ik}{2}\left[\frac{(x_1 - x_c)^2}{R_y + L} + \frac{(y_1 - y_c)^2}{R_y + L}\right]\right\}, \tag{1.44}$$

---

[34] The analytical treatment of the of the quadratic radiation phase terms was introduced in 2007 for the SRW code [Chubar et al., 2008] (cf. §1.3.2 in §1.3 - *X-ray optical simulations*). A more detailed description of the memory and CPU efficient computation of the Fresnel free-space propagator in Fourier optics simulations is given by [Chubar and Celestre, 2019], from which this section is partially based on.

with:

$$F(x_1,y_1,z_1)=\frac{k\exp{(ikL)}}{2\pi iL}\iint\limits_{-\infty}^{\infty}F(x_0,y_0,z_0)\cdot$$
$$\cdot\exp\left\{\frac{ik}{2L}\left[\frac{R_x+L}{R_x}\left(\frac{R_x x_1+Lx_c}{R_x+L}-x_0\right)^2+\frac{R_y+L}{R_y}\left(\frac{R_y y_1+Ly_c}{R_y+L}-y_0\right)^2\right]\right\}\mathrm{d}x_0\mathrm{d}y_0. \quad (1.45)$$

It is evident that much like Eq. 1.21, Eq. 1.45 is a convolution-type integral with analytical Fourier transform of the convolution kernel, hence the discussion presented in *Numerical computation of the Fresnel and Fraunhofer diffraction* in §1.2.1 - *Free-space propagation* is still applicable and the advantages of the wave propagation at very short distances in reciprocal space are maintained. The analytical treatment of the quadratic radiation phase term reduces significantly the required transverse sampling of the wave-field without compromising the accuracy of calculation, as the oscillations of the residual electric field are less rapid and require less dense sampling. Another advantage of such rewriting of the Fresnel diffraction integral is that the convolution shown in Eq. 1.45 takes place with respect to the scaled transverse coordinates $x_1\cdot R_x/(R_x+L)$ and $y_1\cdot R_y/(R_y+L)$. When using the convolution-theorem formulation of free-space propagation (cf. Eqs. 1.26 and 1.27), the scaled coordinates re-scale without any additional re-sampling nor interpolation the output plane by $\Delta x_1=\Delta x_0\cdot(R_x+L)/R_x$ and $\Delta y_1=\Delta y_0\cdot(R_y+L)/R_y$, where Δx_0 and Δy_0 are the input plane dimensions. The formulation shown in Eqs. 1.44 and 1.45 has singularities at $R_x+L=0$ and $R_y+L=0$, which happens when calculating the propagation of a wavefront after a focusing element at the image plane. The singularities can be dealt with by simply applying a $R'_x\neq 0$ and $R'_y\neq 0$ such as they are near R_x and R_y, but avoid the singularity. Using $R'_x\neq 0$ and $R'_y\neq 0$ still reduces the required transverse sampling and re-scales the output plane when propagating the wave-field by using the convolution-theorem formulation. The free-space propagation presented throughout this work is numerically calculated considering the analytical treatment of the quadratic radiation phase term as described in this section.

1.2.3 Optical coherence

Within the context of accelerator-based X-ray sources, more specifically, undulators in storage rings, it has been shown previously that increasing the brilliance of the X-rays by emittance matching (cf. Eq. 1.5 and Fig.1.2) implies increasing the coherent fraction of the emitted X-rays (Eq. 1.8). Later on, this increased coherent flux was used to justify using physical optics among the optical theories (Fig. 1.3) to provide a framework for describing X-rays propagation in free-space and within matter. The word coherence, be it temporal or spatial, has been used throughout this work but without a clear definition. This section should clarify its concept in the context of synchrotron radiation and provide some basic definitions[35].

Mutual coherence function and cross-spectral density

Emission of synchrotron radiation is a fundamentally random process and as such, it should be treated probabilistically. It has been demonstrated that although SR is intrinsically not

---

[35] The developments shown in this section are based on [Mandel and Wolf, 1995, §4].

stationary[36] nor homogeneous[37], under realistic conditions (practical cases of interest) SR can be considered quasi-stationary and quasi-homogeneous thus the formalism of statistical optics can be applied [Geloni et al., 2008].

Consider an arbitrary complex scalar wave-field $u(\mathbf{r}, t)$, where $\mathbf{r} = (x, y, z)$, satisfying the wave-equation 1.13. The correlation between the spatial and temporal fluctuations of $u(\mathbf{r}, t)$ at two different positions in space, that is $\mathbf{r}_1 = (x_1, y_1, z_1)$ and $\mathbf{r}_2 = (x_2, y_2, z_2)$, and separated by a time delay[38] $\tau = t_2 - t_1$ is given by the mutual coherence function[39] (MCF):

$$\Gamma(\mathbf{r}_1, \mathbf{r}_2, \tau) = \langle u^*(\mathbf{r}_1, t) u(\mathbf{r}_2, t + \tau) \rangle, \tag{1.46}$$

where $\bullet^*$ indicates the complex conjugate. The normalised form of this cross-correlation function (Eq. 1.46) is called the complex degree of coherence[40] (CDC):

$$\gamma(\mathbf{r}_1, \mathbf{r}_2, \tau) = \frac{\Gamma(\mathbf{r}_1, \mathbf{r}_2, \tau)}{\sqrt{\Gamma(\mathbf{r}_1, \mathbf{r}_1, 0)\Gamma(\mathbf{r}_2, \mathbf{r}_2, 0)}}, \tag{1.47}$$

where the averaged intensity at a point $\mathbf{r}$ is given by: $\langle I(\mathbf{r}, t) \rangle = \langle u^*(\mathbf{r}, t) u(\mathbf{r}, t) \rangle = \Gamma(\mathbf{r}, \mathbf{r}, 0)$. The absolute value of Eq. 1.47 is limited: $0 \leq |\gamma(\mathbf{r}_1, \mathbf{r}_2, \tau)| \leq 1$, where $|\gamma| = 0$ means total uncorrelation and $|\gamma| = 1$ denotes full correlation of the fluctuations at positions $\mathbf{r}_1 = (x_1, y_1, z_1)$ and $\mathbf{r}_2 = (x_2, y_2, z_2)$ temporally separated by τ [Saleh and Teich, 2019, *§11*]. The extreme cases of $|\gamma(\mathbf{r}_1, \mathbf{r}_2, \tau)| = 0$ and $|\gamma(\mathbf{r}_1, \mathbf{r}_2, \tau)| = 1$ for all possible combinations of $\mathbf{r}_1$ and $\mathbf{r}_2$ are known as fully-incoherent and fully-coherent cases and all values in between those imply partially coherent radiation. Eq. 1.47 is connected to the cross-spectral density (CSD) by a Fourier transform[41] with respect to τ:

$$W(\mathbf{r}_1, \mathbf{r}_2, \omega) = \int_{-\infty}^{\infty} \Gamma(\mathbf{r}_1, \mathbf{r}_2, \tau) \exp(-i\omega t)\, \mathrm{d}\tau. \tag{1.48}$$

The normalised cross-spectral density function[42] is given by:

$$\mu(\mathbf{r}_1, \mathbf{r}_2, \omega) = \frac{W(\mathbf{r}_1, \mathbf{r}_2, \omega)}{\sqrt{W(\mathbf{r}_1, \mathbf{r}_1, \omega) W(\mathbf{r}_2, \mathbf{r}_2, \omega)}}. \tag{1.49}$$

Eq. 1.49 is known as the spectral degree of coherence (SDC) and much like the absolute value of Eq. 1.47, it is bounded by $0 \leq |\mu(\mathbf{r}_1, \mathbf{r}_2, \omega)| \leq 1$. Although the mutual coherence function (Eq. 1.46) and the cross-spectral density (Eq. 1.48) are connected by a Fourier transform, the complex degree of coherence (Eq. 1.47) and the spectral degree of coherence (Eq. 1.49) are not [Mandel and Wolf, 1995, *§4.3.2*].

A well known result from coherence theory and the cross-spectral density representation of the mutual coherence function is the coherent mode representation of partially coherent fields

---

[36] A statistical process is stationarity if all ensemble averages are independent of time, which is not the case for synchrotron radiation. The averaging brackets $\langle \bullet \rangle$ indicate average over the bunches instead.

[37] Homogeneity implies a constant ensemble-averaged intensity along the transverse direction.

[38] The dependency of Γ on τ and not explicitly on (t_1, t_2) comes from the "wide-sense stationary" characteristic of the wave-field [Geloni et al., 2008].

[39] cf. Eq. 4.3-6 in [Mandel and Wolf, 1995].

[40] cf. Eq. 4.3-12a in [Mandel and Wolf, 1995].

[41] Wiener–Khinchin theorem - cf. §2.4 in [Mandel and Wolf, 1995].

[42] cf. Eq. 4.3-47a in [Mandel and Wolf, 1995].

in free-space [Mandel and Wolf, 1995, *§4.7.1*]. It is possible to decompose the CSD in a infinite sum of coherent modes[43]:

$$W(\mathbf{r}_1, \mathbf{r}_2, \omega) = \sum_{j=1}^{\infty} \alpha_j(\omega)\Phi_j^*(\mathbf{r}_1, \omega)\Phi_j(\mathbf{r}_2, \omega), \tag{1.50}$$

where $\alpha_j(\omega)$ are the weights (eigenvalues) of the corresponding modes (eigenfunctions) $\Phi_j(\mathbf{r}, \omega)$. The modes described in Eq. 1.50 form an orthonormal set and maximise the CSD, that is, $0 \leq \alpha_{j+1}(\omega) < \alpha_j(\omega)$, making the truncation optimal. If the wave-field is completely coherent, it can be represented by a single mode [Mandel and Wolf, 1995, *§4.7*]. Equation 1.50 bares the same formalism as the density matrix representation via ensemble average in quantum mechanics [Bazarov, 2012]. Defining the mode occupancy as:

$$\eta_m = \frac{\alpha_m(\omega)}{\sum\limits_{j=1}^{\infty} \alpha_j(\omega)}, \tag{1.51}$$

allows to define the coherent fraction as the occupancy of the first mode η_1 (cf. Eq. 1.8) [Glass and Sanchez del Rio, 2017].

Spatial coherence

In the quasi-monochromatic regime[44] Eqs. 1.46 and 1.47 can be approximated as:

$$\Gamma(\mathbf{r}_1, \mathbf{r}_2, \tau) \approx J(\mathbf{r}_1, \mathbf{r}_2) \exp\left(i\omega_0\tau\right), \tag{1.52}$$

$$\gamma(\mathbf{r}_1, \mathbf{r}_2, \tau) \approx j(\mathbf{r}_1, \mathbf{r}_2) \exp\left(i\omega_0\tau\right). \tag{1.53}$$

The aforementioned approximations are valid given that $|\tau| \ll 1/\Delta\omega$, where $\Delta\omega$ is the radiation bandwidth and ω_0 is its centre. The quantities $J(\mathbf{r}_1, \mathbf{r}_2) \equiv \Gamma(\mathbf{r}_1, \mathbf{r}_2, 0)$ and $j(\mathbf{r}_1, \mathbf{r}_2) \equiv \gamma(\mathbf{r}_1, \mathbf{r}_2, 0)$ are known as the equal-time-correlation functions[45]. $J(\mathbf{r}_1, \mathbf{r}_2)$ is called the mutual optical intensity (MOI) and $j(\mathbf{r}_1, \mathbf{r}_2)$ is the complex degree of spatial coherence. The transverse coherence length can be arbitrarily defined as a $\Delta_{\mathbf{cl}_\perp} = |\mathbf{r}_2 - \mathbf{r}_1|$ to which $j(\mathbf{r}_1, \mathbf{r}_2)$ falls below a certain threshold[46]. Alternatively, the transverse coherence length can be approximated by the van-Cittert-Zernike theorem[47] - cf. [Mandel and Wolf, 1995, *§4.4.4*] and [Saleh and Teich, 2019, *§11.3.C*]. The experiment in classical optics mostly associated with the spatial coherence is the Young's double slit experiment [Goodman, 2015, *§5.2.1*].

---

[43] cf. Eq. 4.7-9 in [Mandel and Wolf, 1995].

[44] Conditions for the quasi-monochromatic regime in the context of SR are discussed in [Geloni et al., 2008, *§2.3*].

[45] cf. Eqs. 4.3-31–4.3-35 in [Mandel and Wolf, 1995].

[46] Threshold values are arbitrary, but commonly encountered metrics are: $1/2$, $1/\mathrm{e}$ or $1/\mathrm{e}^2$ of the normalised peak intensity.

[47] The applicability of the van-Cittert-Zernike theorem to SR is discussed in [Geloni et al., 2008, *§4*].

Temporal coherence

Alternatively, Eqs. 1.46 and 1.47 can be evaluated at a fixed position $\mathbf{r}$, giving rise to to the (temporal) coherence function and the complex degree of (temporal) coherence, respectively: $\Gamma(\mathbf{r},\mathbf{r},\tau)$ and $\gamma(\mathbf{r},\mathbf{r},\tau)$:

$$\Gamma(\mathbf{r},\mathbf{r},\tau) = \langle u^*(\mathbf{r},t)u(\mathbf{r},t+\tau)\rangle, \tag{1.54}$$

$$\gamma(\mathbf{r},\mathbf{r},\tau) = \frac{\Gamma(\mathbf{r},\mathbf{r},\tau)}{\Gamma(\mathbf{r},\mathbf{r},0)}. \tag{1.55}$$

The Fourier transform of Eq. 1.54 with respect to τ, $\mathcal{F}\{\Gamma(\mathbf{r},\mathbf{r},\tau)\} \equiv S(\mathbf{r},\omega)$, is called the spectrum density of the wave-field. Similarly, a longitudinal coherence length can be arbitrarily defined as a $\Delta_{\mathbf{cl}_{\parallel}} = c\tau$ to which $\gamma(\mathbf{r},\mathbf{r},\tau)$ falls below a certain threshold. The experiment in classical optics mostly associated with the temporal coherence is the Michelson's interferometer experiment [Goodman, 2015, *§5.1.1*].

Recommended literature

A comprehensive introduction to the scalar-wave-theory is presented by [Paganin, 2006, *§1* & *§2*] and [Goodman, 2017]. The concept of degree of coherence and its applications to optical problems is presented in [Zernike, 1938] and for a deeper look into statistical optics and partially-coherent fields, please, refer to [Mandel and Wolf, 1995, *§4*], [Born et al., 1999, *§10*] or [Goodman, 2015, *§5*].

1.3 X-ray optical simulations

There are several software packages for optical design in the X-ray range[48]: *SHADOW* [Cerrina, 1984], *RAY* [Schäfers, 2008], *McXtrace* [Bergbäck Knudsen et al., 2013] and *xrt* [Klementiev and Chernikov, 2014] among others for ray-tracing calculations; and *PHASE* [Bahrdt, 1997], *SRW* [Chubar and Elleaume, 1998], *WISEr* [L. Raimondi and Spiga, 2010] and *xrt* [Chernikov and Klementiev, 2017] to name a few wave-propagation codes. From those, *SHADOW* (ray-tracing[49]) and *SRW* (wave-propagation) are by far the most widely used and bench-marked [Sanchez del Rio, 2013; Chubar, 2014]. The choice of technique for optical beamline[50] simulation is based on several criteria, but is usually intimately connected to the expected physical effects to be observed, the degree of coherence of the X-rays and the required accuracy [Sanchez del Rio et al., 2019].

---

[48] As opposed to the optical systems design for the visible range, X-ray optical systems can often use strongly off-axis configurations with grazing incidence angles for reflective optics, crystals and other niche-specific optical elements. X-ray sources also differ from common visible light sources and often require special models (bending magnets, wigglers, undulators). Consequently, traditional approaches and commercial software for visible light are often ill-suited for X-ray optical simulations.

[49] Phase ray-tracing - cf. [Lee and Zhang, 2007; Sanchez del Rio et al., 2011].

[50] In accelerator-based X-ray physics, the optical system transporting the radiation from the accelerator to the sample is called beamline.

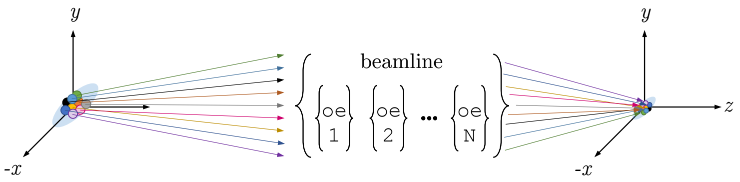

(a) ray-tracing

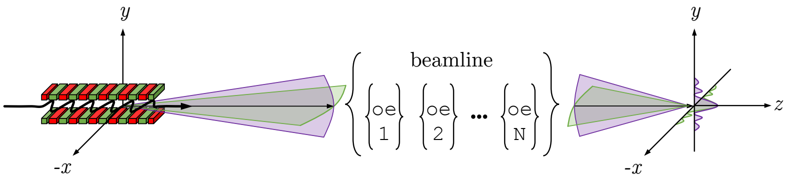

(b) wave-propagation

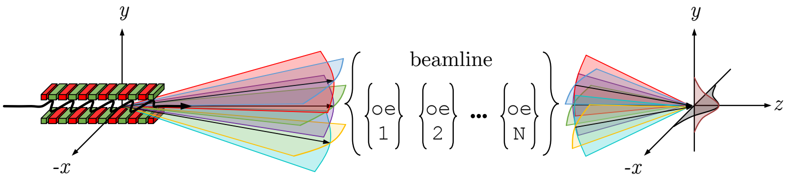

(c) partially-coherent simulation

Fig. 1.8.: X-ray beamline optical simulation methods based on the degree of spatial coherence. A beamline is composed of drift-spaces (free-space) and optical elements (OE). (a) ray tracing methods are more adequate for cases where the degree of spatial coherence is low $\left(|j(\mathbf{r}_1, \mathbf{r}_2)| \approx 0\right)$. (b) When the degree of coherence is close to unity $\left(|j(\mathbf{r}_1, \mathbf{r}_2)| \approx 1\right)$ wave-propagation methods are better suited, as they account for diffraction effects. (c) partially-coherent simulation surpasses the accuracy of pure ray tracing or wave-propagation for cases where $0 \ll |j(\mathbf{r}_1, \mathbf{r}_2)| \ll 1$.

In general[51] synchrotron radiation has very poor temporal coherence properties[52], that is, $|\gamma(\mathbf{r}, \mathbf{r}, \tau)| \approx 0$. It follows that any reference to coherence in this thesis (or lack thereof) implies spatial coherence.

1.3.1 Ray-tracing

For the cases where synchrotron radiation has low spatial coherence, that is, the complex degree of spatial coherence $|j(\mathbf{r}_1, \mathbf{r}_2)| \approx 0$ for a pair of points near opposed edges of the beam footprint, ray-tracing techniques are often employed. The radiation source is simulated by Monte-Carlo sampling of the photon-beam phase-space[53] described by specific numerical models [Canestrari et al., 2013] and each photon sampled from the source is transported through the beamline using geometrical optics[54]. The propagated rays are accumulated at the observation

---

[51] For typical electron-bunch lengths larger than ~ 30 ps, high energies and normal monochromatisation conditions [Geloni et al., 2008].

[52] A poor temporal coherence, typical of synchrotron radiation, is connected by a Fourier transform to the broad-band nature of such radiation. See also [Mandel and Wolf, 1995, *§4.4.3*].

[53] Three spatial coordinates, two transverse angles to describe direction, and the electron-beam energy - the electrons in a storage ring have a Gaussian distribution around the central design energy. The statistical emission of photons is the cause of a change of electron energy leading to energy spread within the electron beam [Wiedemann, 2015, *8.3.1*].

[54] Geometric optics is the limit of the physical optics theory when λ goes to zero [Saleh and Teich, 2019, *§1.3.C* & *§2.3*]. In free-space rays propagate in a straight line and have their direction changed by interacting with optical elements. By adding to this pure geometrical model some physical properties, namely, polarisation, intensity and wavelength, it is possible to account for several optical elements based on specular reflection, refraction and diffraction.

plane. To generate enough statistics and allow the method to converge, several thousands of rays are typically used - cf. Fig. 1.8(a). Ray-tracing is a simple, fast and extremely powerful technique for calculating the main characteristics of the photon beam (size, divergence, photon distribution) at every plane along the beamline when diffraction effects are negligible.

1.3.2 Wave propagation

The other extreme is the fully coherent case, that is $|\jmath(\mathbf{r}_1,\mathbf{r}_2)| \approx 1$ for any two pair of points $\mathbf{r}_1$ and $\mathbf{r}_2$ inside the beam footprint. This regime is often prone to diffraction effects and the framework for dealing with those is best given by wave-propagation, which follows physical optics principles - cf. §1.2 - *Physical optics*. The X-ray source can be simply approximated by any solution of the Helmholtz equation (Eq. 1.15) or its paraxial form given by Eq. 1.19. The most commonly used solutions are the plane wave (Eq. 1.16), the spherical wave (Eq. 1.17), the parabolic wave (Eq. 1.18) and the Gaussian beam (not covered here). Alternatively, the wavefront emerging from any accelerator-based X-ray source described by an arbitrary magnetic field can be calculated [Chubar, 1995, 2001]. This wave-field can then be propagated in the free-space between the optical elements using the diffraction integrals (cf. Eqs. 1.20, 1.21 or 1.25). The interaction between the wave and optical elements in the beamline is done by the calculation of the appropriate transmission element[55]. After the said wave is propagated to the observation plane, the intensity and phase can be calculated.

1.3.3 Partially coherent simulations

When performing optical design for X-ray beamlines in synchrotron radiation facilities, there are several cases of interest that are neither well approximated by $|\jmath(\mathbf{r}_1,\mathbf{r}_2)| \approx 0$ nor by $|\jmath(\mathbf{r}_1,\mathbf{r}_2)| \approx 1$ for a pair of points near opposed edges of the beam footprint. Using pure ray-tracing or a single-wave-field propagation to those partially-coherent cases may lead to inaccurate results [Sanchez del Rio et al., 2019]. With varying accuracy, several methods can account for partial-coherence effects.

Hybrid methods

One class of methods is based on the so-called hybrid methods mixing elements of ray-tracing and wave propagation simulations [Semichaevsky and Testorf, 2001]. One common approach is to simulate the geometric effects from optical elements with ray-tracing and their diffraction contributions[56] with wave optics. The diffraction caused by the optical elements is then integrated into ray-tracing by numerical convolution and sampling the calculated wave-front with rays [Shi et al., 2014]. Another approach is to take into account the optical path followed by individual rays and asserting to them a phase and interpreting them as a localised phase of the wave-front. If sampling is sufficiently high, it is possible to reconstruct a wave-front. These

---

[55] In addition to the theory describing the propagation of X-rays in the matter (§1.2.2 - *Transmission elements*) a variety of optical elements can be simulated within the wave optics by being able to describe them adequately as transmission elements, similar to a transfer function in signals and systems theory - cf. [Canestrari et al., 2014; Li et al., 2017].

[56] Diffraction contributions are usually due to beam clipping by either physical acceptance of an optical element or slits and optical errors.

special rays are propagated through the beamline using ray-tracing techniques and are added coherently[57] at the observation plane [Keller, 1962].

Physical-optics-based methods

A second class of methods involves purely wave-front propagation methods. The radiation from the X-ray source can be decomposed in orthogonal modes. These can be propagated though the beamline using the physical optics principles described in §1.2 - *Physical optics*. Once the modes are propagated to the observation plane, they can be added in intensity[58]. X-rays from undulators are commonly decomposed into Gaussian-Schell modes [Coïsson and Marchesini, 1997; Singer and Vartanyants, 2011], which becomes less accurate when dealing with ultra-low emittance machines. More recently, different factorisations have been proposed to accurately represent beams in low-emittance machines [Lindberg and Kim, 2015; Glass and Sanchez del Rio, 2017].

Alternatively, the fact that for high energies the emission from the electrons is uncorrelated can be explored. Each individual electron in a bunch has a different initial condition in terms of position $s = (x_e, y_e, z_e)$, direction $s' = (x'_e, y'_e)$ and energy γ_e. These electrons spread in the 6D phase-space according to a probabilistic distribution[59] $f(s, s', \gamma_e)$ in phase-space such as $\int f(s, s', \gamma_e)\ \mathrm{d}x_e \mathrm{d}y_e \mathrm{d}z_e \mathrm{d}x'_e \mathrm{d}y'_e \mathrm{d}\gamma_e = 1$. The multi-electron-emission method for partially coherent simulations is based on individually calculating the synchrotron radiation emission of several electrons subjected to the initial conditions sampled from $f(s, s', \gamma_e)$ passing through an arbitrary magnetic field describing the X-ray source [Chubar, 1995]. Each resulting electric field is then propagated through the beamline until the observation point, where the contributions from different electrons are added in intensity. The function $f(s, s', \gamma_e)$ should be statistically well-sampled (Monte-Carlo methods) to guarantee convergence. This multi-electron-emission method was first proposed and implemented by [Chubar et al., 2011]. This method is shown in Fig. 1.8(c).

Other methods

A third class of methods is based on the propagation of the correlation functions[60] through the beamline with methods resembling the ones from physical optics. The theory for such is described in [Parrent, 1959] and [Mandel and Wolf, 1995, *§4.4*]. However, these methods are, at the time of this writing, not very commonly applied to X-ray optical simulations due to being very computationally expensive [Meng et al., 2015, 2017; Ren et al., 2019; Nash et al., 2021] and are certainly not made available on any common software for X-ray optical simulations. ■

References

Ali, S. and Jacobsen, C. (2020). "Effect of tilt on circular zone plate performance". In: *Journal of the Optical Society of America A* **37**.3, p. 374.

---

[57] Taking into account their relative phase.

[58] cf. Eqs. 1.46, 1.48 and 1.50 evaluated for $\mathbf{r} = \mathbf{r}_1 = \mathbf{r}_2$ and $\tau = 0$.

[59] The distribution $f(s, s', \gamma_e)$ is intimately connected to the nature of the X-ray source.

[60] cf. §1.2.3 - *Optical coherence*.

Als-Nielsen, J. and McMorrow, D. (2011). *Elements of Modern X-ray Physics*. Second edition. John Wiley & Sons, Inc.

Attwood, D. (1999). “5 - Synchrotron Radiation”. In: *Soft X-Rays and Extreme Ultraviolet Radiation*. First edition. Cambridge University Press.

Bahrdt, J. (1997). “Wave-front propagation: design code for synchrotron radiation beam lines”. In: *Applied Optics* **36**.19, p. 4367.

Bazarov, I. V. (2012). “Synchrotron radiation representation in phase space”. In: *Physical Review Special Topics - Accelerators and Beams* **15**.5, p. 050703.

Bei, M., Borland, M., Cai, Y., Elleaume, P., Gerig, R., Harkay, K., Emery, L., Hutton, A., Hettel, R., Nagaoka, R., Robin, D., and Steier, C. (2010). “The Potential of an Ultimate Storage Ring for Future Light Sources”. In: *Nuclear Instruments and Methods in Physics Research Section A: Accelerators, Spectrometers, Detectors and Associated Equipment* **622**.3, p. 518.

Bergbäck Knudsen, E., Prodi, A., Baltser, J., Thomsen, M., Kjær Willendrup, P., Sanchez del Rio, M., Ferrero, C., Farhi, E., Haldrup, K., Vickery, A., Feidenhans’l, R., Mortensen, K., Meedom Nielsen, M., Friis Poulsen, H., Schmidt, S., and Lefmann, K. (2013). “McXtrace : a Monte Carlo software package for simulating X-ray optics, beamlines and experiments”. In: *Journal of Applied Crystallography* **46**.3, p. 679.

Biasci, J., Bouteille, J., Carmignani, N., Chavanne, J., Coulon, D., Dabin, Y., Ewald, F., Farvacque, L., Goirand, L., Hahn, M., Jacob, J., LeBec, G., Liuzzo, S., Nash, B., Pedroso-Marques, H., Perron, T., Plouviez, E., Raimondi, P., Revol, J., Scheidt, K., and Serrière, V. (2014). “A Low-Emittance Lattice for the ESRF”. In: *Synchrotron Radiation News* **27**.6, p. 8.

Borland, M., Decker, G., Emery, L., Sajaev, V., Sun, Y., and Xiao, A. (2014). “Lattice design challenges for fourth-generation storage-ring light sources”. In: *Journal of Synchrotron Radiation* **21**.5, p. 912.

Born, M., Wolf, E., Bhatia, A. B., Clemmow, P. C., Gabor, D., Stokes, A. R., Taylor, A. M., Wayman, P. A., and Wilcock, W. L. (1999). *Principles of Optics: Electromagnetic Theory of Propagation, Interference and Diffraction of Light*. Seventh edition. Cambridge University Press.

Bracewell, R. (2000). *The Fourier Transform & Its Applications*. Third edition. McGraw-Hill Science, Engineering, Math.

Buitrago-Duque, C. and Garcia-Sucerquia, J. (2019). “Evaluation of Non-Approximated Numerical Calculation of the Diffraction Integral”. In: *Digital Holography and Three-Dimensional Imaging 2019*. Optical Society of America, W3A.12.

Canestrari, N., Chubar, O., and Reininger, R. (2014). “Partially coherent X-ray wavefront propagation simulations including grazing-incidence focusing optics”. In: *Journal of Synchrotron Radiation* **21**.5, p. 1110.

Canestrari, N., Chubar, O., and Sanchez del Rio, M. (2013). “Improved models for synchrotron radiation sources in SHADOW”. In: *Journal of Physics: Conference Series - Proc. 11th International Conference on Synchrotron Radiation Instrumentation (SRI 2012)* **425**.16, p. 162007.

Celestre, R., Berujon, S., Roth, T., Sanchez del Rio, M., and Barrett, R. (2020). “Modelling phase imperfections in compound refractive lenses”. In: *Journal of Synchrotron Radiation* **27**.2, p. 305.

Cerrina, F. (1984). “Ray Tracing Of Recent VUV Monochromator Designs”. In: *Proc. SPIE 0503, Application, Theory, and Fabrication of Periodic Structures, DiffractionGratings, and Moire Phenomena II*, p. 68.

Chernikov, R. and Klementiev, K. (2017). “Recent progress of the XRT: ray tracing and wave propagation toolkit (Conference Presentation)”. In: *Proc. SPIE 10388, Advances in Computational Methods for X-Ray Optics IV*, p. 6.

Chubar, O. (1995). “Precise computation of electron-beam radiation in nonuniform magnetic fields as a tool for beam diagnostics”. In: *Review of Scientific Instruments* **66**.2, p. 1872.

— (2001). “Wavefront calculations”. In: *Proc. SPIE 4143, X-Ray FEL Optics and Instrumentation*, p. 48.

— (2006). “Simulation of emission and propagation of coherent synchrotron radiation wave fronts using the methods of wave optics”. In: *Infrared Physics & Technology* **49**.1-2, p. 96.

— (2014). “Recent updates in the “Synchrotron Radiation Workshop” code, on-going developments, simulation activities, and plans for the future”. In: *Proc. SPIE 9209, Advances in Computational Methods for X-Ray Optics III*, p. 920907.

Chubar, O., Berman, L., Chu, Y. S., Fluerasu, A., Hulbert, S., Idir, M., Kaznatcheev, K., Shapiro, D., Shen, Q., and Baltser, J. (2011). “Development of partially-coherent wavefront propagation simulation methods for 3rd and 4th generation synchrotron radiation sources”. In: *Proc. SPIE 8141, Advances in Computational Methods for X-Ray Optics II*, p. 814107.

Chubar, O. and Celestre, R. (2019). “Memory and CPU efficient computation of the Fresnel free-space propagator in Fourier optics simulations”. In: *Optics Express* **27**.20, p. 28750.

Chubar, O., Couprie, M. E., Labat, M., Lambert, G., Polack, F., and Tcherbakoff, O. (2008). “Time-dependent FEL wavefront propagation calculations: Fourier optics approach”. In: *Nuclear Instruments and Methods in Physics Research, Section A: Accelerators, Spectrometers, Detectors and Associated Equipment* **593**.1-2, p. 30.

Chubar, O. and Elleaume, P. (1998). “Accurate And Efficient Computation Of Synchrotron Radiation In The Near Field Region”. In: *Proceedings of the European Particle Accelerator Conference (EPAC 98)*, p. 1177.

Clarke, J. A. (2004). *The Science and Technology of Undulators and Wigglers*. First edition. Oxford University Press.

Coïsson, R. and Marchesini, S. (1997). “Gauss–Schell Sources as Models for Synchrotron Radiation”. In: *Journal of Synchrotron Radiation* **4**.5, p. 263.

Cowley, J. M. and Moodie, A. F. (1957). “The scattering of electrons by atoms and crystals. I. A new theoretical approach”. In: *Acta Crystallographica* **10**.10, p. 609.

D’Arcio, L. A., Braat, J. J. M., and Frankena, H. J. (1994). “Numerical evaluation of diffraction integrals for apertures of complicated shape”. In: *Journal of the Optical Society of America A* **11**.10, p. 2664.

Duke, P. J. (2000). *Synchrotron Radiation: Production and Properties*. First edition. Oxford University Press.

Einfeld, D., Plesko, M., and Schaper, J. (2014). “First multi-bend achromat lattice consideration”. In: *Journal of Synchrotron Radiation* **21**.5, p. 856.

Einfeld, D., Schaper, J., and Plesko, M. (1996). “A lattice design to reach the theoretical minimum emittance for a storage ring”. In: *Proceedings of the European Particle Accelerator Conference (EPAC’96)*, p. 638.

Elder, F. R., Gurewitsch, A. M., Langmuir, R. V., and Pollock, H. C. (1947). “Radiation from electrons in a synchrotron”. In: *Physical Review* **71**.11, p. 829.

Elleaume, P. and Ropert, A. (2003). “The ultimate hard X-ray storage-ring-based light source”. In: *Nuclear Instruments and Methods in Physics Research Section A: Accelerators, Spectrometers, Detectors and Associated Equipment* **500**.1-3, p. 18.

Eriksson, M. (2016). “The multi-bend achromat storage rings”. In: *12th International Conference on Synchrotron Radiation Instrumentation (SRI2015)*, p. 020001.

Geloni, G., Kocharyan, V., and Saldin, E. (2015). “Brightness of synchrotron radiation from undulators and bending magnets”. In: *Journal of Synchrotron Radiation* **22**.2, p. 288.

Geloni, G., Saldin, E., Schneidmiller, E., and Yurkov, M. (2008). “Transverse coherence properties of X-ray beams in third-generation synchrotron radiation sources”. In: *Nuclear Instruments and Methods in Physics Research Section A: Accelerators, Spectrometers, Detectors and Associated Equipment* **588**.3, p. 463.

Ginzburg, V. L. and Syrovatskii, S. I. (1965). “Cosmic Magnetobremsstrahlung (Synchrotron Radiation)”. In: *Annual Review of Astronomy and Astrophysics* **3**.1, p. 297.

Glass, M. and Sanchez del Rio, M. (2017). “Coherent modes of X-ray beams emitted by undulators in new storage rings”. In: *{EPL} (Europhysics Letters)* **119**.3, p. 34004.

Goodman, J. W. (2015). *Statistical Optics*. Second edition. John Wiley & Sons, Inc.

— (2017). *Introduction to Fourier Optics*. Fourth edition. W. H. Freeman and Company.

Hetch, E. (2017). *Optics*. Fifth. Pearson Education.

Huang, Z. and Kim, K.-J. (2007). “Review of x-ray free-electron laser theory”. In: *Physical Review Special Topics - Accelerators and Beams* **10**.3, p. 034801.

Ishizuka, K. and Uyeda, N. (1977). “A new theoretical and practical approach to the multislice method”. In: *Acta Crystallographica Section A* **33**.5, p. 740.

Jackson, J. D. (1998). “Ch. 14 - Radiation by moving charges”. In: *Classical Electrodynamics*. Third edition. Wiley, p. 661.

Keller, J. B. (1962). “Geometrical theory of diffraction.” In: *Journal of the Optical Society of America* **52**.2, p. 116.

Kelly, D. P. (2014). “Numerical calculation of the Fresnel transform”. In: *Journal of the Optical Society of America A* **31**.4, p. 755.

Khubbutdinov, R., Menushenkov, A. P., and Vartanyants, I. A. (2019). “Coherence properties of the high-energy fourth-generation X-ray synchrotron sources”. In: *Journal of Synchrotron Radiation* **26**.6, p. 1851.

Kim, K.-J. (1986). “Brightness, coherence and propagation characteristics of synchrotron radiation”. In: *Nuclear Instruments and Methods in Physics Research Section A: Accelerators, Spectrometers, Detectors and Associated Equipment* **246**.1-3, p. 71.

— (1989). “Characteristics of synchrotron radiation”. In: *AIP Conference Proceedings*. Vol. **184**. AIP, p. 565.

Klementiev, K. and Chernikov, R. (2014). “Powerful scriptable ray tracing package xrt”. In: *Proc. SPIE 9209, Advances in Computational Methods for X-Ray Optics III*, 92090A.

Lee, H. J. and Zhang, Z. M. (2007). “Applicability of Phase Ray-Tracing Method for Light Scattering from Rough Surfaces”. In: *Journal of Thermophysics and Heat Transfer* **21**.2, p. 330.

Li, K., Wojcik, M., and Jacobsen, C. (2017). “Multislice does it all—calculating the performance of nanofocusing X-ray optics”. In: *Optics Express* **25**.3, p. 1831.

Lindberg, R. R. and Kim, K.-J. (2015). “Compact representations of partially coherent undulator radiation suitable for wave propagation”. In: *Physical Review Special Topics - Accelerators and Beams* **18**.9, p. 090702.

Mandel, L. and Wolf, E. (1995). *Optical Coherence and Quantum Optics*. First edition. Cambridge University Press.

Meng, X., Shi, X., Wang, Y., Reininger, R., Assoufid, L., and Tai, R. (2017). “Mutual optical intensity propagation through non-ideal mirrors”. In: *Journal of Synchrotron Radiation* **24**.5, p. 954.

Meng, X., Xue, C., Yu, H., Wang, Y., Wu, Y., and Tai, R. (2015). “Numerical analysis of partially coherent radiation at soft x-ray beamline”. In: *Optics Express* **23**.23, p. 29675.

Michette, A. G. and Buckley, C. J., eds. (1993). *X-Ray Science and Technology*. First edition. Institute of Physics Publishing.

Mills, D. M., Helliwell, J. R., Kvick, Å., Ohta, T., Robinson, I. A., and Authier, A. (2005). “Report of the Working Group on Synchrotron Radiation Nomenclature – brightness, spectral brightness or brilliance?” In: *Journal of Synchrotron Radiation* **12**.3, p. 385.

Munro, P. R. T. (2019). “Rigorous multi-slice wave optical simulation of x-ray propagation in inhomogeneous space”. In: *Journal of the Optical Society of America A* **36**.7, p. 1197.

Nash, B., Goldring, N., Edelen, J., Webb, S., and Celestre, R. (2021). “Propagation of partially coherent radiation using Wigner functions”. In: *Physical Review Accelerators and Beams* **24**.1, p. 010702.

Onuki, H. and Elleaume, P., eds. (2013). *Undulators, Wigglers and their Applications*. First edition. Taylor & Francis.

Paganin, D. (2006). *Coherent X-Ray Optics*. First edition. Oxford University Press.

Parrent, G. B. (1959). “On the Propagation of Mutual Coherence”. In: *Journal of the Optical Society of America* **49**.8, p. 787.

Raimondi, L. and Spiga, D. (2010). “Self-consistent computation of x-ray mirror point spread functions from surface profile and roughness”. In: *Proc. SPIE 7732, Space Telescopes and Instrumentation 2010: Ultraviolet to Gamma Ray*, 77322Q.

Raimondi, P. (2017). “Hybrid Multi Bend Achromat: from SuperB to EBS”. In: *Proceedings of the International Particle Accelerator Conference (IPAC’17)*, p. 3670.

Rees, W. G. (1987). “The validity of the Fresnel approximation”. In: *European Journal of Physics* **8**.1, p. 44.

Ren, J., Wang, Y., Meng, X., Shi, X., Assoufid, L., and Tai, R. (2019). “In-plane wavevector distribution in partially coherent X-ray propagation”. In: *Journal of Synchrotron Radiation* **26**.4, p. 1198.

Robinson, A. L. (2015). “History of Synchrotron Radiation”. In: *Synchrotron Radiation News* **28**.4, p. 4.

Röntgen, W. C. (1896a). “Über Eine Neue Art von Strahlen (Fortsetzung)”. In: *Sitzungsberichte der Würzburger Physik.-medic. Gesellschaft, Jg. 1896*, p. 10.

— (1896b). “Über Eine Neue Art von Strahlen (Vorläufige Mittheilung)”. In: *Sonderabbdruck aus den Sitzungsberichten der Würzburger Physik.-medic. Gesellschaft 1895*, p. 132.

— (1897). “Weitere Beobachtungen über die Eigenschaften der X-Strahlen”. In: *Sitzungsberichte der Königlich Preußischen Akademie der Wissenschaften zu Berlin*, p. 576.

Ropert, A., Filhol, J. M., Elleaume, P., Farvacque, L., Hardy, L., Jacob, J., and Weinrich, U. (2000). “Towards the ultimate storage ring-based light source”. In: *Proceedings of the European Particle Accelerator Conference (EPAC’00)*, p. 83.

Saleh, B. E. A. and Teich, M. C. (2019). *Fundamentals of photonics*. Third edition. John Wiley & Sons, Inc.

Sanchez del Rio, M. (2013). “New challenges in ray tracing simulations of X-ray optics”. In: *Journal of Physics: Conference Series - Proc. 11th International Conference on Synchrotron Radiation Instrumentation (SRI 2012)* **425**.16, p. 162003.

Sanchez del Rio, M., Canestrari, N., Jiang, F., and Cerrina, F. (2011). “SHADOW3 : a new version of the synchrotron X-ray optics modelling package”. In: *Journal of Synchrotron Radiation* **18**.5, p. 708.

Sanchez del Rio, M., Celestre, R., Glass, M., Pirro, G., Herrera, J. R., Barrett, R., Silva, J. C. da, Cloetens, P., Shi, X., and Rebuffi, L. (2019). “A hierarchical approach for modeling X-ray beamlines: application to a coherent beamline”. In: *Journal of Synchrotron Radiation* **26**.6, p. 1887.

Schäfers, F. (2008). “The BESSY Raytrace Program RAY”. In: *Modern Developments in X-Ray and Neutron Optics, Springer Series in Modern Optical Sciences*. Ed. by A. Erko, M. Idir, T. Krist, and A. Michette. First. Springer- Verlag, Berlin Heidelberg, p. 9.

Semichaevsky, A. V. and Testorf, M. E. (2001). “Anything optical rays cannot do?” In: *Proc. SPIE 4436, Wave-Optical Systems Engineering*, p. 56.

Shi, X., Reininger, R., Sanchez del Rio, M., and Assoufid, L. (2014). “A hybrid method for X-ray optics simulation: combining geometric ray-tracing and wavefront propagation”. In: *Journal of Synchrotron Radiation* **21**.4, p. 669.

Singer, A. and Vartanyants, I. A. (2011). “Modelling of partially coherent radiation based on the coherent mode decomposition”. In: *Proc. SPIE 8141, Advances in Computational Methods for X-Ray Optics II*, p. 814106.

— (2014). “Coherence properties of focused X-ray beams at high-brilliance synchrotron sources”. In: *Journal of Synchrotron Radiation* **21**.1, p. 5.

Southwell, W. H. (1981). “Validity of the Fresnel approximation in the near field”. In: *Journal of the Optical Society of America* **71**.1, p. 7.

Talman, R. (2006). *Accelerator X-Ray Sources*. First edition. WILEY-VCH Verlag GmbH & Co. KGaA.

Tanaka, T. (2014). “Numerical methods for characterization of synchrotron radiation based on the Wigner function method”. In: *Physical Review Special Topics - Accelerators and Beams* **17**.6, p. 060702.

Tanaka, T. and Kitamura, H. (2009). “Universal function for the brilliance of undulator radiation considering the energy spread effect”. In: *Journal of Synchrotron Radiation* **16**.3, p. 380.

Walker, R. P. (2019). “Undulator radiation brightness and coherence near the diffraction limit”. In: *Physical Review Accelerators and Beams* **22**.5, p. 050704.

Wiedemann, H. (2015). *Particle Accelerator Physics*. Forth edition. Graduate Texts in Physics. Springer International Publishing.

Wielebinski, R. (2006). “Technical Report: History of Synchrotron Radiation in Astrophysics”. In: *Synchrotron Radiation News* **19**.5, p. 4.

Zernike, F. (1938). “The concept of degree of coherence and its application to optical problems”. In: *Physica* **5**.8, p. 785.

X-rays as a branch of optics

2

In the late 1920s, not much longer after their discovery in late 1895, X-rays were already consolidated as a branch of optics. This chapter opens up with a brief account of the early days of X-ray optics and main focusing optical element families. Compound refractive lenses (CRLs), the main topic of this work, are then presented at length and the modelling of ideal CRLs accounting for their thick-element nature is derived. Some figures of merit for their optical performance are also discussed.

2.1 The early days of X-ray optics

Upon reporting the discovery of X-rays [Röntgen, 1896], Röntgen describes several properties, among them: a) that refraction cannot be conclusively observed and if the tested materials[1] do refract the X-rays, their index of refraction cannot be larger than 1.05 [cf. *§7* ibid.]; b) there is no noticeable regular reflection of the rays on any of the substances[2] examined [cf. *§8* ibid.]; c) there are no observable interference phenomena [cf. *§15* ibid.]; d) and finally, that the X-rays cannot be polarised[3] by the usual means [cf. *§17c* ibid.]. At the time of the discovery of the X-rays, their only apparent similarity to visible was that they propagated in a straight line in free-space. It took about 30 years for this appreciation to change.

Between the years of 1904 and 1906 polarisation in X-rays was observed and described by C. Barkla [Barkla, 1904, 1905, 1906]. Speculations and experiments regarding diffraction of X-rays start as early as the 1900s [Haga and Wind, 1903; Walter and Pohl, 1908, 1909], but it was not until the early 1910s that diffraction was successfully described [Laue, 1912], observed [Friedrich et al., 1912] and modelled by what came to be known as the Bragg law of diffraction [W. H. Bragg and W. L. Bragg, 1913]. Early experiments aiming direct observation of refraction failed but helped to narrow the estimation of the index of refraction for the X-ray regime[4] to $0.999995 \leq n \leq 1.000005$ [Barkla, 1916]. Further experimental observations of Bragg's law started showing small deviations between expected and obtained values. These were first reported by Stenström in 1919[5] and were attributed to the refraction of the X-rays as they penetrate the crystal[6], limiting the index of refraction to $n \lesssim 1$ [Stenström, 1919, *§3*].

---

[1] The materials used were water, carbon disulfide, mica, ebonite and aluminium.

[2] Platinum, lead, zinc and aluminium.

[3] In fact, this observation is not accompanied by any experimental observation described in his manuscript, but it comes from him speculating about the X-rays nature: "*If one asks oneself what the X-rays [...] actually are [...]. If the X-rays were to be ultraviolet light, this light should have the property: [...] c) that it cannot be polarised by the usual means;*" [Röntgen, 1896, *§17*].

[4] C. Barkla's experiment aimed to measure the refractive index of potassium bromide for radiation of wavelength in the neighbourhood of 0.5 Å.

[5] The same kind of discrepancies were also observed and reported by Duane and Patterson in 1920 and Siegbahn in 1920 and 1921.

[6] This was met by criticism from Knipping in 1920 (Knipping, 1920). However, as pointed out by A. Compton - cf. [Compton, 1923], theoretical calculations made by Ewald in 1920 showed good agreement between experimental observations and the refraction hypothesis [Ewald, 1920].

The experimental proof of the refraction of X-rays came in the mid-1920s with [Larsson et al., 1924]. Being able to detect refraction was very important, as it directly allows to assume the existence of reflection which can only occur in a boundary surface if there is a discontinuity in the indexes of refraction between the two media. If one of these phenomena is present, then the other one must too exist [Compton, 1928]. Based on earlier reports about the discrepancies observed on the Bragg's law of refraction, A. Compton was able to estimate the glancing angles for polished surfaces of several materials and demonstrate the total external reflection of X-rays [Compton, 1923; Prins, 1927]. In fact, by the end of the 1920s, all fundamental characteristics[7] of light have been found to be present for X-rays, making them undoubtedly a branch of optics [Compton, 1928].

2.1.1 X-ray focusing optics

Parallel to the early observation of the phenomena that showed that X-rays are a branch of optics, came the development of optical elements exploiting diffraction, reflection and refraction for focusing of X-rays[8].

Diffractive optics

The early optical elements based on diffraction for focusing of X-rays were curved crystals operating on the Bragg diffraction condition [Gouy, 1916; Seemann, 1916]. The use of curved crystals[9] for focusing X-rays came in context of optimising the performance of spectrographs (spectrometers) with major contributions from [Johann, 1931; Johansson, 1933; Hámos, 1933, 1937]. Other historical milestones are multi-layer mirrors [Gaponov et al., 1983; Aristov et al., 1986; Underwood et al., 1986][10], monochromators [Smith, 1941; DuMond, 1950] and gratings monochromators [Namioka et al., 1976; McKinney and Howells, 1980; Tonner and Plummer, 1980] and zone-plates[11] [Baez, 1960; Schmahl and Rudolph, 1969; Kirz, 1974]. More recent developments include (multi-layer[12]) Laue lenses [Maser et al., 2004; Kang et al., 2005; Liu et al., 2005], diffractive elements for beam-shaping [Vogt et al., 2006; Jefimovs et al., 2008; Rebernik Ribič et al., 2017; Rösner et al., 2017; Marchesini and Sakdinawat, 2019] and corrective optics for focusing elements [Probst et al., 2020].

Reflective optics

Using total external reflection for focusing X-rays started around the late 1940s with [Ehrenberg, 1947; Kirkpatrick and Baez, 1948; Ehrenberg, 1949; Kirkpatrick, 1950] in the

---

[7] Reflection, refraction, diffraction, polarisation, diffuse scattering, emission and absorption spectra and the photoelectric effect are the essential characteristics of light considered by A. Compton in [Compton, 1928].

[8] This recount of the early days of X-ray focusing optics is oriented to accelerator-based X-rays. The field of X-ray optics for astronomy is very rich but is not covered here. A review is available in [Gorenstein, 2010].

[9] Several early works on curved crystals often refer to "systems operating on Bragg reflection", which is actually an euphemism for diffraction [Hart, 1971].

[10] In multi-layer mirrors it is not the total external reflection effect that reflects the X-rays, but Bragg diffraction from the periodic arrangement of the layered structture on the mirror surface [Morawe and Osterhoff, 2010].

[11] Often referred to X-ray lenses up until the early 1990s, when refractive X-ray lenses were demonstrated for the first time [Snigirev et al., 1996].

[12] For more on multi-layer optics, refer to [Aristov et al., 1988].

context of direct imaging and X-ray microscopy[13], moving away from the spectroscopy application of the previous decades. Soon after, several X-ray mirror designs emerged [Wolter, 1952; Montel, 1957] and continue to do so today [Matsuyama et al., 2017; Yamada et al., 2019, 2020]. X-ray mirrors have very wide use in X-ray optics and general reviews can be found in [Howells, 1993; Susini, 1993].

Refractive optics

Finally, the group of optical elements based on refraction of X-rays for focusing light should be presented. Refractive X-ray optics comprises mainly lenses [Snigirev et al., 1996], kinoform lenses[14] [Snigireva, Snigirev, Rau, et al., 2001; Snigireva, Snigirev, Kuznetsov, et al., 2001; David et al., 2004], prisms in several arrangements [Cederström et al., 2000; Jark et al., 2004] and most recently, free-form objects mainly for optical correction and beam-shaping [Seiboth et al., 2017; Zverev et al., 2017; Márkus et al., 2018; Seiboth et al., 2019, 2020; Dhamgaye et al., 2020]. From those, compound refractive lenses (CRLs) - as X-ray lenses are called - are by far the dominating refractive optical element in use throughout synchrotrons. In retrospective, they are the least mature, dating from the mid-1990s, while the use of diffractive focusing optics dates to the early 1930s and reflective optics to the late 1940s.

- A bit of history[15]

X-ray lenses were long believed to be unfeasible: low refraction index leads to unpractical focal lengths and the transmission of X-rays through matter faces strong absorption. In one of the early works on focusing and imaging with X-ray optics, P. Kirkpatrick and A. Baez stated that: "*about one hundred lens surfaces in series would be required to bring the focal length down to one hundred meters. This would produce a cumbersome and very weak lens system of poor transparency. These discouraging considerations incline us toward other methods*"[16] [Kirkpatrick and Baez, 1948]. On the following year, Kirkpatrick went on to say: "*Although the X-ray lens is thus possible it has the disadvantages of high absorption and strong chromatic aberration, and so would probably be generally inferior to mirror systems*" [Kirkpatrick, 1949].

It was not before 1991 that X-ray lenses would be reconsidered: in a scientific correspondence to the journal Nature, a Japanese group headed by S. Suehiro proposed the use of such elements for the forthcoming third-generation light sources [Suehiro et al., 1991]. Such idea was not met with enthusiasm by the X-ray optics community, who still considered such technologies to be impractical for focusing X-rays as it was made clear by A. Michette, who had written Nature a reply to Suehiro's communication. The text entitled "*No X-ray lens*" criticises the idea of refractive optics for X-rays and lists the reasons why those were considered them unsuitable for focusing X-rays [Michette, 1991]. In "*Fresnel and refractive lenses for X-rays*" by B. X. Yang,

---

[13] Early works on "X-ray microscopy" are based on imaging of the reciprocal space with the necessity of Fourier transformations to recover the image in the direct space [W. L. Bragg, 1939, 1942].

[14] Kinoform lenses are a way of thinning refractive optics, thus reducing absorption. The lens thickness is obtained by removing redundant material causing optical path differences of 2π rad or its integer multiples [Jordan et al., 1970; Ognev, 2005]. Depending on the degree of coherence from the illumination, diffraction effects appear when kinoform lenses are operated outside designed energy or present figure errors.

[15] This was originally published as *§3.1 - Prelude* in [Celestre, 2017].

[16] Using $f = R/\delta$, where f is the focal length and R is the refractive surface radius (cf. Eq 2.3). The estimation shows values for $R = 1$cm, using beryllium lens at $\lambda = 0.71$Å, K$_\alpha$ line of molybdenum Kirkpatrick and Baez, 1948.

written in 1992 and published in 1993, Yang revisited S. Suehiro's idea and proposed ways to overcome the strong absorption of such lenses by using a Fresnel lenses shape instead [Yang, 1993], however, those were of complicated fabrication and were not given too much attention.

The birth of the X-ray refractive lens as known today can be traced back to 1994, when T. Tomie filed a patent for X-ray lenses in Japan [Tomie, 1994] - patents were also filed in US and Germany on the following year. His concept for X-ray lenses was introduced to the scientific community as a poster on the *XRM'96, Int. Conf. X-ray Microscopy and Spectroscopy*, held in Würzburg, Germany, in 1996. The concept was simple, but innovative: a series of drilled holes into a single substrate along a straight line. The proposed design increased mechanical robustness, overcame alignment issues, reduced absorption by placing the drilled holes close to each other and was relatively simple to be manufactured - although T. Tomie never went on to produce them [Tomie, 2010]. Shortly after the presentation of the refractive lens to the scientific community at the XRM'96, the breakthrough came: A. Snigirev and other colleagues produced the first compound refractive lens and demonstrated its efficiency in focusing hard X-rays. It was only 100 years after the discovery of the X-rays that their focusing by refraction was experimentally demonstrated. This first experiment was performed at the European Synchrotron Research Facility (ESRF) in Grenoble, France [Snigirev et al., 1996]. The group used a very similar approach to the one proposed by Tomie. The early lenses had a cylindrical or spherical shape. This limited their wide-spread application. A significant advancement to refractive X-ray optics came in 1999, when parabolic lenses were first demonstrated by B. Lengeler and his group [Lengeler et al., 1999, 2001]. Refractive optics have subsequently entered into widespread use in applications ranging from tabletop sources to large facilities [Snigirev and Snigireva, 2008].

Recommended literature

An interesting account of the early days of X-ray optics is presented by [Compton, 1928, 1931], while a more general account of the history of X-ray optics and science leading up to modern days is presented by [Willmott, 2019, *§1*] and [Jacobsen, 2019, *§2*]. A good review on focusing X-ray optics is available in [Ice et al., 2011; Macrander and Huang, 2017].

2.2 The compound refractive lenses (CRL)

X-ray lenses may have different surface shapes: in initial experiments, a cylindrical surface was used [Snigirev et al., 1996; Protopopov and Valiev, 1998], which was soon replaced by a parabolic shape that almost completely removes geometrical aberrations [Elleaume, 1998; Lengeler et al., 1999]. Parabolic lenses are the most used X-ray lenses in CRL as they can focus in 1D (cylinder with parabolic section) or 2D (paraboloid of revolution) - cf. Fig. 2.1. It is worth noting, that although less usual, X-ray lenses can assume other shapes: an elliptical profile when focusing collimated beams [Evans-Lutterodt et al., 2003], or a Cartesian oval for point-to-point focusing [Sanchez del Rio and Alianelli, 2012]. However, parabolic shapes always present a very good approximation to geometric focusing and reduce the geometrical aberrations to levels that are smaller than contributions from the fabrication errors and diffraction effects.

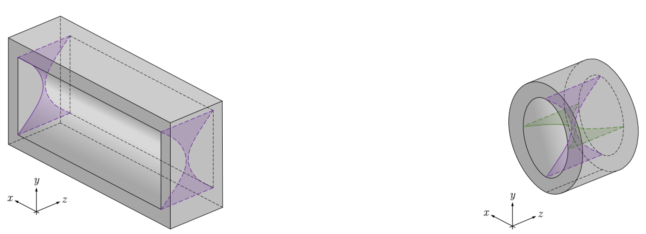

(a) 1D focusing lens (b) 2D focusing lens

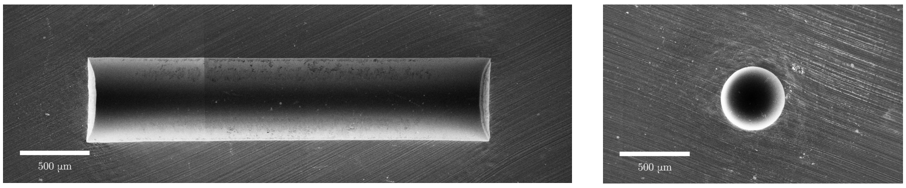

(c) 1D focusing Be lens with $R = 100\ \mu m$ (d) 2D focusing Be lens with $R = 50\ \mu m$

Fig. 2.1.: 1D (left) and 2D focusing (right) X-ray lenses. The top row shows a 3D rendering of such lenses with emphasis on the parabolic profile - shaded in purple is the vertical profile and in green, the horizontal profile. Bottom row shows scanning electron microscope (SEM) images of two Be lenses. Due to the limited field of view, image (c) is stitched, which explains the colour discontinuation on the left side of the image.

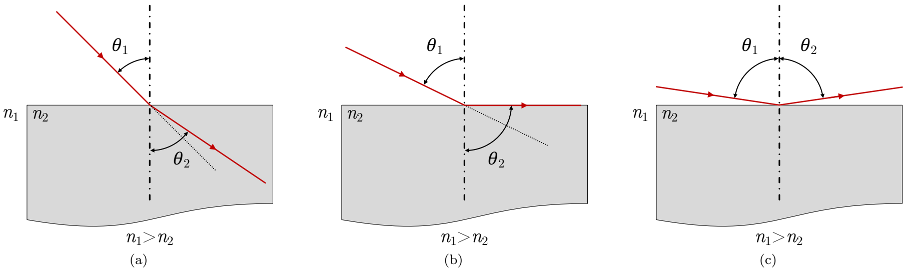

Fig. 2.2.: Refraction and total external reflection in the X-ray regime.

2.2.1 Lens materials and the index of refraction

X-rays are electromagnetic radiation and as such, will primarily interact with the electron clouds in the atoms. When shone in matter, X-rays can either be scattered, absorbed or not interact at all. Scattering can be elastic (Thomson) when there is no energy transfer from the photon to an electron; or inelastic (eg. Compton), where the scattered photon has some energy loss. The absorption process occurs when a photon is absorbed by the atom with a corresponding emission of an electron [Als-Nielsen and McMorrow, 2011, *§1.2-§1.3*]. From the point of view of optical design, there is rarely the need to go into too much depth regarding how X-rays interact with matter[17] and such interactions can be macroscopically described by either the index of refraction in the case of reflection and refraction; or by interference theory in the case of refraction by an ordered array of atoms (Bragg diffraction) or any well-defined geometric structure (physical optics). The index of refraction is commonly written in the X-ray regime as:

$$n(\lambda) = 1 - \delta(\lambda) + i \cdot \beta(\lambda), \tag{2.1}$$

with δ being the refraction index decrement and β, the absorption index. This is the formulation already in use in *The projection approximation* from §1.2.2 - *Transmission elements*. Both δ and β

---

[17] The interactions of X-ray with matter are presented with greater depth by [Als-Nielsen and McMorrow, 2011, *§1*] and [Attwood and Sakdinawat, 2016, *§1* - *§3*].

are positive real numbers much smaller than unity and when observing real part of the index of refraction $\Re\{n\} = 1 - \delta$ one notices that the index of refraction of the lens material is less than that of the vacuum. As a consequence, when applying the law of refraction[18]:

$$n_1 \sin(\theta_1) = n_2 \sin(\theta_2), \tag{2.2}$$

to an X-ray in vacuum (n_1) penetrating the lens material (n_1) with incidence angle θ_1 will refract away from the normal to the surface ($\theta_2 > \theta_1$) as shown in Fig.2.2(a). This is the reason why a focusing lens in the X-ray regime has a concave parabolic section - see Fig.2.1 and Fig. 2.4. The fact that $n_1 > n_2$ in the X-ray regime also explains the total external reflection in the X-ray regime - see Fig.2.2(b)-(c).

From a simplistic point of view, the choice of material for an X-ray lens is guided by maximising the δ/β ratio for a given energy. This means choosing a material that will maximise refraction and minimise absorption within the lens [Serebrennikov et al., 2016; Roth et al., 2017]. This is largest for the lightest elements. On a further step, knowledge about the material inner structure is also very relevant and minimising small-angle scattering from the lenses, speckle formation and unwanted diffraction becomes relevant [Roth et al., 2014; Chubar et al., 2020; Lyatun et al., 2020]. Ultimately, the choice of material is also connected to the manufacturing process of the lenses. Commonly[19] used materials are aluminium and beryllium, which are usually associated with pressed lenses [Lengeler et al., 1999, 2002; Schroer et al., 2002]; nickel and SU-8 polymer for deep X-ray lithography and LIGA [Nazmov et al., 2004, 2005; Nazmov et al., 2007]; SU-8 and other polymeric materials are also associated with 3D printed lenses [Petrov et al., 2017; Sanli et al., 2018; Barannikov et al., 2019]; silicon and diamond for lithography and dry etching [Aristov et al., 2000; Nöhammer, David, et al., 2003; Nöhammer, Hoszowska, et al., 2003; Schroer et al., 2003]; and more recently, diamond for laser ablated lenses [Kononenko et al., 2016; Polikarpov et al., 2016; Antipov, 2020; Medvedskaya et al., 2020]. Figure 2.3 shows δ, β and the ratio δ/β for energies ranging from 5 keV to 100 keV for aluminium, beryllium, diamond and SU-8.

---

[18] The observation of refraction, i.e. *bending* of light as it changes medium, is as old as time, with one of the earliest written references from ca 150 B.C.E. in a philosophical poem "*De Rerum Natura*" by Titus Lucretius Caro [Wilk, 2004]. The first documented attempt to systematic describe refraction with a mathematical formulation and experimental data can be attributed to Claudius Ptolemy of Alexandria. His work, found in "*Optics*" (from ca. 150 C.E.), presents studies on refraction at air-glass and air-water interfaces and arrives at a fairly accurate mathematical formulation for rays close to the optical axis (small-angle approximation) [Kwan et al., 2002], but still not the sine law found in any physics textbook. The sine law found in most physics course books (Eq. 2.2) is commonly attributed to either Willebrord van Roijen Snell (obtained in 1621, but only published after his death by Christiaan Huygens on "*Dioptrica*", 1703) or René Descartes (published in "*La Dioptrique*", annex to "*Discours de la méthode*" - 1637). The understanding and mathematical formulation can be traced back down to Abu Said al-Ala Ibn Sahl with "*On the burning instruments*", 984 [Rashed, 1990]; in a private communication between Johannes Keppler and Thomas Harriot, the latter discloses to Johannes Keppler he knew the sine law as early as of 1602 [Kwan et al., 2002; Lohne, 1959]. In this work, equation 2.2 will be referred to as the *law of refraction*.

[19] A more broad overview on fabrication processes used for refractive X-ray lenses and materials is presented in Table I from the supplementary materials in [Roth et al., 2017].

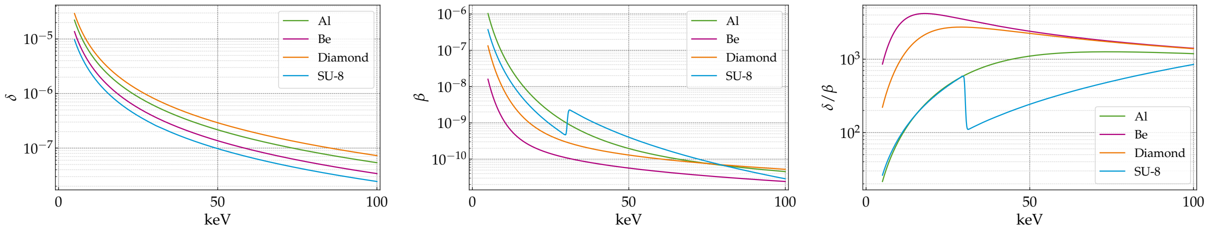

(a) (b) (c)

Fig. 2.3.: (a) refraction index decrement, (b) absorption index and (c) the δ/β ratio for energies ranging from 5 keV to 100 keV for aluminium, beryllium, diamond and SU-8. Figures obtained using the *xraylib* library [Brunetti et al., 2004; Schoonjans et al., 2011].

2.2.2 CRL anatomy

Ideal parabolic X-ray lenses[20] are usually defined by a small set of parameters as shown in Fig. 2.4(a). These are a) material, which, in conjunction with the operation energy defines the complex index of refraction n; b) apex radius of curvature (R_x and R_y for horizontal and vertical radii[21], respectively); c) lens thickness (L) or geometrical aperture (A); and d) distance between the apices of the parabolas ($\mathrm{t_{wall}}$)[22].

Firstly, one should start by defining the optical power $F = f^{-1}$ of a single refracting surface of radius R, where f is its focal length. With the X-ray beam moving along the positive z-direction on Fig. 2.4, the refracting power of the vacuum/lens interface is given by:

$$F \equiv \frac{1}{f} = \frac{n_2 - n_1}{-R} = \frac{\delta}{R}, \tag{2.3}$$

where $n_1 = 1$ and $n_2 = \Re\{1 - \delta + i \cdot \beta\}$. Equation 2.3 considers only the real part of the indices of refraction as this is the part that governs the focusing effect of the lenses. As illustrated by Fig. 2.4(a), lenses are typically formed by two refracting surfaces of nominally the same radii. From paraxial optics, the total optical power of refracting surfaces in intimate contact is the sum of their powers. The same is valid for the cases where the distance between them can be ignored. Typical materials used for X-ray lenses have $10^{-8} < \delta < 10^{-4}$ for their usual application energies [Serebrennikov et al., 2016]. To overcome the weak refraction of a single element, several X-ray lenses are stacked [Tomie, 1994; Snigirev et al., 1996]. Still, under the assumption of thin elements:

$$f_{\text{thin CRL}} = \frac{R}{2N\delta}, \tag{2.4}$$

where the $2N$ comes from stacking N lenslets with two refracting surfaces each, as shown in Fig. 2.4(b). A correction factor can be added to Eq. 2.4 in order to account for the thick-element

---

[20] Throughout this work, a single X-ray lens will be called a lenslet and two or more stacked lenses are referred to as compound refractive lens (CRL).

[21] For a 1D focusing lens, one of the radii goes to infinity on the non-curved surface. For a 2D focusing lens, the manufacturing goal is generally to produce lenses with $R_y = R_y = R$ to avoid astigmatism.

[22] The web thickness ($\mathrm{t_{wall}}$) is directly linked to the absorption and transmission of a X-ray lens, having no useful optical function. It should be kept as small as possible as to minimise absorption but as thick as necessary as to maintain the lenslet mechanical integrity. The exaggerated thinning of the web thickness leads to the risk of breaking the lens in brittle materials and shape deformation in ductile materials, deteriorating the lenslet performance [Lengeler et al., 1998].

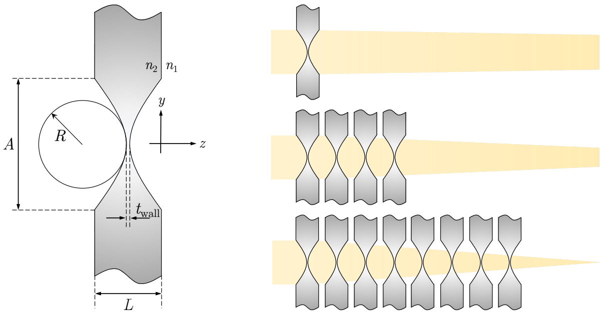

(a) lens sagittal cut

(b) effect of stacking lenslets

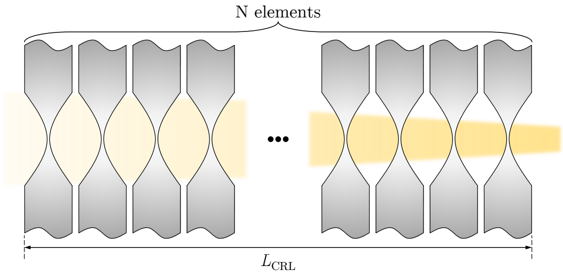

(c) N-stacked lenses to form a CRL

Fig. 2.4.: (a) Sagittal cut of an X-ray lens showing its main geometrical parameters. This concave lens focuses X-rays in the y-direction if $n_1 > n_2$. (b) A single X-ray lens refracts very weakly. To overcome this drawback - pointed out as early as the late 1940s [Kirkpatrick and Baez, 1948] - lenses are usually stacked, hence "compound" in compound refractive lenses. (c) N-stacked lenses to form a CRL.

nature of the CRL, as proposed in [V. Kohn et al., 2003]. The corrected focal length for a thick CRL is given by:

$$f_{\text{CRL}} = \frac{R}{2N\delta} + \frac{L_{\text{CRL}}}{6}. \tag{2.5}$$

This focal distance is taken from the middle of the CRL and L_{CRL} is the CRL longitudinal size, that is, distance from the front surface of the first optical element to the back surface of the last lens - cf. Fig. 2.4(c). The number of lenslets stacked in a CRL is mainly limited by absorption of the X-rays propagating within the lenses.

Another design parameter for an X-ray lens is the geometrical aperture A, as it provides an upper bound for the numerical aperture of the system and, ultimately, to the theoretical optical resolving power. Assuming a parabolic profile of the refracting surface, the lens geometrical aperture can be calculated as:

$$A = 2\sqrt{(L - \text{t}_{\text{wall}})R}, \tag{2.6}$$

where L is the lenslet thickness and t_{wall} is the distance between the apices of the parabolas, commonly referred to as web thickness. For a 1D-focusing lenslet, the aperture related to the uncurved surface is limited only by manufacturing constraints and not the intrinsic lens parameters. Depending on the process used for lens production, it is convenient to isolate L in Eq. 2.6:

$$L = \frac{A^2}{4R} + \text{t}_{\text{wall}}. \tag{2.7}$$

It is clear from Eqs. 2.6 and 2.7 that for a parabolic surface, A and L are intertwined. More often than not, the maximum aperture A is limited by the absorption from the lens thickness on the edge of the parabolic surface (lens active area). The geometrical aperture defined in

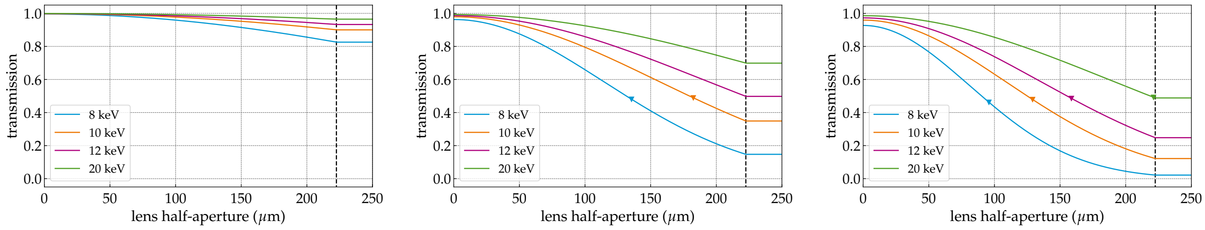

(i) N=1 (ii) N=10 (iii) N=20

(a) intensity transmission

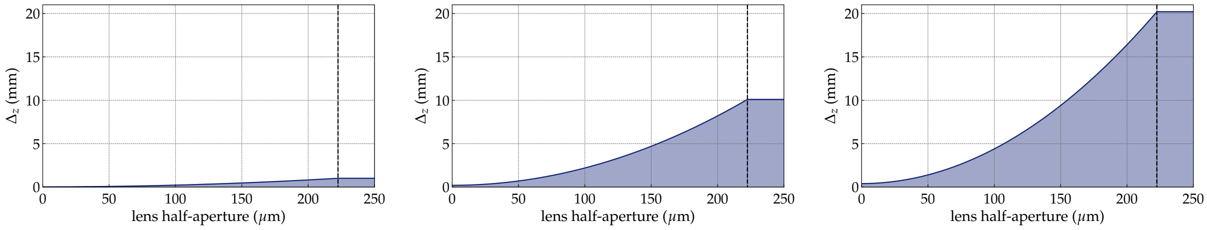

(i) N=1 (ii) N=10 (iii) N=20

(b) accumulated thickness Δ_z

Fig. 2.5.: (a) Normalised intensity transmission and (b) accumulated profile thickness for a CRL composed of (i) 1, (ii) 10 and (iii) 20 2D-beryllium lenses with nominal radius $R = 50$ μm, geometric aperture $A_{\varnothing} = 445$ μm and $t_{\text{wall}} = 20$ μm at different photon energies (for the intensity profiles). Vertical dashed line represents the lens geometrical half-aperture. The triangles in (a) indicate the full width at half maximum (fwhm) for the cases where this value lies within the geometrical aperture.

Eq. 2.6 is greater than or equal to the *effective* lens aperture[23] as indicated by [V. G. Kohn, 2017]. Figure 2.5 shows the transmitted intensity profile of a CRL composed of a different numbers of 2D-beryllium lenses with nominal radius $R = 50$ μm and circular geometric aperture $A_{\varnothing} = 445$ μm at several energies. Unlike visible optics, where the transmitted intensity profile within the aperture, closely follows that of the illumination, the transmitted profile through a (stack of) X-ray lens(es) has strong absorption towards the edge, which defines the CRL as an apodised optical system.

2.2.3 CRL modelling

Ideal thin lens and single-lens equivalent

At any point inside the geometric aperture of a single (bi-concave) paraboloidal X-ray lens, the projected thickness Δ_z can be calculated as:

$$\Delta_z(x,y) = \begin{cases} \dfrac{x^2}{R_x} + \dfrac{y^2}{R_y} + \text{t}_{\text{wall}}, & \forall\,(x,y) \in A, \\ L, & \text{otherwise.} \end{cases} \tag{2.8}$$

If the lens being modelled is a 1D focusing element, that is a cylinder with parabolic section, one of the radii goes to infinity to account for the non-curved surface. The geometric aperture in this direction is not given by Eq. 2.6, but arbitrarily chosen (cf. Fig. 2.1). Eq. 2.8 can be substituted

---

[23] There are several reported ways of defining the *effective* lens aperture - [V. G. Kohn, 2017] discusses and compares some of the different definitions.

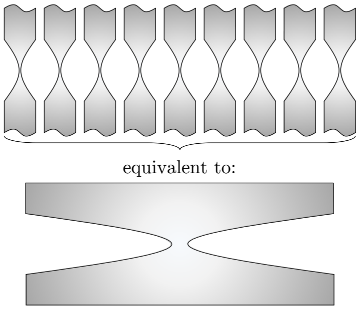

(a) single lens equivalent

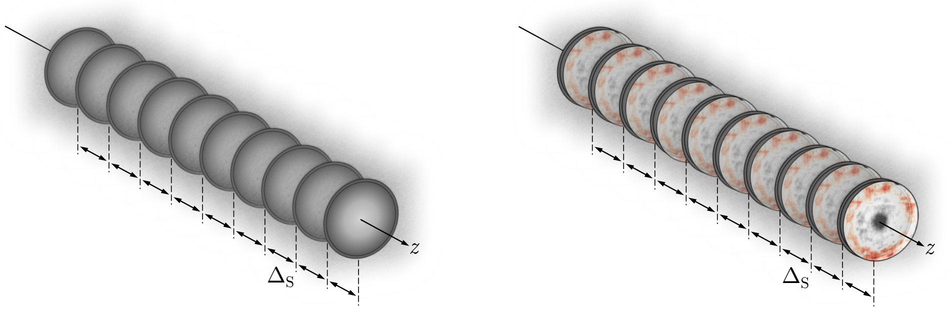

(b) CRL multi-slicing

(c) CRL multi-slicing with figure errors added

Fig. 2.6.: Hierarchical depiction of the CRL. (a) illustrates a single thin element equivalent of several lenslets. This representation accounts for net refraction and absorption in one transmission element but ignores intra-lens spacing. (b) multi-slice representation of a CRL. Here each lens of the stack is represented individually by one transmission element. Those are separated by a drift space corresponding to the typical distance between elements (Δs). (c) Not only can the CRL be represented as a series of thin elements separated by drift spaces, but also figure errors can be added. They are placed directly after the thin element representing a single X-ray lens.

into Eqs. 1.36a and 1.36b to retrieve the complex transmission element expression for an X-ray lens:

$$\mathrm{T}_{\text{single lens}}(\Delta_z) \bullet = \exp\left(-\frac{2\pi}{\lambda}\beta\Delta_z\right) \times \exp\left(-i\frac{2\pi}{\lambda}\delta\Delta_z\right) \bullet . \tag{2.9}$$

Eq. 2.9, the single lens model, accounts for the absorption (first exponential) and phase shift (second exponential) [24]. The complex transmission representing a CRL composed of N elements is, thus, represented by:

$$\mathrm{T}_{\text{CRL}}(\Delta_z) \bullet = \left[\mathrm{T}_{\text{single lens}}(\Delta_z)\right]^N \bullet, \tag{2.10}$$

which is equivalent to multiplying Δ_z by N in Eq. 2.9. The model represented by Eq. 2.10 will be referred to as the single lens equivalent. This model represents a lens stack by a single transmission element with equivalent focal distance and the projected thickness of all the N single lenses as shown in Fig. 2.6(a).

Multi-slicing representation

For a CRL composed of a very high number of lenslets, the single-lens equivalent approximation (Eq. 2.10) may not be adequate to correctly represent such optical systems mainly due to

---

[24] The constant phase shift induced by t_{wall} in Eq. 2.9 (cf. Eq. 2.8) can often be disregarded, as it impinges a constant phase to the wave-field.

the thick[25] nature of the stack - evidenced by Eq. 2.5; and due to the progressive focusing inside the CRL [Schroer and Lengeler, 2005] - exaggerated in Fig. 2.4. For such cases, it is possible to adapt the multi-slicing (MS) techniques[26] for the calculation of the transmission of a wavefront through a CRL. Unlike the methods described by [D. Paganin, 2006] and most recently, by [Li et al., 2017] and [Munro, 2019], where a single weakly-scattering optical element is sliced into several slabs, it is sufficient for most practical cases to break down a CRL into its lenses as shown in Fig. 2.6(b). This can be justified by the fact that at their typical operation energy, the individual lenslets act as weak focusing elements where the projection approximation holds [Protopopov and Valiev, 1998]. The complex transmission representation of a CRL based on the MS approach is given by:

$$\mathrm{T}_{\text{CRL-MS}}(\Delta_z)\bullet = \mathrm{T}_{\text{single lens}}(\Delta_z)\cdot\left[\mathcal{D}(\Delta\mathrm{s})\cdot\mathrm{T}_{\text{single lens}}(\Delta_z)\right]^{N-1}\bullet, \tag{2.11}$$

where $\mathcal{D}(\Delta\mathrm{s})$ is the operator formulation of the Fresnel free-space propagation over a distance Δs (distance between the centres of two adjacent lenses) - cf. Eqs. 1.38 and 1.39.

Eq. 2.11 represents a wavefront $\bullet$ modified by a single lens complex transmission $\mathrm{T}_{\text{single lens}}$, followed by free-space propagation $\mathcal{D}(\Delta\mathrm{s})$ over a distance Δs with the multiplication of the resulting electric field by the transmission element and subsequent free-space propagation done $(N-1)$ times until the N^{th} lens is reached and the last element of the lens stack is accounted for.

Optical imperfections measured with high spatial resolution can be readily converted into a transmission element by direct application of Eq. 1.37 to the height profile, provided it is a 2D map of the phase defects. In this case, the height profile will be the projected thickness of $\Delta_z(x,y)$ in the preceding equations. The MS model introduced earlier in this section can then be adapted to account for the phase errors of the individual lenses:

$$\mathrm{T}_{\text{CRL-MS}}(\Delta_z)\bullet = \mathrm{T}_{\text{imperfect lens}}(\Delta_z)\cdot\left[\mathcal{D}(\Delta\mathrm{s})\cdot\mathrm{T}_{\text{imperfect lens}}(\Delta_z)\right]^{N-1}\bullet, \tag{2.12}$$

with:

$$\mathrm{T}_{\text{imperfect lens}}(\Delta_z) = \mathrm{T}_{\text{figure errors}}(\Delta_z)\cdot\mathrm{T}_{\text{single lens}}(\Delta_z). \tag{2.13}$$

This extended version of the MS model is shown in Fig. 2.6(c). In fact, the modelling of optical elements by means of Eq. 2.12 allows for the description of inhomogenities in the index of refraction within the lens as differences in material density and grain size [Lyatun et al., 2020], inclusions and voids [Roth et al., 2014], and even include effects of diffuse scattering/SAXS for a 2D map with very high spatial resolution [D. M. Paganin and Morgan, 2019].

2.2.4 CRL performance

Diffraction limited focal spot

Even an ideal and the aberration-free finite optical element is not able to image a point-source to a point-like image. Limiting the extent of the focusing element by defining an aperture will induce diffraction effects on the wavefront and these will limit the smallest reachable focus

---

[25] In terms of optical element modelling.

[26] cf. *The Multi-slice approximation* in §1.2.2 - *Transmission elements*.

spot size. The normalised response of the optical system to this point-like source input is called the point-spread-function (PSF). For a system with circular aperture and uniform amplitude across the exit pupil, the intensity of such focused beam at the image plane is proportional to a squared first-order Bessel function of the first kind (Airy pattern). The FWHM of the central cone is given by:

$$d = 1.22\lambda(1-M)\frac{f_{\text{CRL}}}{A}, \tag{2.14}$$

where the M is the magnification of the system, which goes to zero for a plane wave or a very distant source. Systems with nonuniform illumination at the pupil exit, as typically observed for apodised systems such as CRLs, may present a different PSF shape depending on the truncation imposed by the aperture. A very weakly truncated focusing system will have a Gaussian-shaped focal spot as little to no cropping occurs and therefore diffraction effects can be neglected. Increasing the truncation of the beam enhances diffraction effects from the geometric aperture. A strongly truncated focusing system will have a PSF that resembles the diffraction pattern in the far-field associated with the aperture of the system[27] [Mahajan, 1986].

Tolerance conditions for aberrations

Introducing errors to the optical system will reduce the peak intensity in the PSF [Mahajan, 2011, *§8.2*]. The ratio between the peak intensities of the aberrated- and non-aberrated PSF of a system with the same aperture and focal length is referred to as the Strehl ratio - cf. §9.1.3 in [Born et al., 1999]. The optical aberrations on the exit pupil of an optical system can be described by the aberration function $\Phi(x,y)$, with the dimension of metres, which represents any deviation in shape from an ideal profile. For small aberration values, the Strehl ratio can be approximated[28] by:

$$S_{\text{ratio a}} = \frac{I_{\text{aberrated}}}{I_{\text{aberration free}}} \approx 1 - \left(\frac{2\pi}{\lambda}\right)^2 \Delta\Phi^2, \tag{2.15}$$

where $\Delta\Phi$ is the standard deviation of the aberration function $\Phi(x,y)$. An important consequence of Eq. 2.15 is that the reduction in the peak intensity on the focal plane does not depend on the type of aberration nor the focal length of the optical system, but on its standard deviation across the exit pupil of the optical system [Born et al., 1999]. Alternative expressions to Eq. 2.15 are available in §8.3 of [Mahajan, 2011], namely:

$$S_{\text{ratio b}} \approx \left[1 - \left(\frac{2\pi}{\lambda}\right)^2 \frac{\Delta\Phi^2}{2}\right]^2, \tag{2.16}$$

known as the Maréchal expression and:

$$S_{\text{ratio c}} \approx \exp\left[-\left(\frac{2\pi}{\lambda}\right)^2 \Delta\Phi^2\right], \tag{2.17}$$

---

[27] The far-field diffraction pattern of a circular aperture is a squared first-order Bessel function profile while a square aperture will produce a 2D sinc-squared pattern [Guasti and Heredia, 1993].

[28] Eqs. 2.15-2.17 were obtained using a fully-coherent illumination of the optical system, however, defining the Strehl ratio as the ratio between the peak intensities of the aberrated- and non-aberrated optical under study transcends the nature of the illumination. A more complete derivation of the Strehl ratio (Eq. 2.15) can be found in §9.1.3 - *A relation between the intensity and the average deformation of wave-fronts* in [Born et al., 1999].

an empiric expression that fits better numerical results [Wetherell, 1980]. However, for strong aberrations, there is no simple analytic expression to describe the relation between the Strehl ratio and the standard deviation of the aberration function $\Phi(x, y)$ [Kessler, 1981].

It is possible to define an arbitrary minimum acceptable value to the Strehl ratio when evaluating an optical element quality (tolerancing). This value depends on the final application and the desired performance. However, a value of $S_{\text{ratio}} \geq 0.8$ is commonly found throughout literature as an indicator of a well-corrected optical system[29]. Inserting $S_{\text{ratio}} \geq 0.8$ in Eq. 2.15, one obtains:

$$|\Delta\Phi| \leq \frac{\lambda}{14}, \tag{2.18}$$

which is known as the Maréchal criterion for optical quality. Equations 2.16 and 2.17 give similar limits: $\lambda/13.67$ and $\lambda/13.30$, respectively. In order to apply Eq. 2.18 to the case of an X-ray lens, one makes use of Eq. 1.36b with $\Delta\phi = \frac{2\pi}{\lambda}\delta\sigma_z = \frac{2\pi}{\lambda}|\Delta\Phi|$, where $\Delta\phi$ is the standard deviation of the phase, and replaces the projected thickness[30] Δ_z with the standard deviation of the projected figure error σ_z:

$$\sigma_z \leq \frac{\lambda}{14\delta}. \tag{2.19}$$

Equation 2.19 gives an upper limit to the standard deviation of accumulated figure errors for X-ray lenses in order to comply with the Maréchal criterion of tolerable wavefront aberrations, or in other words, to sustain a $S_{\text{ratio}} \geq 0.8$. For a more complete discussion on the aberrated PSF, Strehl ratio and tolerance conditions for primary aberrations, refer to §9 from [Born et al., 1999] and §8 from [Mahajan, 2011]. The limitations and applicability of the Maréchal criterion is presented in [Ross, 2009].

Chromatic aberrations

The optical properties of the X-ray lenses are strongly dependent on the wavelength as both δ and β have an energy dependency - see Fig. 2.3. This energy-dependency causes chromatic aberrations and limitations on the optical performance of the CRL under an X-ray beam with finite bandwidth. The X-ray lens performance focusing degradation due to chromatic aberrations is shown schematically Fig. 2.7. An X-ray lens focusing a beam with a narrow bandwidth ΔE centred around the energy E_0 will have an associated focal length f_0. The lower-energy part of the spectrum, that is, $\text{E}_0 - \Delta\text{E}$ has a higher δ than δ_{E_0}, which is associated with a shorter focal length $f_0 - \Delta f$ as shown in Eq. 2.5. The same reasoning can be applied to the higher-energy part of the spectrum. A beam with energy $\text{E}_0 + \Delta\text{E}$ has a $\delta < \delta_{\text{E}_0}$ and consequently, a larger associated focal length $f_0 + \Delta f$. A sufficiently large bandwidth can cause the change in focal length to be significant, resulting in a blurring of the beam waist. This results in apparent increase of the focal spot and a shift in the apparent focal length. X-ray lenses in storage rings are often used after a monochromator - eg. Si(111) with $\Delta\text{E}/\text{E} \approx 10^{-4}$. Under such conditions the effects of the beam bandwidth can often be neglected, which is not the case for the white- or pink-beam from bending magnets and undulators [Seiboth et al., 2014]. The chromaticity of X-ray lenses

---

[29] This comes from historic reasons: both Rayleigh's $\lambda/4$ criterion for spherical aberrations (1879) and the extended Maréchal criterion for optical quality (1943) yield in a Strehl ratio of ~ 0.8 [Born et al., 1999].

[30] cf. *The projection approximation* in §1.2.2 - *Transmission elements*.

can, however, be used favourably for X-ray harmonic rejection from insertion devices and coarse X-ray spectrum filtering [Vaughan et al., 2011; Polikarpov et al., 2014]. ■

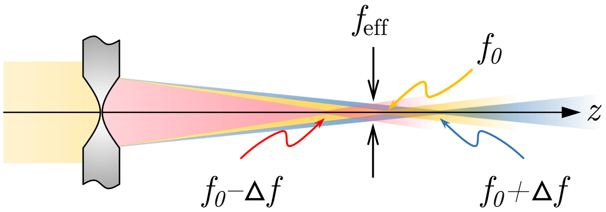

Fig. 2.7.: Chromatic aberrations of an X-ray lens. Lower energy X-rays have a shorter focal length, while more energetic beams focus further away from the lens. If the beam bandwidth is sufficiently large, this causes an increase in the beam waist and a shift in the apparent focal length.

References

Als-Nielsen, J. and McMorrow, D. (2011). *Elements of Modern X-ray Physics*. Second edition. John Wiley & Sons, Inc.

Antipov, S. P. (2020). “Laser microfabrication for applications in x-ray optics: from refractive lens to phase corrector”. In: *Proc. SPIE 11491, Advances in X-Ray/EUV Optics and Components XV* **11491**, p. 23.

Aristov, V., Erko, A., and Martynov, V. (1988). “Principles of Bragg-Fresnel multilayer optics”. In: *Revue de Physique Appliquée* **23**.10, p. 1623.

Aristov, V., Gaponov, S. V., Genkin, V. M., Gorbatov, Y. A., Erko, A. I., Martynov, V. V., Matveev, L. A., Salashchenko, N. N., and Fraerman, A. A. (1986). “Focusing properties of shaped multilayer x-ray mirrors”. In: *Soviet Journal of Experimental and Theoretical Physics Letters* **44**, p. 265.

Aristov, V., Grigoriev, M. V., Kuznetsov, S. M., Shabelnikov, L. G., Yunkin, V. A., Hoffmann, M., and Voges, E. (2000). “X-ray focusing by planar parabolic refractive lenses made of silicon”. In: *Optics Communications* **177**.1, p. 33.

Attwood, D. and Sakdinawat, A. (2016). *X-Rays and Extreme Ultraviolet Radiation*. Second edition. Cambridge: Cambridge University Press.

Baez, A. V. (1960). “A Self-supporting Metal Fresnel Zone-plate to focus Extreme Ultra-violet and Soft X-Rays”. In: *Nature* **186**.4729, p. 958.

Barannikov, A., Polikarpov, M., Ershov, P., Bessonov, V., Abrashitova, K., Snigireva, I., Yunkin, V., Bourenkov, G., Schneider, T., Fedyanin, A. A., and Snigirev, A. (2019). “Optical performance and radiation stability of polymer X-ray refractive nano-lenses”. In: *Journal of Synchrotron Radiation* **26**.3, p. 714.

Barkla, C. G. (1904). “Polarisation in Röntgen Rays”. In: *Nature* **69**.1794, p. 463.

— (1905). “XIII. Polarised Röntgen radiation”. In: *Philosophical Transactions of the Royal Society of London. Series A, Containing Papers of a Mathematical or Physical Character* **204**.372-386, p. 467.

— (1906). “Polarisation in secondary Röntgen radiation”. In: *Proceedings of the Royal Society of London. Series A, Containing Papers of a Mathematical and Physical Character* **77**.516, p. 247.

— (1916). “XXXII. Note on experiments to detect refraction of X-rays”. In: *The London, Edinburgh, and Dublin Philosophical Magazine and Journal of Science* **31**.184, p. 257.

Born, M., Wolf, E., Bhatia, A. B., Clemmow, P. C., Gabor, D., Stokes, A. R., Taylor, A. M., Wayman, P. A., and Wilcock, W. L. (1999). *Principles of Optics: Electromagnetic Theory of Propagation, Interference and Diffraction of Light*. Seventh edition. Cambridge University Press.

Bragg, W. H. and Bragg, W. L. (1913). “The reflection of X-rays by crystals”. In: *Proceedings of the Royal Society of London. Series A, Containing Papers of a Mathematical and Physical Character* **88**.605, p. 428.

Bragg, W. L. (1939). “A new type of ’x-ray microscope’”. In: *Nature* **143**.3625, p. 678.

— (1942). “The X-ray microscope”. In: *Nature* **149**.3782, p. 470.

Brunetti, A., Sanchez del Rio, M., Golosio, B., Simionovici, A., and Somogyi, A. (2004). “A library for X-ray–matter interaction cross sections for X-ray fluorescence applications”. In: *Spectrochimica Acta Part B: Atomic Spectroscopy* **59**.10-11, p. 1725.

Cederström, B., Cahn, R. N., Danielsson, M., Lundqvist, M., and Nygren, D. R. (2000). “Focusing hard X-rays with old LPs”. In: *Nature* **404**.6781, p. 951.

Celestre, R. (2017). “Simulation and characterisation of refractive lenses for X-ray applications”. MSc thesis. Fakultät für Maschinenbau, Technische Universität Ilmenau, Germany.

Chubar, O., Wiegart, L., Antipov, S., Celestre, R., Coles, R., Fluerasu, A., and Rakitin, M. S. (2020). “Analysis of hard x-ray focusing by 2D diamond CRL”. In: *Proc. SPIE 11493, Advances in Computational Methods for X-Ray Optics V*, pp. 11493–20.

Compton, A. H. (1923). “CXVII. The total reflexion of X-rays”. In: *The London, Edinburgh, and Dublin Philosophical Magazine and Journal of Science* **45**.270, p. 1121.

— (1928). “X-Rays as a Branch of Optics”. In: *Journal of the Optical Society of America* **16**.2, p. 71.

— (1931). “The Optics of X-Rays*”. In: *Journal of the Optical Society of America* **21**.2, p. 75.

David, C., Weitkamp, T., Nöhammer, B., and Veen, J. van der (2004). “Diffractive and refractive X-ray optics for microanalysis applications”. In: *Spectrochimica Acta Part B: Atomic Spectroscopy* **59**.10-11, p. 1505.

Dhamgaye, V., Laundy, D., Baldock, S., Moxham, T., and Sawhney, K. (2020). “Correction of the X-ray wavefront from compound refractive lenses using 3D printed refractive structures”. In: *Journal of Synchrotron Radiation* **27**.6.

Duane, W. and Patterson, R. A. (1920). “On the Relative Positions and Intensities of Lines in X-ray Spectra”. In: *Proceedings of the National Academy of Sciences* **6**.9, p. 518.

DuMond, J. W. (1950). “Point-focus x-ray monochromators for low angle diffraction”. In: *Review of Scientific Instruments* **21**.2, p. 188.

Ehrenberg, W. (1947). “X-Ray Optics”. In: *Nature* **160**.4062, p. 330.

— (1949). “X-ray optics; the production of converging beams by total reflection.” In: *Journal of the Optical Society of America* **39**.9, p. 741.

Elleaume, P. (1998). “Optimization of compound refractive lenses for X-rays”. In: *Nuclear Instruments and Methods in Physics Research Section A: Accelerators, Spectrometers, Detectors and Associated Equipment* **412**.2-3, p. 483.

Evans-Lutterodt, K., Ablett, J. M., Stein, A., Kao, C.-C., Tennant, D. M., Klemens, F., Taylor, A., Jacobsen, C., Gammel, P. L., Huggins, H., Ustin, S., Bogart, G., and Ocola, L. (2003). “Single-element elliptical hard x-ray micro-optics”. In: *Opt. Express* **11**.8, p. 919.

Ewald, P. P. (1920). “Zum Reflexionsgesetz der Röntgenstrahlen”. In: *Zeitschrift für Physik* **2**.4, p. 332.

Friedrich, W., Knipping, P., and Laue, M. von (1912). “Interferenz-Erscheinungen bei Röntgenstrahlen”. In: *Sitzungsberichte der Bayerischen Akademie der Wissenschaften zu München, Mathematisch-Physikalische Klasse* **14**, p. 303.

Gaponov, S. V., Gluskin, E. S., Gusev, S. A., Planonov, Y. Y., and Salashchenko, N. N. (1983). “Spherical and plane multilayer normal incidence mirrors for soft x-rays”. In: *Optics Communications* **48**.4, p. 229.

Gorenstein, P. (2010). “Focusing X-Ray Optics for Astronomy”. In: *X-Ray Optics and Instrumentation* **2010**, p. 1.

Gouy, M. (1916). “Sur la catoptrique des rayons X et son application à un spectrographe à foyers réels”. In: *Annales de Physique* **9**.5, p. 241.

Guasti, M. F. and Heredia, M. D. L. C. (1993). “Diffraction Pattern of a Circle/Square Aperture”. In: *Journal of Modern Optics* **40**.6, p. 1073.

Haga, H. and Wind, C. H. (1903). “Die Beugung der Röntgenstrahlen”. In: *Annalen der Physik* **315**.2, p. 305.

Hámos, L. v. (1933). “Röntgenspektroskopie und Abbildung mittels gekrümmter Kristallreflektoren. I. Geometrisch-optische Betrachtungen”. In: *Annalen der Physik* 409.6, p. 716.

— (1937). “The x-ray microscope ”. In: *Nature* **140**.3531, p. 30.

Hart, M. (1971). “Bragg reflection x ray optics”. In: *Reports on Progress in Physics* **34**.2, p. 435.

Howells, M. R. (1993). “Mirrors for Synchrotron-Radiation Beamiines”. In: *New Directions in Research with Third-Generation Soft X-Ray Synchrotron Radiation Sources*. First edition. NATO Advanced Study Institute, p. 1.

Ice, G. E., Budai, J. D., and Pang, J. W. L. (2011). “The Race to X-ray Microbeam and Nanobeam Science”. In: *Science* **334**.6060, p. 1234.

Jacobsen, C. (2019). *X-ray Microscopy*. First edition. Cambridge University Press.

Jark, W., Pérennès, F., Matteucci, M., Mancini, L., Montanari, F., Rigon, L., Tromba, G., Somogyi, A., Tucoulou, R., and Bohic, S. (2004). “Focusing X-rays with simple arrays of prism-like structures”. In: *Journal of Synchrotron Radiation* **11**.3, p. 248.

Jefimovs, K., Vila-Comamala, J., Stampanoni, M., Kaulich, B., and David, C. (2008). “Beam-shaping condenser lenses for full-field transmission X-ray microscopy”. In: *Journal of Synchrotron Radiation* **15**.1, p. 106.

Johann, H. H. (1931). “Die Erzeugung lichtstarker Röntgenspektren mit Hilfe von Konkavkristallen”. In: *Zeitschrift für Physik* **69**.3-4, p. 185.

Johansson, T. (1933). “Über ein neuartiges, genau fokussierendes Röntgenspektrometer - Erste Mitteilung”. In: *Zeitschrift für Physik* **82**.7-8, p. 507.

Jordan, J. A., Hirsch, P. M., Lesem, L. B., and Van Rooy, D. L. (1970). “Kinoform Lenses”. In: *Applied Optics* **9**.8, p. 1883.

Kang, H. C., Stephenson, G. B., Liu, C., Conley, R., MacRander, A. T., Maser, J., Bajt, S., and Chapman, H. N. (2005). “High-efficiency diffractive x-ray optics from sectioned multilayers”. In: *Applied Physics Letters* **86**.15, p. 1.

Kessler, D. (1981). “Image quality criteria in the presence of moderately large aberrations”. PhD thesis. The University of Arizona.

Kirkpatrick, P. (1949). “X-Ray Images by Refractive Focusing”. In: *Journal of the Optical Society of America* 39.9, p. 796.

— (1950). “An Approach to X-Ray Microscopy”. In: *Nature* **166**.4215, p. 251.

Kirkpatrick, P. and Baez, A. V. (1948). “Formation of Optical Images by X-Rays”. In: *Journal of the Optical Society of America* **38**.9, p. 766.

Kirz, J. (1974). “Phase zone plates for x rays and the extreme uv”. In: *Journal of the Optical Society of America* **64**.3, p. 301.

Knipping, P. (1920). “Zur Frage der Brechung der Röntgenstrahlen”. In: *Zeitschrift für Physik* **1**.1, p. 40.

Kohn, V. G. (2017). “Effective aperture of X-ray compound refractive lenses”. In: *Journal of Synchrotron Radiation* **24**.3, p. 609.

Kohn, V., Snigireva, I., and Snigirev, A. (2003). “Diffraction theory of imaging with X-ray compound refractive lens”. In: *Optics Communications* **216**.4-6, p. 247.

Kononenko, T. V., Ralchenko, V. G., Ashkinazi, E. E., Polikarpov, M., Ershov, P., Kuznetsov, S., Yunkin, V., Snigireva, I., and Konov, V. I. (2016). “Fabrication of polycrystalline diamond refractive X-ray lens by femtosecond laser processing”. In: *Applied Physics A* **122**.3, p. 152.

Kwan, A., Dudley, J., and Lantz, E. (2002). “Who really discovered Snell’s law?” In: *Physics World - PhysicsWeb.org* April, p. 64.

Larsson, A., Siegbahn, M., and Waller, I. (1924). “Der experimentelle Nachweis der Brechung von Röntgenstrahlen”. In: *The Science of Nature* **12**.52, p. 1212.

Laue, M. von (1912). “Eine quantitative Prüfung der Theorie für die Interferenz-Erscheinungen bei Röntgenstrahlen”. In: *Sitzungsberichte der Bayerischen Akademie der Wissenschaften zu München, Mathematisch-Physikalische Klasse* **16**, p. 363.

Lengeler, B., Tümmler, J., Snigirev, A., Snigireva, I., and Raven, C. (1998). “Transmission and gain of singly and doubly focusing refractive x-ray lenses”. In: *Journal of Applied Physics* **84**.11, p. 5855.

Lengeler, B., Schroer, C. G., Benner, B., Gerhardus, A., Günzler, T. F., Kuhlmann, M., Meyer, J., and Zimprich, C. (2002). “Parabolic refractive X-ray lenses”. In: *Journal of Synchrotron Radiation* **9**.3, p. 119.

Lengeler, B., Schroer, C. G., Benner, B., Günzler, T. F., Kuhlmann, M., Tümmler, J., Simionovici, A. S., Drakopoulos, M., Snigirev, A., and Snigireva, I. (2001). “Parabolic refractive X-ray lenses: a breakthrough in X-ray optics”. In: *Nuclear Instruments and Methods in Physics Research Section A: Accelerators, Spectrometers, Detectors and Associated Equipment* **467-468**, p. 944.

Lengeler, B., Schroer, C., Tümmler, J., Benner, B., Richwin, M., Snigirev, A., Snigireva, I., and Drakopoulos, M. (1999). “Imaging by parabolic refractive lenses in the hard X-ray range”. In: *Journal of Synchrotron Radiation* **6**.6, p. 1153.

Li, K., Wojcik, M., and Jacobsen, C. (2017). “Multislice does it all—calculating the performance of nanofocusing X-ray optics”. In: *Optics Express* **25**.3, p. 1831.

Liu, C., Conley, R., MacRander, A. T., Maser, J., Kang, H. C., Zurbuchen, M. A., and Stephenson, G. B. (2005). “Depth-graded multilayers for application in transmission geometry as linear zone plates”. In: *Journal of Applied Physics* **98**.11, p. 113519.

Lohne, J. (1959). “Thomas Harriott (1560-1621) - The Tycho Brahe of Optics”. In: *Centaurus* **6**.2, p. 113.

Lyatun, I., Ershov, P., Snigireva, I., and Snigirev, A. (2020). “Impact of beryllium microstructure on the imaging and optical properties of X-ray refractive lenses”. In: *Journal of Synchrotron Radiation* **27**.1, p. 44.

Macrander, A. T. and Huang, X. (2017). “Synchrotron X-Ray Optics”. In: *Annual Review of Materials Research* **47**.1, p. 135.

Mahajan, V. N. (1986). “Uniform versus Gaussian beams: a comparison of the effects of diffraction, obscuration, and aberrations”. In: *Journal of the Optical Society of America A* **3**.4, p. 470.

— (2011). *Aberration Theory Made Simple*. Second. SPIE.

Marchesini, S. and Sakdinawat, A. (2019). “Shaping coherent x-rays with binary optics”. In: *Optics Express* **27**.2, p. 907.

Márkus, O., Greving, I., Kornemann, E., Storm, M., Beckmann, F., Mohr, J., and Last, A. (2018). “Optimizing illumination for full field imaging at high brilliance hard X-ray synchrotron sources”. In: *Optics Express* **26**.23, p. 30435.

Maser, J., Stephenson, G. B., Vogt, S., Yun, W., Macrander, A., Kang, H. C., Liu, C., and Conley, R. (2004). “Multilayer Laue lenses as high-resolution x-ray optics”. In: *Proc. SPIE 5539, Design and Microfabrication of Novel X-Ray Optics II* 5539, p. 185.

Matsuyama, S., Yasuda, S., Yamada, J., Okada, H., Kohmura, Y., Yabashi, M., Ishikawa, T., and Yamauchi, K. (2017). “50-nm-resolution full-field X-ray microscope without chromatic aberration using total-reflection imaging mirrors”. In: *Scientific Reports* **7**.1, p. 46358.

McKinney, W. R. and Howells, M. R. (1980). “Design optimization of "straight groove" toroidal grating monochromators for synchrotron radiation”. In: *Nuclear Instruments and Methods* **172**.1-2, p. 149.

Medvedskaya, P., Lyatun, I., Shevyrtalov, S., Polikarpov, M., Snigireva, I., Yunkin, V., and Snigirev, A. (2020). “Diamond refractive micro-lenses for full-field X-ray imaging and microscopy produced with ion beam lithography”. In: *Optics Express* **28**.4, p. 4773.

Michette, A. G. (1991). “No X-ray lens”. In: *Nature* **353**.6344, p. 510.

Montel, M. (1957). “X-ray microscopy with catamegonic roof mirrors”. In: *X-ray microscopy and microradiography*. FIRST. Academic Press, p. 177.

Morawe, C. and Osterhoff, M. (2010). “Hard X-Ray Focusing with Curved Reflective Multilayers”. In: *X-Ray Optics and Instrumentation* **2010**, p. 1.

Munro, P. R. T. (2019). “Rigorous multi-slice wave optical simulation of x-ray propagation in inhomogeneous space”. In: *Journal of the Optical Society of America A* **36**.7, p. 1197.

Namioka, T., Seya, M., and Noda, H. (1976). “Design and performance of holographic concave gratings”. In: *Japanese Journal of Applied Physics* **15**.7, p. 1181.

Nazmov, V., Reznikova, E., Mohr, J., Snigirev, A., Snigireva, I., Achenbach, S., and Saile, V. (2004). “Fabrication and preliminary testing of X-ray lenses in thick SU-8 resist layers”. In: *Microsystem Technologies*. Vol. **10**. 10, p. 716.

Nazmov, V., Reznikova, E., Snigirev, A., Snigireva, I., DiMichiel, M., Grigoriev, M., Mohr, J., Matthis, B., and Saile, V. (2005). “LIGA fabrication of X-ray Nickel lenses”. In: *Microsystem Technologies* **11**.4-5, p. 292.

Nazmov, V., Reznikova, E., Last, A., Mohr, J., Saile, V., Simon, R., and DiMichiel, M. (2007). “X-ray Lenses Fabricated by LIGA Technology”. In: *AIP Conference Proceedings*. Vol. **879**. AIP, p. 770.

Nöhammer, B., David, C., Rothuizen, H., Hoszowska, J., and Simionovici, A. (2003). “Deep reactive ion etching of silicon and diamond for the fabrication of planar refractive hard X-ray lenses”. In: *Microelectronic Engineering* **67-68**, p. 453.

Nöhammer, B., Hoszowska, J., Freund, A. K., and David, C. (2003). “Diamond planar refractive lenses for third- and fourth-generation X-ray sources”. In: *Journal of Synchrotron Radiation* **10**.2, p. 168.

Ognev, L. I. (2005). “Diffraction calculation for an X-ray refractive Kinoform Lens”. In: *Technical Physics Letters* **31**.4, p. 314.

Paganin, D. (2006). *Coherent X-Ray Optics*. First edition. Oxford University Press.

Paganin, D. M. and Morgan, K. S. (2019). “X-ray Fokker–Planck equation for paraxial imaging”. In: *Scientific Reports* **9**.1, p. 1.

Petrov, A. K., Bessonov, V. O., Abrashitova, K. A., Kokareva, N. G., Safronov, K. R., Barannikov, A. A., Ershov, P. A., Klimova, N. B., Lyatun, I. I., Yunkin, V. A., Polikarpov, M., Snigireva, I., Fedyanin, A. A., and Snigirev, A. (2017). “Polymer X-ray refractive nano-lenses fabricated by additive technology”. In: *Optics Express* **25**.13, p. 14173.

Polikarpov, M., Kononenko, T. V., Ralchenko, V. G., Ashkinazi, E. E., Konov, V. I., Ershov, P., Kuznetsov, S., Yunkin, V., Snigireva, I., Polikarpov, V. M., and Snigirev, A. (2016). “Diamond x-ray refractive lenses produced by femto-second laser ablation”. In: *Proc. SPIE 9963, Advances in X-Ray/EUV Optics and Components XI* **9963**.15, 99630Q.

Polikarpov, M., Snigireva, I., and Snigirev, A. (2014). “X-ray harmonics rejection on third-generation synchrotron sources using compound refractive lenses”. In: *Journal of Synchrotron Radiation* **21**.3, p. 484.

Prins, J. A. (1927). “The Total Reflection of X-rays”. In: *Nature* **120**.3014, p. 188.

Probst, J., Braig, C., Langlotz, E., Rahneberg, I., Kühnel, M., Zeschke, T., Siewert, F., Krist, T., and Erko, A. (2020). “Conception of diffractive wavefront correction for XUV and soft x-ray spectroscopy”. In: *Applied Optics* **59**.8, p. 2580.

Protopopov, V. and Valiev, K. (1998). “Theory of an ideal compound X-ray lens”. In: *Optics Communications* **151**.4-6, p. 297.

Rashed, R. (1990). *A Pioneer in Anaclastics: Ibn Sahl on Burning Mirrors and Lenses*. Vol. **81**. 3, p. 464.

Rebernik Ribič, P., Rösner, B., Gauthier, D., Allaria, E., Döring, F., Foglia, L., Giannessi, L., Mahne, N., Manfredda, M., Masciovecchio, C., Mincigrucci, R., Mirian, N., Principi, E., Roussel, E., Simoncig, A., Spampinati, S., David, C., and De Ninno, G. (2017). “Extreme-Ultraviolet Vortices from a Free-Electron Laser”. In: *Physical Review X* **7**.3, p. 031036.

Röntgen, W. C. (1896). “Über Eine Neue Art von Strahlen (Vorläufige Mittheilung)”. In: *Sonderabbdruck aus den Sitzungsberichten der Würzburger Physik.-medic. Gesellschaft 1895*, p. 132.

Rösner, B., Döring, F., Ribič, P. R., Gauthier, D., Principi, E., Masciovecchio, C., Zangrando, M., Vila-Comamala, J., De Ninno, G., and David, C. (2017). “High resolution beam profiling of X-ray free electron laser radiation by polymer imprint development”. In: *Optics Express* **25**.24, p. 30686.

Ross, T. S. (2009). “Limitations and applicability of the Maréchal approximation”. In: *Applied Optics* **48**.10, p. 1812.

Roth, T., Alianelli, L., Lengeler, D., Snigirev, A., and Seiboth, F. (2017). “Materials for x-ray refractive lenses minimizing wavefront distortions”. In: *MRS Bulletin* **42**.06, p. 430.

Roth, T., Helfen, L., Hallmann, J., Samoylova, L., Kwaśniewski, P., Lengeler, B., and Madsen, A. (2014). “X-ray laminography and SAXS on beryllium grades and lenses and wavefront propagation through imperfect compound refractive lenses”. In: *Proc. SPIE 9207, Advances in X-Ray/EUV Optics and Components IX* 9207, p. 920702.

Sanchez del Rio, M. and Alianelli, L. (2012). “Aspherical lens shapes for focusing synchrotron beams”. In: *Journal of Synchrotron Radiation* **19**.3, p. 366.

Sanli, U. T., Ceylan, H., Bykova, I., Weigand, M., Sitti, M., Schütz, G., and Keskinbora, K. (2018). “3D Nanoprinted Plastic Kinoform X-Ray Optics”. In: *Advanced Materials* **30**.36, p. 1802503.

Schmahl, G. and Rudolph, D. (1969). “Lichstarke Zoneplatten als abbildende Systeme für weiche Röntgenstrahlung”. In: *Optik* **29**, p. 577.

Schoonjans, T., Brunetti, A., Golosio, B., Sanchez del Rio, M., Solé, V. A., Ferrero, C., and Vincze, L. (2011). “The xraylib library for X-ray–matter interactions. Recent developments”. In: *Spectrochimica Acta Part B: Atomic Spectroscopy* **66**.11-12, p. 776.

Schroer, C. G., Kuhlmann, M., Hunger, U. T., Günzler, T. F., Kurapova, O., Feste, S., Frehse, F., Lengeler, B., Drakopoulos, M., Somogyi, A., Simionovici, A. S., Snigirev, A., Snigireva, I., Schug, C., and Schröder, W. H. (2003). “Nanofocusing parabolic refractive x-ray lenses”. In: *Applied Physics Letters* **82**.9, p. 1485.

Schroer, C. G. and Lengeler, B. (2005). “Focusing hard X rays to nanometer dimensions by adiabatically focusing lenses”. In: *Physical Review Letters* **94**.5.

Schroer, C. G., Kuhlmann, M., Lengeler, B., Gunzler, T. F., Kurapova, O., Benner, B., Rau, C., Simionovici, A. S., Snigirev, A. A., and Snigireva, I. (2002). “Beryllium parabolic refractive x-ray lenses”. In: *Proc. SPIE 4783, Design and Microfabrication of Novel X-Ray Optics*. Ed. by D. C. Mancini, p. 10.

Seemann, H. (1916). “Zur Optik der Reflexion von Röntgenstrahlen an Kristallspaliflächen. I”. In: *Annalen der Physik* **356**.20, p. 391.

Seiboth, F., Brückner, D., Kahnt, M., Lyubomirskiy, M., Wittwer, F., Dzhigaev, D., Ullsperger, T., Nolte, S., Koch, F., David, C., Garrevoet, J., Falkenberg, G., and Schroer, C. G. (2020). “Hard X-ray wavefront correction via refractive phase plates made by additive and subtractive fabrication techniques”. In: *Journal of Synchrotron Radiation* **27**.5, p. 27.

Seiboth, F., Kahnt, M., Lyubomirskiy, M., Seyrich, M., Wittwer, F., Ullsperger, T., Nolte, S., Batey, D., Rau, C., and Schroer, C. G. (2019). “Refractive hard x-ray vortex phase plates”. In: *Optics Letters* **44**.18, p. 4622.

Seiboth, F., Schropp, A., Hoppe, R., Meier, V., Patommel, J., Lee, H. J., Nagler, B., Galtier, E. C., Arnold, B., Zastrau, U., Hastings, J. B., Nilsson, D., Uhlén, F., Vogt, U., Hertz, H. M., and Schroer, C. G. (2014). “Focusing XFEL SASE pulses by rotationally parabolic refractive x-ray lenses”. In: *Journal of Physics: Conference Series*. Vol. **499**. 1. Institute of Physics Publishing, p. 12004.

Seiboth, F., Schropp, A., Scholz, M., Wittwer, F., Rödel, C., Wünsche, M., Ullsperger, T., Nolte, S., Rahomäki, J., Parfeniukas, K., Giakoumidis, S., Vogt, U., Wagner, U., Rau, C., Boesenberg, U., Garrevoet, J., Falkenberg, G., Galtier, E. C., Ja Lee, H., Nagler, B., and Schroer, C. G. (2017). “Perfect X-ray focusing via fitting corrective glasses to aberrated optics”. In: *Nature Communications* **8**.1, p. 14623.

Serebrennikov, D., Clementyev, E., Semenov, A., and Snigirev, A. (2016). “Optical performance of materials for X-ray refractive optics in the energy range 8-100 keV”. In: *Journal of Synchrotron Radiation* **23**.6, p. 1315.

Siegbahn, M. (1920). “Nouvelles mesures de précision dans le spectre de rayons X”. In: *Comptes rendus hebdomadaires des séances de l’Académie des sciences* **173**, p. 1350.

— (1921). “Sur le degré d’exactitude de la loi de Bragg pour les rayons X”. In: *Comptes rendus hebdomadaires des séances de l’Académie des sciences* **174**, p. 1121.

Smith, C. S. (1941). “Focusing X-ray monochromators”. In: *Review of Scientific Instruments* **12**.6, p. 312.

Snigirev, A., Kohn, V., Snigireva, I., and Lengeler, B. (1996). “A compound refractive lens for focusing high-energy X-rays”. In: *Nature* **384**.6604, p. 49.

Snigirev, A. and Snigireva, I. (2008). “High energy X-ray micro-optics”. In: *Comptes Rendus Physique* **9**.5-6, p. 507.

Snigireva, I., Snigirev, A., Rau, C., Weitkamp, T., Aristov, V., Grigoriev, M., Kuznetsov, S., Shabelnikov, L., Yunkin, V., Hoffmann, M., and Voges, E. (2001). “Holographic X-ray optical elements: Transition between refraction and diffraction”. In: *Nuclear Instruments and Methods in Physics Research, Section A: Accelerators, Spectrometers, Detectors and Associated Equipment* 467-468.PART II, p. 982.

Snigireva, I., Snigirev, A., Kuznetsov, S., Rau, C., Weitkamp, T., Shabelnikov, L., Grigoriev, M., Yunkin, V., Hoffmann, M., and Voges, E. I. (2001). “Refractive and diffractive x-ray optical elements”. In: *Proc. SPIE 4499, X-Ray Micro- and Nano-Focusing: Applications and Techniques II* **4499**.13, p. 64.

Stenström, K. W. (1919). “Experimentelle Untersuchungen der Röntgenspektra”. PhD thesis. Mathematisch-Naturwissenschaftlichen Sektion der Philosophischen Fakultät zu Lund (present Lunds Universitet), Sweden.

Suehiro, S., Miyaji, H., and Hayashi, H. (1991). “Refractive lens for X-ray focus”. In: *Nature* **352**.6334, p. 385.

Susini, J. (1993). “X-ray mirrors for high-brilliance synchrotron beamlines: R & D at the ESRF”. In: *Proc. SPIE 1740, Optics for High-Brightness Synchrotron Radiation Beamlines*, p. 44.

Tomie, T. (1994). *X-ray lenses*. Japan Patent 6-045288.

— (2010). “The birth of the X-ray refractive lens”. In: *Spectrochimica Acta Part B: Atomic Spectroscopy* **65**.3, p. 192.

Tonner, B. P. and Plummer, E. (1980). “Design criteria and performance of a toroidal grating monochromator”. In: *Nuclear Instruments and Methods* **177**.1, p. 153.

Underwood, J. H., Barbee, T. W., and Frieber, C. (1986). “X-ray microscope with multilayer mirrors”. In: *Applied Optics* **25**.11, p. 1730.

Vaughan, G. B. M., Wright, J. P., Bytchkov, A., Rossat, M., Gleyzolle, H., Snigireva, I., and Snigirev, A. (2011). “X-ray transfocators: focusing devices based on compound refractive lenses”. In: *Journal of Synchrotron Radiation* **18**.2, p. 125.

Vogt, U., Lindblom, M., Charalambous, P., Kaulich, B., and Wilhein, T. (2006). “Condenser for Koehler-like illumination in transmission x-ray microscopes at undulator sources”. In: *Optics Letters* **31**.10, p. 1465.

Walter, B. and Pohl, R. (1908). “Zur Frage der Beugung der Röntgenstrahlen”. In: *Annalen der Physik* **330**.4, p. 715.

— (1909). “Weitere Versuche über die Beugung der Röntgenstrahlen”. In: *Annalen der Physik* **334**.7, p. 331.

Wetherell, W. B. (1980). “The Calculation of Image Quality”. In: *Applied Optics and Optical Engineering*. Vol. **8**, p. 171.

Wilk, S. R. (2004). “Claudius Ptolemy’s Law of Refraction”. In: *Optics & Photonics News* October, p. 14.

Willmott, P. (2019). *An Introduction to Synchrotron Radiation*. Second edition. Wiley.

Wolter, H. (1952). “Spiegelsysteme streifenden Einfalls als abbildende Optiken für Röntgenstrahlen”. In: *Annalen der Physik* **445**.1-2, p. 94.

Yamada, J., Matsuyama, S., Hirose, R., Takeda, Y., Kohmura, Y., Yabashi, M., Omote, K., Ishikawa, T., and Yamauchi, K. (2020). “Compact full-field hard x-ray microscope based on advanced Kirkpatrick–Baez mirrors”. In: *Optica* **7**.4, p. 367.

Yamada, J., Matsuyama, S., Sano, Y., Kohmura, Y., Yabashi, M., Ishikawa, T., and Yamauchi, K. (2019). “Compact reflective imaging optics in hard X-ray region based on concave and convex mirrors”. In: *Optics Express* **27**.3, p. 3429.

Yang, B. X. (1993). “Fresnel and refractive lenses for X-rays”. In: *Nuclear Instruments and Methods in Physics Research Section A: Accelerators, Spectrometers, Detectors and Associated Equipment* **328**.3, p. 578.

Zverev, D., Barannikov, A., Snigireva, I., and Snigirev, A. (2017). “X-ray refractive parabolic axicon lens”. In: *Optics Express* **25**.23, p. 28469.

3

Modelling optical imperfections in refractive lenses

To understand the impact of CRL on the optical design of complete beamlines, it is necessary to be able to simulate them realistically. The basic implementation of X-ray lenses is already available on the two most widespread beamline simulation tools: *SHADOW* [Sanchez del Rio et al., 2011] and *SRW* [Chubar and Elleaume, 1998]. Both implementations, although based on different schemes, ray tracing [Alianelli et al., 2007] and wave optics [Baltser et al., 2011] respectively, are based on an ideal model combining refraction and absorption for the stacked lenses. Much has been done in terms of refining the modelling of ideal X-ray lenses [Umbach et al., 2008; Sanchez del Rio and Alianelli, 2012; Osterhoff et al., 2013; Simons et al., 2017; Pedersen et al., 2018] and, to a certain extent, the modelling of optical imperfections [Pantell et al., 2001; Andrejczuk et al., 2010; Gasilov et al., 2017; Osterhoff et al., 2017]. Except for the work presented in [Roth et al., 2014], investigating and simulating the inner structure of X-ray lenses, the present models consider mainly the lens shape and departure from a perfect parabolic shape. The majority of these models, however, is not publicly available, nor are readily compatible with standard beamline simulations suites like *SHADOW* and *SRW*. Another bottle-neck to the current literature or computer codes for simulating CRLs is that they do not include the data from real lens metrology, as is routinely done for X-ray mirrors simulations [Sanchez Del Rio et al., 2016], which renders more difficult the inclusion of CRLs in simulations of complete beamline configurations in combination with other optical elements.

The modelling and functions presented here[1] are based on the framework of physical optics (cf. §1.2 - *Physical optics*) and are tailored to be used transparently with *SRW* [Chubar and Elleaume, 1998], which already provides a model for the CRL [Baltser et al., 2011] - this basic ideal model combines refraction and absorption for the stacked lenses; optical imperfections from material inhomogeneities (voids, impurities) were later added [Roth et al., 2014]. Expanding this model, we present the optical imperfections in refractive lenses in three different groups: *i*-) misalignments of a single X-ray lens - Fig. 3.1(b)-(c); *ii*-) commonly encountered fabrication errors such as transverse offsets as well as tilts of the individual parabolic sections - Fig. 3.1(d)-(g); *iii*-) and other sources of deviations from the parabolic shape modelled with either polynomial decomposition of error functions or by using metrology data - Fig. 3.9. Each newly added feature is accompanied by a calculation of the residual thickness error, its impact on focusing by CRL and the beam caustic in the vicinity of the focal spot. The Strehl ratios for the different misalignments, fabrication errors and other sources of deviations from the parabolic profile are summarised in Fig. 3.12. Calculations presented in this chapter are merely illustrative and a systematic evaluation is presented in §5 - *Effect of optical imperfections on an X-ray beam*. All simulations shown throughout this chapter have similar conditions, that is, they model misalignments, fabrication errors or arbitrary residual errors of a single 2D-Beryllium lens

---

[1] This chapter is partially based on the work originally published in [Celestre, Chubar, et al., 2020].

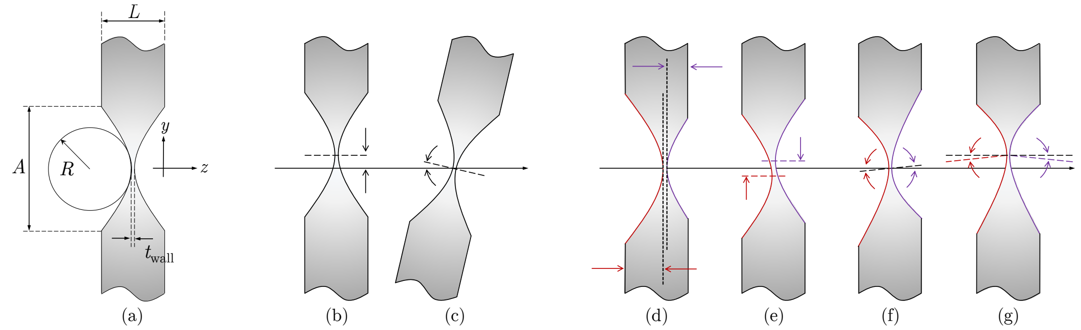

Fig. 3.1.: (a) ideal lens for reference. Lens typical misalignments are the (b) transverse offset and the (c) tilt or a combination of both. Common fabrication errors include the (d) longitudinal offset of the parabolic section, (e) transverse offset of the parabolic section and (f)-(g) tilted parabolic sections.

with nominal radius $R = 50\ \mu$m, geometric aperture $A_{\varnothing} = 440\ \mu$m and $t_{\rm wall} = 20\ \mu$m at 8 keV in fully-coherent simulations. The optical layout used for the simulations is shown in Fig. 3.2. The code main functions implementing the ideal CRL and describing optical imperfections in refractive lenses are subsequently presented. The metrology technique used to measure the phase errors that arise from material inhomogeneities (voids, impurities) and/or figure errors from the lens forming process, namely, X-ray speckle tracking, is discussed in §4 - *Measuring optical imperfections in refractive lenses*.

3.1 Optical imperfections in refractive lenses

In the paraxial approximation, the parabolic shape for a refracting surface is generally regarded as the ideal shape[2] for minimising aberrations. It is legitimate, then, to define as errors any deviation from this ideal parabolic form[3] regardless of their origin. The phase errors induced by an ideal lens misalignment will be presented first, then the typical fabrication errors of bi-concave lenses will be presented shortly after. The misalignment and fabrication errors presented in this section were derived from the accumulated experience in handling beryllium and aluminium bi-concave embossed lenses, which are the most available throughout beamlines in diverse synchrotron facilities. However, the modelling presented here is generic and can be applied to a wide-range of CRL from diverse fabrication processes[4].

The optical layouts used throughout this chapter for all simulations is shown in Fig. 3.2. The emitted radiation is modelled by a filament-electron-beam passing through a CPMU18

---

[2] The shape of a focusing refracting surface can be derived from the Fermat's principle, but the parabolic shape is generally regarded as a good approximation. Large apertures are often necessary when very small focused beams are required, but increasing the geometric aperture of the optical element causes the parabolic approximation to under-perform. Several aspheric surface shapes for different focusing conditions were reported in [Sanchez del Rio and Alianelli, 2012, Fig 4]. For a deeper discussion on aspheric surfaces in the context of optics, please, refer to [Schulz, 1988].

[3] Such definition, however, leaves out discrepancies in the radius of curvature R (designed vs. *de facto*) and the associated defocus it may cause. Discrepancies between designed and executed lenses may render them to be labelled as out-of-specification and may cause the system to under-perform, but are not deviations of the parabolic shape, provided the ideal parabolic shape takes into account the *de facto* radius of curvature. Accounting for such discrepancies can be done using the ideal model described by the transmission element $\mathrm{T}_{\text{single lens}}(\Delta_z)$ (cf. Eq. 2.9) using the *de facto* radius of curvature.

[4] cf. Table 1 from the supplementary material relative to [Roth et al., 2017].

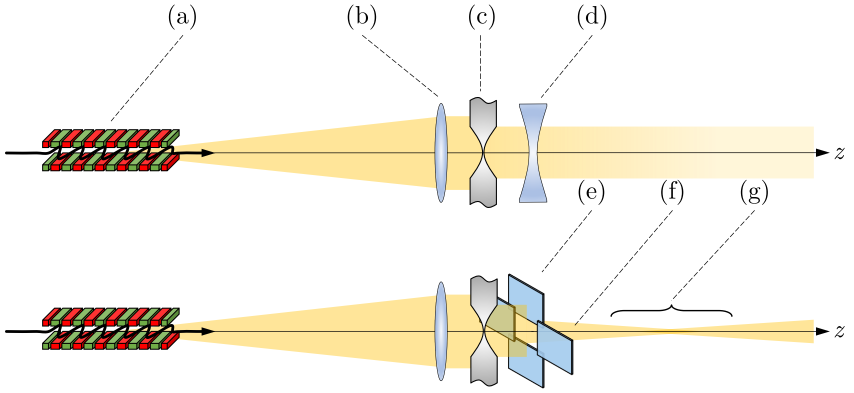

Fig. 3.2.: **top row**: optical setup used for calculating the residual phase and thickness. **bottom row**: setup for phase-contrast radiography, PSF and beam caustics. The illumination is from a filament electron beam passing through an undulator shown in (a). An (b) ideal parabolic phase element is placed to give the illumination a near-plane phase. Downstream of this ideal lens, the (c) X-ray lens is placed. An (d) ideal parabolic phase element can be placed downstream the probe in order to obtain the residual phase. Other measurements require other optical layouts. A (e) slit is put downstream the X-ray lens in order to contain the background and limit the beam to the lens geometric aperture. The phase-contrast image in can be obtained (f) downstream the lens and the beam-caustic range is shown in (g). At the centre of (g) the PSF is calculated.

undulator with 111 magnetic periods with $\Lambda = 18$ mm on-axis magnetic period and magnetic field $B = 0.9863$ T - cf. §1.1.2 - *High brilliance X-ray sources*. The electron-beam parameters are those corresponding to the ESRF-EBS upgrade [Dimper et al., 2014]. An ideal parabolic phase-element with focal length $f = -60$ m is placed 60 m downstream the radiation source. This is done to give the illumination a plane phase - cf. Eq. 1.16. Immediately downstream the ideal lens, the X-ray lens being modelled is placed and any changes to the wave-field after it can be directly attributed to the model studied. A second ideal parabolic phase element can be placed downstream the probe to collimate the beam. This removal of the focusing phase term allows obtaining the residual phase, which can be used to recover a residual thickness error by using Eq. 1.36b[5]. The optical layout for phase-contrast image, beam-caustics and the PSF do not make use of this second ideal element. For reference and to allow subsequent comparison, Fig. 3.3 shows the focusing of a single ideal 2D-beryllium lens with nominal radius $R = 50$ μm, geometric aperture $A_{\varnothing} = 440$ μm and $t_{\text{wall}} = 20$ μm at 8 keV using the basic modelling described in Eq. 2.9.

3.2 Misalignments

Misalignments of optical systems are not optical errors *per se* as they can be mitigated by ensuring proper alignment is done; they will, however, cause changes to the ideal parabolic phase profile if left uncorrected and will affect the optical performance of the system. Although aligning a CRL stack is possible[6], the individual lenslets usually cannot be aligned to each other, hence the interest in modelling such misalignments.

---

[5] Since the residual accumulated thickness translates directly into residual accumulated phase, both terms can be used interchangeably.

[6] The possibility of realignment of the CRL depends on where and how they are installed in the beamline. If their installation is on a bulky transfocator [Vaughan et al., 2011], their realignment is more difficult to be performed. However, when used as a final focusing element, enclosed in small casings or compact transfocators - cf. Fig. 3

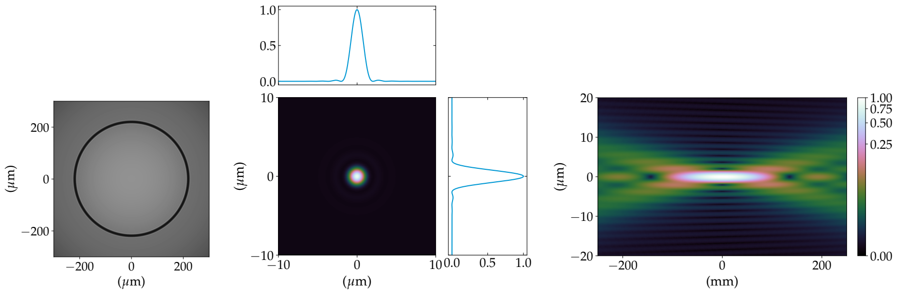

(a) radiography (b) PSF (c) vertical caustics

Fig. 3.3.: Simulations of a single ideal 2D-beryllium lens with nominal radius $R = 50$ μm, geometric aperture $A_{\varnothing} = 440$ μm and $t_{\text{wall}} = 20$ μm at 8 keV - cf. Fig 3.1(a). (a) phase-contrast image 150 mm downstream the ideal lens, (b) point-spread function with cuts centred in $(0, 0)$ and (c) the vertical beam caustics from -250 mm to 250 mm with respect to the focal plane at $f = 4.701$ m.

3.2.1 Transverse offset

Displacing a single element a transverse distance (Δ_x, Δ_y) can be simply done by calculating $\Delta_z(x - \Delta_x, y - \Delta_y)$ in Eq. 2.8. The shifted element is depicted in Fig. 3.1(b). For a pair of coordinates (x, y):

$$\Delta_z(x - \Delta_x, y - \Delta_y) = \begin{cases} \dfrac{(x - \Delta_x)^2}{R_x} + \dfrac{(y - \Delta_y)^2}{R_y} + \text{t}_{\text{wall}}, & \forall\, (x - \Delta_x, y - \Delta_y) \in A, \\ L, & \text{otherwise.} \end{cases} \tag{3.1}$$

Eq. 3.1 is the ideal parabolic profile of a bi-concave lens given by Eq. 2.8 with its vertices centred around (Δ_x, Δ_y). While a single transversely shifted lens considered on its own is innocuous, piling up several shifted lenses has impacts on the overall accumulated phase parabolic shape and resulting geometric aperture. Although the exact effect of relative misalignments between individual lenses on the phase of the wave-field depends on the distance between lenslets, the energy, footprint and divergence of the X-ray beam, some insight can be gained by considering the individual focusing elements as thin-optical elements in intimate contact. Consider N stacked lenses transversely misaligned with their transverse distance to the optical axis given by $(\Delta_{x_j}, \Delta_{y_j})$, with $j = 1,\ 2,\ \ldots,\ N$. Within the intersection of their geometric apertures, the accumulated thickness is given by:

$$\begin{aligned} \Delta_{z_\Sigma}(x, y) &= \sum_{j=1}^{N} \Delta_z(\Delta_{x_j}, \Delta_{y_j}) \\ &= \sum_{j=1}^{N} \underbrace{\frac{x^2}{R_{x_j}} + \frac{y^2}{R_{y_j}}}_{\text{(I)}} \underbrace{- 2x\frac{\Delta_{x_j}}{R_{x_j}} - 2y\frac{\Delta_{y_j}}{R_{y_j}}}_{\text{(II)}} + \underbrace{\frac{\Delta_{x_j}^2}{R_{x_j}} + \frac{\Delta_{y_j}^2}{R_{y_j}} + \text{t}_{\text{wall}_j}}_{\text{(III)}} . \end{aligned} \tag{3.2}$$

The first term in Eq. 3.2, (I) is a quadratic term and it indicates ideal focusing as in Eq. 2.8. The residual terms (II) and (III) are a linear term in x and y and a constant offset term, respectively. The first residual term, i.e. (II), adds a linear phase to the wave-front and acts like a prism,

---

in [Lengeler et al., 1999] and [Kornemann et al., 2017; Narikovich et al., 2019], their realignment can be done more easily.

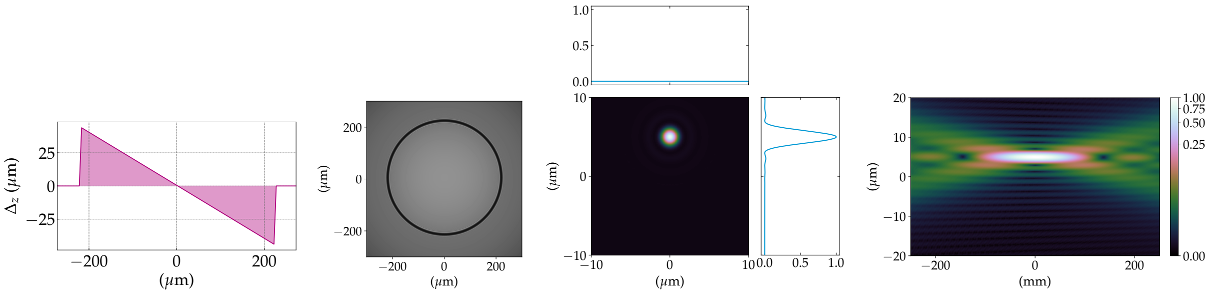

(a) residues (b) radiography (c) PSF (d) vertical caustics

Fig. 3.4.: Simulations of an ideal lens shifted by $\Delta_y = 5$ μm - cf. Fig 3.1(b). (a) Residual thickness, (b) phase-contrast image of the lens, (c) point spread function with cuts centred in $(0, 0)$ and (c) the vertical beam caustics from -250 mm to 250 mm with respect to the focal plane.

not deforming the monochromatic wave-field, but redirecting it. At the focal plane, the image position is transversely shifted but no change to the intensity and phase profiles is added. Symmetrically shifted lenses[7] make (II) go to zero. The residual terms in (III) add a constant phase offset to the transmitted beam in addition to absorption. The effects of the transverse offset to a single X-ray lens are shown in Fig. 3.4.

3.2.2 Tilted lens

When rotating a lens in space as shown in Fig. 3.1(c) and calculating its projected thickness, it is helpful to decouple the rotation of the front and back surfaces. This can be done by defining a point cloud in Cartesian coordinates:

$$z_{\text{front surface}}(x-\Delta_x, y-\Delta_y) = \frac{\Delta_z(x-\Delta_x, y-\Delta_y)}{2}, \tag{3.3a}$$

$$z_{\text{back surface}}(x-\Delta_x, y-\Delta_y) = -\frac{\Delta_z(x-\Delta_x, y-\Delta_y)}{2} \tag{3.3b}$$

where $\Delta_z(x-\Delta_x, y-\Delta_y)$ is given by Eq. 3.1. The projected thickness is given by:

$$\Delta_z(x, y) = z_{\text{front surface}}(x, y) - z_{\text{back surface}}(x, y), \tag{3.4}$$

provided those are calculated on the same grid (x, y). A tilted lens can be described by rotation matrices in three dimensions. In a system where the position is represented[8] as $(x, y, z, 1)$ The transformation matrices allowing a rotation $\theta_{x,y,z}$ around each of the Cartesian axis are [House and Keyser, 2016]:

$$R_{\theta_x} = \begin{bmatrix} 1 & 0 & 0 & 0 \\ 0 & c_x & -s_x & 0 \\ 0 & s_x & c_x & 0 \\ 0 & 0 & 0 & 1 \end{bmatrix}, \quad R_{\theta_y} = \begin{bmatrix} c_y & 0 & s_y & 0 \\ 0 & 1 & 0 & 0 \\ -s_y & 0 & c_y & 0 \\ 0 & 0 & 0 & 1 \end{bmatrix}, \quad R_{\theta_z} = \begin{bmatrix} c_z & -s_z & 0 & 0 \\ s_z & c_z & 0 & 0 \\ 0 & 0 & 1 & 0 \\ 0 & 0 & 0 & 1 \end{bmatrix}, \tag{3.5}$$

where $c_\theta = \cos(\theta)$ and $s_\theta = \sin(\theta)$. R_{θ_x} denotes a rotation around the $x-$axis, R_{θ_y} around the $y-$axis and, finally, R_{θ_z} around the $z-$axis. Matrix multiplication is associative, which implies

---

[7] That is $\Delta_{x_m} = -\Delta_{x_n}$ or $\Delta_{y_m} = -\Delta_{y_n}$ for $m, n \in (1,\ 2,\ \ldots,\ N)$.

[8] Expressing the 3D coordinates as $(x, y, z, 1)$ comes from homogeneous coordinates systems often used in projective geometry [House and Keyser, 2016].

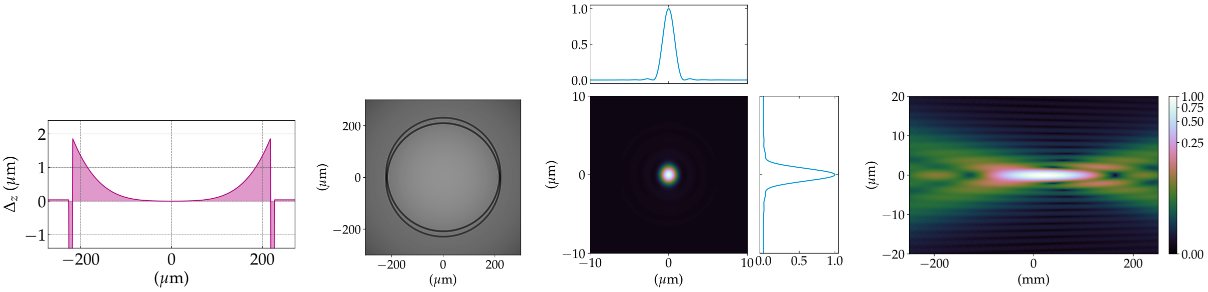

(a) residues (b) radiography (c) PSF (d) vertical caustics

Fig. 3.5.: Simulations of an ideal lens tilted by $\theta_x = 1°$ - cf. Fig 3.1(c). (a) Residual thickness, (b) phase-contrast image of the lens, (c) point spread function with cuts centred in $(0, 0)$ and (c) the vertical beam caustics from -250 mm to 250 mm with respect to the focal plane.

that if multiple rotations are involved, that is R_{θ_x}, R_{θ_y} and R_{θ_z} are applied to a set of points (x, y, z), an equivalent rotation matrix $R_\theta = R_{\theta_z} R_{\theta_y} R_{\theta_x}$ can be calculated and then, applied to those points is space:

$$\begin{aligned} [x_\theta, y_\theta, z_\theta, 1]^{\mathrm{T}} &= R_{\theta_z} R_{\theta_y} R_{\theta_x} [x, y, z, 1]^{\mathrm{T}}, \\ &= R_\theta [x, y, z, 1]^{\mathrm{T}}, \end{aligned} \tag{3.6}$$

where $(x_\theta, y_\theta, z_\theta)$ are the transformed (x, y, z) coordinates after the $R_\theta = R_z R_y R_x$ rotation and the $^{\mathrm{T}}$ in Eq. 3.6 represents transposed matrices. The rotations given by R_θ have to be applied to both the front and back surfaces of the lens independently, with their respective point clouds given by Eqs. 3.3. In order to calculate the projected thickness along the optical axis, the rotated front and back surfaces have to be recalculated on a common grid, which is done by two-dimensional interpolation of $(x_\theta, y_\theta, z_\theta)$ to the original (x, y) grid. The associative property allows for considerable computation time reduction, as the rotation can be done applying a single equivalent rotation matrix as opposed to three individual rotations. On the other hand, matrix multiplication is not commutative and the order of operations matter and should be specified[9,10] when rotating a point cloud. Equations 3.5 have their pivot point centred in the origin of their axis, that is, around $(x, y, z) = (0, 0, 0)$ in Cartesian coordinates. It is possible to define arbitrary pivot points with a combination of translations and rotations. Tilting an optical element in space will introduce aberrations to the beam propagation and its focusing[11]. This is apparent in the residual accumulated thickness in projection approximation shown in Fig. 3.5. The profile shown in Fig. 3.5(a) is proportional to the 4th power of the lateral coordinates in the direction of the shift. This contributes for the elongation of the beam along the propagation direction and shift on the focal plane position as shown in Fig. 3.5(d), which is a typical sign of spherical aberrations. It is also possible to see how the two surfaces (back and front) do not overlap, causing a slight reduction in the geometric aperture area, which gives rise to the the discontinuities in Fig. 3.5(a).

---

[9] The implementation of the affine transformations for rotating CRLs in space follow the order: rotation around the $x-$axis (R_x), rotation around the $y-$axis (R_y) and then, rotation around the $z-$axis (R_z).

[10] For a deeper discussion on the properties of the affine transformations and coordinates systems, please refer to appendices *C-E* in [House and Keyser, 2016].

[11] The interest in tilted optical elements and compensation is an active field, as evidenced by the literature on that subject - cf. [Guizar-Sicairos et al., 2011; Zhou et al., 2019; Ali and Jacobsen, 2020].

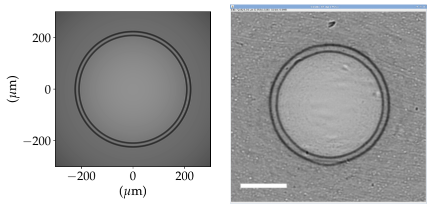

(a) simulation (b) experimental

Fig. 3.6.: (a) Simulated and (b) measured phase-contrast image of a single of a 2D-beryllium lens with nominal radius $R = 50$ μm with designed geometric aperture $A_{\varnothing} = 440$ μm. The scale bar in (b) is 200 μm wide.

3.3 Fabrication errors

Modelling the typical misalignment of X-ray lenses implies calculating the lateral displacements and rotations in space of an ideal X-ray lens. However, bi-concave lenses may also present misalignments between the front and back focusing surfaces, which are closely related to the manufacturing processes involved in the lens production. Here, the front and back focusing surfaces are treated independently, allowing to model longitudinal and transverse misalignments as well as tilts of the front and back focusing surface concerning the optical axis.

3.3.1 Longitudinal offset of the parabolic section

Longitudinal offsets of the parabolic portions of a bi-concave X-ray lens appear when, for the same radius of curvature R, one parabolic portion reaches deeper into the lens disc than the other one - cf. Fig. 3.1(d). The first eminent observation is that front and back surfaces will have different geometric apertures along the focusing direction. The new geometric aperture of the longitudinally offset parabolic profile can be calculated as:

$$A_{\text{offset}} = 2\sqrt{[L - (\text{t}_{\text{wall}} + 2 \cdot \text{offset})]R}, \tag{3.7}$$

where a positive offset increases the apparent web thickness of the half lens to $\text{t}_{\text{wall}}/2 + \text{offset}$ and decreases the geometric aperture for a fixed lens thickness. The aperture given by A_{offset} and the apparent web thickness are used in Eq. 3.4 (cf. Eqs. 3.1 and 3.3) when calculating the projected thickness. Longitudinal offsets do not affect the parabolic accumulated shape of a single lens within A_{offset} and, consequently, do not impose any optical imperfection to an optical system based on such lenses. However, they are often encountered in real lenses[12] and merit the implementation in the lens modelling. Fig. 3.6 shows the simulated profile and a radiography of a real lens showing the effects of the longitudinal offset of the parabolic section.

3.3.2 Transverse offset of the parabolic section

Although parallel to the optical axis, it is possible that the parabolic surfaces axes are not collinear. This is shown in Fig. 3.1(e). The modelling of the transverse offset of the front or/and back surfaces of a lens concerning the optical axis is done by calculating the net offset of each surface, that is the sum of lens transverse offset with the front or/and back surface

---

[12] Especially in embossed lenses, where different penetration depths of the punches often lead to asymmetric lenses.

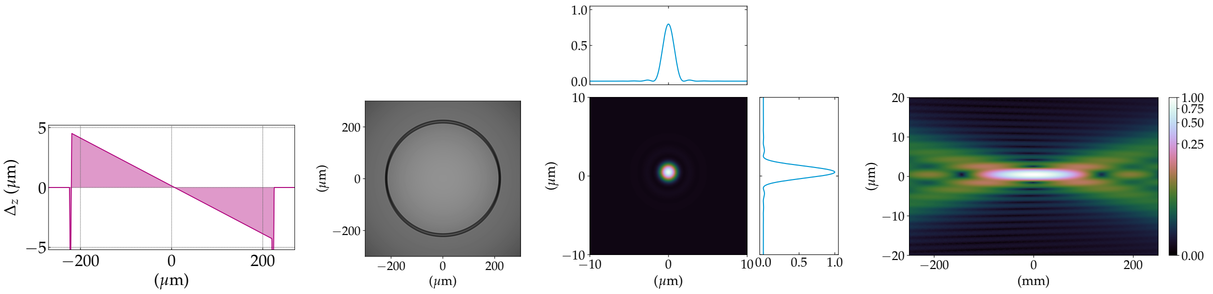

(a) residues (b) radiography (c) PSF (d) vertical caustics

Fig. 3.7.: Simulations of a lens with front focusing parabolic section shifted by $\Delta_y = -2\ \mu$m and back focusing shifted by $\Delta_y = -3\ \mu$m - cf. Fig 3.1(e). (a) Residual thickness, (b) phase-contrast image of the lens, (c) point spread function with cuts centred in $(0, 0)$ and (c) the vertical beam caustics.

transverse offset, and applying it to Eqs. 3.3 when calculating Eq. 3.4. The effects on the residual accumulated phase of non-collinear parabolic surfaces are the same as the one described in the section §3.2.1 - *Transverse offset*, that is, the presence in the residual phase of a linear and a constant term, which can be seen in Fig. 3.7.

3.3.3 Tilted parabolic section

When the axes of the parabolic front or/and back surfaces are not parallel to the optical axis, the lens active area appears to be tilted as shown in Figs. 3.1(f) and (g). Similarly to what was introduced in the section §3.2.2 - *Tilted lens*, both front and back surfaces are rotated according to the rotation matrices described in Eqs. 3.5 and the procedure described by Eq. 3.6. There are two subtle differences: the rotation angles from front and back surfaces can be chosen independently and the rotation is only applied to the curved part of the lens, and not to the whole front and back surfaces including the flat parts. The independent rotations allow for different regimes: one where both imprints are tilted with the same angle as in shown in Fig. 3.1(f), which yields a residual phase similar to the one discussed in §3.2.2 - *Tilted lens*; and one where front and back surfaces are tilted with different angles, which yields an asymmetric residual phase as shown in Fig. 3.8. By not applying the rotation to the plane region the lens projected thickness L is not changed. A close inspection of Fig. 3.8 shows that while the symmetric case has a residual phase proportional to the 4th power of the lateral coordinates in the direction of the tilt, elongating the beam focusing in the propagation direction and shifting it on the same direction - typical of spherical aberrations, the residual phase of the anti-symmetric case has residual phase proportional to the 3rd power of the lateral coordinates in the direction of the tilt and has a PSF typical of coma-aberrated systems. The behaviour of the anti-symmetric case resulting in coma aberrations is commonly encountered in tilted one-sided kinoform lenses and zone-plates as reported in [Guizar-Sicairos et al., 2011; Ali and Jacobsen, 2020].

3.4 Other sources of deviations from the parabolic shape

So far, the modelling described here relies on translations and rotations of an ideal parabolic surface and investigating the residual phase. Another equally valid approach is to manipulate directly the residual phase and add it to the phase of an ideal focusing lens, which can be done

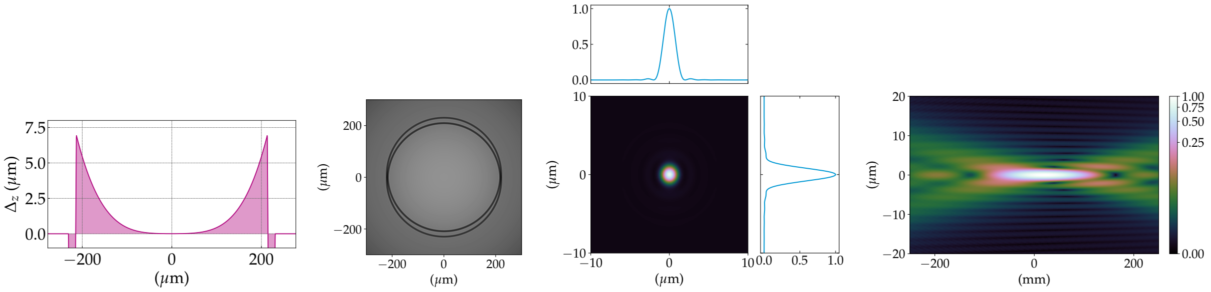

(a) residues (b) radiography (c) PSF (d) vertical caustics

Symmetric tilt of front- and back- surfaces by $\theta_{x_{\text{front}}} = \theta_{x_{\text{back}}} = 1°$

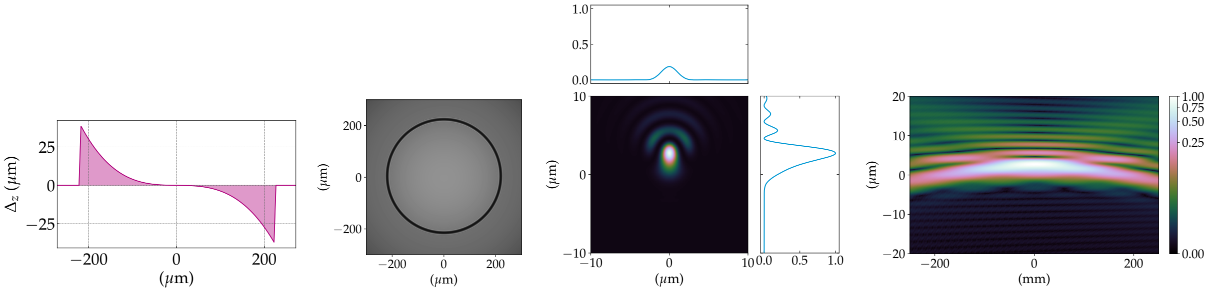

(e) residues (f) radiography (g) PSF (h) vertical caustics

Anti-symmetric tilt of front- and back- surfaces by $\theta_{x_{\text{front}}} = -\theta_{x_{\text{back}}} = 0.5°$

Fig. 3.8.: Simulations of a lens with front and back focusing parabolic sections independently tilted as shown in Fig 3.1(f) and (g). The (a) residual thickness, (b) phase-contrast image, (c) point spread function and (c) the vertical beam caustics of the symmetric tilt are shown on the top row. The (e) residual thickness, (f) phase-contrast image, (g) point spread function and (h) the vertical beam caustics for the anty-symmetric case with the same conditions is presented in the bottom row.

fitting arbitrary surfaces or by introducing data from metrology of the optical element to be simulated.

3.4.1 Orthornormal polynomials

A widespread form of representing optical aberrations of arbitrary shapes is by decomposing them into an orthonormal base. Perhaps the most ubiquitous set of aberration functions is given by the Zernike polynomials for a circular aperture, first described in [Zernike, 1934]. Their appeal comes from the fact that not only they are directly related to Seidel (primary), Schwarzschild (secondary) and tertiary-aberrations[13] but also include piston and tilts; they form an orthonormal base, which means that the value of the coefficients is not affected by the removal of a particular term [Mahajan and Dai, 2007]. Another advantage of the Zernike polynomial decomposition is that each orthonormal aberration coefficient is the standard deviation for that particular aberration over the exit pupil, which is valuable when evaluating the optical system compliance with the Maréchal criteria and calculating the Strehl ratio [Mahajan, 1983].

For the aforementioned decomposition of the aberration function in an orthonormal base to retain its properties, the application of the circular Zernike polynomials must be limited to circular apertures. Other shapes of apertures with- or without obscuration can be obtained by

---

[13] This jargon comes from a power-series expansion of the aberration function. There are five primary aberrations, nine secondary aberrations and fourteen aberration terms for the tertiary aberrations. They all involve spherical aberration, coma, astigmatism, field curvature, distortion and variations of thereof [Mahajan, 2013].

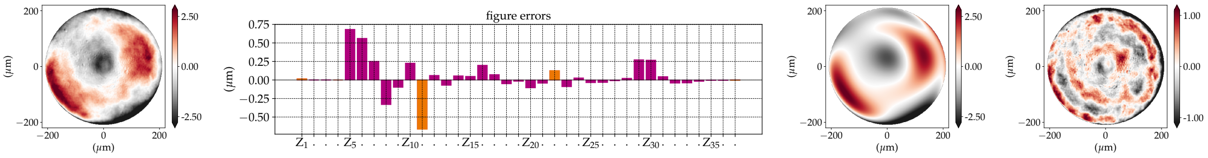

(a) Be lens (b) Polynomial decomposition (c) Reconstructed profile (d) Residual profile

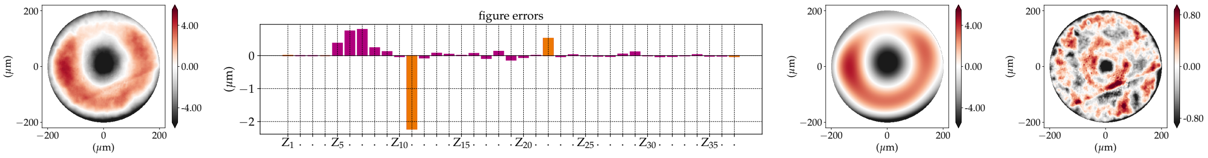

(e) Al lens (f) Polynomial decomposition (g) Reconstructed profile (h) Residual profile

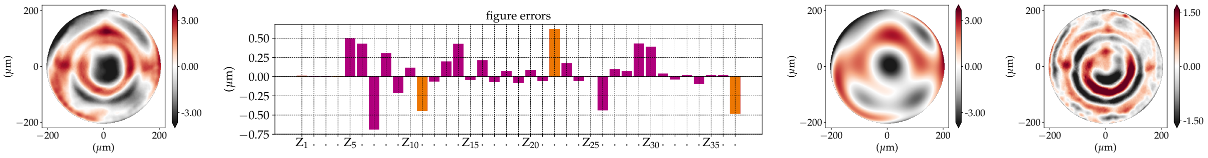

(i) Diamond lens (j) Polynomial decomposition (k) Reconstructed profile (l) Residual profile

Fig. 3.9.: Comparison of the decomposition of errors in Zernike circle polynomials for beryllium, aluminium and diamond 2D lenses. **First row**: Be lens with (a) projected profile with RMS value $\sigma_z = 1.4\ \mu$m; (b) polynomial decomposition of the profile in (a); (c) the reconstruction based on those coefficients with RMS value $\sigma_z = 1.3\ \mu$m; and (d) the residual profile after the fit. **Middle row**: Al lens (e) projected profile with RMS value $\sigma_z = 2.6\ \mu$m; (f) polynomial decomposition of the profile in (e); (g) the reconstruction based on those coefficients with RMS value $\sigma_z = 2.5\ \mu$m; and (h) the residual profile after the fit. **Bottom row**: diamond lens with (i) projected profile with RMS value $\sigma_z = 1.8\ \mu$m; (j) polynomial decomposition of the profile in (i); (k) the reconstruction based on those coefficients with RMS value: $\sigma_z = 1.6\ \mu$m; and (d) the residual profile after the fit.

Gram-Schmidt orthonormalisation and weighting of the Zernike circle polynomials [Swantner and Chow, 1994; Mahajan, 1995]. X-ray optics systems often have a rectangular aperture and two sets of polynomials are of particular interest in optical design: the set of orthonormal Zernike polynomials for a rectangular aperture [Mahajan and Dai, 2007; Mahajan, 2012] and the 2D-Legendre polynomial set for a rectangular aperture [Mahajan, 2010]. Preferentially[14], the Zernike circle polynomials are applied to 2D focusing lenses with a circular aperture. For 2D focusing X-ray lenses with square aperture, low aspect ratio between horizontal and vertical apertures and not strongly astigmatic focusing, e.g. crossed planar X-ray lenses, the Zernike rectangular polynomials are preferred. The 1D focusing lens is better fit by the 2D Legendre polynomial set[15]. Analysing and describing refractive X-ray optics using circular Zernike and 2D Legendre polynomials were first presented by [Koch et al., 2016].

Fitting a surface to a given set of orthonormal polynomials is very useful as it allows to characterise and classify optical systems based on the types of aberrations it presents, which can be useful when mitigation strategies are being drawn (balancing aberrations). In addition to that, surfaces mimicking optical can be generated by asserting coefficients to a given polynomial set. This can be used to understand and isolate the effects of a given type of aberration or be used to represent a real surface when the coefficients for a particular optical element are known. Profiles generated by Zernike circle polynomials are shown in Fig. 3.9. They were generated

---

[14] Prof. V. Mahajan (University of Arizona, USA) and Prof. H. Gross (University of Jena, Germany) are acknowledged for discussions on orthonormal polynomials in wavefront analysis and pointing out relevant literature.

[15] Please, refer to [Ye et al., 2014] for a comparison between 2D orthonormal sets for square apertures.

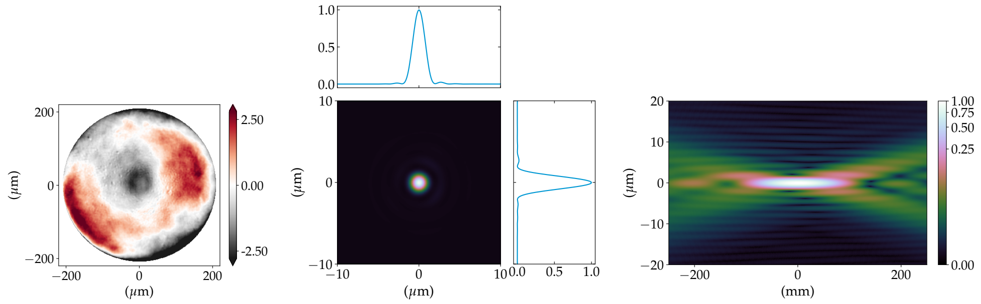

(a) profile (b) PSF (c) vertical caustics

Simulations using the metrology data

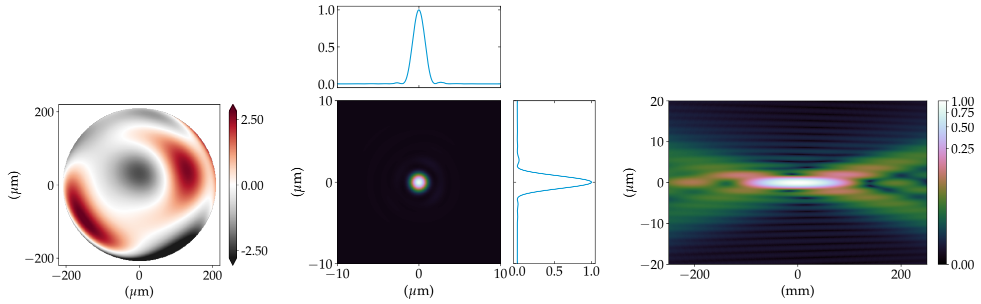

(d) profile (e) PSF (f) vertical caustics

Simulations using the Zernike circle polynomials

Fig. 3.10.: Simulations of a single 2D-beryllium lens with nominal radius $R = 50$ μm, geometric aperture $A_{\varnothing} = 440$ μm and $t_{\text{wall}} = 20$ μm at 8 keV. **top row**: (a) metrology profile, (b) point-spread function with cuts centred in $(0, 0)$ and (c) vertical beam caustics from -250 mm to 250 mm with respect to the focal plane. **bottom row**: (d) profile generated by the Zernike circle polynomials coefficients, (e) PSF and (f) beam caustics.

using coefficients obtained from metrology data. The fit profiles resemble the metrology profiles they are based on - cf. left-hand side of Fig. 3.9. A comparison between the effects on a coherent X-ray beam for both profiles is shown in Fig. 3.10. The difference between both simulation sets is almost imperceivable, whuch can be explained by the similarity between both figure error profiles and the fact that the difference between the figure errors RMS value is almost negligible: $\sigma_z = 1.3$ μm (Zernike polynomial reconstruction) against $\sigma_z = 1.4$ μm (metrology data), while the Maréchal criterion calculated for beryllium lenses illuminated at 8 keV requires the accumulated projected figure errors to be $\sigma_z \leq 2.08$ μm, which makes the impact in the reduction in intensity at the focal position is almost negligible - cf. Eqs. 2.15-2.19 for the Maréchal criteria and Strehl ratio in *Tolerance conditions for aberrations* from §2.2.4 - *CRL performance*. Fig. 3.11 shows the same kind of comparison in Fig. 3.9, but with a less similar fit fit. Simulations still show good agreements, showing the same features: side-lobes (typical of trefoil aberration), elongated tail upstream the focal plane and 'Y'-shaped profile cut downstream.

3.4.2 Metrology data

Any (unintentional) deviation from the parabolic shape can be considered as a manufacturing error. Each manufacturing process has some type of (signature) error associated to it and with the increasing number of exotic - or unconventional - designs and tailored manufacturing strategies, it is unreasonable to create a model that could parametrise all sources of deviations from the parabolic shape. To circumvent that and to accurately model phase imperfections in

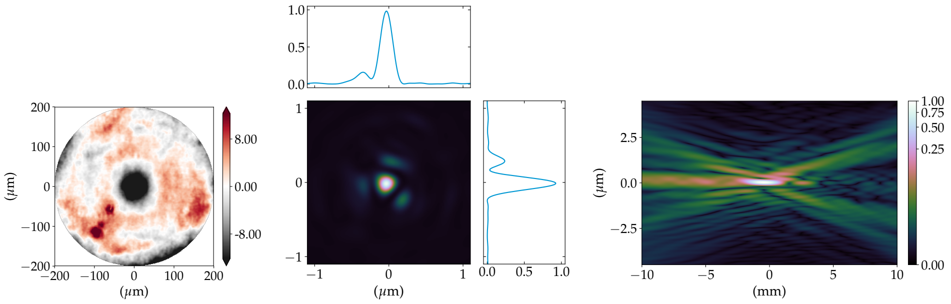

(a) profile (b) PSF (c) vertical caustics

Simulations using the metrology data

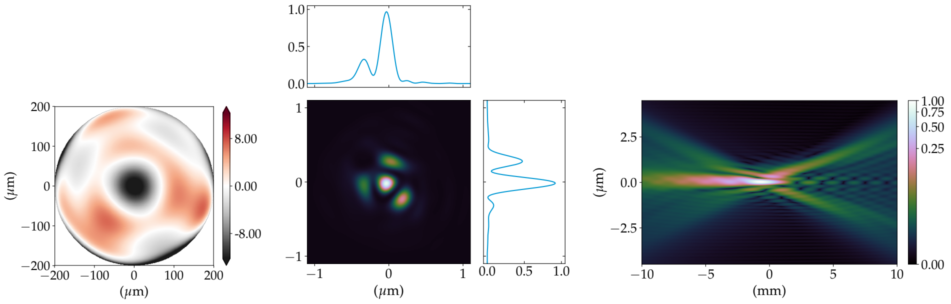

(d) profile (e) PSF (f) vertical caustics

Simulations using the Zernike circle polynomials

Fig. 3.11.: Simulations of 10 stacked 2D-beryllium lenses with nominal radius $R = 50$ μm, geometric aperture $A_{\varnothing} = 440$ μm and $t_{\text{wall}} = 20$ μm at 8 keV. **top row**: (a) metrology profile, (b) point-spread function with cuts centred in $(0, 0)$ and (c) vertical beam caustics from -10 mm to 10 mm with respect to the focal plane. **bottom row**: (d) profile generated by the Zernike circle polynomials coefficients, (e) PSF and (f) beam caustics.

compound refractive lenses, metrology data can also be used for optically imperfect X-ray lenses [Celestre, Berujon, et al., 2020; Chubar et al., 2020]. Fig. 3.9 shows three examples of lens figure errors from (a)-(d) a commercial pressed beryllium lens, (e)-(h) an in-house pressed aluminium lens and a (i)-(l) in-development laser-ablated diamond lens from a commercial partner. The figure errors were measured with at-wavelength metrology[16] and can be directly plugged into simulations [Celestre, Berujon, et al., 2020]. The effects of optical imperfections from metrology data on a coherent X-ray beam are shown in Fig. 3.10 and Fig. 3.11. The systematic use of metrology data for modelling optical imperfections in compound refractive lenses is explored in depth in §5 - *Effect of optical imperfections on an X-ray beam*. The chapter §6 - *Correcting optical imperfections in refractive lenses* exemplifies how the framework developed to model such experimentally determined phase errors also opens the avenue to calculating the effects of any arbitrary phase modifying element.

3.5 Implementation

The implementation of the modelling of X-ray lenses with their typical misalignments, fabrication errors and other sources of optical imperfections is presented in the Python library

---

[16] cf. §4.1 - *At wavelength-metrology*.

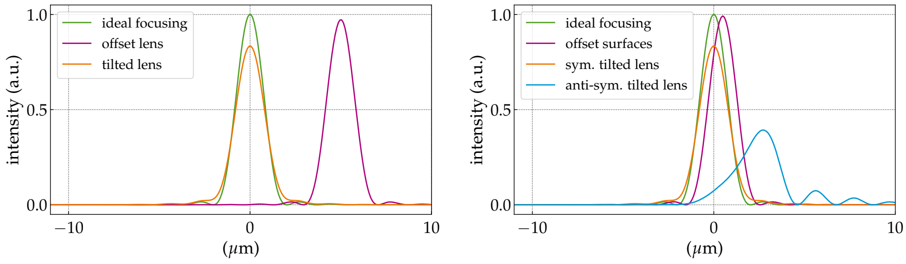

(a) misalignments

(b) fabrication errors

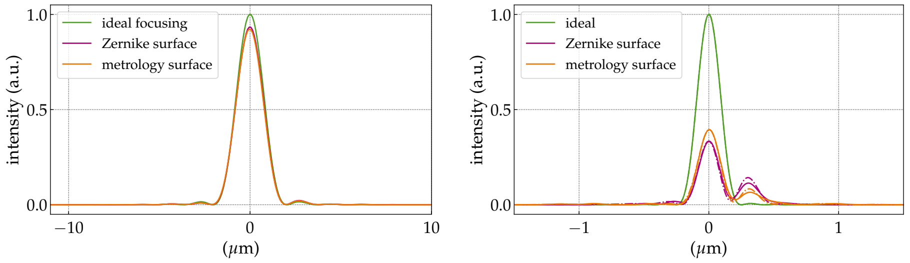

(c) other sources or errors - single lens

(d) other sources or errors - 10x Be lenses

Fig. 3.12.: Strehl ratio of the vertical cut at $x = 0$ summarising the results from the diverse models presented.

`barc4RefractiveOptics`, available on GitLab[17,18] under a CC BY-SA 4.0 license, where more information on the implemented functions can be found. This library contains three main modules, namely: `projected_thickness.py`, `wavefront_fitting.py` and `barc4RefractiveOptics.py`.

The module `projected_thickness.py` is responsible for the calculation of the thickness in projection approximation for the ideal lens (Eq. 2.9); lenses with the misalignments discussed in §3.2 - *Misalignments*; with the fabrication errors presented in §3.3 - *Fabrication errors*; and other sources of deviations from the parabolic profile described in §3.4.1 - *Orthornormal polynomials*, which are based on Zernike (circular and rectangular) polynomials or the 2D Legendre polynomials[19]. To generate an arbitrary profile the user can either use a list with the coefficients or enter an RMS value for their sum, in which case, the coefficients will be randomly calculated and will add up to the RMS value limited by the user input. The fit of a wavefront to a set of orthonormal polynomials is a very important diagnostic tool for optical modelling and is available within the `wavefront_fitting.py` module, which currently supports the Zerkine circle and rectangular as well as the 2D Legendre polynomial sets.

---

[17] `https://gitlab.esrf.fr/celestre/barc4RefractiveOptics`

[18] An OASYS (OrAnge SYnchrotron Suite) distribution to be used with *SRW*, *SHADOW* and *SHADOW*-hybrid mode is being prepared. For updates on that, please, refer to the project GitHub page: `https://github.com/oasys-kit/oasys-barc4ro`. The OASYS implementation of `barc4RefractiveOptics` is being lead by Luca Rebuffi (Argonne National Lab. USA).

[19] The functions used to generate the 2D circular Zernike polynomials contain pieces of codes from the module `libtim-py` from Tim van Werkhoven, that had to be brought to Python 3.7 and in some places, small bugs had to be fixed - this module has a Creative Commons Attribution-Share Alike license. The 2D rectangular Zernike was originally inspired by the analytical formulation from the module `opticspy` from Xing Fan, which has an MIT license. The formulation from the module was based on the equations from [Mahajan and Dai, 2007], but had to be corrected with the errata published in [Mahajan, 2012]. The 2D Legendre polynomials were implemented based on the formulations in [Mahajan, 2010]. A lot of effort was done in bringing all these three distinct libraries into a homogeneous and concise module.

The modules just described generate 2D projected thickness maps and in conjunction with the metrology data (2D height profiles) are interfaced to *SRW*[20] by `barc4RefractiveOptics.py`. This module is written to be used transparently with the optical element class `SRWLOpt` described in the module `srwlib.py` from *SRW*. Each function representing either an X-ray lens or its figure errors returns a class `SRWLOptT` representing a generic transmission element storing amplitude transmission and optical path difference as a function of transverse coordinates. The main calculations for generating the X-ray lens transmission element is performed by the function `srwl_opt_setup_CRL`. The generation of the residual phase errors based on the polynomial expansion of the aberration function in the exit pupil is done by `srwl_opt_setup_CRL_errors`. This function is used in conjunction with `srwl_opt_setup_CRL` as modelled in Eq. 2.13. The generation of a surface based on the metrology data is done by `srwl_opt_setup_CRL_metrology`. The metrology data should be saved as an ASCII file (.dat) as defined by the function `srwl_uti_save_intens_ascii` from the module `srwlib.py`. The function `srwl_opt_setup_CRL_metrology` can be used to simulate figure errors, in which case, much like `srwl_opt_setup_CRL_errors` it requires the use of `srwl_opt_setup_CRL` or it can be used to simulate a full measured profile.

Separating the calculation of the projected thickness Δ_z from the interface to SRW allows the module `projected_thickness.py` to be used in any X-ray optical simulation code based on physical optics as the transmission elements can be directly calculated from the 2D surface maps by using the Eq. 1.37. ■

References

Ali, S. and Jacobsen, C. (2020). “Effect of tilt on circular zone plate performance”. In: *Journal of the Optical Society of America A* **37**.3, p. 374.

Alianelli, L., Sánchez del Río, M., and Sawhney, K. J. (2007). “Ray-tracing simulation of parabolic compound refractive lenses”. In: *Spectrochimica Acta - Part B Atomic Spectroscopy* **62**.6-7 SPEC. ISS. P. 593.

Andrejczuk, A., Krzywiski, J., Sakurai, Y., Itou, M., Krzywiński, J., Sakurai, Y., and Itou, M. (2010). “The role of single element errors in planar parabolic compound refractive lenses”. In: *Journal of Synchrotron Radiation* **17**.5, p. 616.

Baltser, J., Knudsen, E., Vickery, A., Chubar, O., Snigirev, A., Vaughan, G., Feidenhans’l, R., and Lefmann, K. (2011). “Advanced simulations of x-ray beam propagation through CRL transfocators using ray-tracing and wavefront propagation methods”. In: *Proc. SPIE 8141, Advances in Computational Methods for X-Ray Optics II* 8141, p. 814111.

Celestre, R., Berujon, S., Roth, T., Sanchez del Rio, M., and Barrett, R. (2020). “Modelling phase imperfections in compound refractive lenses”. In: *Journal of Synchrotron Radiation* **27**.2, p. 305.

Celestre, R., Chubar, O., Roth, T., Sanchez del Rio, M., and Barrett, R. (2020). “Recent developments in X-ray lenses modelling with SRW”. In: *Proc. SPIE 11493, Advances in Computational Methods for X-Ray Optics V*, pp. 11493–17.

Chubar, O. and Elleaume, P. (1998). “Accurate And Efficient Computation Of Synchrotron Radiation In The Near Field Region”. In: *Proceedings of the European Particle Accelerator Conference (EPAC 98)*, p. 1177.

---

[20] Available at `https://github.com/ochubar/srw`

Chubar, O., Wiegart, L., Antipov, S., Celestre, R., Coles, R., Fluerasu, A., and Rakitin, M. S. (2020). "Analysis of hard x-ray focusing by 2D diamond CRL". In: *Proc. SPIE 11493, Advances in Computational Methods for X-Ray Optics V*, pp. 11493–20.

Dimper, R., Reichert, H., Raimondi, P., Sanchez Ortiz, L., Sette, F., and Susini, J. (2014). *ESRF Upragde programme phase II - The Orange Book*. ESRF, p. 75.

Gasilov, S., Rolo, T. d. S., Mittone, A., Polyakov, S., Terentyev, S., Farago, T., Blank, V., Bravin, A., and Baumbach, T. (2017). "Generalized pupil function of a compound X-ray refractive lens". In: *Optics Express* **25**.21, p. 25090.

Guizar-Sicairos, M., Narayanan, S., Stein, A., Metzler, M., Sandy, A. R., Fienup, J. R., and Evans-Lutterodt, K. (2011). "Measurement of hard x-ray lens wavefront aberrations using phase retrieval". In: *Applied Physics Letters* **98**.11, p. 111108.

House, D. H. and Keyser, J. C. (2016). *Foundations of Physically Based Modeling & Animation*. First edition. A K Peters/CRC Press.

Koch, F. J., Detlefs, C., Schröter, T. J., Kunka, D., Last, A., and Mohr, J. (2016). "Quantitative characterization of X-ray lenses from two fabrication techniques with grating interferometry". In: *Opt. Express* **24**.9, p. 9168.

Kornemann, E., Márkus, O., Opolka, A., Zhou, T., Greving, I., Storm, M., Krywka, C., Last, A., and Mohr, J. (2017). "Miniaturized compound refractive X-ray zoom lens". In: *Optics Express* **25**.19, p. 22455.

Lengeler, B., Schroer, C., Tümmler, J., Benner, B., Richwin, M., Snigirev, A., Snigireva, I., and Drakopoulos, M. (1999). "Imaging by parabolic refractive lenses in the hard X-ray range". In: *Journal of Synchrotron Radiation* **6**.6, p. 1153.

Mahajan, V. N. (1983). "Strehl ratio for primary aberrations in terms of their aberration variance ". In: *Journal of the Optical Society of America* **73**.6, p. 860.

— (1995). "Zernike-Gauss Polynomials and Optical Aberrations of Systems with Gaussian Pupils". In: *Applied Optics* **34**.34, p. 8057.

— (2010). "Orthonormal aberration polynomials for anamorphic optical imaging systems with rectangular pupils". In: *Applied Optics* **49**.36, p. 6924.

— (2012). "Orthonormal polynomials in wavefront analysis: analytical solution: errata". In: *Journal of the Optical Society of America A* **29**.8, p. 1673.

— (2013). "Optical Wavefronts and Their Aberrations". In: *Optical Imaging and Aberrations, Part III: Wavefront Analysis*. Society of Photo-Optical Instrumentation Engineers, p. 15.

Mahajan, V. N. and Dai, G.-m. (2007). "Orthonormal polynomials in wavefront analysis: analytical solution". In: *Journal of the Optical Society of America A* **24**.9, p. 2994.

Narikovich, A., Polikarpov, M., Barannikov, A., Klimova, N., Lushnikov, A., Lyatun, I., Bourenkov, G., Zverev, D., Panormov, I., Sinitsyn, A., Snigireva, I., and Snigirev, A. (2019). "CRL-based ultra-compact transfocator for X-ray focusing and microscopy". In: *Journal of Synchrotron Radiation* **26**.4, p. 1208.

Osterhoff, M., Karkoulis, D., and Ferrero, C. (2013). "A wave-optical toolbox for multiple CRL transfocators". In: *Journal of Physics: Conference Series* **425**.16, p. 162005.

Osterhoff, M., Detlefs, C., and Ferrero, C. (2017). "Aberrations in compound refractive lens systems: analytical and numerical calculations". In: *Proc. SPIE 10388, Advances in Computational Methods for X-Ray Optics IV* 10388, p. 21.

Pantell, R. H., Feinstein, J., Beguiristain, H. R., Piestrup, M. A., Gary, C. K., and Cremer, J. T. (2001). "The effect of unit lens alignment and surface roughness on x-ray compound lens performance". In: *Review of Scientific Instruments* **72**.1, p. 48.

Pedersen, A. F., Simons, H., Detlefs, C., and Poulsen, H. F. (2018). "The fractional Fourier transform as a simulation tool for lens-based X-ray microscopy". In: *Journal of Synchrotron Radiation* **25**.3, p. 717.

Roth, T., Alianelli, L., Lengeler, D., Snigirev, A., and Seiboth, F. (2017). "Materials for x-ray refractive lenses minimizing wavefront distortions". In: *MRS Bulletin* **42**.06, p. 430.

Roth, T., Helfen, L., Hallmann, J., Samoylova, L., Kwaśniewski, P., Lengeler, B., and Madsen, A. (2014). "X-ray laminography and SAXS on beryllium grades and lenses and wavefront propagation through imperfect compound refractive lenses". In: *Proc. SPIE 9207, Advances in X-Ray/EUV Optics and Components IX* 9207, p. 920702.

Sanchez del Rio, M. and Alianelli, L. (2012). "Aspherical lens shapes for focusing synchrotron beams". In: *Journal of Synchrotron Radiation* **19**.3, p. 366.

Sanchez Del Rio, M., Bianchi, D., Cocco, D., Glass, M., Idir, M., Metz, J., Raimondi, L., Rebuffi, L., Reininger, R., Shi, X., Siewert, F., Spielmann-Jaeggi, S., Takacs, P., Tomasset, M., Tonnessen, T., Vivo, A., and Yashchuk, V. (2016). "DABAM: An open-source database of X-ray mirrors metrology". In: *Journal of Synchrotron Radiation* **23**.3, p. 665.

Sanchez del Rio, M., Canestrari, N., Jiang, F., and Cerrina, F. (2011). "SHADOW3 : a new version of the synchrotron X-ray optics modelling package". In: *Journal of Synchrotron Radiation* **18**.5, p. 708.

Schulz, G. (1988). "IV Aspheric Surfaces". In: *Progress in Optics* **25**.C, p. 349.

Simons, H., Ahl, S. R., Poulsen, H. F., and Detlefs, C. (2017). "Simulating and optimizing compound refractive lens-based X-ray microscopes". In: *Journal of Synchrotron Radiation* **24**.2, p. 392.

Swantner, W. and Chow, W. W. (1994). "Gram–Schmidt orthonormalization of Zernike polynomials for general aperture shapes". In: *Applied Optics* **33**.10, p. 1832.

Umbach, M., Nazmov, V., Simon, M., Last, A., and Saile, V. (2008). "Numerical simulations of achromatic x-ray lenses". In: *Proc. SPIE 7077, Advances in X-Ray/EUV Optics and Components III* 7077, 70770G.

Vaughan, G. B. M., Wright, J. P., Bytchkov, A., Rossat, M., Gleyzolle, H., Snigireva, I., and Snigirev, A. (2011). "X-ray transfocators: focusing devices based on compound refractive lenses". In: *Journal of Synchrotron Radiation* **18**.2, p. 125.

Ye, J., Gao, Z., Wang, S., Cheng, J., Wang, W., and Sun, W. (2014). "Comparative assessment of orthogonal polynomials for wavefront reconstruction over the square aperture". In: *Journal of the Optical Society of America A* **31**.10, p. 2304.

Zernike, v. F. (1934). "Beugungstheorie des Schneidenverfahrens und seiner verbesserten Form, der Phasenkontrastmethode". In: *Physica* **1**.7-12, p. 689.

Zhou, T., Wang, H., Fox, O. J., and Sawhney, K. J. (2019). "Optimized alignment of X-ray mirrors with an automated speckle-based metrology tool". In: *Review of Scientific Instruments* **90**.2, p. 021706.

Measuring optical imperfections in refractive lenses

4

Surface metrology methods commonly applied to X-ray mirrors [Alcock et al., 2016; Vivo et al., 2019] are not broadly employed for the metrology of X-ray lenses mainly due to their small apertures and steep parabolic surfaces (cf. Fig. 3.3) [I. I. Lyatun et al., 2015]. Non-destructive methods using X-rays are often more appropriate for X-ray lens metrology. This section presents some of the commonly used at-wavelength metrology methods, with emphasis on X-ray speckle vectorial tracking (XSVT), the experimental technique used throughout this work. The metrology of single- and stacked 2D-beryllium lens with $R = 50\ \mu$m is presented and the results are compared. The experimental data shown in this chapter were acquired during several beamtimes[1] at the BM05 beamline - ESRF [Ziegler et al., 2004] (from 2017 to 2018 - before the ESRF long shutdown for the EBS upgrade), at the 1-BM beamline - APS [Macrander et al., 2016] (during the ESRF long shutdown in 2019) and the ID06 beamline - ESRF [Kutsal et al., 2019] (in 2020 during the commissioning period of the ESRF-EBS upgrade).

4.1 At wavelength-metrology

Surface metrology of X-ray optical elements is often done using the visible spectral range [Alcock et al., 2016; Vivo et al., 2019] even if, ultimately, they will be employed in a different spectral range. At-wavelength metrology is an umbrella term for measurements of optical elements at photon energies closer to the ones they will be ultimately used - in the case of X-ray lenses, in the range of few to several kilo-electron-volts. What follows is a non-exhaustive description of commonly used techniques for quality control applied to X-ray lenses and their compliance to a parabolic shape. Other relevant at-wavelength characterisations of X-ray lenses such as X-ray small-angle scattering [Roth et al., 2014; Chubar et al., 2020] or the impact of material micro-structures or shape errors on imaging [Chubar et al., 2020; I. Lyatun et al., 2020] are not covered here. A more complete survey on characterisation methods for X-ray lenses is presented in the supplementary material from [Roth et al., 2017].

The simplest at-wavelength techniques consist of the direct imaging of a lens with X-rays by propagation-based phase-contrast imaging [Endrizzi, 2018] since absorption contrast imaging only generates a reduced contrast for a single lens and a low signal to noise ratio. With such simple techniques, 2D shapes and distances can be measured (e.g. radiographs for controlling the distance and alignment between the parabolic surfaces of X-ray lenses). Still based on propagation based-imaging techniques, X-ray laminography [Helfen et al., 2011; Roth et al., 2014] and X-ray tomography [Landis and Keane, 2010; Narikovich et al., 2017] of X-ray

---

[1] Acknowledgements to Sébastien Bérujon and Ruxandra Cojocaru (BM05-ESRF); Xianbo Shi, Zhi Qiao, Michael Wojcik and Lahsen Assoufid (1-BM-APS); and to Carsten Detlefs (ID06-ESRF) for the help during the experimental sessions.

lenses provide a 3D reconstruction of the lens volume with high spatial resolution information. These techniques provide data on the shape of the refracting surfaces and the internal features (inhomogeneities) and can be used for modelling optical imperfections in refractive lenses.

Another large family of experimental techniques used for lens metrology and aiming at quantitative optical characterisation can be grouped under the wave-front sensing branch[2]. Wavefront-sensing is often employed as a beam-diagnostics tool for highly coherent sources [Seaberg et al., 2019]. Two conceptual approaches are often used: *i*-) absolute wavefront metrology at a specific point of the beam path measures the global state of the wavefront or *ii*-) differential measurements are done with and without the optical element under investigation, the differences in the wavefront being attributed to the optical contribution of the element under test. Current wavefront-sensing techniques used so far in the community for evaluating the phase errors of CRLs (or individual X-ray lenses) are: *i*-) the Ronchi test, an interferometric technique that provides qualitative[3] information on third-order optical aberrations [Nilsson et al., 2012; Uhlén et al., 2014]; *ii*-) the use of X-ray Shack–Hartmann sensors [Mayo and Sexton, 2004; Mercere et al., 2005; Mikhaylov et al., 2020]; *iii*-) the ptychographic reconstruction of the wavefront emerging from a strongly focusing optics [Schropp et al., 2013; Sala et al., 2017; Seiboth et al., 2017]; *iv*-) grating interferometry and its variations [David et al., 2012; Koch et al., 2016; Grizolli et al., 2017]; *v*-) and the near-field-speckle-imaging-based (SBI) methods [Berujon et al., 2013; M.-C. Zdora et al., 2018; Berujon et al., 2020a]. The latter is the main experimental technique used in this project primarily due to its easy experimental implementation and high spatial resolution. The remainder of this chapter will focus more deeply on its theoretical and experimental aspects.

4.1.1 X-ray (near field) speckle vector tracking (XSVT)

The X-ray near-field-speckle-imaging is currently the chosen technique for systematic at-wavelength metrology of X-ray lenses at the ESRF[4] and is available at the BM05 beamline [Berujon et al., 2020a] and more recently, at the ID06 beamline. The principal reasons for this choice are: *i*-) the low requirements on transverse- and longitudinal coherence [Zanette et al., 2014; M. C. Zdora et al., 2015; Wang et al., 2016]; *ii*-) no requirement of specially tailored optics (nor accompanying complicated alignment procedures) [Morgan et al., 2012; Wang et al., 2016]; *iii*-) successful benchmark against more established wave-front sensing techniques [Kashyap et al., 2016; Romell et al., 2017]; and *iv*-) its versatility as a metrology tool being able to measure mirrors, single- and stacked lenses [Berujon et al., 2020a]. Although the basic principles of the several X-ray near-field-speckle-based techniques are the same, the focus is given here to the X-ray (near field) speckle vector tracking (XSVT) as implemented and used for the metrology of single- and stacked X-ray lenses used in this work [Berujon et al., 2020a,b]. An interesting

---

[2] With the advent of more coherent sources of X-rays as encapsulated by the emergence of 4th-generation synchrotrons and free-electron lasers, the topic of wavefront sensing has seen increased attention [Seaberg et al., 2019].

[3] It has been demonstrated that the Ronchi test can also retrieve quantitative information [Lee and Guizar-Sicairos, 2010], but it has not yet been applied to X-ray lenses metrology.

[4] Other synchrotron facilities also offer X-ray lens metrology with the X-ray near field speckle imaging technique: 1-BM at the APS in the U.S.A. [Qiao, Shi, Wojcik, et al., 2020] and the B16 beamline at the Diamond Light Source in the U.K. [Sawhney et al., 2013].

review of different techniques using X-ray near-field speckle imaging is given by [M.-C. Zdora, 2018] and [Berujon et al., 2020b].

4.1.2 Foundation

Near-field speckle is a manifestation in intensity of the summation of several complex electric fields when the amplitudes and phases of such fields have random values. The resulting intensities may be locally high due to constructive interference or low, due to destructive interference [Goodman, 2020, *§1*]. For a speckle pattern over a defined region of interest, the speckle contrast (or visibility) can be defined[5] as:

$$v = \frac{\sigma_I}{\overline{I}}, \tag{4.1}$$

where σ_I is the standard deviation and $\overline{I}$ is the mean value of the intensity value of the speckle pattern. In the X-ray regime, it appears when a sufficiently coherent X-ray beam is transmitted through matter with random spatial variation of δ and β, where the local optical path length varies significantly when compared to the scale of the wavelength.

For a static random modulation of the wavefield (stationary scatterer[6]), it has been demonstrated that the speckle-grains[7] preserve shape and size for free-space propagation distances limited to:

$$z < \Delta_{\mathbf{cl}_\perp} \xi k, \tag{4.2}$$

where $\Delta_{\mathbf{cl}_\perp}$ is transverse coherence length[8] and ξ is the typical transverse length of the modulator, that is, the region where the spatial variation of δ and β is negligible [Cerbino et al., 2008]. For propagation distances smaller than the imposed limit in Eq. 4.2, speckles can be used as a wavefront marker, since the transverse position of the speckle grains in two parallel planes along the propagation direction can be inferred geometrically. The near-field regime is of particular interest for the X-ray energy range, as very low wavelengths lead to an extended near-field regime. A stationary scatterer and the associated speckle-pattern are shown in Fig. 4.1.

Based on the uniqueness of each speckle grain, speckle-imaging-based techniques rely on identifying similar patterns in two different images or image sets: a reference image and an image in the presence of the probe (perturbed) - cf. Fig. 4.2. The numerical implementations used for tracking the lateral displacement of the speckle grains in the detector plane can be several: cross-correlation peak calculation [Bérujon et al., 2012; Morgan et al., 2012] and least-square-minimisation [Zanette et al., 2014; M. C. Zdora et al., 2017] based approaches are the two most used methods[9,10]. The lateral displacement of the speckle grain in the detector

---

[5] Other definitions are commonly found in the literature: $v = \frac{I_{\text{max}} - I_{\text{min}}}{I_{\text{max}} + I_{\text{min}}}$ and $v = \frac{I_{\text{max}} - I_{\text{min}}}{2\overline{I}}$, where I_{max} and I_{min} are the maximum and minimum intensities found in the region of interest [M.-C. Zdora, 2018].

[6] As opposed to time-varying modulation of the speckle-field as in [Morgan et al., 2010; Goikhman et al., 2015].

[7] Continous regions in space with a slowly-varying intensity that can be visually clustered together.

[8] cf. *Spatial coherence* in §1.2.3 - *Optical coherence*.

[9] Recently, an Euclidean-distance minimisation of the wavelet-transform method has been reported. Compared to correlation-based techniques it is less computationally demanding and more robust to noise [Qiao, Shi, Celestre, et al., 2020].

[10] Regardless of the tracking method, the displacement vector ν must be equivalent, as it is linked to the sample shape and material.

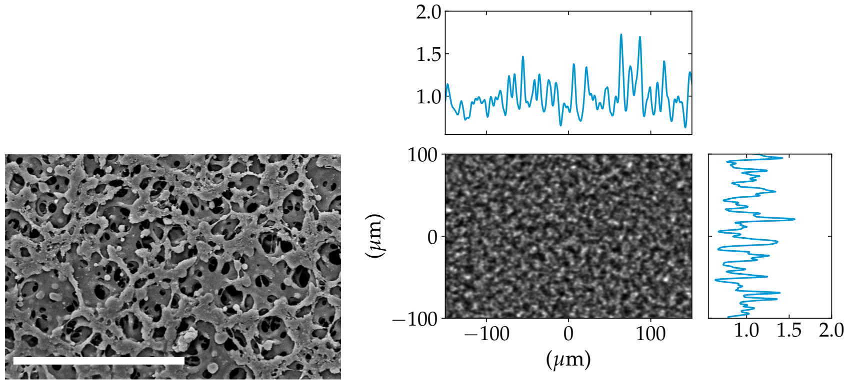

(a) SEM (b) experimental

Fig. 4.1.: (a) SEM image of the cellulose acetate membrane filters with mean pore size of 1.2 μm used as the stationary diffuser. The white bar in (b) represents 50 μm and (b) associated speckle-pattern measured at 17 keV at 800 mm downstream the membrane with visibility $v \sim 0.19$.

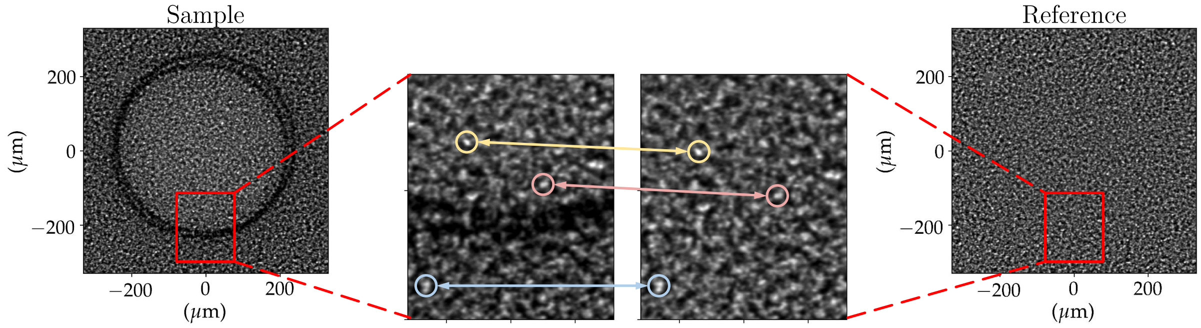

Fig. 4.2.: Tracking of speckle grains. The highlighted grains in yellow and red are inside the sample and have their transverse position changed. The highlighted grain in blue is outside the lens active area and has no apparent shift in the transverse position. The speckle grains in the image of the sample have their intensity reduced due to absorption of the bulk material. The sample is a single 2D-beryllium lens with nominal radius $R = 50$ μm, geometric aperture $A_{\varnothing} \sim 440$ μm. The data were collected ~800mm downstream of the speckle-membrane at 17 keV.

plane between the reference and the disturbed image is defined by the displacement vector $\nu = (\Delta_x, \Delta_y)$, where Δ_x and Δ_y are the respective horizontal and vertical displacements of the speckle grain in the presence of the sample - cf. Fig. 4.3. With knowledge of the distance between sample and detector d, it is possible to calculate the deflection angle $\alpha = (\alpha_x, \alpha_y) \approx \nu/d$. The deflection angle, the wave-field phase $\phi(x, y)$ and wavefront $\mathcal{W}(x, y)$ are linked together by the relationship:

$$k\frac{\nu}{d} \approx k\alpha = \nabla\phi(x, y) = k\nabla\mathcal{W}(x, y). \tag{4.3}$$

The beam phase $\phi(x, y)$ or wavefront $\mathcal{W}(x, y)$ can hence be retrieved by numerical integration of the phase gradients obtained experimentally.

4.1.3 Experimental setup

X-ray speckle imaging (SBI) can be implemented in several geometries depending on the metrology subject (mirrors, strong focusing mirrors, lenses, stacked lenses) and mode (absolute or differential) - cf. [Berujon et al., 2020a]. In this section the X-ray (near field) speckle vector

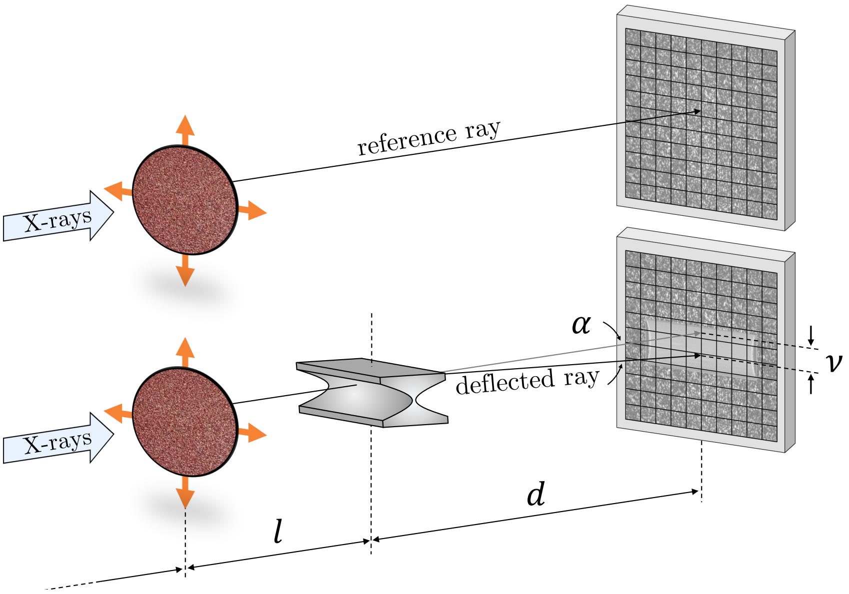

Fig. 4.3.: Generic speckle-based imaging measurement geometry for the XSVT technique and the origin of the displacement vector ν arising from the lens refraction. From left to right: X-ray beam, speckle-membrane, sample and 2D imaging detector. The distance between sample and detector is noted d, the deflection angle is α and the transverse displacement vector in the detector plane is ν.

tracking (XSVT) in the differential mode, as originally implemented at BM05 and shown in Figs. 4.3, 4.4 and 4.5 is described.

Illumination

Unlike other wavefront sensing techniques, speckle-based metrology has low requirements on transverse and longitudinal coherence[11] as demonstrated by [Zanette et al., 2014; M. C. Zdora et al., 2015; Wang et al., 2016]. The degree of lateral coherence of the illumination is intimately connected with two important factors: the speckle contrast (cf. Eq. 4.1) and the propagation distance where shape and size of the speckle grains are preserved (cf. Eq. 4.2). X-rays with lower transverse coherence will produce speckle with low visibility (appearing thus as a smeared out or blurred image) and the numerical process of tracking signals will lose some of its accuracy. For metrology applications, a minimum contrast of 0.1 (Eq. 4.1) is expected [Berujon et al., 2020a] for the algorithms to show an acceptable accuracy. A reduced propagation distance d between the sample and the detector (cf. Fig. 4.3 and 4.4) arising from a reduced coherence length $\Delta_{\mathbf{cl}_\perp}$ (Eq. 4.2) diminishes the angular sensitivity and will impact on the residual height error measurement sensitivity. When selecting an X-ray source, a higher degree of transverse coherence is preferred. Nonetheless, bending magnets[12] are readily well suited for speckle-imaging-based metrology since their beam usually offer the necessary minimum transverse coherence.

---

[11] Phase-contrast imaging with low-coherence sources has been demonstrated [Cloetens et al., 1996; Wilkins et al., 1996; Pfeiffer et al., 2006; Munro et al., 2012].

[12] At BM05, a bending magnet was the X-ray source used in this project until the ESRF-EBS upgrade long shutdown (December 2018). The BM05 bending magnet in place since the opening of the ESRF in 1994 was decommissioned in favour of a much shorter and brighter 2-pole wiggler, installed early 2020. All the data collected at BM05 and presented hereafter were collected before this upgrade.

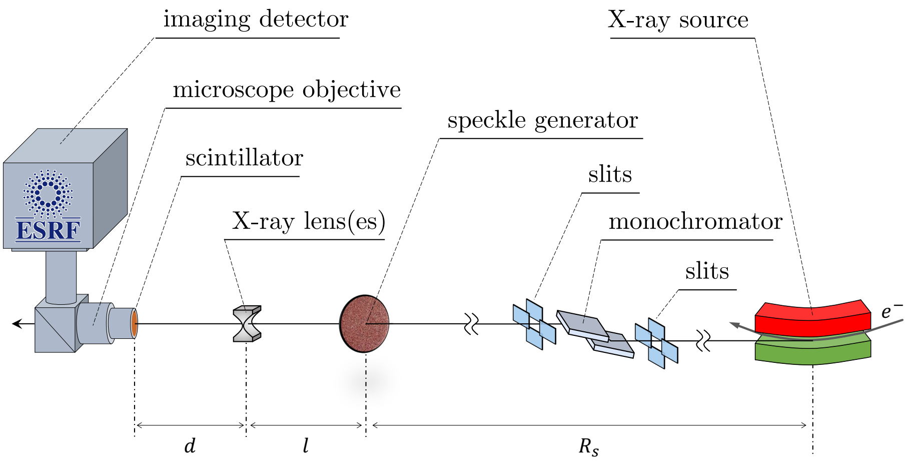

Fig. 4.4.: Generic speckle-based imaging experimental setup as originally implemented at the BM05 beamline of the ESRF. **right to left**: an X-ray source (bending magnet) delivers a beam whose large spectral bandwidth is reduced with a Si(111) double crystal monochromator down to $\Delta\mathrm{E}/\mathrm{E} \approx 10^{-4}$. The now monochromatic beam hits the speckle-generator at a distance R_S from the source. The stationary diffuser is composed of several stacked cellulose acetate membrane filters with a mean pore size of 1.2 μm. The membranes are mounted on a (piezoelectric) nano-positioner transverse translation stage so that the membranes can be scanned in the $xy-$plane. At a distance l downstream of the membrane, the sample is placed and aligned on the optical axis. Further downstream the probe, at a distance d, a scintillator converts the X-rays into visible light. The scintillator is imaged into a 2D imaging sensor, which is coupled with a microscope objective to reach a small pixel size. Such experimental setup, without any structural change, was later on used at the 1-BM (APS) and ID06 (ESRF) beamlines. Conversely to what depicted here, the X-ray source at the ID06 is an undulator and not a bending magnet.

Choosing the optimal experiment energy[13] for X-ray lens metrology is about reaching a compromise between several competing constraints. For a fixed distance d, the energy should be high enough so that the speckle grains being transmitted through the lens geometric aperture are not excessively deformed by focusing at the detection plane - the higher the energy, the longer the focal length of an X-ray lens is (cf. Eq. 2.4) - on the other hand, lower energy gives larger refraction angles, which increases the sensitivity of the experimental technique. Excessive deformation of the detected speckle field, however, causes the tracking to fail in delivering credible results. Higher energy is also beneficial when considering the limit to the distance d imposed by Eq. 4.2. On the other hand, increasing the energy decreases the coherent fraction of the emitted beam, which in turn reduces the speckle visibility[14]. Lastly, the source spectrum (Fig. 1.1) and detector efficiency have also to be considered, as a higher photon flux allows for shorter acquisition time, meaning that experiments require less time and possible instabilities (vibrations, long time drifts and other external perturbations) have a lower impact on the acquired data. Requirements on the illumination monochromaticity are not stringent for SBI, but the metrology of X-ray lenses requires narrow bandwidths as these optics display intrinsic

---

[13] The energy chosen for most metrology experiments was $\mathrm{E} = 17$ keV with $\Delta\mathrm{E}/\mathrm{E} \approx 10^{-4}$ by using a Si(111) DCM. This energy was originally set at BM05 due to the source higher flux at this energy and the good compromise between absorption and sensitivity such working wavelength offer. Later, this same energy was also adopted for experiments at other beamlines to facilitate direct comparison during the data-analysis.

[14] Slitting down the beam and increasing the propagation distance from the source to the speckle-membrane (R_s in Fig. 4.4) both help to increase the coherence length at the expense of photon flux - cf. van-Cittert-Zernike theorem in [Mandel and Wolf, 1995, *§4.4.4*] or the applicability to SR in [Geloni et al., 2008, *§4*].

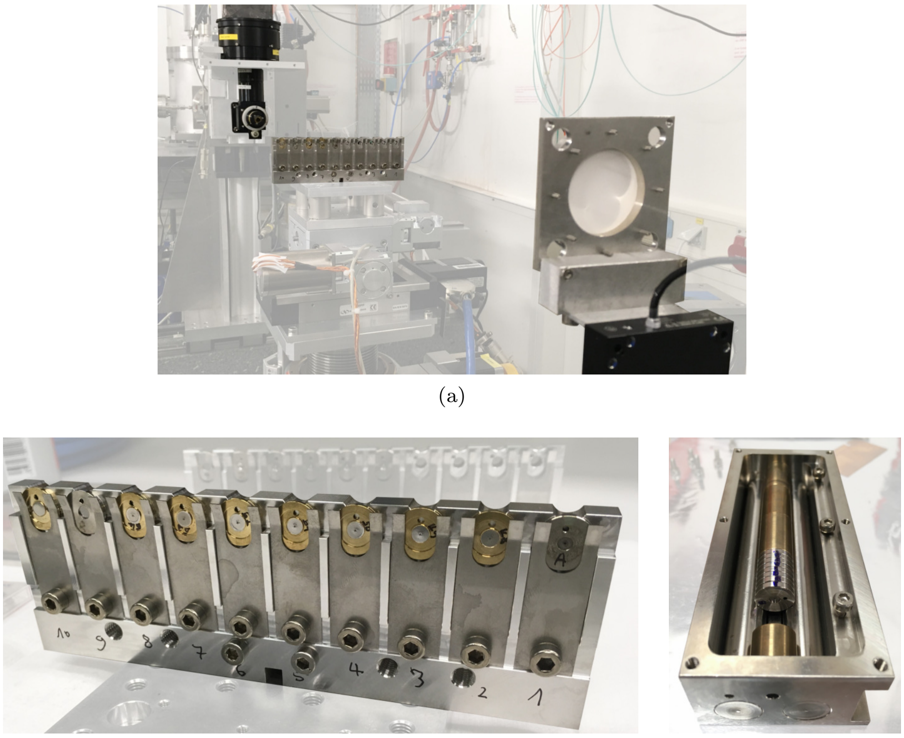

(a)

(b)

(c)

Fig. 4.5.: (a) image inside the experimental hutch of the ESRF BM05. The picture highlights the three main components shown schematically in Fig. 4.3: the detector in the back-plane, the sample-holder specially designed to hold up to 10 lenslets for batch measurements and the speckle-membrane mounted in a (piezoelectric) nano-positioner in the first plane. (b) typical lenslets mounted on the holder designed to provide easy alignment of the lenses in the X-ray beam and ensure repeatable positioning in the lens mount. This holder is designed for single-lens measurement. (c) box required for the mounting of stacked lenses to be measured together.

strong chromatic aberrations. In order to achieve a good lateral resolution, a Si(111) double crystal monochromator (DCM)[15] is usually used to bring down the bandwidth to $\Delta E/E \approx 10^{-4}$.

Speckle membrane

Unlike other wavefront techniques that require specially tailored optics that may need laborious alignment procedures such as reference phase-objects (Siemens star) or gratings, SBI requires a transmission element with transversely randomly distributed small features. The random optical path differences generated by these objects or grains must be capable of producing speckles that cover a few pixels (<10 pixels) at the detector with visibility of $v > 0.1$ [Berujon et al., 2020a, *§2.3*]. Early experiments were done by stacking commercially available abrasive paper (sandpaper) until the desired speckle pattern was obtained[16] [Morgan et al., 2012; Wang et al., 2016]. The choice of a modulator depends on the experiment energy and the detector, but often, static granular materials, sandpaper of diverse grits and filters with

---

[15] Yet, an experimental comparison between the metrology data obtained with a Si(111) DCM with $\Delta E/E \approx 10^{-4}$ and a multi-layer monochromator with $\Delta E/E \approx 10^{-2}$ showed very good agreement between both data-sets [Berujon et al., 2020a, *§3.3.3*].

[16] More recent guidelines helping to choose the appropriate sandpaper grain size (grit) for an experimental setup were published by [Tian et al., 2020].

micrometric pore-sizes can be used[17]. Low transmission, poor time stability and/or the presence of strong diffraction are characteristics that should be avoided when choosing a speckle generator. Due to the random nature of the wavefront (static) modulation, the membrane does not require any precise alignment with the beam.

XSVT is a scanning technique and usually[18] N reference images are taken at N different transverse positions of the speckle generator with respect to the optical axis. The sample is put into the beam and another set of N images are taken with the speckle generator located at the exact previous N positions - cf. orange arrows in Fig. 4.3. The reproducibility of the speckle generator transverse positions is of key importance as the difference in the speckle grain positions from reference to sample image is attributed to the modulation of the beam. To make sure that during the collection of the j^{th} $(j \in [1, 2, ..., N])$ pair of images the position of the speckle generator is repeated with precision as good as a fraction of effective pixel size, the modulator is mounted on a precise (piezoelectric) nano-positioner with a travel range of a few hundred micrometres.

Sample

X-ray speckle vectorial tracking is a very attractive technique as it can measure weakly-focusing optics as well as very strong focusing systems with minor modifications of the setup - cf. [Berujon et al., 2020a] for some examples. Typically, two types of optical elements are today routinely measured at the ESRF: individual lenses and moderately focusing CRLs. Figure 4.5(b) and (c) shows typical lenses in their holder. Single lenses are mounted in an in-house-designed holder conceived to hold up to 10 lenslets next to each other, allowing serial measurements and minimising manual intervention to change samples. Stacked lenses are measured in typical casings. The lens holder has to be mounted on a motorised support that can move transversely to the beam ($xy-$plane) and has yaw, pitch, and roll rotations[19] to compensate for the residual phase errors generated from misalignments - cf. §3.2 - *Misalignments*.

Detection

Although subpixel resolution for XSVT has been recently reported [Qiao, Shi, Celestre, et al., 2020], generally, the lateral resolution of the 2D surface maps obtained with XSVT is limited to the detector effective pixel size. This makes the use of a 2D high-resolution imaging detectors common for speckle-based imaging. In real-space imaging with X-rays, since high resolution over a large field of view is usually wished, it is common to use indirect detection. Converting X-rays into visible-light and subsequently imaging it onto a pixelated detector allows one to access to smaller pixel sizes thanks to the use of magnifying optics and small pixel sensors designed for visible-light detection.

---

[17] Experiments showed here used a stack of cellulose acetate membrane filters with a mean pore size of 1.2 μm used as the stationary diffuser.

[18] More details in data acquisition are provided by §4.1.4 - *Data acquisition, processing and analysis*.

[19] Yaw was defined in our case as the rotation around the $z-$axis, the pitch is around the $y-$axis and roll, the $x-$axis.

A typical detection system[20] is composed of three main parts: *i*-) the scintillator, which is responsible for converting the X-rays into visible light. Its choice is a compromise between the yield in converting X-ray photons in visible photons and image resolution: a thin scintillator will generally result in a higher spatial resolution image, but at a cost of reduced photon flux, while a thicker one will generate more light, but due to scattering in the bulk material, a low-resolution image will result; *ii*-) the transport optics that magnify and images the scintillator onto the sensor plane, but also may introduce aberrations to the system, this can be calibrated with the XSVT technique - cf. [Berujon et al., 2020a, *§2.2*]; and *iii*-) the imaging sensor, which ideally should be a low-noise 2D pixelated sensor with fast read-out. The final effective pixel size is a convolution of the contributions from the choice of scintillator, magnification and point spread function of the transport optics and the imaging device.

4.1.4 Data acquisition, processing and analysis

Data acquisition & analysis

The first implementations of X-ray speckle-tracking (XST) for metrology consisted of acquiring solely two images: the reference- and the sample-image with the same speckle pattern (cf. Fig. 4.2). The algorithms used to match the patterns in both images relied in setting in the reference image a small window around a pixel of interest $w_{\text{reference}}(x_l, y_m)$ and searching for it (possibly distorted) in a larger window in the sample image: $w_{\text{probe}}(x_l, y_m)$. The reference window is rastered through the whole sample image ($L \times M$ pixels from the whole image) to reconstruct two 2D displacement maps (horizontal and vertical) with lateral resolution limited to the speckle-grain size. In order to improve the limited resolution of XST, XSVT relies on transversely scanning[21] the speckle-generator across the X-ray beam and taking images at the N different points of the scan. Once the reference data-set is taken, the sample is inserted in the beam and the scan is repeated at the exact same diffuser position. Each data set (reference and probe) contains $N_{L\times M}$ images where the j^{th} ($j \in [1, 2, ..., N]$) image in each stack indicates the same transverse coordinates of the scatterer scan - cf. Fig. 4.6. For a sufficiently large N, a vector is obtained by sampling each j^{th} image of the reference data-set around a pixel coordinate (x_l, y_m) with $l \in [1, 2, ..., L]$ and $m \in [1, 2, ..., M]$. This reference signal $I_{\text{reference}}(x_l, y_m, j)$ is shown in green in Fig. 4.6. A ROI centred around (x_l, y_m) is set in the sample data-set and for each pixel coordinate within this ROI, that is $(x_{l+\Delta l}, y_{m+\Delta m})$, a corresponding intensity vector is obtained: $I_{\text{probe}}(x_{l+\Delta l}, y_{m+\Delta m}, j)$ - cf. magenta and orange signals in Fig. 4.6. The $I_{\text{reference}}(x_l, y_m, j)$ vector is compared[22] individually to each of the $I_{\text{probe}}(x_{l+\Delta l}, y_{m+\Delta m}, j)$ vectors. Fig. 4.7 shows the normalised cross-correlation values for a particular lens, which are

---

[20] The detection systems use at the ESRF are composed of a 10 μm thick LSO:Tb scintillator that is imaged onto an sCMOS PCO Edge 4.2 or a FReLoN E2V CCD camera (2048 × 2048 pixels), coupled with a 10× magnification microscope objective to reach a theoretical pixel size of about $\sim 0.62 \times 0.62$ μm^2. At the APS, the scintillator used was a 100 μm thick LuAG:Ce imaged into an Andor Neo sCMOS camera with 2560 × 2180 pixels also with a 10× magnification resulting in a pixel size of $\sim 0.65 \times 0.65$ μm^2.

[21] The nature of the scan is not particularly relevant for the data analysis in this particular metrology mode.

[22] Which can be either using a cross-correlation peak calculation [Bérujon et al., 2012; Morgan et al., 2012], a least-square-minimisation [Zanette et al., 2014; M. C. Zdora et al., 2017] or an Euclidean-distance minimisation of the wavelet-transform of the reference- and probe- vectors [Qiao, Shi, Celestre, et al., 2020]. In this work the cross-correlation peak calculation is the preferred method for speckle-vector tracking [Bérujon et al., 2012; Morgan et al., 2012].

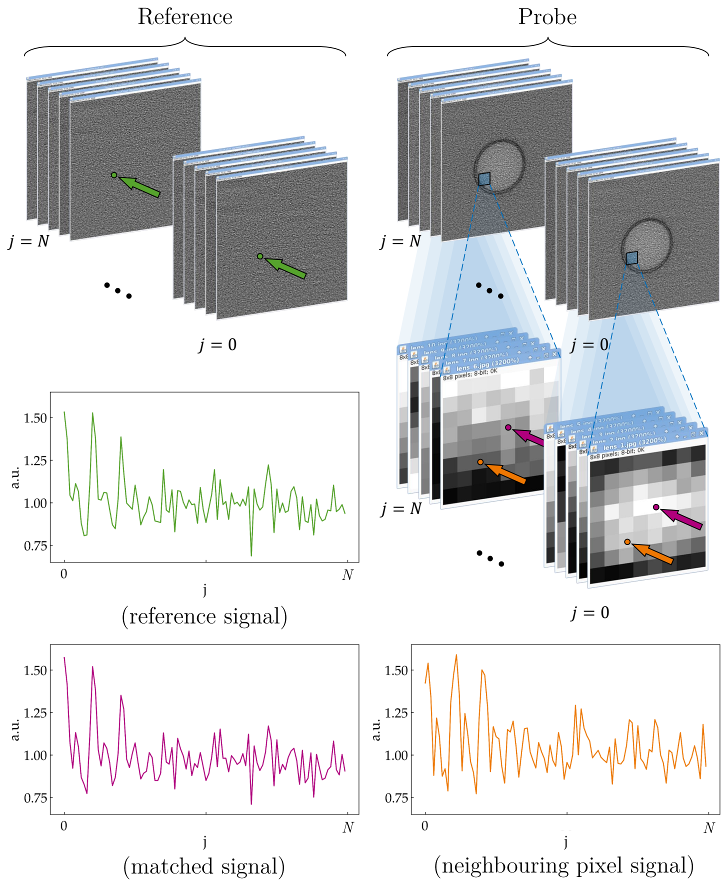

Fig. 4.6.: X-ray (near field) speckle vector tracking (XSVT). In the differential mode, two data-sets are taken: the reference and the one with the imaged sample. Each of the j^{th} image pair of the data-set is taken at a different transverse scan position of the speckle-generator across the X-ray beam. However, for a particular j^{th} image-pair (reference and probe) the exact same diffuser position must be maintained. A reference intensity vector $I_{\text{reference}}(x_l, y_m, j)$ (green) is searched in the sample stack,in a ROI centred around (x_l, y_m, j), where $I_{\text{probe}}(x_{l+\Delta l}, y_{m+\Delta m}, j)$ vectors are probed for a matching value. The purple signal is a well matched signal, while the orange signal shows the neighbouring-pixel intensity vector $I_{\text{probe}}(x_{l-2}, y_{m-2}, j)$.

used to evaluate the convergence of the tracking method. By repeating this procedure for all $L \times M$ pixels, it is possible to obtain two 2D displacement maps (vertical and horizontal) with lateral resolution down to the $\sim$ effective-pixel-size of the detector at the expense of an increased data-collection and data-processing time [Berujon and Ziegler, 2016; Berujon et al., 2020b].

Surface reconstruction & analysis

The phase gradients $\nabla\phi(x, y)$ can be obtained from the two displacement maps by multiplying them by the wavenumber k and dividing the product by the distance between the sample and detector (d) - cf. Eq. 4.3. An example of the horizontal and vertical gradient for a 2D-beryllium lens with $R = 50$ μm measured at 17 keV with $d = 800$ mm and pixel size $\Delta_{\text{pixel}} = 0.63$ μm is shown in Fig. 4.8(a)-(b) where the mismatch between front- and back- focusing surfaces is obvious - cf. Fig. 4.7. An ideal lens has phase gradients with linear dependencies on the focusing direction. From Eq. 1.36b and Eq. 2.8:

$$\nabla\phi(x, y) = \left(\frac{\partial\phi(x, y)}{\partial x}, \frac{\partial\phi(x, y)}{\partial y}\right) = -2k\delta\left(\frac{x}{R_x}, \frac{y}{R_y}\right), \tag{4.4}$$

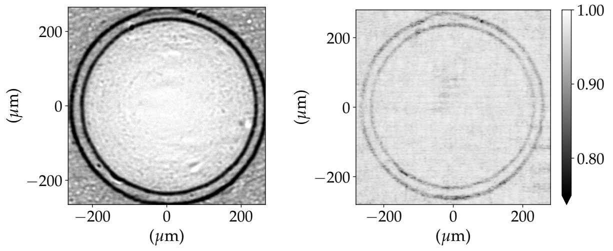

(a) radiography (b) cross-correlation map

Fig. 4.7.: (a) radiography of a 2D-beryllium lens with $R = 50$ μm measured at 17 keV with $d = 800$ mm and pixel size $\Delta_{\text{pixel}} = 0.63$ μm. The different penetration depths of the parabolic profiles cause the reduction of the geometric aperture, evidenced by the two concentric rings. (b) the normalised cross-correlation peak for the vector tracking algorithm. Regions with darker colours have lower correlation peaks.

which is a linear function with the slope of the linear phase-gradient in the focusing direction inversely proportional to the radius of curvature of the X-ray lens. This information can be experimentally retrieved with the knowledge of the X-ray energy used and the lens material (refraction index decrements). The phase gradient residues (or errors) are accessible by removing a linear fit from the gradients, which is shown in Fig. 4.8(c)-(d). In order to recover the thickness profile in projection approximation from the phase gradient (or from the residual phase gradient), the main step is the numerical 2D integration[23] of the differential fields, which is done using either the Frankot-Chelappa method [Frankot and Chellappa, 1988] or the Harker-O'Leary method (grad2surf) [Harker and O'Leary, 2015]. The profile resulting from the 2D integration of the (residual) phase gradients can be converted into thickness in projection approximation by (cf. Eq. 1.36b):

$$\Delta_z(x,y) = -\frac{\phi(x,y)}{k\delta}. \tag{4.5}$$

Equation 4.5 is based on the assumption that the X-ray lens has a refractive index decrement δ with no variations in (x, y, z). Eq. 4.5 also justifies the use of a monochromator in the experimental setup (cf. Fig. 4.4) since δ has a significant energy dependency. The figure errors from a lens can be obtained by two approaches: *i*-) by first integrating the phase gradients, then fit and remove from the resulting surface either a cylinder with a parabolic section or a paraboloid of revolution depending on whether the lens is a 1D or 2D focusing element. The treatment shown in Eq. 4.5 is applied to this residual phase; or by *ii*-) directly integrating the residual phase gradients and application of Eq. 4.5 to the integrated field. The residual thickness in projection approximation for the previous lens is shown in Fig. 4.9(a). Valuable information such as the RMS value of the figure errors; the decomposition of the wavefront into orthonormal polynomials (cf. §3.4.1 - *Orthornormal polynomials*) for the systematic study of the optical imperfections; and the power spectral density (PSD) of horizontal- and vertical- profile cuts showing the spatial frequency distribution of the optical errors can all be obtained from the residual thickness profile as shown in Fig. 4.9. The recovered thickness profile in Fig. 4.9(a) can be later used as a $\Delta_z(x, y)$ map in Eq. 1.37 to simulate the effects of optical imperfections in X-ray lenses as discussed in §3.4.2 - *Metrology data*.

---

[23] More on numerical integration of gradient fields in [Huang et al., 2015] and [Agrawal et al., 2006].

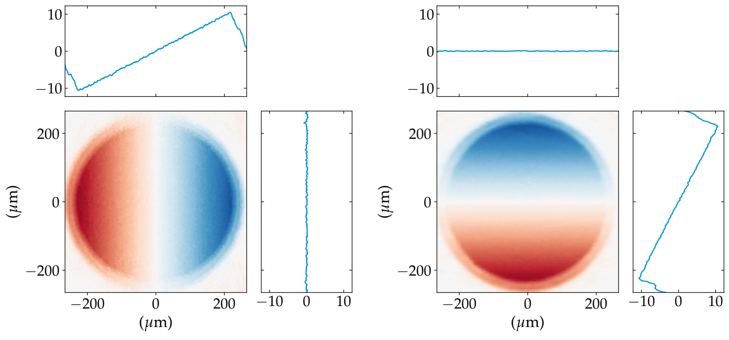

(a) horizontal gradient (μrad)

(b) vertical gradient (μrad)

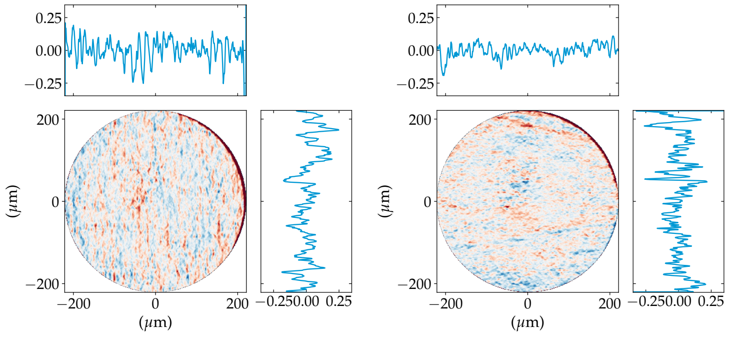

(c) horizontal gradient residue (μrad)

(d) vertical gradient residue (μrad)

Fig. 4.8.: Phase gradients and respective gradient residues for a 2D-beryllium lens with $R = 50\ \mu$m measured at 17 keV with $d = 800$ mm and a pixel size $\Delta_{\text{pixel}} = 0.63\ \mu$m - cf. Fig. 4.7.

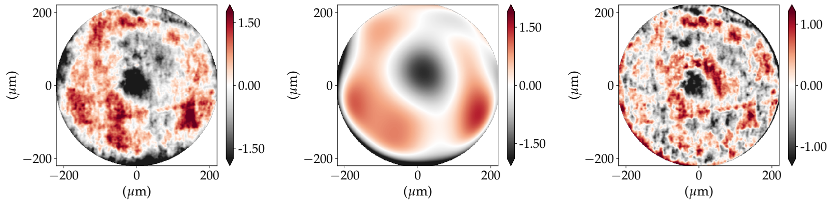

(a) thickness error

(b) Zernike circle pol. fit

(c) residues

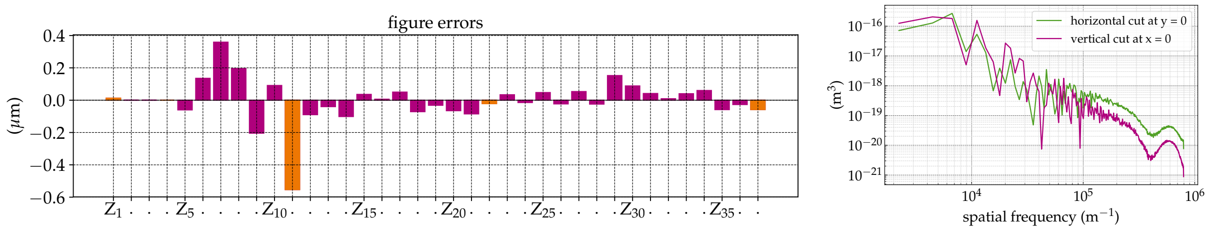

(d) Zernike circle polynomial fit coefficients

(e) PSD

Fig. 4.9.: (a) Recovered figure errors in projection approximation of a 2D-beryllium lens with $R = 50\ \mu$m measured at 17 keV with $d = 800$ mm and pixel size $\Delta_{\text{pixel}} = 0.63\ \mu$m, (b) Zernike circle polynomial fit of the figure errors and (c) the residues from the fit. The coefficients of the fit are shown in (d). (e) Horizontal and vertical power spectrum density of the lens.

Measurement sensitivity

Finally, some considerations on the measurement sensitivity are presented. Supposing an ideal detection system with effective pixel size Δ_{pixel}, the minimum measurable deflection angle is:

$$\alpha_{\text{min}} = \eta \frac{\Delta_{\text{pixel}}}{d}, \tag{4.6}$$

where η is a factor accounting for the ability of the algorithm to track a displacement vector with subpixel accuracy. Consider that the probe can be laterally sampled with the detector spatial resolution Δ_{pixel} as shown in Fig. 4.10(a). Each projected pixel will have a mean height value and the minimum detectable height difference between two adjacent pixels is Δz_{min}. The angle α_{min} can be attributed to refraction caused by the local slope ϑ between two adjacent projected pixel - cf. Fig. 4.10(b). A ray that is parallel to the optical axis will intercept this local slope at an angle $\theta_1 = \vartheta$ and will be refracted with an angle $\theta_2 = \vartheta + \alpha_{\text{min}}$. With the law of refraction (Eq. 2.2) it is possible to estimate[24] the longitudinal sensitivity of the XSVT as[25]:

$$\Delta z_{\text{min}} = \Delta_{\text{pixel}} \cdot \frac{\sin(\alpha_{\text{min}})}{\dfrac{1}{1-\delta} - \cos(\alpha_{\text{min}})}. \tag{4.7}$$

Figure 4.11 shows the XSVT longitudinal sensitivity (Δz_{min}) based on Eq. 4.7 for beryllium, one of the most common materials for refractive optics manufacturing. From Eq. 4.7, it is clear that longitudinal resolution of the XSVT technique depends on several factors: distance between speckle-generator and detector d; material and experiment energy expressed as index of refraction decrement δ; and the effective pixel size Δ_{pixel}, which is directly impacted by the PSF of the magnifying optics of the detector system. Other factors that contribute to the reduction in lateral resolution (increase of η): *i*-) the thickness of the scintillator used (blurring from thicker materials), *ii*-) temporal beam-instabilities as they may reduce the apparent transverse coherence if the integration time of the detector is longer than the instabilities period; *iii*-) vibrations of the sample holder with amplitudes larger than half of the pixel size and faster than the acquisition time; *iv*-) a low reproducibility of the speckle-generator membrane positioning.

Equation 4.7 is a geometric approximation of the problem and does not take into account propagation of uncertainties associated with the different components in the experiment, template-matching accuracy of the tracking routines nor numerical errors associated with the

---

[24] From Fig. 4.7(a) one obtains: $\tan(\vartheta) = \dfrac{\Delta z_{\text{min}}}{\Delta_{\text{pixel}}}$. Using $n_1 = 1$, $n_2 = 1 - \delta$, $\theta_1 = \vartheta$ and $\theta_2 = \vartheta + \alpha_{\text{min}}$ in the law of refraction: $\sin(\vartheta) = (1-\delta)\sin(\vartheta + \alpha_{\text{min}})$. Writing $\sin(\vartheta + \alpha_{\text{min}}) = \sin(\vartheta)\cos(\alpha_{\text{min}}) + \sin(\alpha_{\text{min}})\cos(\vartheta)$ and collecting terms, one obtains Eq. 4.7. Similar reasoning can be applied to a model with two refracting surfaces giving very similar numerical results.

[25] It is also possible to derive an approximate expression by using physical-optics arguments. The accumulated phase of a wave passing through a material with thickness Δ_z and index of refraction $n = 1 - \delta + i \cdot \beta$ is $\phi(x,y) = k\delta\Delta_z$ as shown in Eq. 1.36b. The gradient of this phase is: $\nabla\phi(x,y) = \left(k\delta\dfrac{\partial}{\partial x}\Delta_z; k\delta\dfrac{\partial}{\partial y}\Delta_z\right)$. The partial derivatives (local slopes) can be calculated as: $\dfrac{\partial}{\partial x}\Delta_z = \dfrac{\partial}{\partial y}\Delta_z = \dfrac{\Delta_z}{\Delta_{\text{pixel}}}$ as a first approximation for a square pixel. With the help of Eq. 4.3 and Eq. 4.6 one arrives at: $\Delta z_{\text{min}} = \Delta_{\text{pixel}} \cdot \dfrac{\alpha_{\text{min}}}{\delta}$.

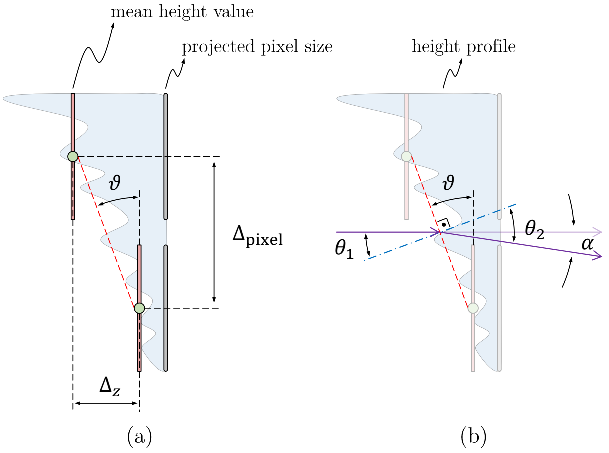

Fig. 4.10.: Sketch for aiding the calculation of the XSVT longitudinal sensitivity. The lateral resolution to which the probe is sampled generates a local slope between adjacent pixels (red dashed line with inclination given by ϑ). A beam parallel to the optical axis (purple) hits the sample is refracted with an angle θ_2.

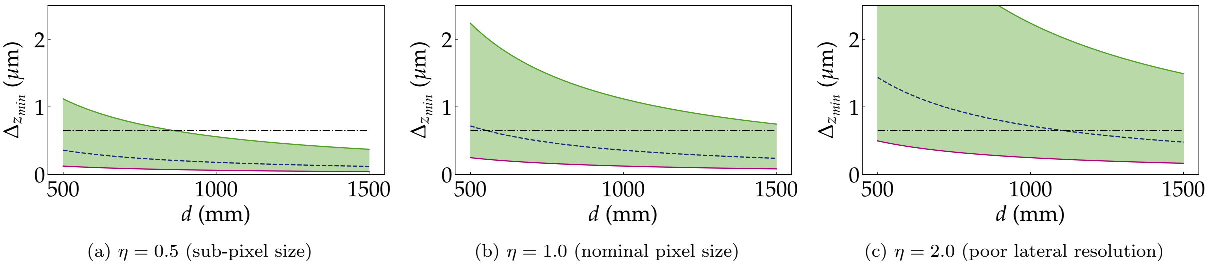

(a) $\eta = 0.5$ (sub-pixel size)

(b) $\eta = 1.0$ (nominal pixel size)

(c) $\eta = 2.0$ (poor lateral resolution)

Fig. 4.11.: X-ray speckle vectorial tracking longitudinal sensitivity (Δz_{min}) for beryllium. The solid red line indicates the performance of the method at 10 keV, while the solid green line for 30 keV. The dashed purple line indicates the experimental performance at 17 keV (used energy for such experiments in this work.). Black point-dashed line indicates the nominal pixel size of the imaging detector $\Delta_{\text{pixel}} = 0.65$ μm.

wavefront reconstruction as described by [Fried, 1977; Southwell, 1980]. Those can be globally estimated by applying the XSVT data analysis routine to two different reference data-sets taken under the exact same experimental conditions. These two 2D deflection angle maps allow to obtain the angular sensitivity lower threshold and to estimate η under the conditions imposed by the experimental setup. Figure 4.12 shows an example of such calculation with data taken at 17 keV with $d = 875$ mm and pixel size $\Delta_{\text{pixel}} = 0.63$ μm. The horizontal and vertical gradients RMS values for this particular experiment is 0.026 μrad and 0.025 μrad, respectively. Using Eq. 4.6, one can infer the $\eta > 0.036$. Those gradient maps can be integrated to obtain the phase noise level (see Eq. 4.3) and an associated thickness can be estimated by using Eq. 4.5.

4.2 X-ray lens metrology

Since early 2017, metrology of individual X-ray lenses has been systematically performed at the ESRF. Measurements have been applied to quality control of commercially acquired X-ray lenses for assessing the optical quality of already purchased lenses and for verifying if newly-purchased lenses meet specifications. The metrology profiles extracted from such

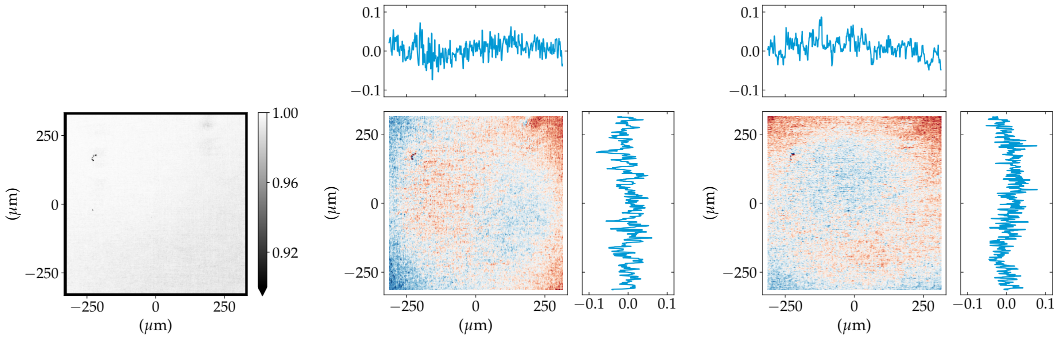

(a) cross-correlation map (b) horizontal gradient (c) vertical gradient

Fig. 4.12.: X-ray speckle vectorial tracking angular sensitivity calculated by applying the XSVT routine to two distinct sets of reference images taken taken shortly after each other. The experiment was performed at 17 keV with $d = 875$ mm and pixel size $\Delta_{\text{pixel}} = 0.63$ μm.

measurements have been used in X-ray beamline simulations[26] [Celestre et al., 2020]. More recently, metrology started to be used to aid manufacturing of X-ray lenses produced in-house[27] or as a co-development with external lens developers as it can offer insight into the relation between production parameters and their effects on the lens profile.

4.2.1 Single lens measurements

Tables 4.1 and 4.2 show a compilation of radii, figure errors and useful geometric aperture for two sets of ten 2D-beryllium lenses with nominal radius $R = 50$ μm and geometric aperture $A_{\varnothing} = 440$ μm measured individually and as stacks. These are the lenslets used in the optical simulations shown in §5 - *Effect of optical imperfections on an X-ray beam* and §6 - *Correcting optical imperfections in refractive lenses*. The figure errors are divided in full profile, Zernike circle polynomial fit (low frequency - LF) and residues from the fit (high-frequency - HF). For the particular case of the 2D-beryllium lenses, Zernike circle polynomials until the 37th order (3rd order spherical aberration) were used. In the context of this work, the low-frequencies (LF) span from ~ 500 μm or 2×10^3 m^{-1} (geometrical aperture of a lenslet) to ~ 50 μm or 2×10^4 m^{-1}, while the mid- and high-frequencies span from ~ 50 μm or 2×10^4 m^{-1} to ~ 0.5 μm or 2×10^6 m^{-1}, which is obtained from the Nyquist frequency[28] of the measured data.

Individually measured lenses can be artificially stacked to study the effects of pilling up lenses and to be later compared to the measurement of stacked lenses. This artificial stacking can be done by propagating a plane wave through the CRL using the model described by Eq. 2.12 and extracting any developed quadratic phase term at the exit pupil - Fig. 4.13 shows a typical optical setup for artificially stacking lenses. The phase can be readily converted into a thickness profile in projection approximation with the aid of Eq. 1.36b. The accumulated[29] profiles for the stacks 1 and 2 are shown in Figs. 4.14 and 4.16 and compiled in Tables 4.1 and 4.2.

---

[26] Simulations using optical metrology of X-ray lenses have been reported in [Chubar et al., 2020].

[27] See [Celestre, 2020].

[28] Nyquist frequency is defined as one over twice the effective pixel size $\Delta_{\text{pixel}} = 0.65$ μm.

[29] The progressive increase of figure errors for the full-, fit- and residual- profiles is shown in Fig. 5.9 from §5.5.1 - *Metrology of individual lenses vs. stacked lenses*

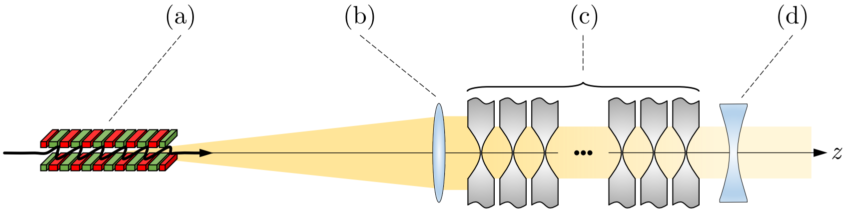

Fig. 4.13.: Optical setup used for artificially stacking lenses and calculating the phase errors. (a) The illumination is the emission of a filament electron beam. An (b) ideal parabolic phase element is used to give this illumination a plane phase. The stacked X-ray lenses are shown in (c). They follow the model described by Eq. 2.12, that is, the CRL multi-slicing with figure errors added. An (d) ideal parabolic phase element with a radius of curvature matching the developed quadratic term is then added and the residuals (phase errors) can be extracted.

4.2.2 Stacked lenses measurements

Being able to measure stacked lenses is of high interest as it allows not only to predict the performance of such focusing compound elements in conditions relatively similar to their employment in beamlines but also enables the design of optical corrections for an aberrated system [Seiboth et al., 2017, 2020]. The values for radii, figure errors and useful geometric aperture for the two stacks used in this work are shown in Tables 4.1 and 4.2 and Figs. 4.15 and 4.17. The stacks, composed of the lenses described in §4.2.1 - *Single lens measurements* can be compared with the artificially accumulated profiles as shown in Figs. 4.14 and 4.16, which shows reasonable qualitative agreement - improving the agreement between the two types of measurements is important as it allows the prediction of performance and correction of a CRL composed of an arbitrary set of already measured and catalogued lenses. ■

Tab. 4.1.: Compilation of radii, figure errors and clear aperture for lenses L01 to L10 (stack 1) obtained with XSVT metrology.

lens	**radius**	figure errors[†] (r.m.s) μm			**useful aperture**
number	μm	full profile	pol. fit	residues	μm
L01	48.77	0.57	0.45	0.35	439
L02	48.24	0.80	0.69	0.43	442
L03	48.76	0.77	0.55	0.54	432
L04	49.20	1.05	0.92	0.51	435
L05	48.41	0.81	0.67	0.44	440
L06	48.70	1.07	0.72	0.79	443
L07	48.91	0.70	0.53	0.46	442
L08	49.23	0.84	0.62	0.56	447
L09	48.09	0.93	0.79	0.49	434
L10	48.10	0.88	0.76	0.44	431
accumulated:		4.84	4.36	2.18	400
Stack 01:	5.46	5.75	5.20	2.47	399

[†] values given for $A_\varnothing = 400$ μm

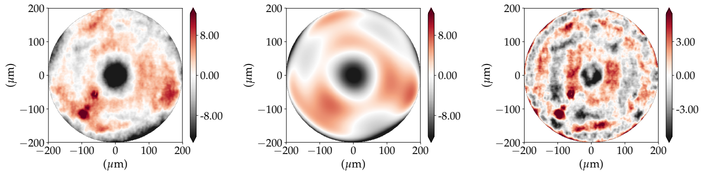

(a) full profile (b) polynomial fit (c) residues

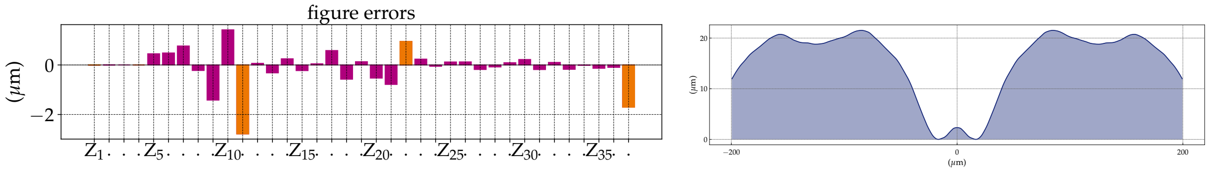

(d) polynomial decomposition (e) azimuthal averaged profile

Fig. 4.14.: Individually measured and artificially stacked lenses forming the stack 1. The individual lenses parameters are shown in Table 4.1. Profiles calculated for a geometric aperture of $A_\varnothing = 400$ μm.

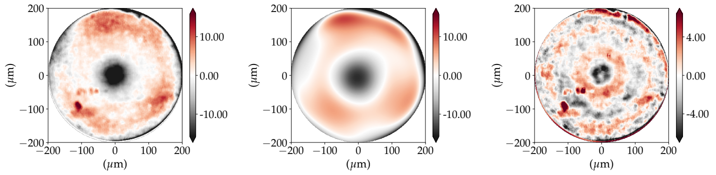

(a) full profile (b) polynomial fit (c) residues

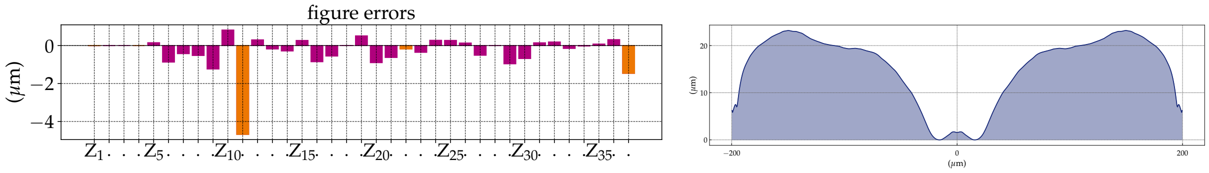

(d) polynomial decomposition (e) azimuthal averaged profile

Fig. 4.15.: Measurement of a CRL composed of the lenses L01-L10 described in Table 4.1 (stack 1). Profiles calculated for a geometric aperture of $A_\varnothing = 400$ μm.

Tab. 4.2.: Compilation of radii, figure errors and useful aperture for lenses L11 to L20 (stack 2) obtained with XSVT metrology.

lens number	**radius** μm	figure errors† (r.m.s) μm full profile	pol. fit	residues	**useful aperture** μm
L11	49.05	0.71	0.57	0.43	440
L12	49.27	0.80	0.68	0.44	460
L13	48.98	0.94	0.75	0.56	435
L14	48.26	1.06	0.95	0.47	452
L15	48.25	1.44	1.36	0.46	444
L16	49.25	0.69	0.55	0.42	443
L17	48.94	0.72	0.61	0.39	433
L18	48.30	1.22	1.15	0.42	439
L19	47.78	1.24	1.21	0.25	419
L20	48.62	0.80	0.72	0.36	456
	accumulated	6.28	6.10	1.62	400
Stack 02:	5.67	6.47	5.97	2.49	407

† values given for $A_{\varnothing} = 395$ μm

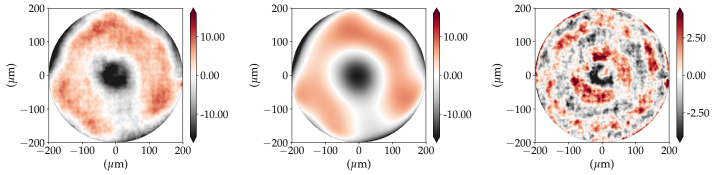

(a) full profile (b) polynomial fit (c) residues

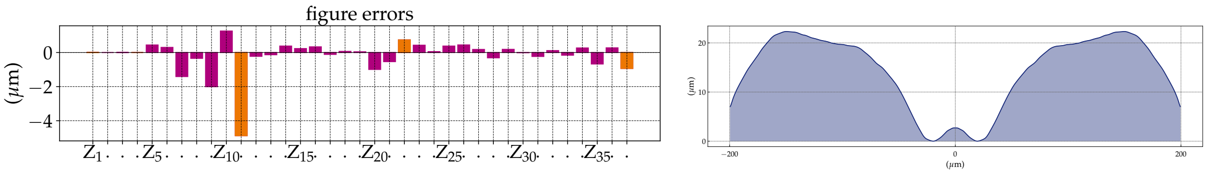

(d) polynomial decomposition (e) azimuthal averaged profile

Fig. 4.16.: Individually measured and artificially stacked lenses forming the stack 2. The individual lenses parameters are shown in Table 4.2. Profiles calculated for a geometric aperture of $A_{\varnothing} = 400$ μm.

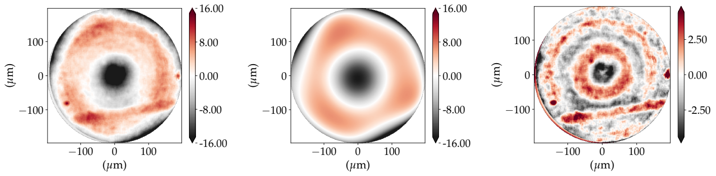

(a) full profile (b) polynomial fit (c) residues

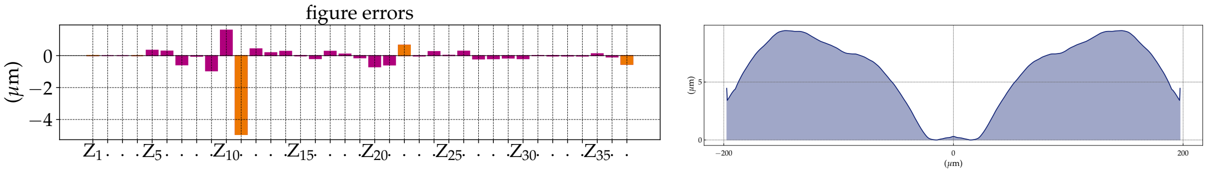

(d) polynomial decomposition (e) azimuthal averaged profile

Fig. 4.17.: Measurement of a CRL composed of the lenses L11-L20 described in Table 4.2 (stack 2). Profiles calculated for a geometric aperture of $A_{\varnothing} = 400$ μm.

References

Agrawal, A., Raskar, R., and Chellappa, R. (2006). "What is the range of surface reconstructions from a gradient field?" In: *Lecture Notes in Computer Science (including subseries Lecture Notes in Artificial Intelligence and Lecture Notes in Bioinformatics)*. Vol. **3951 LNCS**. Springer Verlag, p. 578.

Alcock, S. G., Nistea, I., and Sawhney, K. (2016). "Nano-metrology: The art of measuring X-ray mirrors with slope errors <100 nrad". In: *Review of Scientific Instruments* **87**.5, p. 051902.

Berujon, S., Wang, H., and Sawhney, K. J. (2013). "At-wavelength metrology using the X-ray speckle tracking technique: Case study of a X-ray compound refractive lens". In: *Journal of Physics: Conference Series*. Vol. **425**. PART 5. Institute of Physics Publishing, p. 052020.

Berujon, S., Cojocaru, R., Piault, P., Celestre, R., Roth, T., Barrett, R., and Ziegler, E. (2020a). "X-ray optics and beam characterization using random modulation: experiments". In: *Journal of Synchrotron Radiation* **27**.2, p. 293.

— (2020b). "X-ray optics and beam characterization using random modulation: theory". In: *Journal of Synchrotron Radiation* **27**.2, p. 284.

Berujon, S. and Ziegler, E. (2016). "X-ray Multimodal Tomography Using Speckle-Vector Tracking". In: *Physical Review Applied* **5**.4, p. 044014.

Bérujon, S., Ziegler, E., Cerbino, R., and Peverini, L. (2012). "Two-dimensional x-ray beam phase sensing". In: *Physical Review Letters* **108**.15, p. 158102.

Celestre, R. (2020). "Refractive lenses, at-wavelength metrology and optics simulation". In: *12th 3-Way Meeting X-ray Optics Workshop (ESRF), Grenoble, France* (presentation).

Celestre, R., Berujon, S., Roth, T., Sanchez del Rio, M., and Barrett, R. (2020). "Modelling phase imperfections in compound refractive lenses". In: *Journal of Synchrotron Radiation* **27**.2, p. 305.

Cerbino, R., Peverini, L., Potenza, M. A., Robert, A., Bösecke, P., and Giglio, M. (2008). "X-ray-scattering information obtained from near-field speckle". In: *Nature Physics* **4**.3, p. 238.

Chubar, O., Wiegart, L., Antipov, S., Celestre, R., Coles, R., Fluerasu, A., and Rakitin, M. S. (2020). "Analysis of hard x-ray focusing by 2D diamond CRL". In: *Proc. SPIE 11493, Advances in Computational Methods for X-Ray Optics V*, pp. 11493–20.

Cloetens, P., Barrett, R., Baruchel, J., Guigay, J. P., and Schlenker, M. (1996). "Phase objects in synchrotron radiation hard x-ray imaging". In: *Journal of Physics D: Applied Physics* **29**.1, p. 133.

David, C., Rutishauser, S., Sprung, M., Zanette, I., and Weitkamp, T. (2012). "X-ray grating interferometry - Applications in metrology and wave front sensing". In: *AIP Conference Proceedings*. Vol. **1466**. 1. American Institute of PhysicsAIP, p. 23.

Endrizzi, M. (2018). "X-ray phase-contrast imaging". In: *Nuclear Instruments and Methods in Physics Research, Section A: Accelerators, Spectrometers, Detectors and Associated Equipment* **878**, p. 88.

Frankot, R. T. and Chellappa, R. (1988). "A Method for Enforcing Integrability in Shape from Shading Algorithms". In: *IEEE Transactions on Pattern Analysis and Machine Intelligence* **10**.4, p. 439.

Fried, D. L. (1977). "Least-square fitting a wave-front distortion estimate to an array of phase-difference measurements". In: *Journal of the Optical Society of America* **67**.3, p. 370.

Geloni, G., Saldin, E., Schneidmiller, E., and Yurkov, M. (2008). "Transverse coherence properties of X-ray beams in third-generation synchrotron radiation sources". In: *Nuclear Instruments and Methods in Physics Research Section A: Accelerators, Spectrometers, Detectors and Associated Equipment* **588**.3, p. 463.

Goikhman, A., Lyatun, I., Ershov, P., Snigireva, I., Wojda, P., Gorlevsky, V., Semenov, A., Sheverdyaev, M., Koletskiy, V., and Snigirev, A. (2015). "Highly porous nanoberyllium for X-ray beam speckle suppression". In: *Journal of Synchrotron Radiation* **22**.3, p. 796.

Goodman, J. W. (2020). *Speckle Phenomena in Optics: Theory and Applications*. Second edition. SPIE Press.

Grizolli, W. C., Shi, X., Assoufid, L., Kolodziej, T., and Shvyd'ko, Y. (2017). "Single-grating Talbot imaging for wavefront sensing and x-ray metrology". In: *Proc. SPIE 10385, Advances in Metrology for X-Ray and EUV Optics VII, 1038502* **10385**.7, p. 1.

Harker, M. and O'Leary, P. (2015). "MATLAB toolbox for the regularized surface reconstruction from gradients". In: *Proc. SPIE 9534, Twelfth International Conference on Quality Control by Artificial Vision 2015* **9534**, 95341E.

Helfen, L., Myagotin, A., Mikulk, P., Pernot, P., Voropaev, A., Elyyan, M., Di Michiel, M., Baruchel, J., and Baumbach, T. (2011). "On the implementation of computed laminography using synchrotron radiation". In: *Review of Scientific Instruments* **82**.6, p. 063702.

Huang, L., Idir, M., Zuo, C., Kaznatcheev, K., Zhou, L., and Asundi, A. (2015). "Comparison of two-dimensional integration methods for shape reconstruction from gradient data". In: *Optics and Lasers in Engineering* **64**, p. 1.

Kashyap, Y., Wang, H., and Sawhney, K. (2016). "Experimental comparison between speckle and grating-based imaging technique using synchrotron radiation X-rays". In: *Optics Express* **24**.16, p. 18664.

Koch, F. J., Detlefs, C., Schröter, T. J., Kunka, D., Last, A., and Mohr, J. (2016). "Quantitative characterization of X-ray lenses from two fabrication techniques with grating interferometry". In: *Opt. Express* **24**.9, p. 9168.

Kutsal, M., Bernard, P., Berruyer, G., Cook, P. K., Hino, R., Jakobsen, A. C., Ludwig, W., Ormstrup, J., Roth, T., Simons, H., Smets, K., Sierra, J. X., Wade, J., Wattecamps, P., Yildirim, C., Poulsen, H. F., and Detlefs, C. (2019). "The ESRF dark-field x-ray microscope at ID06". In: *IOP Conference Series: Materials Science and Engineering* **580**, p. 12007.

Landis, E. N. and Keane, D. T. (2010). "X-ray microtomography". In: *Materials Characterization* **61**.12, p. 1305.

Lee, S. and Guizar-Sicairos, M. (2010). "Validation of quantitative Ronchi test through numerical propagation". In: *Optics Express* **18**.18, p. 18525.

Lyatun, I. I., Goikhman, A. Y., Ershov, P. A., Snigireva, I. I., and Snigirev, A. A. (2015). "On the problem of the metrology of refractive X-ray optics". In: *Journal of Surface Investigation* **9**.3, p. 446.

Lyatun, I., Ershov, P., Snigireva, I., and Snigirev, A. (2020). "Impact of beryllium microstructure on the imaging and optical properties of X-ray refractive lenses". In: *Journal of Synchrotron Radiation* **27**.1, p. 44.

Macrander, A., Erdmann, M., Kujala, N., Stoupin, S., Marathe, S., Shi, X., Wojcik, M., Nocher, D., Conley, R., Sullivan, J., Goetze, K., Maser, J., and Assoufid, L. (2016). "X-ray optics testing beamline 1-BM at the advanced photon source". In: *AIP Conference Proceedings*. Vol. **1741**. 1. American Institute of Physics Inc., p. 030030.

Mandel, L. and Wolf, E. (1995). *Optical Coherence and Quantum Optics*. First edition. Cambridge University Press.

Mayo, S. C. and Sexton, B. (2004). "Refractive microlens array for wave-front analysis in the medium to hard x-ray range". In: *Optics Letters* **29**.8, p. 866.

Mercere, P., Bucourt, S., Cauchon, G., Douillet, D., Dovillaire, G., Goldberg, K. A., Idir, M., Levecq, X., Moreno, T., Naulleau, P. P., Rekawa, S., and Zeitoun, P. (2005). "X-ray beam metrology and x-ray optic alignment by Hartmann wavefront sensing". In: *Proc. SPIE 5921, Advances in Metrology for X-Ray and EUV Optics* **5921**, p. 592109.

Mikhaylov, A., Reich, S., Zakharova, M., Vlnieska, V., Laptev, R., Plech, A., and Kunka, D. (2020). "Shack-Hartmann wavefront sensors based on 2D refractive lens arrays and super-resolution multi-contrast X-ray imaging". In: *Journal of Synchrotron Radiation* **27**.3, p. 788.

Morgan, K. S., Irvine, S. C., Suzuki, Y., Uesugi, K., Takeuchi, A., Paganin, D. M., and Siu, K. K. (2010). "Measurement of hard X-ray coherence in the presence of a rotating random-phase-screen diffuser". In: *Optics Communications* **283**.2, p. 216.

Morgan, K. S., Paganin, D. M., and Siu, K. K. (2012). "X-ray phase imaging with a paper analyzer". In: *Applied Physics Letters* **100**.12, p. 124102.

Munro, P. R., Ignatyev, K., Speller, R. D., and Olivo, A. (2012). “Phase and absorption retrieval using incoherent X-ray sources”. In: *Proceedings of the National Academy of Sciences of the United States of America* **109**.35, p. 13922.

Narikovich, A. S., Ershov, P. A., Leitsin, V. N., Savin, V. V., and Snigirev, A. A. (2017). “X-ray tomography as a diagnostic method of X-ray refractive optics”. In: *Instruments and Experimental Techniques* **60**.3, p. 390.

Nilsson, D., Uhlén, F., Holmberg, A., Hertz, H. M., Schropp, A., Patommel, J., Hoppe, R., Seiboth, F., Meier, V., Schroer, C. G., Galtier, E., Nagler, B., Lee, H. J., and Vogt, U. (2012). “Ronchi test for characterization of nanofocusing optics at a hard x-ray free-electron laser”. In: *Optics Letters* **37**.24, p. 5046.

Pfeiffer, F., Weitkamp, T., Bunk, O., and David, C. (2006). “Phase retrieval and differential phase-contrast imaging with low-brilliance X-ray sources”. In: *Nature Physics* **2**.4, p. 258.

Qiao, Z., Shi, X., Celestre, R., and Assoufid, L. (2020). “Wavelet-transform-based speckle vector tracking method for X-ray phase imaging”. In: *Optics Express* **28**.22, p. 33053.

Qiao, Z., Shi, X., Wojcik, M., Rebuffi, L., and Assoufid, L. (2020). “Single-shot speckle tracking method based on wavelet transform and multi-resolution analysis”. In: *Proc. SPIE 11492, Advances in Metrology for X-Ray and EUV Optics IX*, pp. 11492–22.

Romell, J., Zhou, T., Zdora, M., Sala, S., Koch, F. J., Hertz, H. M., and Burvall, A. (2017). “Comparison of laboratory grating-based and speckle-tracking x-ray phase-contrast imaging”. In: *Journal of Physics: Conference Series*. Vol. **849**. 1. Institute of Physics Publishing, p. 12035.

Roth, T., Alianelli, L., Lengeler, D., Snigirev, A., and Seiboth, F. (2017). “Materials for x-ray refractive lenses minimizing wavefront distortions”. In: *MRS Bulletin* **42**.06, p. 430.

Roth, T., Helfen, L., Hallmann, J., Samoylova, L., Kwaśniewski, P., Lengeler, B., and Madsen, A. (2014). “X-ray laminography and SAXS on beryllium grades and lenses and wavefront propagation through imperfect compound refractive lenses”. In: *Proc. SPIE 9207, Advances in X-Ray/EUV Optics and Components IX* 9207, p. 920702.

Sala, S., Daurer, B. J., Hantke, M. F., Ekeberg, T., Loh, N. D., Maia, F., and Thibault, P. (2017). “Ptychographic imaging for the characterization of X-ray free-electron laser beams”. In: *Journal of Physics: Conference Series*. Vol. **849**. 1. Institute of Physics Publishing, p. 12032.

Sawhney, K., Wang, H., Sutter, J., Alcock, S., and Berujon, S. (2013). “At-wavelength Metrology of X-ray Optics at Diamond Light Source”. In: *Synchrotron Radiation News* **26**.5, p. 17.

Schropp, A., Hoppe, R., Meier, V., Patommel, J., Seiboth, F., Lee, H. J., Nagler, B., Galtier, E. C., Arnold, B., Zastrau, U., Hastings, J. B., Nilsson, D., Uhlén, F., Vogt, U., Hertz, H. M., and Schroer, C. G. (2013). “Full spatial characterization of a nanofocused X-ray free-electron laser beam by ptychographic imaging”. In: *Scientific Reports* **3**.1, p. 1.

Seaberg, M., Cojocaru, R., Berujon, S., Ziegler, E., Jaggi, A., Krempasky, J., Seiboth, F., Aquila, A., Liu, Y., Sakdinawat, A., Lee, H. J., Flechsig, U., Patthey, L., Koch, F., Seniutinas, G., David, C., Zhu, D., Mikeš, L., Makita, M., Koyama, T., Mancuso, A. P., Chapman, H. N., and Vagovič, P. (2019). “Wavefront sensing at X-ray free-electron lasers”. In: *Journal of Synchrotron Radiation* **26**.4, p. 1115.

Seiboth, F., Brückner, D., Kahnt, M., Lyubomirskiy, M., Wittwer, F., Dzhigaev, D., Ullsperger, T., Nolte, S., Koch, F., David, C., Garrevoet, J., Falkenberg, G., and Schroer, C. G. (2020). “Hard X-ray wavefront correction via refractive phase plates made by additive and subtractive fabrication techniques”. In: *Journal of Synchrotron Radiation* **27**.5, p. 27.

Seiboth, F., Schropp, A., Scholz, M., Wittwer, F., Rödel, C., Wünsche, M., Ullsperger, T., Nolte, S., Rahomäki, J., Parfeniukas, K., Giakoumidis, S., Vogt, U., Wagner, U., Rau, C., Boesenberg, U., Garrevoet, J., Falkenberg, G., Galtier, E. C., Ja Lee, H., Nagler, B., and Schroer, C. G. (2017). “Perfect X-ray focusing via fitting corrective glasses to aberrated optics”. In: *Nature Communications* **8**.1, p. 14623.

Southwell, W. H. (1980). “Wave-front estimation from wave-front slope measurements”. In: *Journal of the Optical Society of America* **70**.8, p. 998.

Tian, N., Jiang, H., Li, A., Liang, D., Yan, S., and Zhanga, Z. (2020). “Influence of diffuser grain size on the speckle tracking technique”. In: *Journal of Synchrotron Radiation* **27**.1, p. 146.

Uhlén, F., Rahomäki, J., Nilsson, D., Seiboth, F., Sanz, C., Wagner, U., Rau, C., Schroer, C. G., and Vogt, U. (2014). “Ronchi test for characterization of x-ray nanofocusing optics and beamlines”. In: *Journal of Synchrotron Radiation* **21**.5, p. 1105.

Vivo, A., Barrett, R., and Perrin, F. (2019). “Stitching techniques for measuring X-ray synchrotron mirror topography”. In: *Review of Scientific Instruments* **90**.2, p. 021710.

Wang, H., Kashyap, Y., and Sawhney, K. (2016). “From synchrotron radiation to lab source: Advanced speckle-based X-ray imaging using abrasive paper”. In: *Scientific Reports* **6**.1, p. 1.

Wilkins, S. W., Gureyev, T. E., Gao, D., Pogany, A., and Stevenson, A. W. (1996). “Phase-contrast imaging using polychromatic hard X-rays”. In: *Nature* **384**.6607, p. 335.

Zanette, I., Zhou, T., Burvall, A., Lundström, U., Larsson, D. H., Zdora, M., Thibault, P., Pfeiffer, F., and Hertz, H. M. (2014). “Speckle-based x-ray phase-contrast and dark-field imaging with a laboratory source”. In: *Physical Review Letters* **112**.25, p. 253903.

Zdora, M. C., Thibault, P., Pfeiffer, F., and Zanette, I. (2015). “Simulations of x-ray speckle-based dark-field and phase-contrast imaging with a polychromatic beam”. In: *Journal of Applied Physics* **118**.11.

Zdora, M. C., Thibault, P., Zhou, T., Koch, F. J., Romell, J., Sala, S., Last, A., Rau, C., and Zanette, I. (2017). “X-ray Phase-Contrast Imaging and Metrology through Unified Modulated Pattern Analysis”. In: *Physical Review Letters* **118**.20, p. 203903.

Zdora, M.-C. (2018). “State of the Art of X-ray Speckle-Based Phase-Contrast and Dark-Field Imaging”. In: *Journal of Imaging* **4**.5, p. 60.

Zdora, M.-C., Zanette, I., Zhou, T., Koch, F. J., Romell, J., Sala, S., Last, A., Ohishi, Y., Hirao, N., Rau, C., and Thibault, P. (2018). “At-wavelength optics characterisation via X-ray speckle- and grating-based unified modulated pattern analysis”. In: *Optics Express* **26**.4, p. 4989.

Ziegler, E., Hoszowska, J., Bigault, T., Peverini, L., Massonnat, J. Y., and Hustache, R. (2004). “The ESRF BM05 metrology beamline: Instrumentation and performance upgrade”. In: *AIP Conference Proceedings*. Vol. **705**. 1. American Institute of Physics Inc., p. 436.

5

Effect of optical imperfections on an X-ray beam

The effects of the optical imperfections modelled and measured in Chapter 4 to an X-ray beam are presented in this chapter in terms of fully- and partially- coherent simulations were done with the *SRW* code and the specially developed Python library for refractive optics (barc4RefractiveOptics) presented in Chapter 3. The fully-coherent simulations include the beam-caustics and the point-spread function (PSF - intensity and phase) for the system being modelled. Partially-coherent simulations comprise the beam characteristics at the image plane and the beam profile at selected positions along the optical axis. These simulations are used to extensively evaluate the performance of commercially available Be lenses; compare the validity of individually measured and artificially stacked lenses against the stack measurement; and the different effects of distinct spatial frequency ranges in figure errors to the optical performance of the CRL.

5.1 Lenses and lens stacks

The modelled lenses are 2D-Be lenses with a nominal radius of $R = 50\ \mu$m chosen as representative of lenses used widely at beamlines at many synchrotrons - see Fig. 2.1(b) and (d). Such lenses have typically 1 mm thickness and are held in a 2 mm thick lens frame (newer ones 1.6 mm thick), which delimits the spacing Δs $= 2$ mm between individual lenses in Eq. 2.12. Those lenses can be manufactured with wall thickness in the range of ~ 30 to $40\ \mu$m. Applying Eq. 2.6, one obtains $A_{\varnothing} \leq 440\mu$m. At 8 keV, the energy used for the simulations, the index of refraction for beryllium is $n = 1 - 5.318 \times 10^{-6} + i \cdot 2.071 \times 10^{-9}$ and the corresponding intensity transmission of this lenslet is shown in Fig. 2.5(a). Applying Eq. 2.4 with $N = 1$, one obtains the focal length for a single lens: $f_{\text{lens}} = 4.701$ m. The lens stacks used are composed of $N = 10$ lenses, except for the stacks used in the simulations shown in Fig. 5.5, where the number of lenses N varies ($N = 1, 5, 10$). The lens stack focal distance can be obtained by applying Eq. 2.5 with $N = 10$ and $L = (N - 1) \cdot 2$ mm $= 18$ mm: $f_{\text{CRL}} = 473$ mm, giving a magnification of approximately $126 : 1$ ($M \approx 8 \times 10^{-3}$ for a source 60 m away from the centre of the CRL) and a diffraction-limited spot size (Eq. 2.14) of ~ 200 nm. The error profiles used for the simulations have been described in §4.2.1 - *Single lens measurements* when measured individually and in §4.2.2 - *Stacked lenses measurements* when measured as a 10-element stack.

The comparison between the simulations using 10 different individually measured lenses against simulations using metrology from a lens stack composed of those very same lenses is shown in Fig. 5.3 for lenses L01-L10 and in Fig. 5.4 for the lenses L11-L20. Simulations of a single lens (L01), five stacked lenses (L01-L05) and ten stacked lenses (L01-L10) are used to investigate the deterioration of the X-ray beam profile upon stacking lenses. These can be seen in Fig. 5.5. The effect of different spatial frequency ranges in the X-ray beam is shown in Fig. 5.6, where the performance of the accumulated figure error profile of lenses L01-L10 is compared

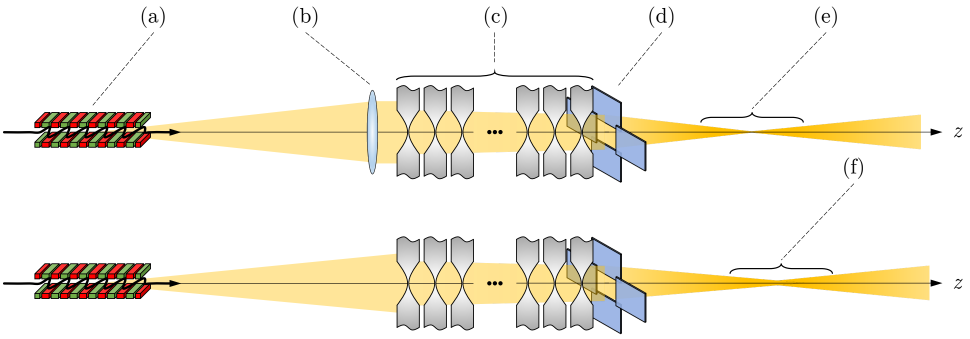

Fig. 5.1.: **top row**: beamline used for §5.3 - *Fully coherent simulations*. **bottom row**: beamline used for §5.4 - *Partially coherent simulations*. (a) shows the X-ray source: a CPMU18 undulator. An (b) ideal parabolic phase element with radius of curvature $R = -60$ m is placed 60 m downstream the radiation source to give the illumination a near-plane phase - cf. Eq. 1.16. This ideal element is only present for the fully-coherent simulations. The lenses being studied are shown in (c). They are immediately followed by a set of (d) slits to ensure the same geometric aperture for all simulations and aid direct calculation of the Strehl ratio. For the fully-coherent simulations, the beam-caustic range is shown in (e) and the PSF is calculated at the centre of it. For the partially-coherent simulations, the beam profile evolution along the optical axis is shown in (f) and the beam characteristics at the focal position are calculated at its centre.

against the performance of its decomposition in Zernike circular polynomials and the residues of such fit. Finally, the lens stack formed by individually measured lenses L01-L10 is meticulously studied under fully- and partially-coherent illumination. Figure 5.7 shows transverse cuts along the optical axis, the beam caustics, PSF (intensity and phase) and the demagnified image of the X-ray source (CPMU18[1]).

5.2 Software and computing infrastructure

All simulations presented here were done using the "Synchrotron Radiation Workshop" (SRW) [Chubar and Elleaume, 1998][2], as it conveniently offers the possibility of fully- and partially-coherent calculations[3], and presents parallelisation with the MPI standard [Chubar et al., 2011]. Fully coherent calculations were done using a single CPU of an Intel(R) Xeon(R) CPU E5-2680 v4 @ 2.40GHz, while partial coherent simulations used 28 CPUs of the same type (NICE OAR cluster at the ESRF). The specially developed python library for dealing with the refractive lenses with the addition of optical imperfections (barc4RefractiveOptics) presented in Chapter 3 was also used in the simulations.

5.3 Fully coherent simulations

For this set of simulations, the X-ray source is a filament electron-beam passing through a CPMU18 undulator with 111 magnetic periods, $\Lambda = 18$ mm magnetic period and magnetic field $B = 0.9863$ T emitting a 1st harmonic photon beam at 8 keV (resonance). The photon source size and divergence are given by the specific radiation pattern size and divergence of

---

[1] Cryogenic Permanent Magnet Undulator.

[2] Available at `https://github.com/ochubar/srw`

[3] See §1.3.2 - *Wave propagation* and §1.3.3 - *Partially coherent simulations*.

the insertion device and the emission is fully coherent[4] - see §1.1.2 - *High brilliance X-ray sources*. At 60 m away from the source, the beam footprint[5] is large enough to illuminate the full geometric aperture of a lens with $A_{\varnothing} \leq 440\mu$m with an intensity variation of 2% (centre to the edge). The illumination profile in conjunction with the transmission profile of the lenses being modelled (Fig. 2.5) allows classifying such systems as apodised. In the paraxial approximation, the radiation phase for this source is dominated by a quadratic phase term [Chubar et al., 1999, 2001; Chubar and Celestre, 2019]. At the position along the optical axis where the intensity is calculated, this quadratic phase term can be compensated by placing an ideal lens with focal length $f = -60$ m. This ensures a plane-wave illumination (Eq. 1.16) downstream the ideal element, which is used to illuminate the different CRL models being studied. The lens stack and imperfect lenses are modelled using the CRL multi-slice approach with errors added described by Eq. 2.12 and shown in Fig. 2.6(c) in §2.2.3 - *CRL modelling*. The evaluation of the effect of optical imperfections on an X-ray beam is performed at the image plane of the focusing system and in its vicinity. The beamline used for the fully-coherent simulations is shown in Fig. 5.1.

Tab. 5.1.: Summary of the beam sizes in FWHM for various CRL models. The extended source image sizes are taken from the partially coherent simulations averaging the intensity of 10^4 wavefronts.

		PSF (nm)		**source image** (nm)	
	lens model	hor.	ver.	hor.	ver.
	analytic equations	223.3		603.8	241.7
	ideal CRL	217.5	218.7	626.4	247.5
Fig. 5.3	L01-L10	208.8	210.1	680.1	254.4
	stack 01	206.2	219.5	692.0	254.1
Fig. 5.4	L11-L20	194.7	197.5	835.1	374.8
	stack 02	192.1	203.1	748.6	268.9
Fig. 5.5	single ideal lens	1959.4		-	-
	L01	1954.0	1957.3	-	-
	five ideal stacked lenses	401.3		-	-
	L01-L05	384.5	399.0	-	-
Fig. 5.6	LF L01-L10	214.8	206.0	731.4	263.7
	HF L01-L10	225.1	231.6	637.5	246.1

5.3.1 The PSF: ideal focusing

After passage through the CRL model being studied, the plane wave used for illuminating the optical system will develop a quadratic phase term that has a curvature radius equivalent to the effective focal distance of the optical system, which is given by Eq. 2.5. The propagation of the wavefront from the exit pupil of the CRL to the image plane located at a focal length distance is equivalent to an optical 2D-Fourier transform of the system pupil function. The PSF of the optical system corresponds to the squared modulus of this Fourier transform, which is the wavefront intensity at the focal plane, considering a plane wave illumination [Goodman, 2017, *§2.3.1* & *§6.2*]. The phase of the propagated field at the focal position, the normalised PSF and relative intensities of the aberrated PSF normalised to the ideal case (Strehl ratio) are shown in Figs. 5.3-5.4(b-c) and (e); Fig. 5.5(b)-(d); Fig. 5.6(b-c) and (e); and Fig. 5.7(d)-(e).

---

[4] cf. §1.2.3 - *Optical coherence*.

[5] Although commonly approximated by Gaussian distributions, undulator emission does not possess Gaussian distribution not even at resonance. Please, refer to footnote 14 in §1.1.2 - *High brilliance X-ray sources* for a deeper discussion on the emission profile of undulator radiation and for further references.

Tab. 5.2.: Comparison of the Strehl ratio for the simulated models in Figs. 5.3-5.7

	lens model	σ_z (μm)	S_a (Eq. 2.15)	S_b (Eq. 2.16)	S_c (Eq. 2.17)	$S_\text{ratio coh.}$	$S_\text{ratio part.-coh.}$
Fig. 5.3	L01-L10	4.84	0.067	0.285	0.393	0.394	0.409
	stack 01	5.75	-	0.054	0.215	0.374	0.375
Fig. 5.4	L11-L20	6.28	-	0.007	0.160	0.185	0.211
	stack 02	6.48	-	0.001	0.142	0.243	0.247
Fig. 5.5	L01	0.57	0.985	0.985	0.985	0.981	-
	L01-L05	2.67	0.669	0.696	0.718	0.684	-
Fig. 5.6	LF L01-L10	4.36	0.116	0.311	0.413	0.335	0.359
	HF L01-L10	2.18	0.779	0.791	0.802	0.796	0.778

The calculated FWHM of the central lobe of the PSF for the simulated models presented in Figs. 5.3-5.7 are displayed on Table 5.1 and the respective Strehl ratio, compiled in Table 5.2.

5.3.2 The beam caustics

The beam characteristics at the image plane are very important and the PSF simulations in Figs. 5.3 to 5.7 show obvious differences between ideal and aberrated focusing of CRLs. It is necessary, however, to complement this with investigations of the effect of optical imperfections away from the focal position, especially because several experimental applications may use a defocused beam for obtaining a larger footprint. To get an overview of the beam evolution up- and downstream of the focal position, one can propagate the wavefront along the optical axis and for each position extract a cross-section of the beam. This will be referred to as the beam caustic[6]. The beam caustics are shown in Figs. 5.3-5.6(a); and Fig. 5.7(c). The beam cross-section for selected positions along the beam optical axis can be seen in Fig. 5.7(b). The vertical cuts were taken at $x = 0$. The zero position along the optical axis is given by the distance from the centre of the CRL to the image plane, position where the PSF is calculated. To calculate the beam caustics, the wavefront was propagated from 10 mm upstream of the focal position to 10 mm downstream in 4001 equally spaced steps along the optical axis.

5.4 Partially coherent simulations

The PSF and beam caustic simulations presented previously are both fully-coherent calculations. They present the focusing of a perfect plane wavefront to a diffraction-limited spot. This shows the intrinsic limitations of the optical system, but inherently neglects the effects of an extended and partially coherent source.

5.4.1 X-ray source

The emission of a single electron passing through an undulator (filament beam) is fully coherent. By changing the electron initial conditions (positions, direction and energy), propagating the emission of this electron through the beamline and adding up intensities, one can simulate

---

[6] Strictly speaking, the beam caustic is the envelope of light rays after passing through an optical element - see p. 60 [Lawrence, 1972]. A more comprehensive theory of caustics in optics is given by [Kravstov and Orlov, 1999; Nye, 1999].

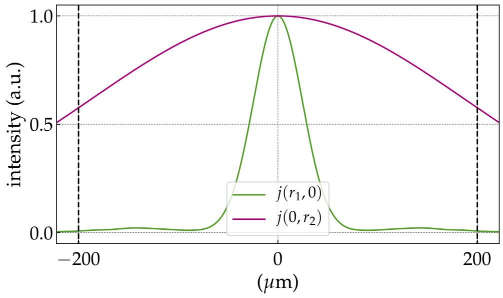

Fig. 5.2.: Horizontal ($j(\mathbf{r}_1, 0)$) and vertical ($j(0, \mathbf{r}_2)$) cuts of the complex degree of coherence function immediately before the CRL - see §5.4.1 - *X-ray source*. The vertical dashed lines indicate the geometric aperture used for the simulations.

partially coherent radiation if the electron beam phase space (5D) is sufficiently sampled as discussed in §1.3.3 - *Partially coherent simulations* - see also [Chubar et al., 2011].

For this section, a hypothetical beamline operating on the new Extremely Brilliant Source (ESRF-EBS) magnetic lattice [Dimper et al., 2014] is implemented. This beamline is shown in Fig.5.1. The beamline sits on a straight section and has a CPMU18 undulator as an insertion device. The undulator was tuned to its first harmonic at 8 keV for all simulations. The photon source size is $\sim 71.9 \times 12.4\ \mu\mathrm{m}^2$ and its divergence $\sim 17.7 \times 14.7\ \mu\mathrm{rad}^2$ (FWHM, horizontal vs. vertical). The first optical element was placed 60 m downstream of the centre of the undulator to ensure a beam footprint larger than the geometric aperture of the CRL being studied ($A_{\varnothing} \sim 440\ \mu$m) and a constant intensity over it. The transverse coherence length $\Delta_{\mathbf{cl}_\perp}$ at the entrance of the optical system is estimated to be $\sim 60 \times 448\ \mu\mathrm{m}^2$ (FWHM, horizontal vs. vertical), from the calculation of the complex degree of spatial coherence[7] $j(\mathbf{r}_1, \mathbf{r}_2)$ - see Fig. 5.2. This difference between the horizontal and vertical transverse coherence length is a direct consequence of the photon-source size asymmetry and the van-Cittert-Zernike theorem [Geloni et al., 2008, *§4*]. If there is no spatial filtering, the horizontal direction is less coherent than in the vertical, leading to stronger blurring of the image in the less coherent direction [Goodman, 2017, *§7.5*].

On the convergence of the simulations

In a conservative approach, the partially coherent simulations presented here were done using 10^4 wavefronts to ensure convergence. The convergence of the partially-coherent simulations is connected to the sampling of the electron distribution $f(s, s', \gamma_e)$, where each electron in a bunch has a different initial condition in terms of position $s = (x_e, y_e, z_e = 0)$, direction $s' = (x'_e, y'_e)$ and energy γ_e - see *Physical-optics-based methods* in §1.3.3 - *Partially coherent simulations*. Commonly used criteria for evaluating the quality of the sampling of the electron distribution are *i*-) smooth and homogeneous illumination at the aperture of the first optical element; *ii*-) the beamline overall transmission; and *iii*-) the smoothness of the beam profile at the end of the optical system prior to taking into account optical imperfections [Sanchez del Rio et al., 2019].

---

[7] see *Spatial coherence* in §1.2.3 - *Optical coherence*.

5.4.2 Beam characteristics at the focal position

The image of the extended X-ray source is similar to the convolution between the geometrically demagnified image of the source and the 2D-PSF of the imaging system, provided the beam is not strongly cropped anywhere in the beamline being simulated. For the cases being studied here, the beam footprint at the entrance pupil of the CRL system is several times larger than the geometric aperture of a single lens and this convolution approach is not valid, hence the necessity of the partially-coherent simulations for imaging the source in the centre of the CPMU18. Figures 5.3-5.4(e), Fig. 5.6(e) and Fig. 5.7(f) show the normalised demagnified image of the undulator photon source while Table 5.1 presents the horizontal and vertical FWHM for those simulations. Figures 5.3-5.4(f) and Fig. 5.6(f) show graphical representation of the intensity profiles of the different focusing conditions on a normalised scale where the ideal diffraction-limited focusing peak intensity is 1. Consequently, the peak intensities of the other profiles give the Strehl irradiance ratios for the corresponding configuration. These values are compiled in Table 5.2.

5.4.3 Beam profile evolution along the optical axis

Calculating the full beam caustic with partially-coherent simulations is impractical using current simulation methods and computers/clusters especially if: *i*-) the beamline does not present a very high degree of coherence, thus requiring a very large number of wavefronts to accurately simulate the partial-coherence; *ii*-) the beamline has a low transmission (strong beam cropping, diffraction orders outside apertures); or *iii*-) the sampling along the optical axis is high. Still, many applications require to operate up- or downstream of the focal position and assessing the beam quality on such positions is essential. Figure 5.7(a) shows the beam profile evolution spanning 20 mm along the optical axis for selected positions up- and downstream the image plane. Images are displayed showing their relative intensity to the beam in the focal plane. The positions chosen were the same as in Fig. 5.7(b), selected cuts along the beam caustics, so direct comparison between fully- and partially-coherent simulations can be done.

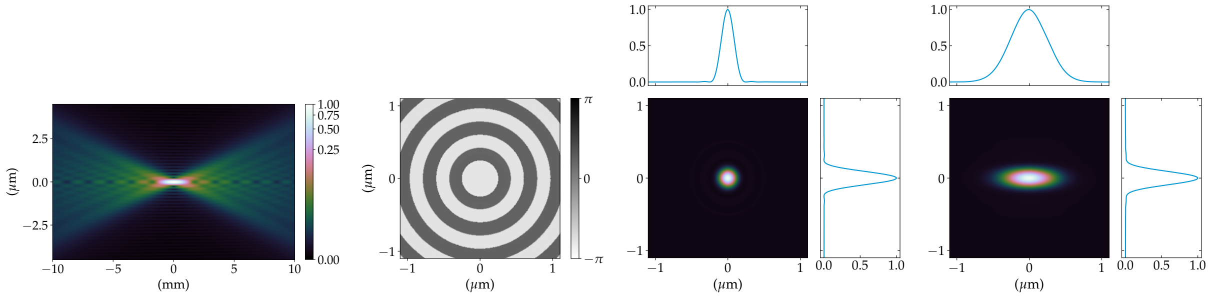

(a) vertical caustics (b) PSF phase (rad) (c) PSF intensity (d) source image

ideal stacked lenses

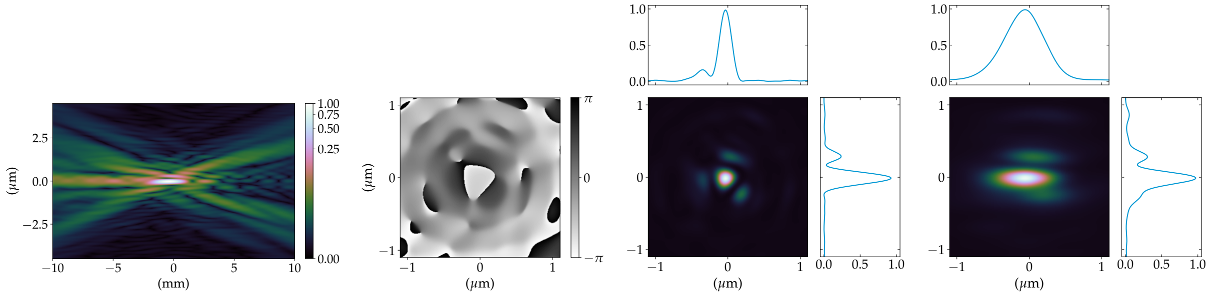

(a) vertical caustics (b) PSF phase (rad) (c) PSF intensity (d) source image

artificially stacked lenses L01-L10

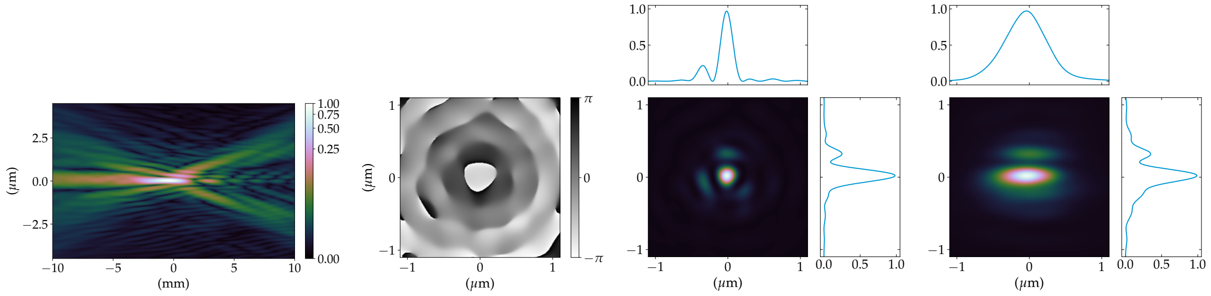

(a) vertical caustics (b) PSF phase (rad) (c) PSF intensity (d) source image

stack 1

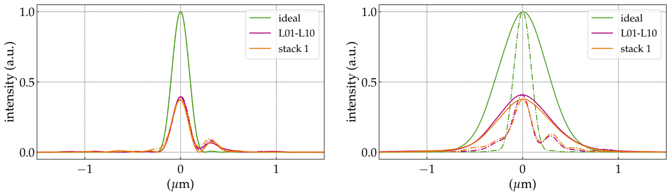

(e) fully-coherent (f) partially-coherent

normalised intensity profile cuts

Fig. 5.3.: Comparison between individually-measured lenses L01-L10 against the stack metrology of the same lenses. **top row**: ideal CRL, **upper middle row**: L01-L10 artificially stacked lenses measured individually. **lower middle row**: lenses measured as a stack. **bottom row**: horizontal (solid lines) and vertical (dashed lines) intensity cuts for coherent- and partially-coherent simulations. The simulated CRLs are composed of 10 2D-beryllium lens with nominal radius $R = 50\ \mu$m, geometric aperture $A_{\varnothing} = 440\ \mu$m and $t_{\text{wall}} = 20\ \mu$m at 8 keV. The error profiles used are the measured ones shown in Fig. 4.14 and 4.15.

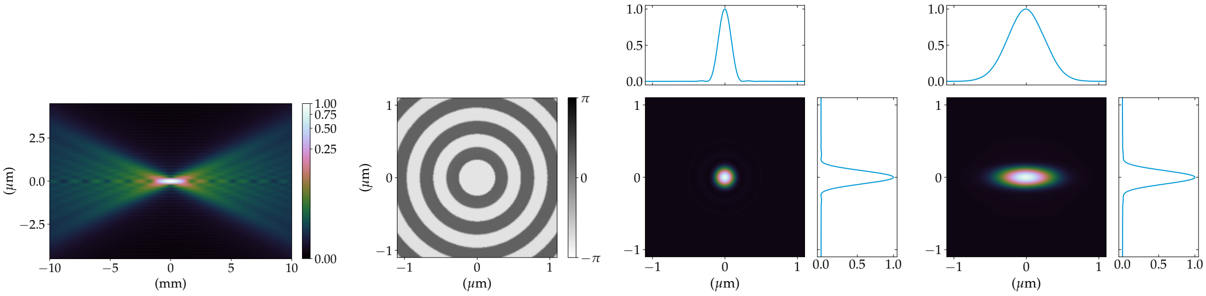

(a) vertical caustics (b) PSF phase (rad) (c) PSF intensity (d) source image

ideal stacked lenses

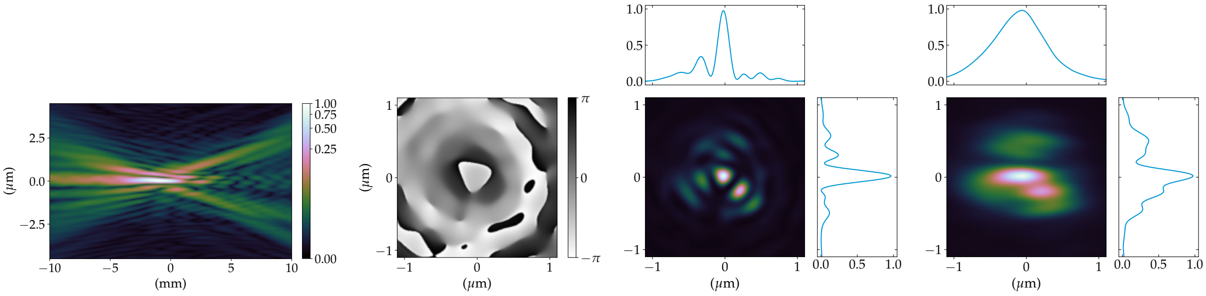

(a) vertical caustics (b) PSF phase (rad) (c) PSF intensity (d) source image

artificially stacked lenses L11-L20

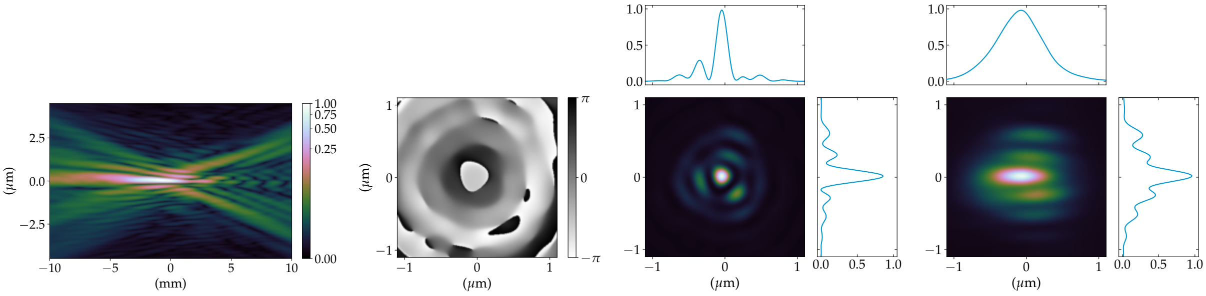

(a) vertical caustics (b) PSF phase (rad) (c) PSF intensity (d) source image

stack 2

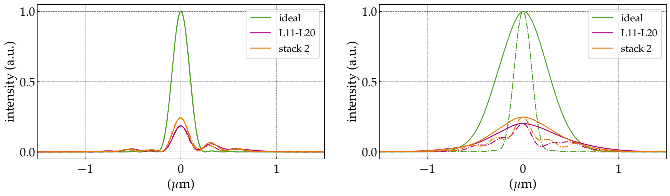

(e) fully-coherent (f) partially-coherent

normalised intensity profile cuts

Fig. 5.4.: Comparison between individually-measured lenses L11-L20 against the stack metrology of the same lenses. **top row**: ideal CRL, **upper middle row**: L11-L20 artificially stacked lenses measured individually. **lower middle row**: lenses measured as a stack. **bottom row**: horizontal (solid lines) and vertical (dashed lines) intensity cuts for coherent- and partially-coherent simulations. The simulated CRLs are composed of 10 2D-beryllium lens with nominal radius $R = 50$ μm, geometric aperture $A_{\varnothing} = 440$ μm and $t_{\text{wall}} = 20$ μm at 8 keV. The error profiles used are the measured ones shown in Fig. 4.16 and 4.17.

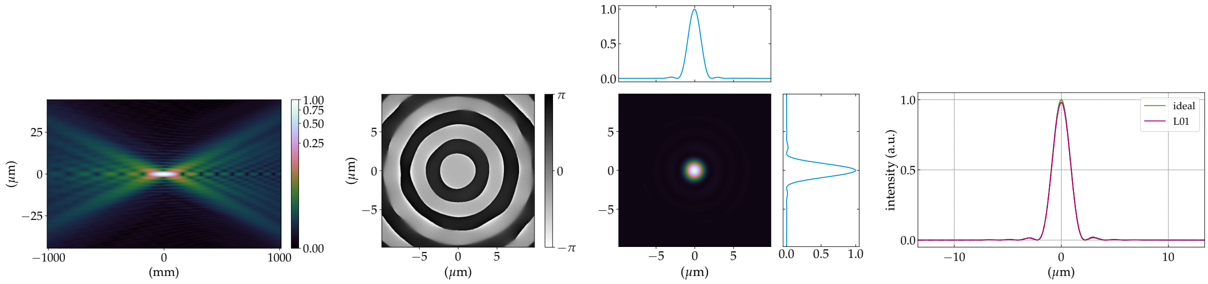

(a) vertical caustics (b) PSF phase (rad) (c) PSF intensity (d) normalised intensity profile cuts

L01

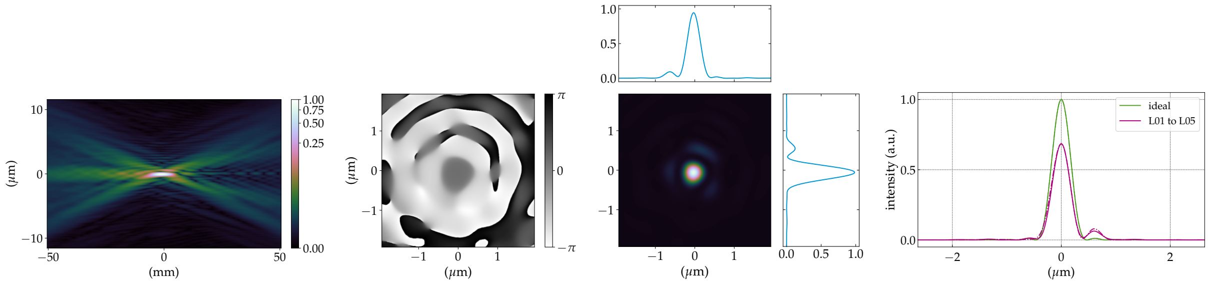

(a) vertical caustics (b) PSF phase (rad) (c) PSF intensity (d) normalised intensity profile cuts

L01 to L05 stack

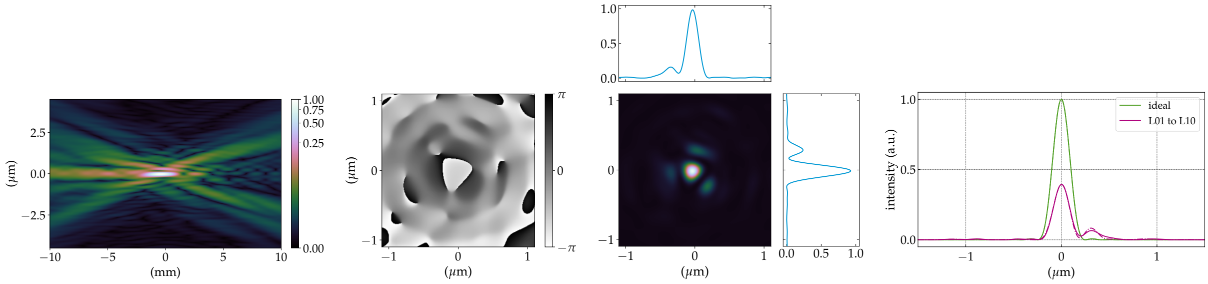

(a) vertical caustics (b) PSF phase (rad) (c) PSF intensity (d) normalised intensity profile cuts

L01 to L10 stack

Fig. 5.5.: Effects of artificially stacking individually measured lenses. **top row**: single L01 lens performance). **middle row**: L01-L05 artificially stacked lenses. **bottom row** L01-L10 artificially stacked lenses. The simulated CRLs are composed of 2D-beryllium lens with nominal radius $R = 50\ \mu$m, geometric aperture $A_{\varnothing} = 440\ \mu$m and $t_{\text{wall}} = 20\ \mu$m at 8 keV.

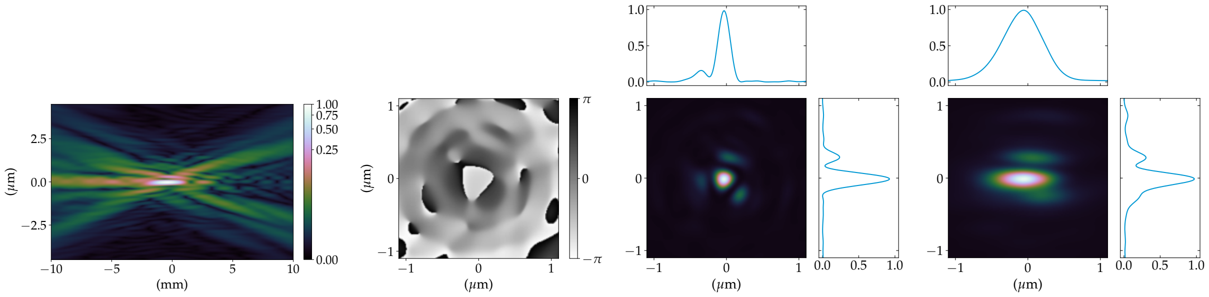

(a) vertical caustics (b) PSF phase (rad) (c) PSF intensity (d) source image

figure errors

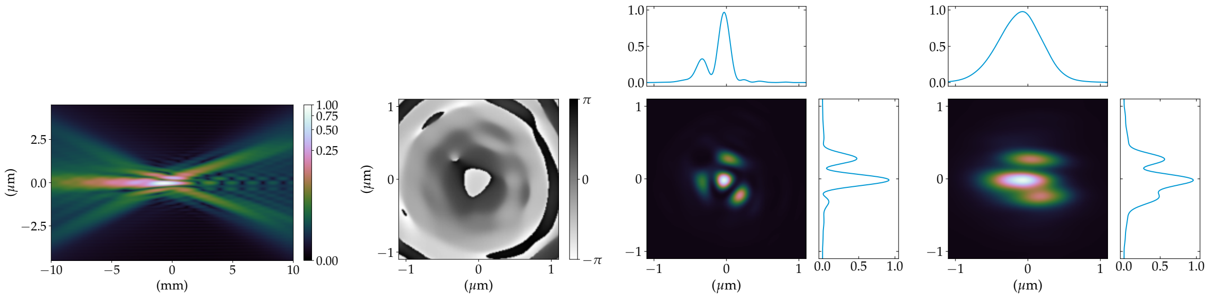

(a) vertical caustics (b) PSF phase (rad) (c) PSF intensity (d) source image

polynomial fit profile

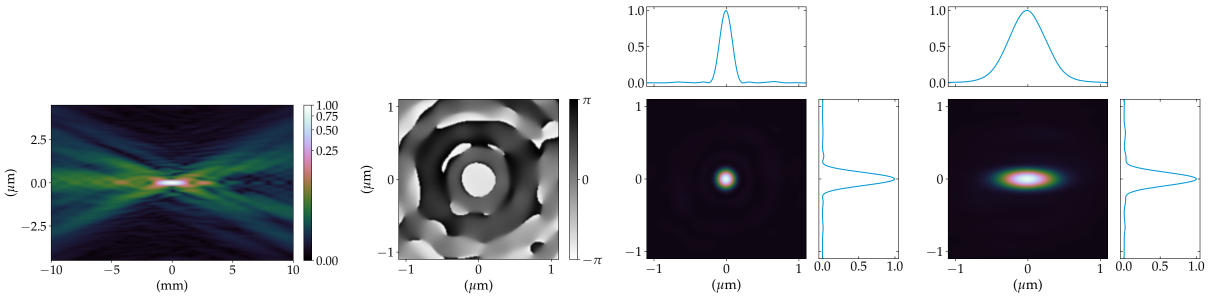

(a) vertical caustics (b) PSF phase (rad) (c) PSF intensity (d) source image

residue profile

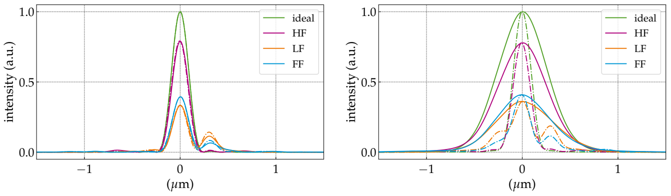

(e) fully-coherent (f) partially-coherent

normalised intensity profile cuts

Fig. 5.6.: Effects of different spatial frequencies ranges on a X-ray beam. **top row**: full accumulated profile of individually measured and artificially measured L01-L10 lenses. **second row**: Zernike circle polynomial reconstruction of the accumulated profile. **third row**: residual profile from the fit added to ideal lenses. **bottom row**:(−) horizontal (solid lines) and vertical (dashed lines) intensity cuts for coherent- and partially-coherent simulations. The simulated CRLs are composed of 10 2D-beryllium lens with nominal radius $R = 50\ \mu$m, geometric aperture $A_{\varnothing} = 440\ \mu$m and $t_{\text{wall}} = 20\ \mu$m at 8 keV. The error profiles used are shown in Fig. 4.14.

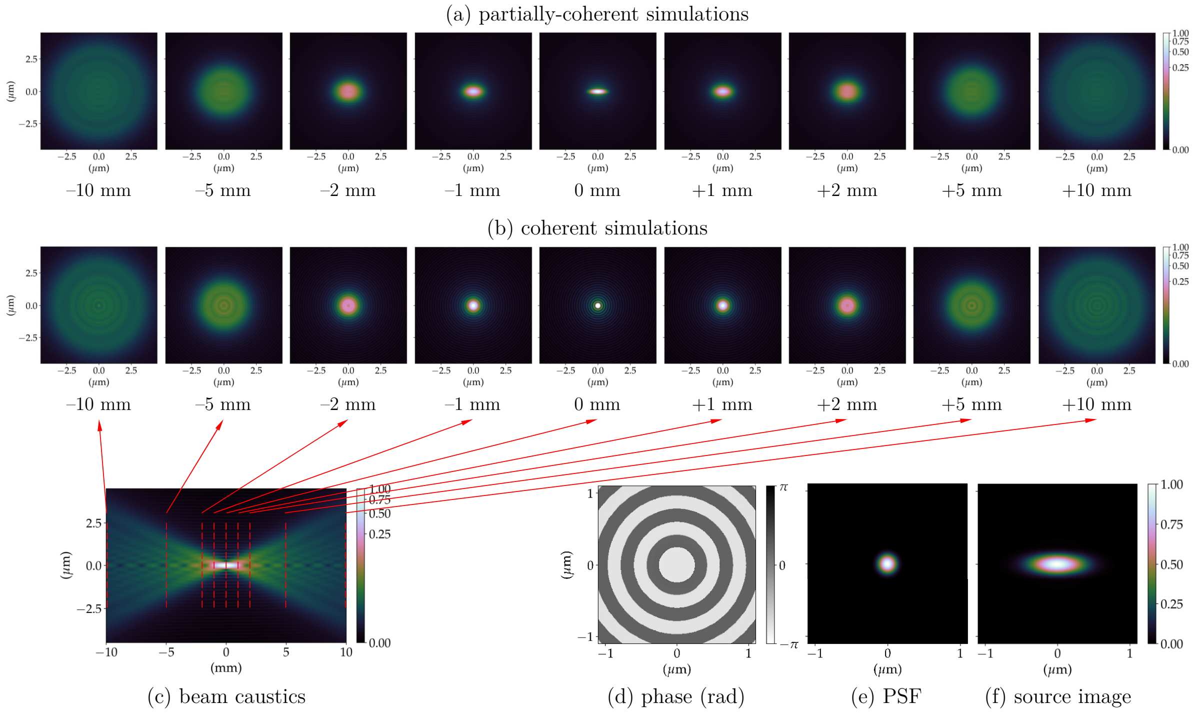

(a) partially-coherent simulations

(b) coherent simulations

(c) beam caustics (d) phase (rad) (e) PSF (f) source image

ideal lenses

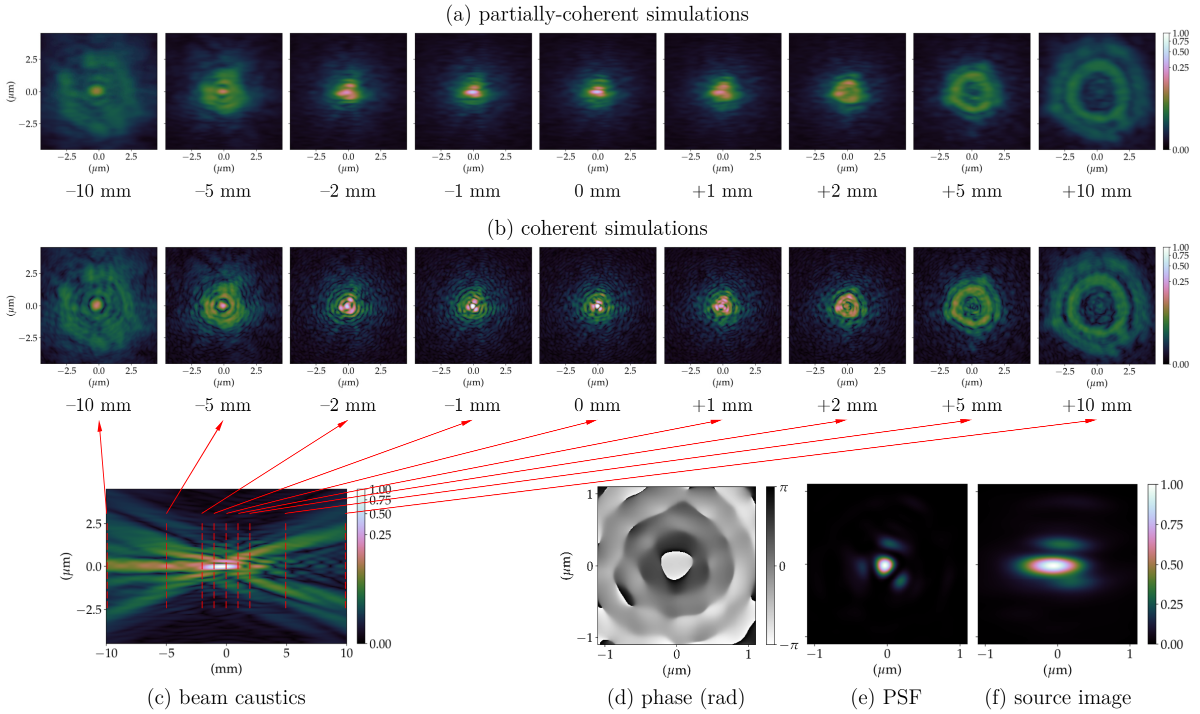

(a) partially-coherent simulations

(b) coherent simulations

(c) beam caustics (d) phase (rad) (e) PSF (f) source image

L01 to L10 stack

Fig. 5.7.: Lens stack formed by individually measured lenses L01-L10 studied under fully- and partially-coherent illumination. (a) partially-coherent simulations show the beam profile up- and downstream the focal position averaging 10^4 wavefronts to simulate the radiation emitted by an undulator; (b) the coherent simulations show the beam profile of a plane wavefront being focused; (c) beam propagation near the focal position (beam caustics) for a fully coherent beam (horizontal cut around $y = 0$); (d) phase and (e) intensity of the PSF calculated focusing a plane-wavefront; (f) demagnified image of the undulator photon-source (extended source). The simulated CRLs are composed of 10 2D-beryllium lens with nominal radius $R = 50\ \mu$m, geometric aperture $A_{\varnothing} = 440\ \mu$m and $t_{\text{wall}} = 20\ \mu$m at 8 keV. The error profiles used are shown in Fig. 4.14.

5.5 Discussion

The main results drawn from the simulations presented previously are discussed in this section. Firstly, some considerations on the effect of optical imperfections on a (partially) coherent X-ray beam are drawn. The merit of using the Strehl ratio for X-ray lens tolerancing is also discussed. Finally, some comments on the simulation times are presented.

5.5.1 Metrology of individual lenses vs. stacked lenses

The metrology of single lenses and that of lens stacks was already discussed in §4.2 - *X-ray lens metrology*. The qualitative agreement between the obtained profiles from the measurement of a lens stack and the individually measured and artificially stacked lenses is shown in Figs. 4.14-4.17 and Tables 4.1 and 4.2. This qualitative agreement is confirmed by the simulations as shown in Figs. 5.3 and 5.4. Both sets of simulations, that is L01-L10 vs. stack 1 and L11-L20 vs. stack 2, show good agreement for the beam caustic, PSF and source image. The lenses L11-L20 and stack 2 show a lower degree of similarity in the partially-coherent simulation as shown in Fig. 5.4(d). This can be attributed to the differences in the relative alignment of the lenses in the stack versus the lens holder in the individual measurements when performing the lenses metrology and subsequent software stacking. Figure 5.8 shows the Strehl ratio for both coherent and partially-coherent simulations for both stacks. The coherent Strehl ratio shows very good agreement in terms of beam profile for both sets, despite the difference in intensity for the L11-L20 simulations. The L01-L10 simulations preserve the agreement on the partially-coherent simulations, but the L11-L20 set shows more difference between the individually measured lenses and the stack - see also Fig. 5.4(d), but the general beam profile is maintained. When comparing the results in Fig. 5.8 with the predicted Strehl ratios in Table 5.2, a large discrepancy between the simulations of the L01-L10 lenses (individually measured and stack) is observed. It is predicted that the simulations using the metrology data from the lens stack (as opposed to the individually measured lenses) would have a much lower intensity due to a higher figure error value across the pupil, which is not observed. Although a deeper discussion on the Strehl ratio is presented in §5.5.3 - *The Strehl ratio for X-ray lenses*, it is worth noting that the probable cause for this comes from the fact that the Strehl ratio predictions from Eqs. 2.15-2.17 were applied without weighing the errors with the beam transmission for this system - see Fig. 2.5. The stack measurement has a smaller effective aperture due to the absorption and phase-contrast effects. The values of the figure errors towards the edge of the effective aperture are large and tend to be misrepresented when providing a single metric such as an RMS value for the figure error σ_z over the full aperture. This, however, does not seem to be the case for the lens stack 2.

The effect on the resulting aberrations of stacking X-ray lenses has been modelled and discussed in depth by [Osterhoff et al., 2017]. The progressive increase in the resulting figure errors from artificially stacked lenses is shown in Fig. 5.9, which shows the evolution of the (a) full figure errors, (b) the polynomial fit of the full profile and (c) the residuals when stacking lenses. The simulations in Fig. 5.5 show the progressive deterioration of an X-ray beam by adding the figure errors to the simulations by showing three scenarios: a single lens, five lenses and ten lenses, representing a low-, a moderate- and a high-aberrated system. This sensitivity study is only possible because the metrology of individual lenses is available. Using the metrology of

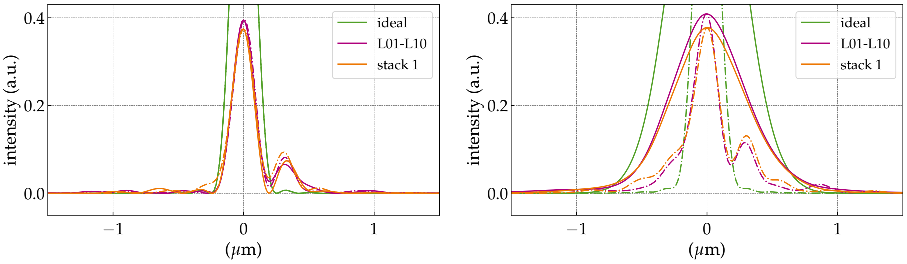

(a) fully-coherent (b) partially-coherent

L01-L10 vs. stack 1

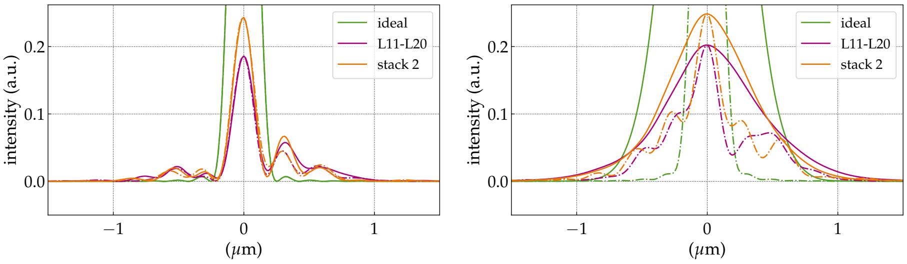

(c) fully-coherent (d) partially-coherent

L11-L20 vs. stack 2

Fig. 5.8.: Horizontal (solid lines) and vertical (dashed lines) intensity cuts for coherent- and partially-coherent simulations for the profiles in Figs. 4.14-4.15 (**top row**) and the for the profiles in Figs. 4.16 and 4.17 (**bottom row**) at 8 keV.

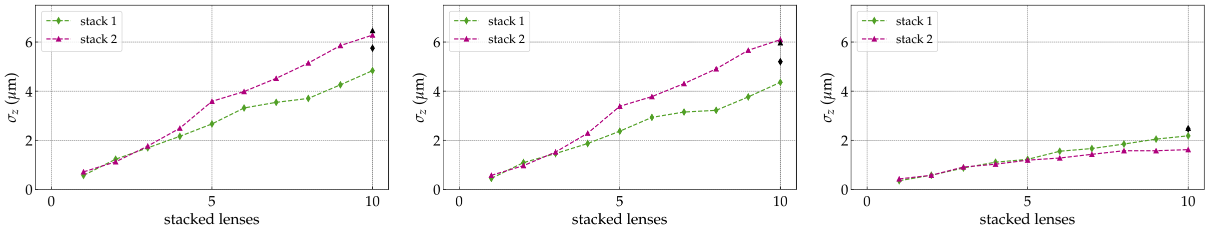

(a) full profile (b) polynomial fit (c) residues

Fig. 5.9.: Progressive increase of figure errors for the (a) full-, (b) fit- and (c) residual- profiles. The green-diamond shaped marker indicates the artificially stacked lenses from the stack 1, while the magenta triangles, the stack 2. The black markers indicate the corresponding measured stack. Figure errors calculated for a geometric aperture of $A_{\varnothing} = 400\ \mu$m.

a full-stack and scaling it would not adequately represent the system due to the existence of correlated- and uncorrelated figure errors as pointed out by [Osterhoff et al., 2017] and shown in Fig. 5.9.

5.5.2 The effect of optical imperfections

Applying the Maréchal criterion (Eq. 2.18) calculated for beryllium lenses illuminated at 8 keV requires the accumulated projected figure errors to be $\sigma_z \leq 2.08\ \mu$m. Tables 4.1 and 4.2 show that the accumulated thickness for both stacks is larger and that the optical system is operating far from ideal as the system exceeds the limit imposed by the Maréchal criterion. The decomposition of the figure error profiles into orthonormal polynomials and their resulting residuals is convenient because it allows investigating the effects of specific frequency ranges in the X-ray beam degradation. Following [Harvey et al., 1995], the figure errors of the lenses can be specified in terms of their spatial frequency, as they often have different effects on the image quality. Three regions are commonly used for that: low-, mid- and high-spatial-frequencies. The low-spatial frequencies (LF) are responsible for changing the beam profile and reducing the peak intensity. They are related to the conventional optical aberrations [Born et al., 1999, *§9.1-3*] and they can be described by a set of orthonormal polynomials, which has been described in §3.4.1 - *Orthornormal polynomials*. Mid- and high-spatial frequencies (HF) are responsible for scattering the light around the (focused) beam and have potential for broadening it, together with the expected reduction of the Strehl ratio. In this work, the mid- and high- frequencies are the residuals from the polynomial fit of the aberrated profile. The full profile comprises all spatial frequencies and is referred to as FF. From the analysis of the experimental data from 2D-beryllium lenses with nominal radius $R = 50\ \mu$m and geometric aperture $A_{\varnothing} = 440\ \mu$m, Zernike circle polynomials until the 37th order (3rd order spherical aberration) were used. Which causes the low-frequencies (LF) to span from $\sim 500\ \mu$m or 2×10^3 m^{-1} (geometrical aperture of a lenslet) to $\sim 50\ \mu$m or 2×10^4 m^{-1}, while the mid- and high-frequencies span from $\sim 50\ \mu$m or 2×10^4 m^{-1} to $\sim 0.5\ \mu$m or 2×10^6 m^{-1}, which is obtained from the Nyquist frequency of the measured data. Figure 5.6 shows the effects of different spatial frequencies ranges on an X-ray beam.

The addition of the mid- and high-spatial frequency errors to an ideal CRL model is related to scattering around the focused beam, contributing thus to increasing background and consequently reducing the peak intensity following [Harvey et al., 1995]. Using a linear scale, both the ideal PSF and the demagnified source image in Figs. 5.3(c)-(d) are almost indistinguishable from their aberrated counterparts in Figs. 5.6(c)-(d), which is because the accumulated figure error complies to the Maréchal criterion. As pointed out by [Cocco, 2015; Cocco and Spiga, 2019], a high Strehl ratio does not guarantee a homogeneous beam profile up- and downstream of the focal position. This is apparent in the beam caustic shown in Fig. 5.6. The profile shown in Fig. 4.15(c) is not random and presents some concentric rings. This comes from the tooling of the punches used in the hot-embossing process of the Be lens fabrication. A more diverse profile, such as the one shown in Fig. 5.10, which also comes from the metrology of real Be lenses artificially stacked, allows to simulate the effects of a random HF error profile in the beam shape and its contribution to the scattering of light outside the beam envelope defined by the ideal beam caustics - this is shown in Fig. 5.11. Comparing these simulations with the ones in Fig. 5.7 permits to say that the high-frequency errors lead to scattering of the beam and speckles, but generally, do not change the beam shape even away from the focal position.

When considering the low-spatial-frequency figure errors, however, the beam shape starts to change more drastically even at the focal position. The appearance of satellite peaks becomes pronounced in the PSF and the demagnified source image. The beam caustics start presenting an elongated tail-like structure upstream of the focal position and a ring-like structure downstream. The elongation of the beam along the optical axis and the presence of homogeneous concentric rings on the PSF are a classical signature of spherical aberration, which is a major component of the LF figure errors - cf. Z_{11} in Figs. 4.15(d)-4.16(d). The predominance of spherical aberration on 2D parabolic Be lenses has already been observed; see Fig. 6.14 of [Seiboth, 2016]. The PSF due to spherical aberration can be seen also in Figs. 8.5 and 8.6 from [Mahajan, 2011]. In the partially-coherent simulations, the satellite peaks around the main lobe seen at the PSF

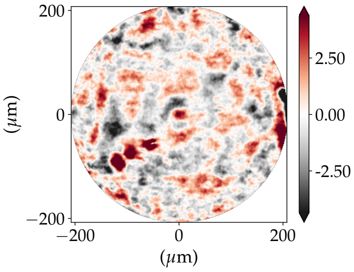

Fig. 5.10.: Artificially stacked high frequency error profile from 10 individually measure 2D-beryllium lens with nominal radius $R = 50$ μm, geometric aperture $A_{\varnothing} = 440$ μm and $t_{\text{wall}} = 20$ μm used in the simulations shown in Fig. 2.15 and Fig. 5.11. The profile has a $\sigma_z = 1.74$ μm and the colour bar scale is in μm.

simulations are stretched horizontally to the point that their visibility is maintained vertically, but horizontal cuts (Fig. 5.6(d)) show almost no trace of them, due to the reduction in transverse horizontal coherence (blurring effect). Small misalignments between the lenslets and some residual tilt from the LF errors contribute to a lateral displacement of the beam in the image plane. Using the full-frequency-range figure errors yields a combined effect that is analogous to the superposition of the HF and LF figure errors. The complete set of simulations of the lenses L01-L10 using the CRL-MS modelling given by Eq. 2.12 can be seen in Fig. 5.7. The diffraction effects from the aperture of the CRL are not easily observable because the system has an apodised Gaussian intensity at the exit pupil [Mahajan, 1986], but they contribute to the concentric ring structures seen on the ideal lenses simulation in Fig. 5.7. In terms of wavefront preservation, X-ray lenses are more susceptible to the low-frequency figure errors, as they are the ones that change the beam profile up- and downstream the focal position. Fortunately, the low frequencies are those that can be readily corrected by the fitting of corrective optics - which will be discussed in §6 - *Correcting optical imperfections in refractive lenses*.

The simulations shown in Figs. 5.3 to 5.7 paint a very consistent picture of the beam shape along the optical axis. Upstream of the image plane, a persistent central lobe is observed, albeit much less intense, with a high background around it thus reducing the signal to noise ratio. Downstream, the beam has a drop in intensity in the middle, looking like a doughnut when a cut transverse the optical axis is made. This behaviour is observed both on fully- and partially-coherent simulations and is more evident in the simulations shown in Fig. 5.7 (beam profiles). Such beam caustics have been extensively reported by experimental groups working under high coherent conditions, with similar optics and ptychographic reconstruction of X-ray beams - cf. Fig. 3 in [Schropp et al., 2013], Fig. 2 in [Seiboth et al., 2016], Fig. 3 in [Gasilov et al., 2017] and Fig. 4 in [Seiboth et al., 2020].

(a) partially-coherent simulations

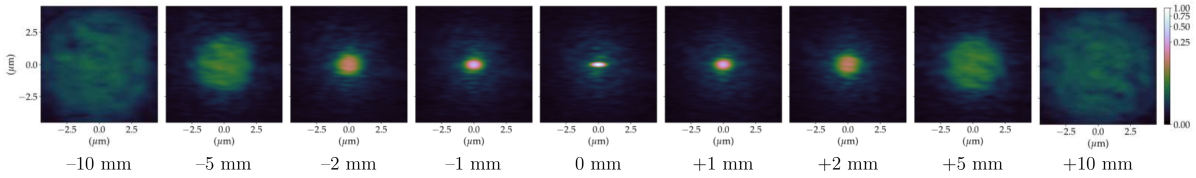

(b) coherent simulations

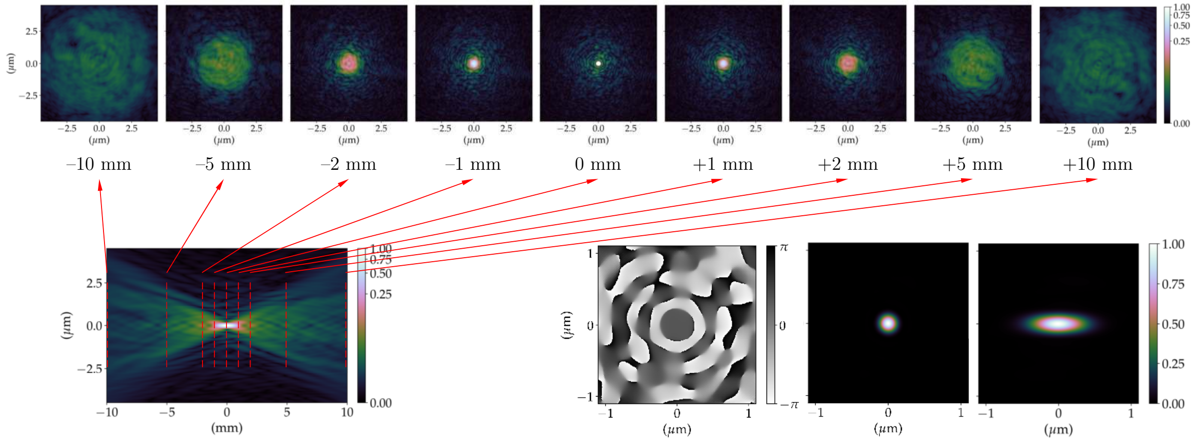

(c) beam caustics (d) phase (rad) (e) PSF (f) source image

Fig. 5.11.: High frequency error profile studied under fully- and partially-coherent illumination. (a) partially-coherent simulations show the beam profile up- and downstream the focal position averaging 10^4 wavefronts to simulate the radiation emitted by an undulator; (b) the coherent simulations show the beam profile of a plane wavefront being focused; (c) beam propagation near the focal position (beam caustics) for a fully coherent beam (horizontal cut around $y = 0$); (d) phase and (e) intensity of the PSF calculated focusing a plane-wavefront; (f) demagnified image of the undulator photon-source (extended source). The simulated CRLs are composed of 10 2D-beryllium lens with nominal radius $R = 50$ μm, geometric aperture $A_{\varnothing} = 440$ μm and $t_{\text{wall}} = 20$ μm at 8 keV. The error profile used is shown in Fig. 5.10.

5.5.3 The Strehl ratio for X-ray lenses

The Strehl ratio for the CRL models is presented in Table 5.2. In the numerical simulations, the intensity at the centre of the beam is normalised to the intensity obtained by the ideal model. What is generally observed is that for values lower than the Maréchal criterion (Eq. 2.18), the analytic equations Eqs. 2.15-2.17 show a good agreement and can be used to estimate the performance of an optical system close to the ideal performance. However, for moderate or strong values of aberrations the approximations used to derive those equations start to break down and other factors have to be taken into account, such as spatial distribution of the error profile and the transmission profile across the exit pupil. The values shown on Table 5.2 do not show a clear trend when it comes to the Strehl ratio and the RMS value of the figure error across the exit pupil of the system. In order to understand the numerically dependence of the Strehl ratio on the height error, each individual profile used to generate the profile shown in Fig. 5.10 was scaled by a constant value to allow for a scanning of the total projected figure error σ_z. The results in Figure 5.12 show the expected Strehl ratio as a function of the projected figure errors σ_z for different analytical approximations (Eqs. 2.15-2.17) and for the numerical calculations with a fully- and partially-coherent illumination - these numerical calculations are also shown in Fig. 5.13. All approaches show very good agreement up to $S_{\text{ratio}} > 0.8$, when they start diverging. The expressions for $S_{\text{ratio a}}$ (Eq. 2.15) and $S_{\text{ratio b}}$ (Eq. 2.16) can be considered as

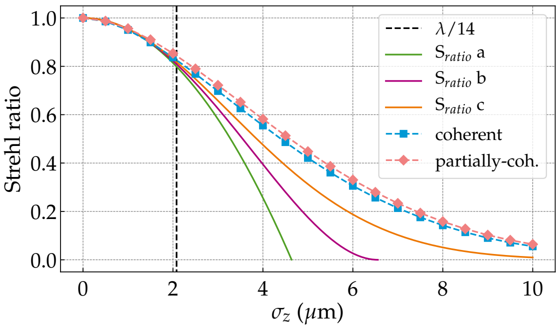

Fig. 5.12.: Strehl ratio from numerical simulations and from the application of different approximations (Eqs. 2.15-2.17) as a function of the figure error σ_z from a lens stack made of beryllium illuminated at 8 keV. The vertical dashed black line indicates the maximum tolerable thickness error (Eq. 2.19) for complying with the Maréchal criterion (Eq. 2.18), that is, $\sigma_{\lambda/14} \approx 2.08\ \mu$m.

approximations for $S_{\text{ratio c}}$ (Eq. 2.17), therefore are only expected to be valid over a restricted range (large S_{ratio}). A fit of the simulation data (coral rhombuses and blue squares in Fig. 5.12) give:

$$S_{\text{ratio coh.}} \approx \exp\big(-2.32\cdot 10^{10}\sigma_z^2 - 6.13\cdot 10^4\sigma_z + 2.54\cdot 10^{-2}\big), \tag{5.1a}$$

$$S_{\text{ratio part.-coh.}} \approx \exp\big(-2.28\cdot 10^{10}\sigma_z^2 - 5.07\cdot 10^4\sigma_z + 2.29\cdot 10^{-2}\big). \tag{5.1b}$$

Unfortunately, due to the nature of the projected figure errors (in the range of few micrometres r.m.s.), it is not possible to discard the non-quadratic terms. Equations 5.1 can be rewritten as:

$$S_{\text{ratio simulation}} \approx \exp\left[-\left(\frac{2\pi}{\lambda}\right)^2(\kappa_1\Delta\Phi)^2 - \frac{2\pi}{\lambda}\kappa_2\Delta\Phi - \kappa_3\right], \tag{5.2}$$

where κ are scaling constants that, in principle, depend on the number of elements, lens material, energy and, mostly importantly, the spatial distribution of the accumulated errors over the optical element aperture. For our particular examples, $\kappa_1 = 0.71$, $\kappa_2 = 0.28$ and $\kappa_3 = 2.54\cdot 10^{-2}$ for the coherent case and $\kappa_1 = 0.70$, $\kappa_2 = 0.24$ and $\kappa_3 = 2.29\cdot 10^{-2}$ for the partially-coherent case. When comparing Eq. 5.2 with Eq. 2.17, a $\kappa < 1$ suggests that there is some weighting of the phase errors reducing their effect, but simply multiplying the accumulated thickness errors (cf. Figs. 4.15-4.16) with the normalised optical system transmission (cf. Fig. 2.5) does not allow prediction of κ and this is still as an open question at the time of writing, which strengths the case for the simulation framework developed for this thesis.

5.5.4 Simulation time

Increasing the complexity of the simulation model comes at the expense of increasing the overall simulation time, but as long as the transverse wavefront sampling is maintained, memory consumption is not affected from one model to another. The time increase in the simulations is mainly due to: *i*) increase in the number of drift spaces and the number of optical elements; *ii*) from reading the densely sampled metrology data. Table 5.3 presents the typical simulation times for this work. Those are particularly high because the transverse sampling of the wavefronts is several times larger than the nominal minimal sampling necessary to mitigate artefacts or under-resolved features on the wavefront. Employing 10^4 wavefronts for the partially coherent

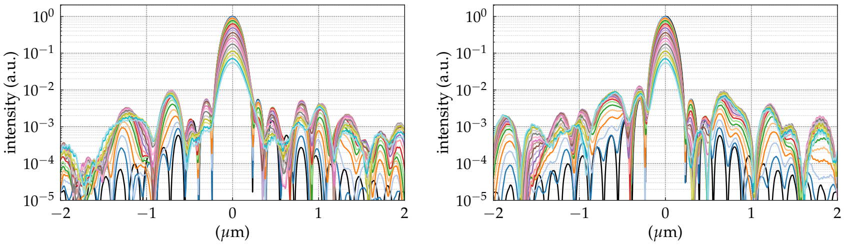

(a) horizontal cut (b) vertical cut

coherent simulations

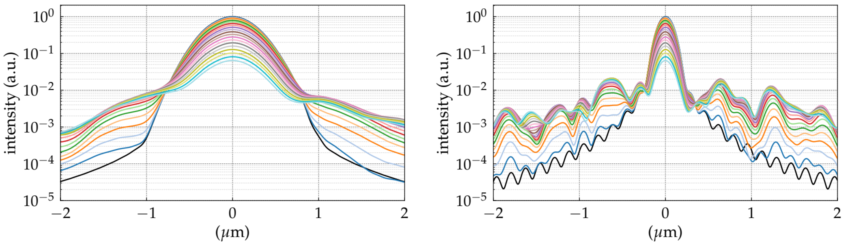

(c) horizontal cut (d) vertical cut

partially-coherent simulations

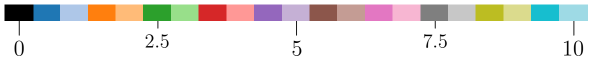

(e) figure error (μm)

Fig. 5.13.: Intensity cuts as a function of the figure error σ_z from a lens stack made of beryllium illuminated at 8 keV. The accumulated profile used presents predominantly the high-frequency content and is shown in Fig. 5.10. The associated Strehl ratio are shown in Fig. 5.12. This spatial frequency range is related to scattering around the focused beam, contributing thus to increased background and consequently reducing the peak intensity.

simulations is also exaggerated but was done to ensure that any changes on the simulation come from the change of model being studied and not from statistical nature of the sampling of the electron-beam phase-space. The simulation times presented on Table 5.3 can be certainly be reduced without loss of accuracy by adopting a more sensible sampling. ■

Tab. 5.3.: Summary of the simulation times for different CRL models. From the most simple one (single lens equivalent) up to the more complex multi-slicing (MS) with figure errors. Simulations were performed on a Intel(R) Xeon(R) CPU E5-2680 v4 @ 2.40GHz cluster at the ESRF. Partially coherent calculations were done using 28 cores in parallel.

model	**fully coherent**	**partially coherent**	**caustics**
single lens equivalent (Eq. 2.10)	33 s	2 h 44 min	1 h 32 min
multi-slicing (Eq. 2.11)	58 s	5 h 12 min	1 h 33 min
MS + figure errors (Eq. 2.12)	2 min 48 s	5 h 42 min	1 h 35 min
	(1 wavefront)	(10^4 wavefronts)	(4001 pts.)

References

Born, M., Wolf, E., Bhatia, A. B., Clemmow, P. C., Gabor, D., Stokes, A. R., Taylor, A. M., Wayman, P. A., and Wilcock, W. L. (1999). *Principles of Optics: Electromagnetic Theory of Propagation, Interference and Diffraction of Light*. Seventh edition. Cambridge University Press.

Chubar, O., Elleaume, P., and Snigirev, A. (1999). “Phase analysis and focusing of synchrotron radiation”. In: *Nuclear Instruments and Methods in Physics Research, Section A: Accelerators, Spectrometers, Detectors and Associated Equipment* **435**.3, p. 495.

— (2001). “Phase corrections for synchrotron radiation”. In: *Nuclear Instruments and Methods in Physics Research, Section A: Accelerators, Spectrometers, Detectors and Associated Equipment* **467-468**, p. 932.

Chubar, O., Berman, L., Chu, Y. S., Fluerasu, A., Hulbert, S., Idir, M., Kaznatcheev, K., Shapiro, D., Shen, Q., and Baltser, J. (2011). “Development of partially-coherent wavefront propagation simulation methods for 3rd and 4th generation synchrotron radiation sources”. In: *Proc. SPIE 8141, Advances in Computational Methods for X-Ray Optics II*, p. 814107.

Chubar, O. and Celestre, R. (2019). “Memory and CPU efficient computation of the Fresnel free-space propagator in Fourier optics simulations”. In: *Optics Express* **27**.20, p. 28750.

Chubar, O. and Elleaume, P. (1998). “Accurate And Efficient Computation Of Synchrotron Radiation In The Near Field Region”. In: *Proceedings of the European Particle Accelerator Conference (EPAC 98)*, p. 1177.

Cocco, D. (2015). “Recent Developments in UV Optics for Ultra-Short, Ultra-Intense Coherent Light Sources”. In: *Photonics* **2**.1, p. 40.

Cocco, D. and Spiga, D. (2019). “Wavefront preserving optics for diffraction-limited storage rings and free-electron lasers”. In: *Proc. SPIE 11111: X-Ray Lasers and Coherent X-Ray Sources: Development and Applications XIII* **11111**, p. 37.

Dimper, R., Reichert, H., Raimondi, P., Sanchez Ortiz, L., Sette, F., and Susini, J. (2014). *ESRF Upragde programme phase II - The Orange Book*. ESRF, p. 75.

Gasilov, S., Rolo, T. d. S., Mittone, A., Polyakov, S., Terentyev, S., Farago, T., Blank, V., Bravin, A., and Baumbach, T. (2017). “Generalized pupil function of a compound X-ray refractive lens”. In: *Optics Express* **25**.21, p. 25090.

Geloni, G., Saldin, E., Schneidmiller, E., and Yurkov, M. (2008). “Transverse coherence properties of X-ray beams in third-generation synchrotron radiation sources”. In: *Nuclear Instruments and Methods in Physics Research Section A: Accelerators, Spectrometers, Detectors and Associated Equipment* **588**.3, p. 463.

Goodman, J. W. (2017). *Introduction to Fourier Optics*. Fourth edition. W. H. Freeman and Company.

Harvey, J. E., Lewotsky, K. L., and Kotha, A. (1995). “Effects of surface scatter on the optical performance of x-ray synchrotron beam-line mirrors”. In: *Appl. Opt.* **34**.16, p. 3024.

Kravstov, Y. and Orlov, Y. (1999). *Caustics, Catastrophes and Wave Fields*. Second edition. Springer-Verlag.

Lawrence, J. D. (1972). *A catalog of special plane curves*. First edition. Dover Publications.

Mahajan, V. N. (1986). “Uniform versus Gaussian beams: a comparison of the effects of diffraction, obscuration, and aberrations”. In: *Journal of the Optical Society of America A* **3**.4, p. 470.

— (2011). *Aberration Theory Made Simple*. Second. SPIE.

Nye, J. F. (1999). *Natural Focusing and Fine Structure of Light: Caustics and Wave Dislocations*. First edition. Institute of Physics Publishing.

Osterhoff, M., Detlefs, C., and Ferrero, C. (2017). “Aberrations in compound refractive lens systems: analytical and numerical calculations”. In: *Proc. SPIE 10388, Advances in Computational Methods for X-Ray Optics IV* 10388, p. 21.

Sanchez del Rio, M., Celestre, R., Glass, M., Pirro, G., Herrera, J. R., Barrett, R., Silva, J. C. da, Cloetens, P., Shi, X., and Rebuffi, L. (2019). “A hierarchical approach for modeling X-ray beamlines: application to a coherent beamline”. In: *Journal of Synchrotron Radiation* **26**.6, p. 1887.

Schropp, A., Hoppe, R., Meier, V., Patommel, J., Seiboth, F., Lee, H. J., Nagler, B., Galtier, E. C., Arnold, B., Zastrau, U., Hastings, J. B., Nilsson, D., Uhlén, F., Vogt, U., Hertz, H. M., and Schroer, C. G. (2013). “Full spatial characterization of a nanofocused X-ray free-electron laser beam by ptychographic imaging”. In: *Scientific Reports* **3**.1, p. 1.

Seiboth, F. (2016). “Refractive Hard X-ray Nanofocusing at Storage Ring and X-ray Free-Electron Lasers Sources”. PhD thesis. Fakultät für Mathematik, Informatik, und Naturwissenschaften, Fachbereich Physik, Universität Hamburg.

Seiboth, F., Brückner, D., Kahnt, M., Lyubomirskiy, M., Wittwer, F., Dzhigaev, D., Ullsperger, T., Nolte, S., Koch, F., David, C., Garrevoet, J., Falkenberg, G., and Schroer, C. G. (2020). “Hard X-ray wavefront correction via refractive phase plates made by additive and subtractive fabrication techniques”. In: *Journal of Synchrotron Radiation* **27**.5, p. 27.

Seiboth, F., Kahnt, M., Scholz, M., Seyrich, M., Wittwer, F., Garrevoet, J., Falkenberg, G., Schropp, A., and Schroer, C. G. (2016). “Quantitative characterization of aberrations in x-ray optics”. In: *Proc. SPIE 9963, Advances in X-Ray/EUV Optics and Components XI*, 99630P.

6

Correcting optical imperfections in refractive lenses

The interest and possibility of arbitrarily manipulating the X-ray wavefront has been teased since, at least, the early 2000s [Chubar et al., 1999, 2001]. It was not until the advent of extremely accurate additive and subtractive manufacturing techniques [Stöhr et al., 2015; M. Polikarpov, Kononenko, et al., 2016; Petrov et al., 2017; Roth et al., 2018; Sanli et al., 2018; Seiboth et al., 2019; Abrashitova et al., 2020; Antipov, 2020; Lin et al., 2020; Medvedskaya et al., 2020] that the demonstration of free-form X-ray refractive optics[1] was done [Sawhney et al., 2016; Seiboth et al., 2017; Laundy et al., 2019; Seiboth et al., 2020; Dhamgaye et al., 2020]. The possibility of producing very accurate free-form optics for the correction of optical aberrations has brought renewed interest in wavefront sensing [Berujon et al., 2015; Seaberg et al., 2019] and optical design simulations [Laundy et al., 2020]. This chapter presents the early results on correcting optical imperfections in refractive lenses obtained at the ESRF. The design and expected performance is based on the lenses presented in §4.2.1 - *Single lens measurements* and the simulations shown in Chapter 5 - *Effect of optical imperfections on an X-ray beam*.

6.1 Corrective optics

Correcting optical imperfections can be done by actively reshaping an optical element (adaptive optics) [Sutter et al., 2012; Alcock et al., 2013] or by inserting a static (passive) optical element specially fitted to compensate the deviations from a perfect profile or the wavefront error in relation to an idealised intensity [Donato et al., 2020] or phase profile. Phase manipulation for wavefront manipulation can be done with diffractive elements [Probst et al., 2020] or with refractive elements [Sawhney et al., 2016; Seiboth et al., 2017; Laundy et al., 2019; Seiboth et al., 2020; Dhamgaye et al., 2020]. As indicated by the vast literature, refractive optics is the most popular method for correcting phase errors in partially-coherent X-ray beams. This section presents the design of refractive optical correctors for refractive lens stacks.

6.1.1 Design

Formally, the computation of the phase correction[2] for any optical system is done by assuming that the wave-field will develop a specific phase $\phi_{\text{exit}}(x,y)$ distribution after passing through an arbitrary optical system. Perfect focusing of a wave-field to a point-source at a distance r from the exit pupil requires that the developed phase $\arg[U_{\text{exit}}(x,y)]$ to be that of a spherical-wave as in Eq. 1.17 [Chubar et al., 1999]. Given the typical geometric apertures

---

[1] Although not discussed here, significant work for producing novel wavefronts has also been done using diffractive optics. Please, refer to *Diffractive optics* in §2.1.1 - *X-ray focusing optics* for references to diffractive optics for wavefront manipulation.

[2] The design of optical correctors for synchrotron radiation was first described in [Chubar et al., 1999, *§2*], revisited in [Chubar et al., 2001] and first implemented for a 2D CRL in [Seiboth et al., 2017].

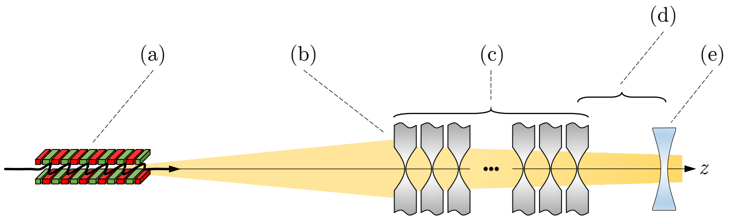

Fig. 6.1.: Schematic for residual phase extraction. (a) an arbitrary X-ray source delivers a (b) wave-field $U_{\text{illum.}}(x,y)$ immediately before the (c) optical system being studied. The wave-field exits the optical system and can be propagated a (d) distance $\Delta_{z_{\text{pp}}}$ from the exit pupil. At this position, the (e) extraction of the ideal phase from $U_{\text{exit}}(x,y)$ is done according to Eq. 6.2.

and focal distances of a CRL composed of a few individual lenses[3], it is possible to use the phase of the paraxial approximation of Eq. 1.17, that is, the parabolic-phase of the wavefront in Eq. 1.18. If the wavefront illuminating the optical system is given by $U_{\text{illum.}}(x,y)$, then, after passing through an aberrated lens system, $U_{\text{exit}}(x,y)$ is given by:

$$U_{\text{exit}}(x,y) = \mathcal{D}(\Delta_{z_{\text{pp}}}) \cdot \left[\mathrm{T}_{\text{CRL-MS}}(\Delta_z) \cdot U_{\text{illum.}}(x,y)\right], \tag{6.1}$$

where $\mathcal{D}(\Delta_{z_{\text{pp}}})$ is a free-space propagation from the exit pupil of the optical system to the position along the optical axis where the phase correction is performed (Eq. 1.39) and $\mathrm{T}_{\text{CRL-MS}}(\Delta_z)$ is the operator description of a lens stack given by Eq. 2.12. The phase shift necessary to correct such wavefront can be calculated as:

$$\phi_{\text{correction}}(x,y) = \arg\left[\frac{\exp\left(-ik\frac{x^2+y^2}{2z_f}\right)}{U_{\text{exit}}(x,y)}\right]. \tag{6.2}$$

Where z_f is the distance from the phase corrector to the image plane [Seiboth et al., 2017]. This phase extraction procedure is illustrated in Fig. 6.1. A phase corrector based on refractive optics can be calculated directly from the phase obtained in Eq. 6.2 and the transmission element in projection approximation phase-thickness relationship described by Eq. 1.36b:

$$\Delta_{\text{pp}}(x,y) = -\frac{\phi_{\text{correction}}(x,y)}{k\delta_{\text{pp}}(x,y)}. \tag{6.3}$$

Where $\Delta_{\text{pp}}(x,y)$ is the local phase plate thickness in projection approximation and δ_{pp} is the refraction index decrement of the material used for correcting $\phi_{\text{exit}}(x,y)$. The resulting correction plate described by Eq. 6.3 is directly proportional to the phase errors at each (x,y) coordinate pair. Typical error maps are shown in Figs. 3.9, 4.9, 4.14-4.17. Current micro- and nanofabrication techniques used for manufacturing X-ray optics are capable of reproducing such intricate shapes with high spatial and depth resolution, however the use of such correction plate in an experimental setup is rather impractical due to the several degrees of freedom concerned when aligning it against the aberrated optical system. Furthermore, it has been observed that 2D lenses produced by (hot) embossing are dominated by spherical aberration terms (primary, secondary, tertiary...) and other azimuathally symmetric errors due to intrinsic manufacturing processes [Schropp et al., 2013; Uhlén et al., 2014; Seiboth et al., 2016, 2017; Celestre et al.,

---

[3] Assuming that the focusing inside the CRL is negligible - cf. [Schroer and Lengeler, 2005] and [Seiboth et al., 2018, §6].

2020; Seiboth et al., 2020] - see also the Zernike polynomial bar plots (orange bars) in Figs. 3.9, 4.9, 4.14-4.17. Trading some of the correction accuracy for more practicality when employing the correction plate in a beamline, it is possible to obtain a correction profile by azimuthally averaging $\Delta_{\text{pp}}(x, y)$:

$$\Delta_{\text{pp}}(r) = \frac{\int\limits_0^{2\pi} \Delta_{\text{pp}}(r,\theta) r \mathrm{d}\theta}{\int\limits_0^{2\pi} r \mathrm{d}\theta}, \tag{6.4}$$

where $r = \sqrt{x^2 + y^2}$ and $\theta = \arctan{(y/x)}$ are the transformation from Cartesian to polar coordinates. The correction plate as calculated by Eqs. 6.3 and 6.4 is tailored for a specific set of lenses operating at a defined energy, due to the dispersion properties of δ_{pp}. Although true that a correction plate design is suited to a specific lens combination, for a moderate number of lenses where the focusing inside the CRL can be neglected, it has been demonstrated that the correction plate can be used over a range of energies around the design energy E_{design} as the index of refraction decrement δ is proportional to λ^2 [Seiboth et al., 2018, *§6*]. This can be done by shifting the plate along the optical axis closer or further away from the design position $\Delta_{z_{\text{pp}}}$ if the new operation energy is lower or higher than E_{design}. The same considerations on the beam chromaticity in *Chromatic aberrations* in §2.2.4 - *CRL performance* apply to the phase correctors.

Materials

It is natural to envision adopting the same materials used in X-ray lenses for the phase correctors. As for the lenses, the material used for the phase plate is intimately connected to the manufacturing process. Phase plates for optical correction have been produced using fused silica [Seiboth et al., 2017], diamond [M. Polikarpov, Kononenko, et al., 2016; Antipov, 2020] and sapphire [Lin et al., 2020], manufactured with laser ablation or ion-beam lithography [Medvedskaya et al., 2020] (subtractive manufacturing); and polymeric resists such as SU-8 (commonly used in LIGA [Nazmov et al., 2004] and other polymeric lenses [Stöhr et al., 2015]) and the proprietary IP-S used in additive manufacturing via two-photon polymerisation [Petrov et al., 2017; Sanli et al., 2018; Abrashitova et al., 2020; Lin et al., 2020].

6.1.2 Correction phase plate calculation

Applying the correction plate design methodology (Eqs. 6.1-6.4) to the individually measured and artificially stacked lenses L01-L10, which have been studied in depth - see Table. 4.1 and Figs. 4.14, 5.3 and 5.7; it is possible to recover a phase plate that will improve the performance of that particular optical system. An optical corrector to be used 10 mm downstream of the last lens of the stack, made of diamond and designed to operate at 8 keV is shown (cut) in Fig. 6.2. Due to the process described by Eq. 6.4, the profile of the corrective plate is smooth and does not have high spatial-frequency components. The obtained profile is similar to the ones reported in [Seiboth et al., 2017, 2018, 2020], which were obtained for stacks composed of similar lenses. The correction plate was designed using diamond due to its relatively large refractive index decrement δ_{C^*} at the expense of a higher absorption, good thermal and mechanical properties and volume homogeneity which translates into low X-ray small-angle scattering

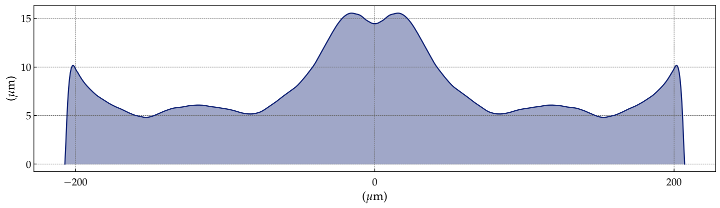

Fig. 6.2.: Profile cut of a diamond corrective plate for the lenses L01-L10 at 8 keV - cf. Fig. 4.14. The correction plate was calculated 10 mm downstream of the exit pupil of the CRL.

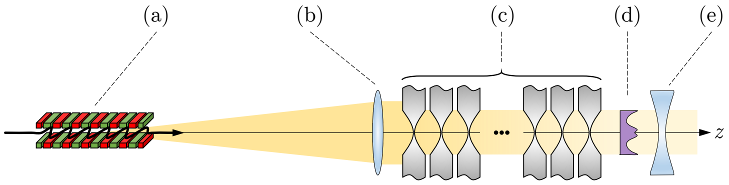

Fig. 6.3.: Schematic for residual thickness error calculation after phase correction. (a) shows an arbitrary X-ray source. An (b) ideal parabolic phase element is placed downstream the radiation source to give the illumination a plane phase. The stacked X-ray lenses are placed immediately downstream. Any changes to the wave-field after (c) can be directly attributed to the model under study. The phase plate is placed in (d) to correct the accumulated phase errors. An (e) ideal parabolic phase element with a radius of curvature matching the developed quadratic term is then added and the residues (phase errors) can be extracted.

when compared to beryllium lenses [Chubar et al., 2020]. These properties make diamond a very interesting material for (refractive) X-ray optics [M. Polikarpov, V. Polikarpov, et al., 2016; Shvyd'Ko et al., 2017].

Using the optical setup shown in Fig. 6.3, it is possible to recover the residual figure error profile after the correction plate, as shown in Fig. 6.4(a) and described in Table 6.1. The profiles in Fig. 6.4(b)-(c) are substantially changed from the Fig. 4.14(b)-(c). The polynomial fit in Fig. 6.4(b) has virtually no spherical aberration terms. The concentric rings from the pressing tool apparent in Fig. 4.14(c) are completely removed from the residual errors in Fig. 6.4(c). Figure 6.3(d) reinforces the observation of the reduction in the figure errors by the use of a azimuthally symmetric phase plate. The radially symmetric components (orange bars) in Fig. 6.3(d) are almost completely removed, while the purple bars remain almost unchanged. Finally, Fig. 6.3(e) shows a residual profile that is several times smaller than the one in Fig. 4.14(e).

Tab. 6.1.: Residual figure error profile r.m.s. value for L01-L10 (Fig. 4.14) and for the corrected system (Fig. 6.4).

	figure errors† (r.m.s) μm		
	full profile	pol. fit	residues
L01-L10:	4.84	4.36	2.18
L01-L10 + PP:	3.27	2.84	1.63

† values given for $A_\varnothing = 400\ \mu$m

Expected performance

By reproducing the simulations from §5.3 - *Fully coherent simulations* and §5.4 - *Partially coherent simulations* to the corrected optical system as shown in Fig. 6.5, it is possible to evaluate

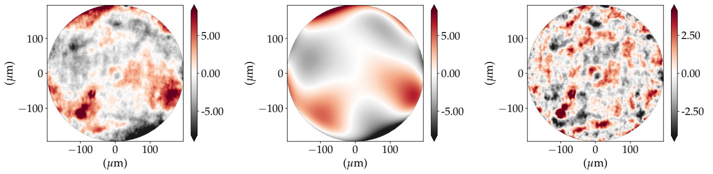

(a) full profile (b) polynomial fit (c) residues

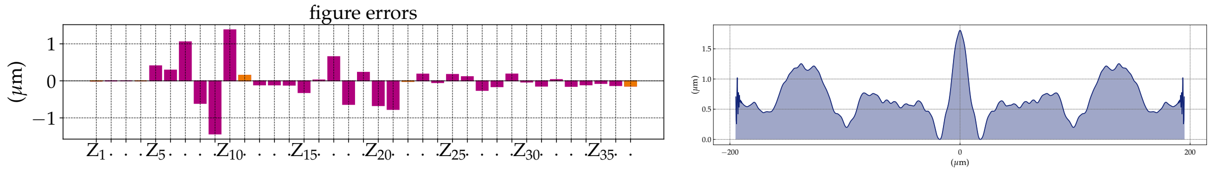

(d) polynomial decomposition (e) azimuthally averaged profile

Fig. 6.4.: Residual thickness error of the individually measured and artificially stacked lenses L01-L10 corrected with the diamond phase plate displayed in Fig. 6.2.

Tab. 6.2.: Comparison of the Strehl ratio for aberrated system composed of L01-L10 and the corrected system as shown in Fig. 6.7.

		σ_z (μm)	S_a (Eq. 2.15)	S_b (Eq. 2.16)	S_c (Eq. 2.17)	$S_\text{ratio coh.}$	$S_\text{ratio part.-coh.}$
Fig. 6.7	L01-L10	4.84	0.067	0.285	0.393	0.394	0.409
	L01-L10 + PP	3.27	0.503	0.545	0.608	0.595	0.671

the correction plate performance and predict its effect in a coherent- and partially-coherent X-ray beam. Figure 6.6 summarises the simulations and can be directly compared to Fig. 5.7 as it shows the beam profile at selected positions up- and downstream the focal plane for a (a) partially- and for a (b) coherent beam. The beam caustic is shown in Fig. 6.6(c), while the (d) phase and (e) amplitude of the PSF, as well as the (f) source image, are shown right next to it. A graphical representation of the Strehl ratio for the aberrated system and corrected system is shown in Fig. 6.7 for the coherent and partially-coherent cases.

Tolerancing[4]

The expected performance of the correction plate shown in Figs. 6.6 and 6.7 and compiled in the Tables 6.1 and 6.2 always assumes that the phase plate is perfectly centred in respect to the optical axis, at the designed distance Δ_{z_pp} from the CRL and that it presents no tilt in relation to the optical axis. However, when mounting the phase-plate in a real experimental setup, these are very difficult to reproduce. To understand and establish the precision to which the alignment has to be done, a series of scans is presented in Fig. 6.8, which shows the simulations of a (a) longitudinal, a (b) transverse and an angular scan of the phase plate around its nominal (designed) position. The transverse alignment is clearly very important. The longitudinal alignment is, to a lesser extent, also important. The plate shows a relative insensitivity to angular misalignments. Although Fig. 6.8 shows only coherent simulations, it is believed that the results can be applied to a moderately partially-coherent X-ray beam without great loss.

---

[4] This section came to be after some discussions with Andreas Schropp and Frank Seiboth (DESY, Germany) on the phase plate sensitivity to the alignment precision.

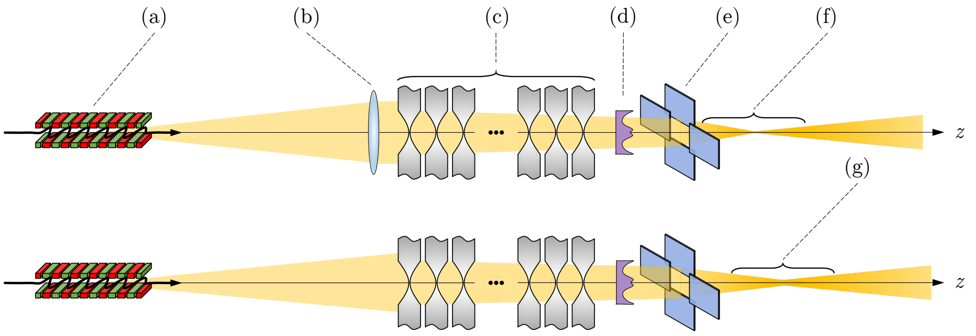

Fig. 6.5.: **top row**: beamline used for §5.3 - *Fully coherent simulations*. **bottom row**: beamline used for §5.4 - *Partially coherent simulations*. (a) shows the X-ray source. An (b) ideal parabolic phase element is placed downstream the radiation source to give the illumination plane phase. This ideal element is only present for the fully-coherent simulations. The lenses being studied are shown in (c), which are followed by the (d) the correction plate. A set of (e) slits to ensure the same geometric aperture for all simulations. For the fully-coherent simulations, the beam-caustic range is shown in (f) and the PSF is calculated at the centre of it. For the partially-coherent simulations, the beam profile evolution along the optical axis is shown in (g) and the beam characteristics at the focal position are calculated at its centre.

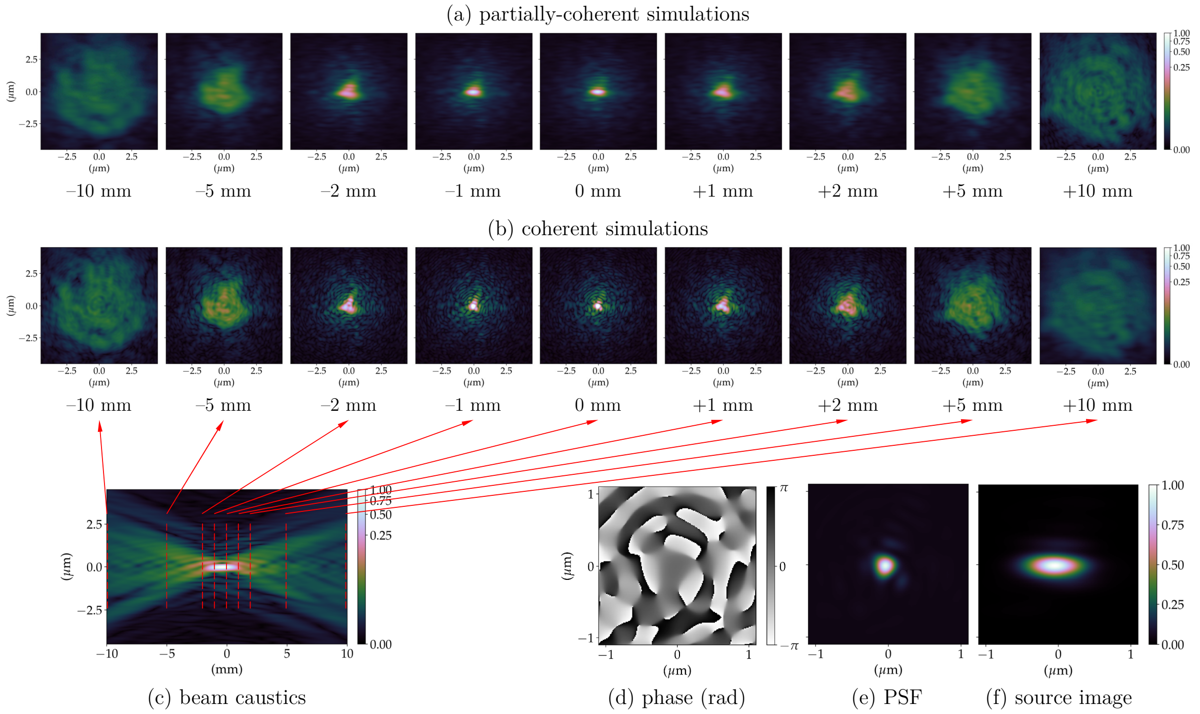

Fig. 6.6.: Expected performance of the diamond phase corrector. (a) partially-coherent simulations show the beam profile up- and downstream the focal position averaging 10^4 wavefronts to simulate the radiation emitted by an undulator; (b) the coherent simulations show the beam profile of a plane wavefront being focused; (c) beam propagation near the focal position (beam caustics) for a fully coherent beam (horizontal cut around $y = 0$); (d) phase and (e) intensity of the PSF calculated focusing a plane-wavefront; (f) demagnified image of the undulator photon-source (extended source). The phase-plate was designed in diamond and a cut is shown in Fig. 6.3. The residual error profile after the correction is shown in Fig. 6.2.

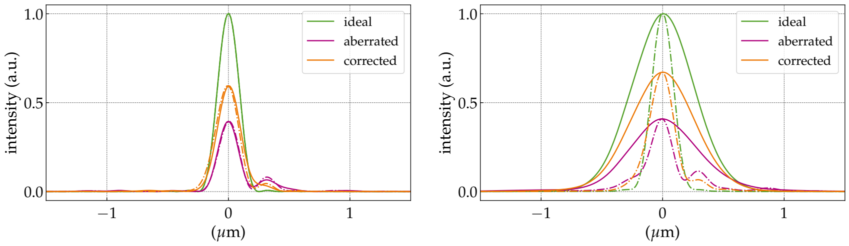

(a) fully-coherent (b) partially-coherent

Fig. 6.7.: Visual representation of the Strehl ratio for the aberrated and corrected optical system. Coherent simulations are shown in (a) and partially-coherent simulations in (b) at 8 keV.

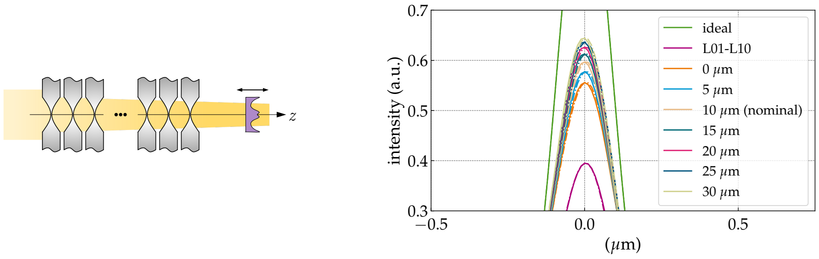

(a) (b)

longitudinal scan

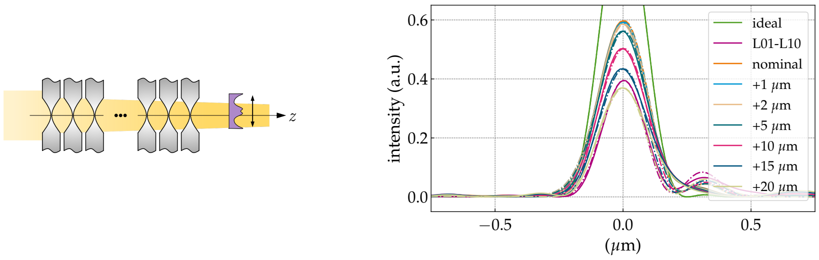

(c) (d)

transverse scan

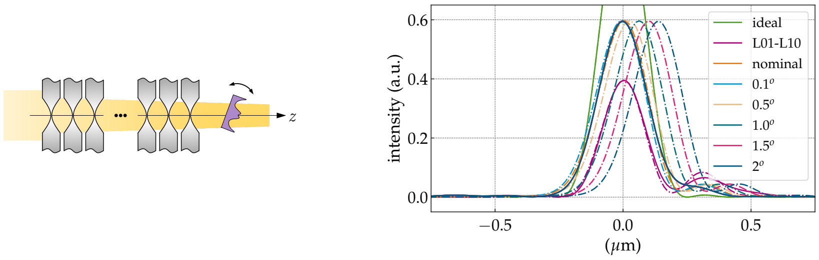

(e) (f)

angular scan

Fig. 6.8.: Study of the precision requirements on longitudinal, transverse and angular alignment of the phase plate based on the optimisation of the Strehl ratio for a fully-coherent beam.

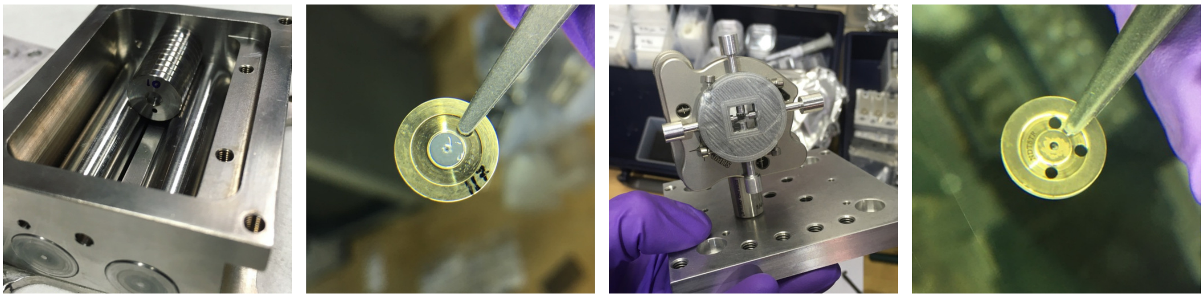

(a) typical lens casing (b) lens in the frame (c) 1st gen. correction plate (d) 2nd gen. correction plate

Fig. 6.9.: Typical lens casing, lens frame and both generation of correction plates.

6.2 Prototype

A series of phase plates designed to correct the accumulated figure error of 10 Be lenses (L01-L10) was commissioned based on the profile shown in Fig. 6.2, which was calculated to be placed 10 mm downstream the last lens of the stack and to correct the errors at 8 keV. The plates were ablated from diamond (HPHT IIb) by a femtosecond laser (515 nm, 3 W, 60 kHz, 200 fs) by a third-party company. The refractive phase plates produced by such technique have a surface roughness of ∼700 nm, but the company offers polishing, which lowers the surface roughness down to ∼100 nm, at the expense of removing some high-spatial frequency features of the correctors, but it is possible to account for the uneven material removal during polishing on the design of the phase plate[5] [Antipov, 2020]. Regardless of the surface finishing, a high shape fidelity to the profile in Fig. 6.2 is expected from the prototypes. Lastly, to facilitate the use of the phase correctors, it was requested that the phase plates come in frames compatible with those used for X-ray lenses - see Fig. 6.9. The phase-plate should be precisely centred in the $\varnothing = 12$ mm aluminium-bronze disk, so it can be easily installed in the lens housing minimising the performance degradation from misalignments shown in Fig. 6.8.

6.2.1 Early tests on an X-ray beam

So far, only two generations of correction plates were produced - see Fig. 6.9. The first generation of phase-plates was received and measured in Dec. 2019 with the XSVT technique described in §4 - *Measuring optical imperfections in refractive lenses*. This first iteration did not aim to produce useful plates, but it allowed to gain useful insights for the production of the second generation correctors, which was delivered in June 2020 - this time to be used for correction of optical imperfections in real CRLs. The phase-plates from the second generation design were chosen to demonstrate some of the preliminary results correcting optical imperfections in refractive lenses available at the ESRF.

The second generation of phase plates consisted of a set of three correction plates (PP01.v1 to PP01.v3) based on the design shown in Fig. 6.2. The difference among the three plates is the script used for laser ablation and the presence or not of surface post-processing. The v1 refers to an undisclosed laser polishing, while v2 and v3 have no post-processing. The PP01.v3 plate uses a different script for surface removal [Antipov, 2020]. Figure 6.10 shows the retrieved

---

[5] At the time of this writing this has not yet been tested.

Tab. 6.3.: Residual figure error profile r.m.s. value for L01-L10 (Fig. 4.14) and for the corrected system (Fig. 6.4).

	figure errors† (r.m.s) μm		
	full profile	pol. fit	residues
stack 01:	4.89	4.73	1.41
stack 01 + PP01.v1:	3.03	2.91	1.66
stack 01 + PP01.v2:	4.26	3.95	1.51
stack 01 + PP01.v3:	3.44	3.10	1.44

† values given for $A_\varnothing = 320$ μm

profile using the XSVT technique and experimental setup described in §4 - *Measuring optical imperfections in refractive lenses*. The profiles are very similar among each other and no strong effect in the surface shape of the polished phase-plate can be observed with XSVT. For the phase-plate PP01.v2, the manufacturer provided visible light metrology (scanning confocal laser microscopy), which is shown in Fig. 6.11. The surface roughness of the non-polished plate is evident in Fig. 6.11(c). Figure 6.12 shows a profile cut of the retrieved thicknesses measured with XSVT and visible-light metrology against the designed profile, showing a initial good agreement for the central part of the phase plate and lesser agreement towards the edge of the geometric aperture.

Once measured individually, the phase plates were added directly to the lens casing relying on the assumption that the phase-plates were perfectly centred within their frames and thus, would ideally be perfectly aligned to the lens stack - see Fig. 6.9. The lens stack with the correction plate was then re-measured with the XSVT. For comparison, the lens stack without any correction was also measured under the very same conditions. The metrology is shown in Fig. 6.13 and summarised in Table 6.3. It is evident that the correction plates are not centred within the lateral tolerance defined by Fig. 6.8(c)-(d) as no significant improvement in the residual profile can be seen.

To be able to test the correction effectiveness and performance, it was decided to mount a phase-plate outside the lens case so at least the transverse alignment could be done. The phase-plate chosen for these tests was the PP01.v2 due to its good agreement with he designed profile in Fig. 6.2. The simplest alignment of the phase plate is based on maximising the peak intensity at the image plane. This approach, however, could not be employed due to the saturation of the detector at the image plane even after a set of attenuators was used. Instead, the alignment of the phase-corrector was done trying to visually optimise, in terms of homogeneity, the far-field beam-profile several tens of millimetres downstream the focal plane. Once the best transverse position was found, a series of 2D images up- and downstream the optical axis was taken with the same 2D imaging detector used for the XSVT (pixel size of ~0.63 μm). The beam caustics can be obtained from this series of images and it is shown in Fig. 6.14 for the aberrated and corrected system. Due to the saturation in the vicinity of the focal plane, a quantitative assessment of the improvement cannot be done, however, a clear qualitative improvement on the beam profile up- and downstream the focal plane is seen.

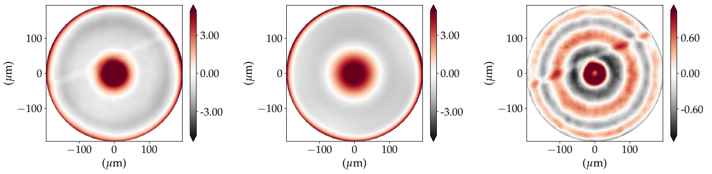

(a) full profile (b) polynomial fit (c) residues

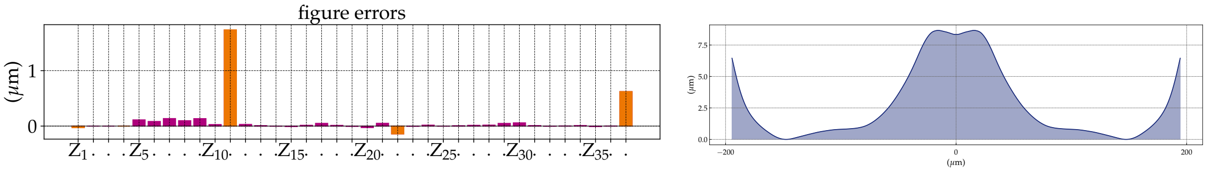

(d) polynomial decomposition (e) azimuthally averaged profile

PP01.v1

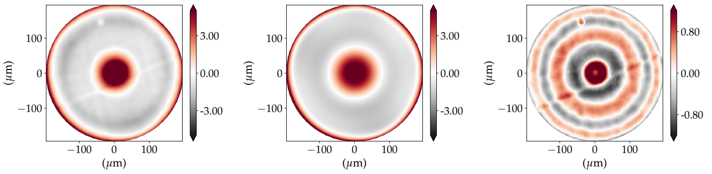

(a) full profile (b) polynomial fit (c) residues

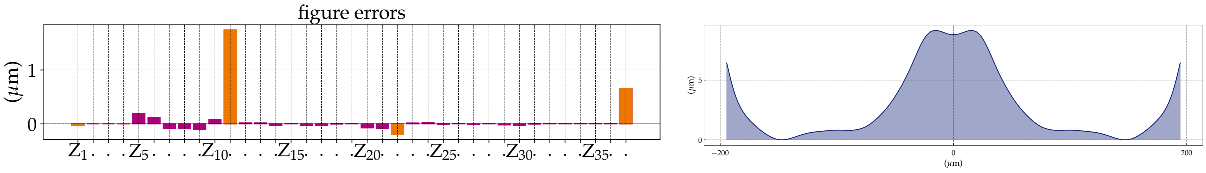

(d) polynomial decomposition (e) azimuthally averaged profile

PP01.v2

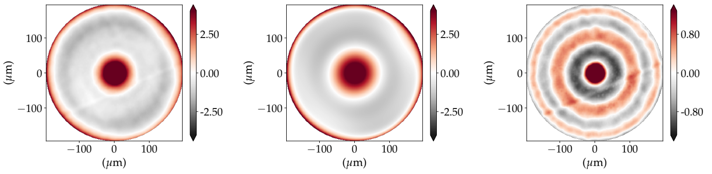

(a) full profile (b) polynomial fit (c) residues

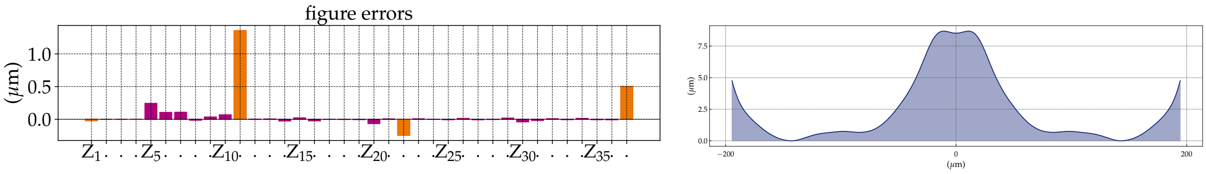

(d) polynomial decomposition (e) azimuthally averaged profile

PP01.v3

Fig. 6.10.: Phase-plate metrology using the XSVT as described in §4 - *Measuring optical imperfections in refractive lenses*.

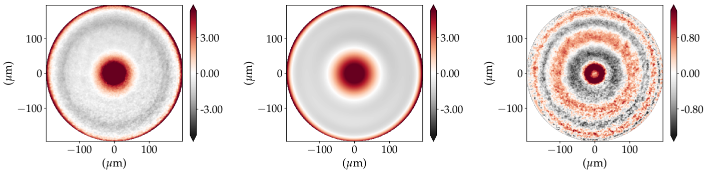

(a) full profile (b) polynomial fit (c) residues

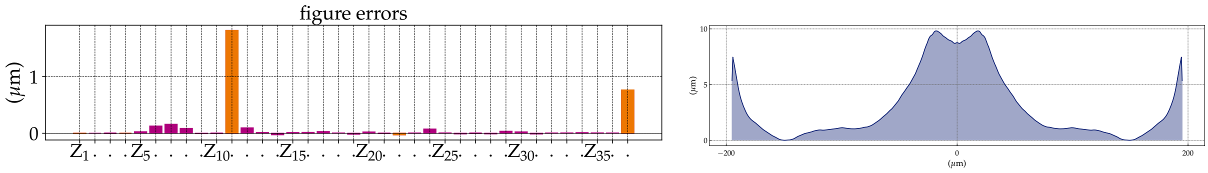

(d) polynomial decomposition (e) azimuthally averaged profile

Fig. 6.11.: Scanning confocal laser microscopy of the PP01.v2 phase-plate provided by the manufacturer.

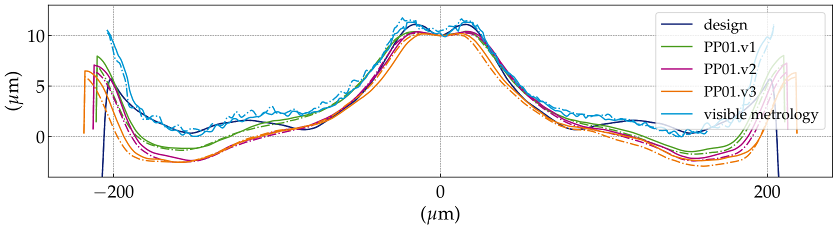

Fig. 6.12.: Profile cuts of the correction plates P01.v1-v3 measured with the XSVT metrology and from the P01.v2 plate measured with the visible-light metrology.

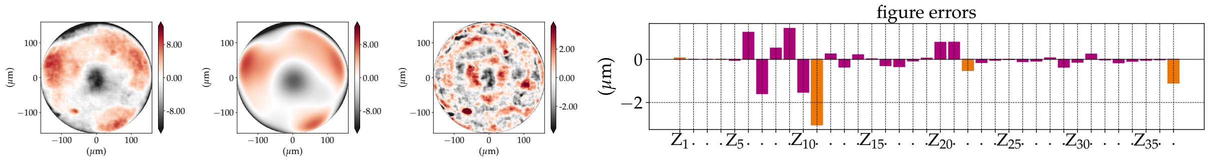

(a) (b) (c) (d)

lens stack 01

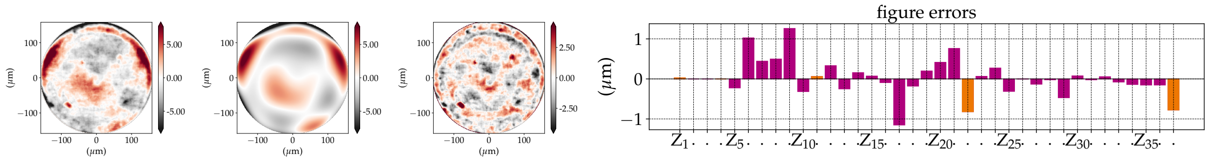

(a) (b) (c) (d)

lens stack 01 + PP01.v1

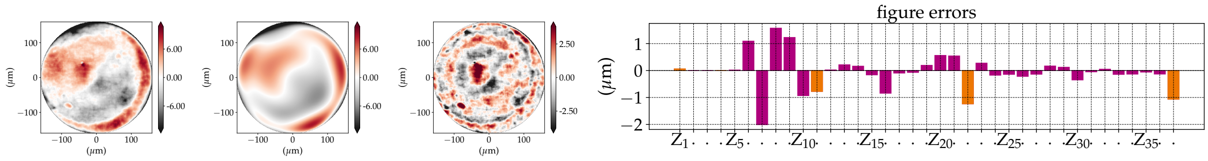

(a) (b) (c) (d)

lens stack 01 + PP01.v2

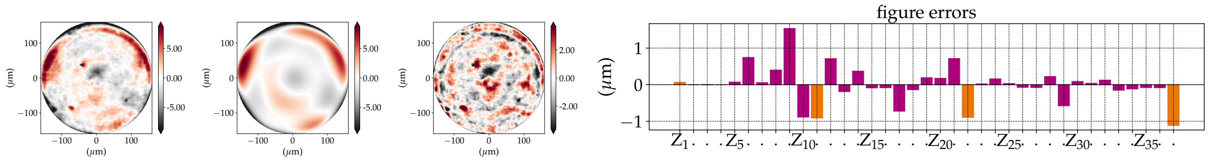

(a) (b) (c) (d)

lens stack 01 + PP01.v3

Fig. 6.13.: **top row**: thickness error of lens stack 01. **centre-top** to **bottom row**: residual thickness after installation of the correction plates PP01.v1, PP01.v2 and PP01.v3 respectively.

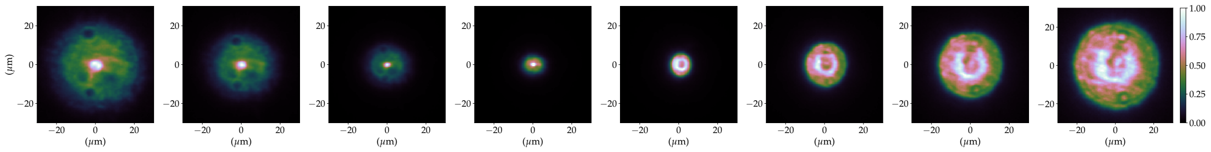

(a) -40 mm (b) -30 mm (c) -20 mm (d) -10 mm (e) +10 mm (f) +20 mm (g) +30 mm (h) +40 mm

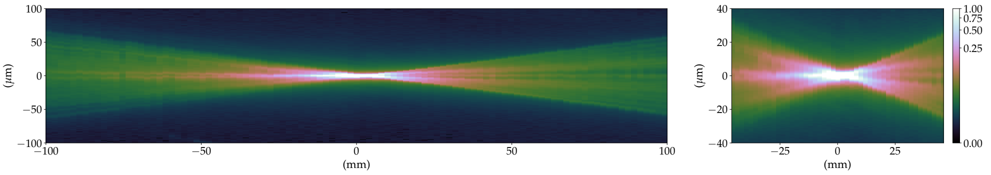

(i) beam caustics (j) zoomed beam caustics

aberrated system

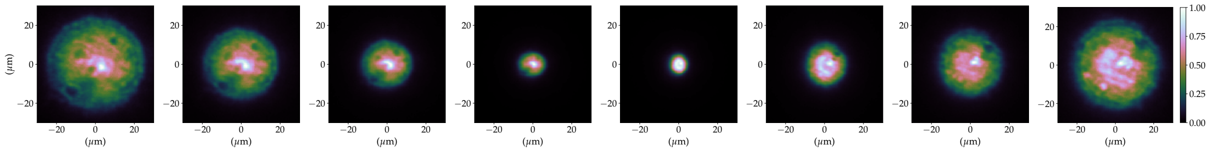

(a) -40 mm (b) -30 mm (c) -20 mm (d) -10 mm (e) +10 mm (f) +20 mm (g) +30 mm (h) +40 mm

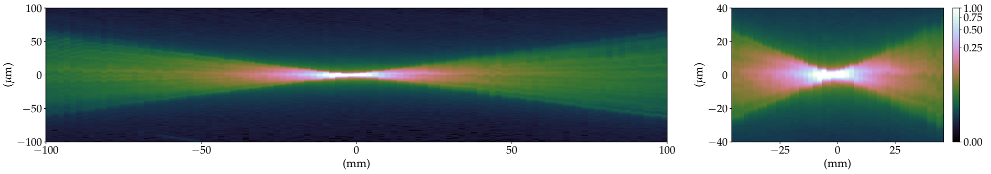

(i) beam caustics (j) zoomed beam caustics

corrected system

Fig. 6.14.: Experimental beam caustics taken at 10.6 keV for the aberrated and corrected system.

6.3 Discussion

6.3.1 Design and expected performance

The concept and design of optical correction for the aberrated system are quite simple and can be represented by the Eq. 6.3. Although current micro- and nano-manufacturing techniques can reproduce such intricate profiles, its alignment on a beamline can be cumbersome and render the correction plate impractical. A successful compromise for 2D focusing CRLs is the adoption of a radially symmetric correction plate described by Eq. 6.4 - these have been demonstrated to work by other groups [Seiboth et al., 2017, 2018, 2020; Dhamgaye et al., 2020].

Using the approach guided by Eq. 6.4, a design to compensate for the accumulated errors from lenses L01-L10 (see Fig. 4.14) was calculated and it is shown in Fig. 6.2. Placing this ideal diamond phase-plate on the simulations and extracting the residual profile allows gaining some insight into the expected performance of the corrected system. Although most, if not all spherical aberration was removed, there is still a high content on non-symmetric aberrations as shown in Figure 6.4(d), which will still degrade the beam focusing quality, but to a lesser extent. Figure 6.4(e) shows a (much reduced) residual profile, which indicates that the correction plate should be calculation over a few iterations until the azimuthally averaged profile goes below what is currently possible to be manufactured. Table 6.1 shows that the overall figure error r.m.s. value over the exit pupil is reduced to ~68% of the L01-L10 figure error. The low-frequencies are more affected, being reduced to 65% its original value. The high frequencies are reduced to 75% of the value before the correction. This reduction in the figure errors is accompanied by an increase in the Strehl ratio as evidenced by Table 6.2 and Fig. 6.7. The improvement of the Strehl ratio for the coherent case differs from the one for the partially-coherent case. Figure 5.12 already showed a very small difference between both cases, but it was deemed to be insignificant. This difference shows the necessity of further studying the impact of the optical correction for moderate- and low-coherence systems.

The expected improvements brought by the optical correction also apply to the beam up- and down-stream the image plane as the several cuts along the beam caustics in Fig. 6.6 show. The elongated tail before the image plane and the doughnut shape from Fig. 5.7 are no longer present, however, at the image plane vicinity, satellite structures are seen around the main lobe. The image plane is greatly improved for both the fully- and partially-coherent simulations with great suppression of the side lobes, showing some similarities with the beam performance predicted in Fig. 5.11. In fact, the better the correction plate is, the closer the system will behave as in Fig. 5.11, a result of the high-frequency profile shown in Fig. 5.10. The performance of very well corrected systems will be limited by the high-frequency content, which does not significantly changes the main-lobe, but significantly increases the background around it, as shown in Fig. 5.13.

It is important to point out that the expected performance and all previously improvements are only obtained for the perfectly aligned phase-plate. Tolerance simulations were done to narrow down the most critical degrees of freedom when aligning the phase-plate in respect to the CRL to be corrected. The longitudinal scan is a useful tool when operating the phase plate outside the design energy. Figure 6.8(a)-(b) shows that a longitudinal scan of a phase-plate operating at its designed energy. Bringing the plate upstream of the nominal position $\Delta_{z_{\text{pp}}}$ degrades its performance, but going downstream moderately improves it. This is probably due to the higher absorption towards the edge of the plate and a smaller footprint of the beam. The transverse alignment is by far the most sensitive degree of freedom and a moderate misalignment may compromise the correction, bringing the Strehl ratio to the same value the aberrated system originally had. Figure 6.8(c)-(d) reinforces what has been observed by other groups [Seiboth, 2016, Fig. 5.12]. Finally, in terms of the Strehl ratio, the phase-plate is not too much influenced by the angular alignment, provided it is kept reasonably small. A tilt is introduced to the system, which laterally shifts the focused beam, but its intensity remains largely unchanged.

6.3.2 Early phase plate tests on an X-ray beam

The early tests with the second generation of phase-plate are encouraging and help delineate strategies for further development of phase correctors to be used with the CRLs. Three phase plates were produced trying to replicate the shape in Fig. 6.2 with differences in the scripts used for engraving the diamond slab and with post polishing or not. Figures 6.10 and 6.11 show a very similar profile for all three plates where the low-frequencies are well represented, but the residues from the polynomial fit show a clear limitation of XSVT in showing the difference between a polished and non-polished plate. Although the effects of polishing are noticeable in the far-field (presence of small-angle scattering and speckle), XSVT cannot show the surface roughness as visible-light metrology does - Fig. 6.11. This makes the case for using complementary metrology methods for a complete characterisation of the phase-plates. When overlapping the profile cuts, as in Fig. 6.12, the difference in the profiles becomes more evident. Visible light metrology and designed plate have a more similar profile, while the data collected with XSVT show lower height values towards the edges of the phase-plate. The differences may come from the processing of the phase-gradients from the XSVT, small inaccuracies when measuring the distances in the experimental setup or a difference between the tabled index of refraction/density and the real index of refraction from the plate - something similar has been speculated in [Seiboth et al., 2020, *§3.2*] for justifying differences between design and measured phase-plates produced using IP-S resist, a much less studied material than diamond.

One of the key aspects of the commissioned phase-plates is that they come perfectly centred in a frame compatible to the ones used for encasing X-ray lenses - Fig. 6.9(b) and (c), which is done to circumvent the degradation in performance from the lateral misalignment in Fig. 6.8(c)-(d). Unfortunately, the phase plates of the current generation do not yet meet such requirements as the metrology of the CRL with the correction plates suggests - see Fig. 6.13; improvements in the centring of the phase plates are expected from the partner company, but are also separately under way within the X-ray optics group at the ESRF.

Aligning the phase-plate to the CRL also revealed a very important aspect: the lack of an internal protocol for alignment. Ideally, one would scan the phase-plate transversely at each position of the scan, the residual wavefront would be calculated and the minimisation of figure errors would be sought. This approach is impractical for the XSVT due to the data acquisition and processing time, not to mention the very large data-set it would generate. This highlights the necessity to re-implement speckle-tracking based on only two images (XST)[6] for a fast evaluation of the figure errors at the expense of a lower spatial resolution. This technique was less frequently used within the X-ray Optics Group due to the many advantages of XSVT [Berujon et al., 2020], but there is a necessity to use XST for a faster characterisation.

Trying to align the phase-plate by maximising the peak intensity was the next obvious step. However, these particular experiments took place at the ID06 beamline after the ESRF-EBS upgrade, an undulator beamline that naturally has a very high photon flux at the harmonics when compared to the typical emission of bending magnets[7]. This increase in photon flux is welcome for the metrology but causes the imaging detector to saturate at the image plane even after attenuators were placed in the beam. As an alternative to the optimisation of the peak intensity, the qualitative improvement of the beam profile downstream the focal plane was done. The phase plate was scanned transversely while the far-field was registered. The final position of the phase plate was where the beam was more homogeneous and the doughnut shape less evident. The drawing of general guidelines for the alignment of the phase-plates and metrics to evaluate it are the topic of future work[8].

The beam caustics and profiles shown in Fig. 6.14 for the aberrated beam confirm the results from the modelling presented in the chapter 5 - *Effect of optical imperfections on an X-ray beam*

---

[6] Refer to §4.1.2 - *Foundation* in §4 - *Measuring optical imperfections in refractive lenses*.

[7] Refer to §1.1.1 - *X-ray sources*.

[8] With the resumption of the ESRF user service mode, more access to beamtime is expected. The ESRF reopened to the public on the 25th of August 2020, despite the COVID-19 pandemic [Cho, 2020].

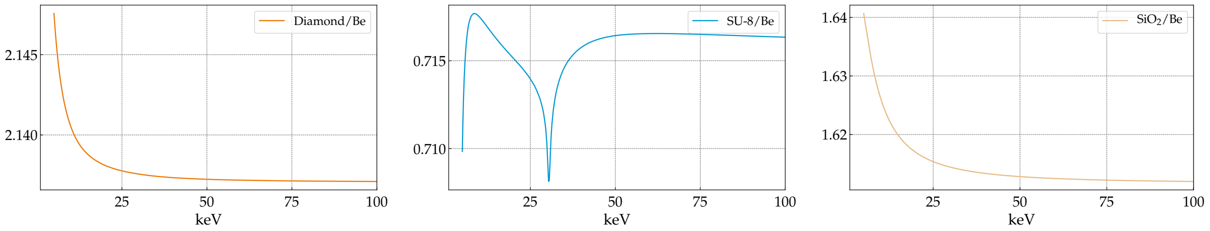

(a) (b) (c)

Fig. 6.15.: (a) diamond, (b) SU-8 and (c) fused silica (SiO_2) refraction index decrement ratio against beryllium. Figures obtained using the *xraylib* library [Brunetti et al., 2004; Schoonjans et al., 2011].

and published in [Celestre et al., 2020]. The presence of the tail upstream of the focal plane and the doughnut shape downstream are clearly present. A direct comparison with the simulations is not possible due to the limited caustic step and detector pixel size, but the main elements and trends are present. Once the phase-plate is inserted and aligned, an improvement in the beam profile homogeneity is seen, although quantification is not possible, due to the saturation of the detector. The central tail is reduced, although still present upstream the image plane. More remarkable is the suppression of the doughnut shape. The performance of the correction plate is better near the image plane, but that could be from the low spatial resolution of the detector.

The experiments were conducted at 10.6 keV, while the design of the phase-plate was optimised for 8 keV. As mentioned previously, the correction plates can be used outside the designed energy if they were calculated for a modest number of lenses by shifting them along the optical axis as described by [Seiboth et al., 2018, *§6*]. Figure 6.15 shows the ratio of the index of refraction decrement and the δ of beryllium, which confirms an almost negligible variation over such a small energy difference. Figure 6.15 reinforces the conclusions in [Seiboth et al., 2018, *§6*] for commonly used phase plate materials.

The correction performance is, at the moment, far from the expected simulated performance or the reported performance from other groups [Seiboth et al., 2017, 2018, 2020; Dhamgaye et al., 2020]. These are the performance of second-generation phase plates and with beamtime availability. Addressing the aforementioned issues with alignment, wavefront-sensing and protocols for evaluating the performance of the phase-plates, improvements in the design and fabrication of phase plates are expected. ■

References

Abrashitova, K. A., Kulagin, G. E., Petrov, A. K., Bessonov, V. O., and Fedyanin, A. A. (2020). “Pyrolyzed 3D compound refractive lens”. In: *Journal of Physics: Conference Series*. Vol. **1461**. 1. Institute of Physics Publishing, p. 12129.

Alcock, S. G., Sutter, J. P., Sawhney, K. J., Hall, D. R., McAuley, K., and Sorensen, T. (2013). “Bimorph mirrors: The Good, the Bad, and the Ugly”. In: *Nuclear Instruments and Methods in Physics Research Section A: Accelerators, Spectrometers, Detectors and Associated Equipment* 710, pp. 87–92.

Antipov, S. P. (2020). “Laser microfabrication for applications in x-ray optics: from refractive lens to phase corrector”. In: *Proc. SPIE 11491, Advances in X-Ray/EUV Optics and Components XV* **11491**, p. 23.

Berujon, S., Cojocaru, R., Piault, P., Celestre, R., Roth, T., Barrett, R., and Ziegler, E. (2020). “X-ray optics and beam characterization using random modulation: theory”. In: *Journal of Synchrotron Radiation* **27**.2, p. 284.

Berujon, S., Ziegler, E., and Cloetens, P. (2015). “X-ray pulse wavefront metrology using speckle tracking”. In: *Journal of Synchrotron Radiation* **22**.4, p. 886.

Brunetti, A., Sanchez del Rio, M., Golosio, B., Simionovici, A., and Somogyi, A. (2004). “A library for X-ray–matter interaction cross sections for X-ray fluorescence applications”. In: *Spectrochimica Acta Part B: Atomic Spectroscopy* **59**.10-11, p. 1725.

Celestre, R., Berujon, S., Roth, T., Sanchez del Rio, M., and Barrett, R. (2020). “Modelling phase imperfections in compound refractive lenses”. In: *Journal of Synchrotron Radiation* **27**.2, p. 305.

Cho, A. (2020). “Rebirth of leading European facility promises revolutionary advances in x-ray science”. In: *Science*.

Chubar, O., Elleaume, P., and Snigirev, A. (1999). “Phase analysis and focusing of synchrotron radiation”. In: *Nuclear Instruments and Methods in Physics Research, Section A: Accelerators, Spectrometers, Detectors and Associated Equipment* **435**.3, p. 495.

— (2001). “Phase corrections for synchrotron radiation”. In: *Nuclear Instruments and Methods in Physics Research, Section A: Accelerators, Spectrometers, Detectors and Associated Equipment* **467-468**, p. 932.

Chubar, O., Wiegart, L., Antipov, S., Celestre, R., Coles, R., Fluerasu, A., and Rakitin, M. S. (2020). “Analysis of hard x-ray focusing by 2D diamond CRL”. In: *Proc. SPIE 11493, Advances in Computational Methods for X-Ray Optics V*, pp. 11493–20.

Dhamgaye, V., Laundy, D., Baldock, S., Moxham, T., and Sawhney, K. (2020). “Correction of the X-ray wavefront from compound refractive lenses using 3D printed refractive structures”. In: *Journal of Synchrotron Radiation* **27**.6.

Donato, S., Arfelli, F., Brombal, L., Longo, R., Pinto, A., Rigon, L., and Dreossi, D. (2020). “Flattening filter for Gaussian-shaped monochromatic X-ray beams: an application to breast computed tomography”. In: *Journal of Synchrotron Radiation* **27**.2, p. 503.

Laundy, D., Dhamgaye, V., Moxham, T., and Sawhney, K. (2019). “Adaptable refractive correctors for x-ray optics”. In: *Optica* **6**.12, p. 1484.

— (2020). “Measurements and simulations of wavefront correcting refractive x-ray optics”. In: *Proc. SPIE 11493, Advances in Computational Methods for X-Ray Optics V*, p. 16.

Lin, H., Yang, S.-N., and Liu, X.-Q. (2020). “X-ray kinoform lenses made using femtosecond laser technique”. In: *Proc. SPIE 11491, Advances in X-Ray/EUV Optics and Components XV*, p. 37.

Medvedskaya, P., Lyatun, I., Shevyrtalov, S., Polikarpov, M., Snigireva, I., Yunkin, V., and Snigirev, A. (2020). “Diamond refractive micro-lenses for full-field X-ray imaging and microscopy produced with ion beam lithography”. In: *Optics Express* **28**.4, p. 4773.

Nazmov, V., Reznikova, E., Mohr, J., Snigirev, A., Snigireva, I., Achenbach, S., and Saile, V. (2004). “Fabrication and preliminary testing of X-ray lenses in thick SU-8 resist layers”. In: *Microsystem Technologies*. Vol. **10**. 10, p. 716.

Petrov, A. K., Bessonov, V. O., Abrashitova, K. A., Kokareva, N. G., Safronov, K. R., Barannikov, A. A., Ershov, P. A., Klimova, N. B., Lyatun, I. I., Yunkin, V. A., Polikarpov, M., Snigireva, I., Fedyanin, A. A., and Snigirev, A. (2017). “Polymer X-ray refractive nano-lenses fabricated by additive technology”. In: *Optics Express* **25**.13, p. 14173.

Polikarpov, M., Kononenko, T. V., Ralchenko, V. G., Ashkinazi, E. E., Konov, V. I., Ershov, P., Kuznetsov, S., Yunkin, V., Snigireva, I., Polikarpov, V. M., and Snigirev, A. (2016). “Diamond x-ray refractive lenses produced by femto-second laser ablation”. In: *Proc. SPIE 9963, Advances in X-Ray/EUV Optics and Components XI* **9963**.15, 99630Q.

Polikarpov, M., Polikarpov, V., Snigireva, I., and Snigirev, A. (2016). “Diamond X-ray Refractive Lenses with High Acceptance”. In: *Physics Procedia*. Vol. **84**. Elsevier B.V., p. 213.

Probst, J., Braig, C., Langlotz, E., Rahneberg, I., Kühnel, M., Zeschke, T., Siewert, F., Krist, T., and Erko, A. (2020). “Conception of diffractive wavefront correction for XUV and soft x-ray spectroscopy”. In: *Applied Optics* **59**.8, p. 2580.

Roth, T., Koch, F., Berujon, S., Celestre, R., Zinn, T., David, C., and Barrett, R. (2018). “2D focusing kinoform lenses produced by 3D direct printing”. In: *International Conference on X-ray Optics and Applications (XOPT2018), Yokohama, Japan* (presentation).

Sanli, U. T., Ceylan, H., Bykova, I., Weigand, M., Sitti, M., Schütz, G., and Keskinbora, K. (2018). “3D Nanoprinted Plastic Kinoform X-Ray Optics”. In: *Advanced Materials* **30**.36, p. 1802503.

Sawhney, K., Laundy, D., Dhamgaye, V., and Pape, I. (2016). “Compensation of X-ray mirror shape-errors using refractive optics”. In: *Applied Physics Letters* **109**.5, p. 051904.

Schoonjans, T., Brunetti, A., Golosio, B., Sanchez del Rio, M., Solé, V. A., Ferrero, C., and Vincze, L. (2011). “The xraylib library for X-ray–matter interactions. Recent developments”. In: *Spectrochimica Acta Part B: Atomic Spectroscopy* **66**.11-12, p. 776.

Schroer, C. G. and Lengeler, B. (2005). “Focusing hard X rays to nanometer dimensions by adiabatically focusing lenses”. In: *Physical Review Letters* **94**.5.

Schropp, A., Hoppe, R., Meier, V., Patommel, J., Seiboth, F., Lee, H. J., Nagler, B., Galtier, E. C., Arnold, B., Zastrau, U., Hastings, J. B., Nilsson, D., Uhlén, F., Vogt, U., Hertz, H. M., and Schroer, C. G. (2013). “Full spatial characterization of a nanofocused X-ray free-electron laser beam by ptychographic imaging”. In: *Scientific Reports* **3**.1, p. 1.

Seaberg, M., Cojocaru, R., Berujon, S., Ziegler, E., Jaggi, A., Krempasky, J., Seiboth, F., Aquila, A., Liu, Y., Sakdinawat, A., Lee, H. J., Flechsig, U., Patthey, L., Koch, F., Seniutinas, G., David, C., Zhu, D., Mikeš, L., Makita, M., Koyama, T., Mancuso, A. P., Chapman, H. N., and Vagovič, P. (2019). “Wavefront sensing at X-ray free-electron lasers”. In: *Journal of Synchrotron Radiation* **26**.4, p. 1115.

Seiboth, F. (2016). “Refractive Hard X-ray Nanofocusing at Storage Ring and X-ray Free-Electron Lasers Sources”. PhD thesis. Fakultät für Mathematik, Informatik, und Naturwissenschaften, Fachbereich Physik, Universität Hamburg.

Seiboth, F., Brückner, D., Kahnt, M., Lyubomirskiy, M., Wittwer, F., Dzhigaev, D., Ullsperger, T., Nolte, S., Koch, F., David, C., Garrevoet, J., Falkenberg, G., and Schroer, C. G. (2020). “Hard X-ray wavefront correction via refractive phase plates made by additive and subtractive fabrication techniques”. In: *Journal of Synchrotron Radiation* **27**.5, p. 27.

Seiboth, F., Kahnt, M., Lyubomirskiy, M., Seyrich, M., Wittwer, F., Ullsperger, T., Nolte, S., Batey, D., Rau, C., and Schroer, C. G. (2019). “Refractive hard x-ray vortex phase plates”. In: *Optics Letters* **44**.18, p. 4622.

Seiboth, F., Kahnt, M., Scholz, M., Seyrich, M., Wittwer, F., Garrevoet, J., Falkenberg, G., Schropp, A., and Schroer, C. G. (2016). “Quantitative characterization of aberrations in x-ray optics”. In: *Proc. SPIE 9963, Advances in X-Ray/EUV Optics and Components XI*, 99630P.

Seiboth, F., Schropp, A., Scholz, M., Wittwer, F., Rödel, C., Wünsche, M., Ullsperger, T., Nolte, S., Rahomäki, J., Parfeniukas, K., Giakoumidis, S., Vogt, U., Wagner, U., Rau, C., Boesenberg, U., Garrevoet, J., Falkenberg, G., Galtier, E. C., Ja Lee, H., Nagler, B., and Schroer, C. G. (2017). “Perfect X-ray focusing via fitting corrective glasses to aberrated optics”. In: *Nature Communications* **8**.1, p. 14623.

Seiboth, F., Wittwer, F., Scholz, M., Kahnt, M., Seyrich, M., Schropp, A., Wagner, U., Rau, C., Garrevoet, J., Falkenberg, G., and Schroer, C. G. (2018). “Nanofocusing with aberration-corrected rotationally parabolic refractive X-ray lenses”. In: *Journal of Synchrotron Radiation* **25**.1, p. 108.

Shvyd’Ko, Y., Blank, V., and Terentyev, S. (2017). “Diamond X-ray optics: Transparent, resilient, high-resolution, and wavefront preserving”. In: *MRS Bulletin* **42**.6, p. 437.

Stöhr, F., Simons, H., Jakobsen, A. C., Nielsen, C. H., Michael-Lindhard, J., Jensen, F., Poulsen, H. F., Hansen, O., and Hübner, J. (2015). “Injection molded polymeric hard X-ray lenses”. In: *Optical Materials Express* **5**.12, p. 2804.

Sutter, J., Alcock, S., and Sawhney, K. (2012). “In situ beamline analysis and correction of active optics”. In: *Journal of Synchrotron Radiation* **19**.6, p. 960.

Uhlén, F., Rahomäki, J., Nilsson, D., Seiboth, F., Sanz, C., Wagner, U., Rau, C., Schroer, C. G., and Vogt, U. (2014). “Ronchi test for characterization of x-ray nanofocusing optics and beamlines”. In: *Journal of Synchrotron Radiation* **21**.5, p. 1105.

Conclusion

7.en

The new 4th generation of storage rings puts stringent requirements on the quality of optical elements as to minimise the degradation of the X-ray beam [Schroer and Falkenberg, 2014; Yabashi et al., 2014]. The aim of this thesis, namely investigating and modelling the effect of optical imperfections in compound refractive lenses on a partially-coherent X-ray beam, addresses important aspects of the ESRF-EBS X-ray optics R&D programme as laid out in the Orange book [Dimper et al., 2014].

Based on the physical optics concepts presented in Chapter 1 and the already implemented optical elements in SRW [Baltser et al., 2011], an expanded model for a thick ideal CRL was presented. This model is similar to the multi-slicing technique already used for optical modelling [Li et al., 2017; Ali and Jacobsen, 2020], where each lens is considered to be a slice of the CRL. The complex transmission element representing a thick CRL is given by Eq. 2.11 and shown in Fig. 2.6(b). This ideal model of a thick CRL can be modified to account for optical imperfections when a 2D map of the figure errors of each lens is available. This model is shown in Fig. 2.6(c) and described by Eq. 2.12. This modelling of CRL as a thick optical element becomes more relevant when the lens stack is composed of a large number of lenslets and there is significant focusing inside the CRL [Schroer and Lengeler, 2005]. The extended modelling of CRLs was published in [Celestre, Berujon, et al., 2020].

Once the framework for the modelling of thick CRLs was defined, the attention was directed towards modelling individual lenses. Typical misalignments and fabrication errors commonly present in embossed X-ray lenses (Fig. 3.1) were parametrised by allowing more degrees of freedom to the ideal model for a single lens described in [Baltser et al., 2011]. This parametrisation is general enough to apply to lenses produced by other techniques, but this modelling could profit from adding the choice of the conic section to be used, currently limited to the parabolic case, as already implemented by [Sanchez del Rio and Alianelli, 2012; Andrejczuk et al., 2010] for ray-tracing. Some groups have already experimented with non-parabolic shapes for focusing X-rays [Alianelli et al., 2007; Evans-Lutterodt et al., 2003; Alianelli et al., 2015; Sutter and Alianelli, 2017] and the availability of simulation tools could revive the interest in non-orthodox designs. It would be amiss not to mention the similarities between the modelling presented here and the work presented by [Andrejczuk et al., 2010], where the modelling of the role of single element errors in X-ray lenses is implemented for ray-tracing, but the analysis is limited to the beam width and intensity in the image plane. The modelling of more intricate shape errors was enabled by employing the Zernike or 2D Legendre orthonormal polynomials. This was done by unifying some already existing parts of Python libraries, adding new polynomial sets and interfacing them to be compatible with the framework already described. This unified and expanded Python library was used throughout the thesis for fitting the figure errors presented throughout Chapters 3-6. The modelling of shape errors by either allowing more degrees of freedom to the ideal lens model or by directly generating the shape errors through orthonormal polynomials is a useful tool for delineating tolerances on the manufacturing of X-ray lenses, which is of particular relevance for the ESRF in-house fabricated Al-lens project. Any arbitrary 2D map of surface imperfections (eg. metrology data or free-form surfaces for beam shaping) can also be incorporated in the simulations using this framework. Several authors have developed tools with different degrees of complexity for simulating X-ray lenses and their aberrations. However, not only are those tools not available to the public but also the modelling is often not compatible with already existing wide-spread simulation tools for X-ray optical design such as SHADOW (ray-tracing) and SRW (wavefront propagation). The modelling presented here is open source, tailored to be used transparently with SRW and is currently available in a public repository in GitLab until the eventual merge with the SRW official distribution. Parallel to it, the code is being incorporated in the OASYS toolkit [Rebuffi and Sanchez del Rio, 2017] to be made available for their distributions of SHADOW, hybrid ray-tracing and SRW. These recent developments on X-ray lenses modelling were presented in [Celestre, Chubar, et al., 2020] and used in some of the simulations from [Chubar et al., 2020].

Ultimately, for simulations with realistic levels of imperfections, the modelling of the figure errors on individual X-ray lenses was done with metrology data from 2D maps of local deviations of the parabolic profile. The experimental metrology technique used for this thesis was the X-ray vectorial speckle tracking (XSVT). In addition to being relatively simple to implement, this technique has a high lateral resolution and good sensitivity. Furthermore, it delivers a 2D map of figure errors in projection approximation, which can conveniently be used with the wave-optical simulations. Several measurement campaigns at the ESRF, APS and ESRF-EBS were performed to assess the quality of in-house produced lenses; lenses and free-form optics in the context of scientific collaborations; and newly-acquired commercial lenses. As a result, a large and diverse database of metrology files was built. After some curation, a possible expansion of the DABAM (database for X-ray mirrors metrology) [Sanchez Del Rio et al., 2016] is envisioned. Making the metrology data of X-ray lenses available through an open-source database would help the consolidation of the framework developed here since DABAM is also distributed and interfaced by OASYS. Before that, however, more effort has to be put into making the metrology of single lens and subsequent stacking by software converge with the metrology of a lens stack composed by those same lenslets. The current state show some qualitative agreement (Fig. 4.14-4.17), which is transferred to the simulations shown in Figs. 5.3-5.4 and Fig. 5.8. This is sufficient for preliminary studies but leaves room for improvements and delineation of protocols for the metrology both in terms of sample alignment and data processing - these should be the aim of future work. The major importance of reliably being able to artificially stack individually measured lenses is the possibility of evaluating the performance of a CRL composed of any arbitrary selection of lenses off-line, with immediate application to the design of optical correctors. The experience gained in the metrology campaigns and advancements in the post-processing of the acquired data resulted in modest contributions to [Berujon et al., 2020a,b; Qiao et al., 2020].

A subset of lenses in the database was chosen to showcase the effect of optical imperfections on partially coherent X-ray beam degradation. The simulations, shown in the first part of Chapter 5 and summarised by Fig. 5.7, show a beam caustic that has been reported several times in literature for the same type of X-ray lenses [Schropp et al., 2013; Seiboth et al., 2017, 2020]. The experimental measurement of the beam caustics for this lens stack also shows similarity to what was predicted by the simulations - cf. Fig. 6.14. The similarity between the simulations and experimental data helps to validate the framework presented in this thesis and it is believed that they allow to qualitatively assess the effects of optical imperfections on the degradation of the X-ray beam profile. The simulations also allow investigating the adequacy of the Strehl ratio as a figure of merit for the optical design of systems operating far from the Maréchal criterion for optical quality. Generally, the equations used for estimating the Strehl ratio tend to underestimate the system performance in that region (Fig. 5.12). The failed attempt in obtaining simple replacement equations (cf. Eq. 5.2) indicate that the most straightforward way to evaluate the Strehl ratio is by optical simulation of the system using realistic figure errors. It is also relevant to mention that although fully- and partially coherent simulations do not differ significantly, it is premature to generalise this behaviour as the partially-coherent simulations were done for a hypothetical undulator beamline operating at the upgraded ESRF magnetic lattice. Another result from the simulations is the prediction that the systems with high spatial frequency figure errors do not present a broadening of the beam size at the focal plane, instead, the intensity is reduced by the scattering of photons around the main lobe, increasing the background level - Fig. 5.13. The effects of high-spatial-frequency figure errors are important as well-corrected optical systems would have them as a predominant source of shape errors. This analysis was published in [Celestre, Berujon, et al., 2020].

The multi-slice modelling of a CRL including the metrology data of individually measured lenses (Eq. 2.12) allows the extraction of the accumulated figure errors of a lens stack. This was used to model a phase-plate in diamond to correct for those errors at the exit pupil of the system. Due to the limitations of the phase-plate alignment in a beamline, the symmetric design is preferred in detriment to the correction performance - reported results show excellent performance even with this trade-off [Seiboth et al., 2020; Dhamgaye et al., 2020]. The beam profile shown in Fig. 6.6 is more homogeneous up- and downstream the image plane and resembles the simulations for a system with predominantly high-spatial frequencies in Fig. 5.10. However, when analysing the Strehl ratio, the performance of the modelled phase-plate is limited and beyond what other groups have reported. The main reasons for such discrepancies are the fact that the profile to be corrected (Fig. 4.14) has significant non-symmetric components (trefoil aberration) in addition to the classical predominance of spherical aberrations. The lack of asymmetry found by other groups is likely connected to the fact that a larger number of lenses are used in their stacks and the addition of correlated errors of randomly rotated lenses would act to give a more symmetric shape to the accumulated errors by averaging out the non-symmetric components. Randomly rotating the lenses in the simulations could help to improve the expected Strehl ratio and similar procedure could be applied to the lens stack in an experiment. The designed phase-plates were commissioned from a commercial partner and they were ablated from diamond by a femtosecond laser. Initial tests on an X-ray beam showed that the phase plates were not centred in the frame within the calculated tolerances, which is crucial for their performance. The phase-plate had to be aligned concerning the lens stack, which posed an initial problem, as at the time no alignment protocols were delineated. This also brought to the surface the necessity of re-implementation of faster wavefront sensing techniques which were discontinued in favour of a higher spatial resolution. Other issues such as overexposure of the detector even after strong attenuation of the beam limited the tests that could be done with the correction plate, so no quantitative value was generated to evaluate the correction performance, however, a beam caustic could be recorded for the aberrated and corrected system (Fig. 6.14) qualitatively showing a more homogeneous beam especially in the vicinity of the focal plane, with a better performance downstream.

The early results are promising but show the necessity of further beamtimes aimed to looking for alternative ways for rapidly extracting the residual wavefront and aligning the correction plate, measuring the beam-caustics and quantitatively evaluating the correction performance. Exploring additive manufacturing for designing the corrective optics in other materials should also be investigated as an alternative to diamond and lowering the prototyping costs. ■

References

Ali, S. and Jacobsen, C. (2020). “Effect of tilt on circular zone plate performance”. In: *Journal of the Optical Society of America A* **37**.3, p. 374.

Alianelli, L., Sánchez del Río, M., and Sawhney, K. J. (2007). “Ray-tracing simulation of parabolic compound refractive lenses”. In: *Spectrochimica Acta - Part B Atomic Spectroscopy* **62**.6-7 SPEC. ISS. P. 593.

Alianelli, L., Sánchez del Rio, M., Fox, O. J. L., and Korwin-Mikke, K. (2015). “Aberration-free short focal length x-ray lenses”. In: *Optics Letters* **40**.23, p. 5586.

Andrejczuk, A., Krzywiski, J., Sakurai, Y., Itou, M., Krzywiński, J., Sakurai, Y., and Itou, M. (2010). “The role of single element errors in planar parabolic compound refractive lenses”. In: *Journal of Synchrotron Radiation* **17**.5, p. 616.

Baltser, J., Knudsen, E., Vickery, A., Chubar, O., Snigirev, A., Vaughan, G., Feidenhans’l, R., and Lefmann, K. (2011). “Advanced simulations of x-ray beam propagation through CRL transfocators using ray-tracing and wavefront propagation methods”. In: *Proc. SPIE 8141, Advances in Computational Methods for X-Ray Optics II* 8141, p. 814111.

Berujon, S., Cojocaru, R., Piault, P., Celestre, R., Roth, T., Barrett, R., and Ziegler, E. (2020a). “X-ray optics and beam characterization using random modulation: experiments”. In: *Journal of Synchrotron Radiation* **27**.2, p. 293.

— (2020b). “X-ray optics and beam characterization using random modulation: theory”. In: *Journal of Synchrotron Radiation* **27**.2, p. 284.

Celestre, R., Berujon, S., Roth, T., Sanchez del Rio, M., and Barrett, R. (2020). “Modelling phase imperfections in compound refractive lenses”. In: *Journal of Synchrotron Radiation* **27**.2, p. 305.

Celestre, R., Chubar, O., Roth, T., Sanchez del Rio, M., and Barrett, R. (2020). “Recent developments in X-ray lenses modelling with SRW”. In: *Proc. SPIE 11493, Advances in Computational Methods for X-Ray Optics V*, pp. 11493–17.

Chubar, O., Wiegart, L., Antipov, S., Celestre, R., Coles, R., Fluerasu, A., and Rakitin, M. S. (2020). “Analysis of hard x-ray focusing by 2D diamond CRL”. In: *Proc. SPIE 11493, Advances in Computational Methods for X-Ray Optics V*, pp. 11493–20.

Dhamgaye, V., Laundy, D., Baldock, S., Moxham, T., and Sawhney, K. (2020). “Correction of the X-ray wavefront from compound refractive lenses using 3D printed refractive structures”. In: *Journal of Synchrotron Radiation* **27**.6.

Dimper, R., Reichert, H., Raimondi, P., Sanchez Ortiz, L., Sette, F., and Susini, J. (2014). *ESRF Upragde programme phase II - The Orange Book*. ESRF, p. 75.

Evans-Lutterodt, K., Ablett, J. M., Stein, A., Kao, C.-C., Tennant, D. M., Klemens, F., Taylor, A., Jacobsen, C., Gammel, P. L., Huggins, H., Ustin, S., Bogart, G., and Ocola, L. (2003). "Single-element elliptical hard x-ray micro-optics". In: *Opt. Express* **11**.8, p. 919.

Li, K., Wojcik, M., and Jacobsen, C. (2017). "Multislice does it all—calculating the performance of nanofocusing X-ray optics". In: *Optics Express* **25**.3, p. 1831.

Qiao, Z., Shi, X., Celestre, R., and Assoufid, L. (2020). "Wavelet-transform-based speckle vector tracking method for X-ray phase imaging". In: *Optics Express* **28**.22, p. 33053.

Rebuffi, L. and Sanchez del Rio, M. (2017). "OASYS (OrAnge SYnchrotron Suite): an open-source graphical environment for x-ray virtual experiments". In: *Proc. SPIE 10388, Advances in Computational Methods for X-Ray Optics IV*, p. 28.

Sanchez del Rio, M. and Alianelli, L. (2012). "Aspherical lens shapes for focusing synchrotron beams". In: *Journal of Synchrotron Radiation* **19**.3, p. 366.

Sanchez Del Rio, M., Bianchi, D., Cocco, D., Glass, M., Idir, M., Metz, J., Raimondi, L., Rebuffi, L., Reininger, R., Shi, X., Siewert, F., Spielmann-Jaeggi, S., Takacs, P., Tomasset, M., Tonnessen, T., Vivo, A., and Yashchuk, V. (2016). "DABAM: An open-source database of X-ray mirrors metrology". In: *Journal of Synchrotron Radiation* **23**.3, p. 665.

Schroer, C. G. and Lengeler, B. (2005). "Focusing hard X rays to nanometer dimensions by adiabatically focusing lenses". In: *Physical Review Letters* **94**.5.

Schroer, C. G. and Falkenberg, G. (2014). "Hard X-ray nanofocusing at low-emittance synchrotron radiation sources". In: *Journal of Synchrotron Radiation* **21**.5, pp. 996–1005.

Schropp, A., Hoppe, R., Meier, V., Patommel, J., Seiboth, F., Lee, H. J., Nagler, B., Galtier, E. C., Arnold, B., Zastrau, U., Hastings, J. B., Nilsson, D., Uhlén, F., Vogt, U., Hertz, H. M., and Schroer, C. G. (2013). "Full spatial characterization of a nanofocused X-ray free-electron laser beam by ptychographic imaging". In: *Scientific Reports* **3**.1, p. 1.

Seiboth, F., Brückner, D., Kahnt, M., Lyubomirskiy, M., Wittwer, F., Dzhigaev, D., Ullsperger, T., Nolte, S., Koch, F., David, C., Garrevoet, J., Falkenberg, G., and Schroer, C. G. (2020). "Hard X-ray wavefront correction via refractive phase plates made by additive and subtractive fabrication techniques". In: *Journal of Synchrotron Radiation* **27**.5, p. 27.

Seiboth, F., Schropp, A., Scholz, M., Wittwer, F., Rödel, C., Wünsche, M., Ullsperger, T., Nolte, S., Rahomäki, J., Parfeniukas, K., Giakoumidis, S., Vogt, U., Wagner, U., Rau, C., Boesenberg, U., Garrevoet, J., Falkenberg, G., Galtier, E. C., Ja Lee, H., Nagler, B., and Schroer, C. G. (2017). "Perfect X-ray focusing via fitting corrective glasses to aberrated optics". In: *Nature Communications* **8**.1, p. 14623.

Sutter, J. P. and Alianelli, L. (2017). "Aberration-free aspherical lens shape for shortening the focal distance of an already convergent beam". In: *Journal of Synchrotron Radiation* **24**.6, pp. 1120–1136.

Yabashi, M., Tono, K., Mimura, H., Matsuyama, S., Yamauchi, K., Tanaka, T., Tanaka, H., Tamasaku, K., Ohashi, H., Goto, S., and Ishikawa, T. (2014). "Optics for coherent X-ray applications". In: *Journal of Synchrotron Radiation* **21**.5, pp. 976–985.

Conclusion

7.fr

La quatrième génération d'anneaux de stockage, récemment lancée, impose des exigences strictes quant à la qualité des éléments optiques afin de minimiser la dégradation du faisceau de rayons X [Schroer and Falkenberg, 2014; Yabashi et al., 2014]. Cette thèse, dont l'objectif consiste à étudier et à modéliser l'effet des imperfections optiques des lentilles réfractives composées sur un faisceau de rayons X partiellement cohérent, aborde des aspects importants du programme de R&D en optique des rayons X de l'ESRF-EBS, tel qu'il est exposé dans le *Orange book* [Dimper et al., 2014].

Basé sur les concepts d'optique physique présentés au chapitre 1 et les éléments optiques disponibles dans SRW [Baltser et al., 2011] un modèle étendu à une lentille réfractive composée (CRL) idéale et épaisse a été présenté. Ce modèle s'apparente à la technique de découpage multi-coupes déjà utilisée pour la modélisation optique [Li et al., 2017; Ali and Jacobsen, 2020], où chaque lentille est considérée comme une tranche de la CRL. L'élément de transmission complexe représentant une CRL épaisse est donné par Eq. 2.11 et illustré par la Fig. 2.6(b). Ce modèle idéal d'une CRL épaisse peut être modifié pour prendre en compte des imperfections optiques lorsqu'une cartographie 2D des erreurs de forme de chaque lentille est disponible. Il est illustré par la Fig. 2.6(c) et décrit par Eq. 2.12. Cette modélisation de la CRL en tant qu'élément optique épais devient plus pertinente lorsque l'empilement est composé d'un grand nombre de lentilles et que la focalisation au sein du CRL est importante [Schroer and Lengeler, 2005]. La modélisation étendue des CRL a été publiée dans [Celestre, Berujon, et al., 2020].

Les erreurs de fabrication couramment présentes dans les lentilles rayons X en relief (Fig. 3.1) ont été paramétrées en offrant plus de degrés de liberté au modèle idéal pour une seule lentille comme décrit dans [Baltser et al., 2011]. Ce paramétrage est assez général pour s'appliquer aux lentilles produites par d'autres techniques, mais cette modélisation pourrait être améliorée en offrant le choix de la section conique à utiliser, actuellement limitée au cas parabolique, comme cela a déjà été implémenté pour le ray-tracing par [Sanchez del Rio and Alianelli, 2012; Andrejczuk et al., 2010]. Certains groupes ont déjà expérimenté des formes non paraboliques pour la focalisation des rayons X [Alianelli et al., 2007; Evans-Lutterodt et al., 2003; Alianelli et al., 2015; Sutter and Alianelli, 2017] et la disponibilité d'outils de simulation pourrait raviver l'intérêt pour les conceptions non orthodoxes. Il serait inconvenant de ne pas mentionner les similitudes entre la modélisation présentée ici et les travaux présentés par [Andrejczuk et al., 2010], où la modélisation du rôle des erreurs d'un seul élément dans les lentilles à rayons X est utilisée dans le ray-tracing, l'analyse étant cependant limitée à la largeur et à l'intensité du faisceau dans le plan image. La modélisation d'erreurs de forme plus complexes a été rendue possible par l'utilisation des polynômes orthonormaux de Zernike ou de Legendre 2D. Cela a été fait en unifiant certaines parties déjà existantes des bibliothèques Python, en ajoutant de nouveaux ensembles de polynômes et en les interfaçant pour les rendre compatibles avec le cadre déjà décrit. Cette bibliothèque Python unifiée et étendue a été utilisée tout au long de la thèse pour ajuster les erreurs de forme présentées tout au long des chapitres 3-6. La modélisation des erreurs de forme réalisée soit en accordant plus de degrés de liberté au modèle de lentille idéal, soit en générant directement les erreurs de forme par des polynômes orthonormaux, est un outil utile pour définir les tolérances de fabrication des lentilles rayons X, ce qui est particulièrement pertinent pour le projet de fabrication en interne de lentilles en aluminium. Toute cartographie arbitraire des imperfections de surface (par exemple issue de données de métrologie ou de surfaces free-form pour la mise en forme du faisceau) peut également être intégrée dans les simulations. Plusieurs auteurs ont développé de nombreux outils avec différents degrés de complexité pour simuler les lentilles rayons X et leurs aberrations. Toutefois, non seulement ces outils ne sont pas accessibles au public, mais la modélisation n'est souvent pas compatible avec les outils de simulation déjà largement répandus pour la conception des optiques rayons X, tels que SHADOW (ray-tracing) et SRW (propagation du front d'onde). La modélisation présentée ici est de type open source, pouvant être utilisée de manière transparente avec SRW et est actuellement disponible dans un dépôt public sur GitLab jusqu'à la fusion éventuelle avec la distribution officielle de SRW. Parallèlement, le code est incorporé dans la boîte à outils OASYS [Rebuffi and Sanchez del Rio, 2017] qui sera disponible pour les distributions de SHADOW, du ray-tracing hybride et de SRW. Ces développements récents sur la modélisation des lentilles rayons X ont été présentés dans [Celestre, Chubar, et al., 2020] et utilisés dans certaines des simulations de [Chubar et al., 2020].

Finalement, pour réaliser les simulations avec des niveaux d'imperfections réalistes, la modélisation des erreurs de forme sur les lentilles rayons X individuelles a été faite avec des données de métrologie sous forme de cartographie des déviations locales du profil parabolique. La technique de métrologie utilisée pour cette thèse était le XSVT (X-ray vectorial speckle tracking). En plus d'être relativement simple à mettre en œuvre, cette technique possède une résolution latérale élevée et une bonne sensibilité. De plus, elle fournit une cartographie des erreurs de forme dans l'approximation de la projection, qui peut être facilement utilisée avec les simulations de front d'ondes. Plusieurs campagnes de mesures ont été effectuées à l'ESRF, à l'APS et à l'ESRF-EBS pour évaluer la qualité des lentilles produites en interne, des lentilles et des optiques free-form dans le cadre de collaborations scientifiques et des lentilles commerciales nouvellement acquises. En conséquence, une base de données importante et diversifiée de fichiers de métrologie a été constituée. Une expansion possible de DABAM (base de données pour la métrologie des miroirs rayons X) [Sanchez Del Rio et al., 2016] est envisagée. La mise à disposition des données de métrologie des miroirs rayons X par le biais d'une base de données open-source aiderait à consolider le projet développé ici puisque DABAM est également distribuée et interfacée par OASYS. Auparavant, il faudra cependant parvenir à la convergence des résultats de metrologie obtenus sur un empilement de lentilles avec celui du calcul logiciel réalisé à partir de la métrologie des lentilles qui le composent. L'état actuel montre un certain accord qualitatif (Fig. 4.14-4.17)), qui est transféré aux simulations présentées dans les Figs. 5.3-5.4 et Fig. 5.8. Cela est suffisant pour les études préliminaires mais laisse une marge de manœuvre pour améliorer et délimiter les protocoles de métrologie, tant en termes d'alignement des échantillons que de traitement des données - ce qui devrait être l'objectif de futurs études. L'intérêt majeur de pouvoir empiler de manière fiable des lentilles mesurées individuellement étant de pouvoir évaluer les performances d'une CRL composée d'une sélection arbitraire de lentilles, et concevoir les correcteurs optiques nécessaires. L'expérience acquise lors des campagnes de métrologie et les progrès réalisés dans le traitement des données acquises ont permis d'apporter de modestes contributions à [Berujon et al., 2020a,b; Qiao et al., 2020].

Les simulations, présentées dans la première partie du chapitre 5 et résumées par la figure 5.7,, montrent une caustique du faisceau qui a été mentionnée plusieurs fois dans la littérature pour le même type de lentilles rayons X [Schropp et al., 2013; Seiboth et al., 2017, 2020]. La mesure expérimentale de la caustique du faisceau pour cet empilement de lentilles montre également une similarité avec ce qui a été prédit par les simulations - cf. Fig. 6.14. L'accord entre simulations et données expérimentales contribue à valider l'approche du sujet de cette thèse et on estime que les simulations permettent d'évaluer qualitativement les effets des imperfections optiques sur la dégradation du profil du faisceau de rayons X. Elles permettent également d'étudier la pertinence du rapport de Strehl comme facteur de qualité pour la conception de systèmes optiques fonctionnant loin du critère de Maréchal pour la qualité optique. En général, les équations utilisées pour estimer le rapport de Strehl tendent à sous-estimer la performance du système dans cette région (Fig. 5.12). L'impossibilité d'obtenir des équations de remplacement simples (cf. Eq. 5.2) indique que la manière la plus simple d'évaluer le rapport de Strehl est la simulation optique du système en utilisant des erreurs de forme réalistes. Il faut également souligner que bien que les simulations entièrement et partiellement cohérentes ne diffèrent pas de manière significative, il est prématuré de généraliser ce comportement car les simulations partiellement cohérentes sont basées sur une hypothétique ligne de lumière fonctionnant avec le réseau magnétique ESRF amélioré. Un autre résultat des simulations est la prédiction que les systèmes avec des erreurs de forme à haute fréquence spatiale ne présentent pas un élargissement de la taille du faisceau au plan focal, mais que l'intensité est plutôt réduite par la diffusion des photons autour du lobe principal, ce qui augmente le bruit de fond - Fig. 5.13. Les effets des erreurs de forme à haute fréquence spatiale sont importants, car pour des systèmes optiques bien corrigés ils seraient une source prédominante d'erreurs de forme. Cette analyse a été publiée dans [Celestre, Berujon, et al., 2020].

La modélisation multi-coupes d'une CRL incluant les données métrologiques des lentilles mesurées individuellement (Eq. 2.12) permet l'extraction des erreurs de forme cumulées d'un empilement de lentilles. Ceci a été utilisé pour modéliser une plaque de phase en diamant destinée à corriger ces erreurs en sortie du système. Afin de faciliter l'alignement de cette plaque, celle-ci est conçue de façon symétrique au détriment de la performance corrective - les résultats rapportés montrent une excellente performance malgré ce compromis [Seiboth et al., 2020; Dhamgaye et al., 2020]. Le profil du faisceau illustré par la figure 6.6 est plus homogène en amont et en aval du plan image et ressemble aux simulations pour un système à prédominance de hautes fréquences spatiales - figure 5.10. Cependant, lors de l'analyse du rapport de Strehl, la performance de la plaque de phase modélisée est limitée et dépasse ce que d'autres groupes ont rapporté. Les principales raisons de ces divergences sont le fait que le profil à corriger (Fig. 4.14) comporte des composantes non symétriques importantes (aberration en trèfle) en plus de la prédominance classique des aberrations sphériques. L'absence d'asymétrie constatée par d'autres groupes est probablement liée au fait qu'un plus grand nombre de lentilles sont utilisées dans leurs empilements, ainsi les erreurs corrélées des lentilles dont la position en rotation est aléatoire seraient rendues plus symétriques par rapport aux erreurs accumulées par un effet de moyennage des composantes non symétriques. La rotation aléatoire des lentilles dans les simulations pourrait contribuer à améliorer le rapport de Strehl attendu et une procédure similaire pourrait être appliquée à l'empilement de lentilles dans le cadre d'une expérience. Les plaques de phase conçues ont été commandées à un partenaire commercial et sont obtenues par ablation du diamant avec un laser femtoseconde. Les premiers essais sur un faisceau de rayons X ont montré que le centrage des plaques de phase dans leur cadre ne respectait pas les tolérances calculées, ce qui est crucial pour leur performance. En l'absence de protocole d'alignement lors des premiers essais, cela a posé un problème, la plaque de phase devant être alignée par rapport à la pile de lentilles. Cela a également mis en évidence la nécessité de réimplémenter des techniques de détection de front d'onde plus rapides, qui ont été abandonnées au profit d'une résolution spatiale plus élevée. D'autres problèmes tels que la surexposition du détecteur, même après une forte atténuation du faisceau, ont limité les tests qui pouvaient être effectués avec la plaque corrective, de sorte qu'aucune valeur quantitative n'a pu être obtenue pour évaluer la performance de la correction. Cependant, une caustique du faisceau a pu être enregistrée pour le système aberré et corrigé (Fig. 6.14) montrant qualitativement un faisceau plus homogène surtout au voisinage du plan focal, avec une meilleure performance en aval. Les premiers résultats sont prometteurs mais nécessitent de programmer de nouvelles expériences sur ligne de lumière, de trouver des moyens d'extraire rapidement le front d'onde résiduel et d'aligner la plaque de correction, de mesurer la caustique du faisceau et d'évaluer quantitativement les performances de la correction. L'exploration de la fabrication additive pour la conception d'optiques correctives dans d'autres matériaux devrait également être étudiée comme alternative au diamant et pour réduire les coûts de prototypage. ■

References

Ali, S. and Jacobsen, C. (2020). "Effect of tilt on circular zone plate performance". In: *Journal of the Optical Society of America A* **37**.3, p. 374.

Alianelli, L., Sánchez del Río, M., and Sawhney, K. J. (2007). "Ray-tracing simulation of parabolic compound refractive lenses". In: *Spectrochimica Acta - Part B Atomic Spectroscopy* **62**.6-7 SPEC. ISS. P. 593.

Alianelli, L., Sánchez del Rio, M., Fox, O. J. L., and Korwin-Mikke, K. (2015). "Aberration-free short focal length x-ray lenses". In: *Optics Letters* **40**.23, p. 5586.

Andrejczuk, A., Krzywiski, J., Sakurai, Y., Itou, M., Krzywiński, J., Sakurai, Y., and Itou, M. (2010). "The role of single element errors in planar parabolic compound refractive lenses". In: *Journal of Synchrotron Radiation* **17**.5, p. 616.

Baltser, J., Knudsen, E., Vickery, A., Chubar, O., Snigirev, A., Vaughan, G., Feidenhans'l, R., and Lefmann, K. (2011). "Advanced simulations of x-ray beam propagation through CRL transfocators using ray-tracing and wavefront propagation methods". In: *Proc. SPIE 8141, Advances in Computational Methods for X-Ray Optics II* 8141, p. 814111.

Berujon, S., Cojocaru, R., Piault, P., Celestre, R., Roth, T., Barrett, R., and Ziegler, E. (2020a). "X-ray optics and beam characterization using random modulation: experiments". In: *Journal of Synchrotron Radiation* **27**.2, p. 293.

— (2020b). "X-ray optics and beam characterization using random modulation: theory". In: *Journal of Synchrotron Radiation* **27**.2, p. 284.

Celestre, R., Berujon, S., Roth, T., Sanchez del Rio, M., and Barrett, R. (2020). "Modelling phase imperfections in compound refractive lenses". In: *Journal of Synchrotron Radiation* **27**.2, p. 305.

Celestre, R., Chubar, O., Roth, T., Sanchez del Rio, M., and Barrett, R. (2020). "Recent developments in X-ray lenses modelling with SRW". In: *Proc. SPIE 11493, Advances in Computational Methods for X-Ray Optics V*, pp. 11493–17.

Chubar, O., Wiegart, L., Antipov, S., Celestre, R., Coles, R., Fluerasu, A., and Rakitin, M. S. (2020). "Analysis of hard x-ray focusing by 2D diamond CRL". In: *Proc. SPIE 11493, Advances in Computational Methods for X-Ray Optics V*, pp. 11493–20.

Dhamgaye, V., Laundy, D., Baldock, S., Moxham, T., and Sawhney, K. (2020). "Correction of the X-ray wavefront from compound refractive lenses using 3D printed refractive structures". In: *Journal of Synchrotron Radiation* **27**.6.

Dimper, R., Reichert, H., Raimondi, P., Sanchez Ortiz, L., Sette, F., and Susini, J. (2014). *ESRF Upragde programme phase II - The Orange Book*. ESRF, p. 75.

Evans-Lutterodt, K., Ablett, J. M., Stein, A., Kao, C.-C., Tennant, D. M., Klemens, F., Taylor, A., Jacobsen, C., Gammel, P. L., Huggins, H., Ustin, S., Bogart, G., and Ocola, L. (2003). "Single-element elliptical hard x-ray micro-optics". In: *Opt. Express* **11**.8, p. 919.

Li, K., Wojcik, M., and Jacobsen, C. (2017). "Multislice does it all—calculating the performance of nanofocusing X-ray optics". In: *Optics Express* **25**.3, p. 1831.

Qiao, Z., Shi, X., Celestre, R., and Assoufid, L. (2020). "Wavelet-transform-based speckle vector tracking method for X-ray phase imaging". In: *Optics Express* **28**.22, p. 33053.

Rebuffi, L. and Sanchez del Rio, M. (2017). "OASYS (OrAnge SYnchrotron Suite): an open-source graphical environment for x-ray virtual experiments". In: *Proc. SPIE 10388, Advances in Computational Methods for X-Ray Optics IV*, p. 28.

Sanchez del Rio, M. and Alianelli, L. (2012). "Aspherical lens shapes for focusing synchrotron beams". In: *Journal of Synchrotron Radiation* **19**.3, p. 366.

Sanchez Del Rio, M., Bianchi, D., Cocco, D., Glass, M., Idir, M., Metz, J., Raimondi, L., Rebuffi, L., Reininger, R., Shi, X., Siewert, F., Spielmann-Jaeggi, S., Takacs, P., Tomasset, M., Tonnessen, T., Vivo, A., and Yashchuk, V. (2016). "DABAM: An open-source database of X-ray mirrors metrology". In: *Journal of Synchrotron Radiation* **23**.3, p. 665.

Schroer, C. G. and Lengeler, B. (2005). "Focusing hard X rays to nanometer dimensions by adiabatically focusing lenses". In: *Physical Review Letters* **94**.5.

Schroer, C. G. and Falkenberg, G. (2014). "Hard X-ray nanofocusing at low-emittance synchrotron radiation sources". In: *Journal of Synchrotron Radiation* **21**.5, pp. 996–1005.

Schropp, A., Hoppe, R., Meier, V., Patommel, J., Seiboth, F., Lee, H. J., Nagler, B., Galtier, E. C., Arnold, B., Zastrau, U., Hastings, J. B., Nilsson, D., Uhlén, F., Vogt, U., Hertz, H. M., and Schroer, C. G. (2013). "Full spatial characterization of a nanofocused X-ray free-electron laser beam by ptychographic imaging". In: *Scientific Reports* **3**.1, p. 1.

Seiboth, F., Brückner, D., Kahnt, M., Lyubomirskiy, M., Wittwer, F., Dzhigaev, D., Ullsperger, T., Nolte, S., Koch, F., David, C., Garrevoet, J., Falkenberg, G., and Schroer, C. G. (2020). "Hard X-ray wavefront correction via refractive phase plates made by additive and subtractive fabrication techniques". In: *Journal of Synchrotron Radiation* **27**.5, p. 27.

Seiboth, F., Schropp, A., Scholz, M., Wittwer, F., Rödel, C., Wünsche, M., Ullsperger, T., Nolte, S., Rahomäki, J., Parfeniukas, K., Giakoumidis, S., Vogt, U., Wagner, U., Rau, C., Boesenberg, U., Garrevoet, J., Falkenberg, G., Galtier, E. C., Ja Lee, H., Nagler, B., and Schroer, C. G. (2017). "Perfect X-ray focusing via fitting corrective glasses to aberrated optics". In: *Nature Communications* **8**.1, p. 14623.

Sutter, J. P. and Alianelli, L. (2017). "Aberration-free aspherical lens shape for shortening the focal distance of an already convergent beam". In: *Journal of Synchrotron Radiation* **24**.6, pp. 1120–1136.

Yabashi, M., Tono, K., Mimura, H., Matsuyama, S., Yamauchi, K., Tanaka, T., Tanaka, H., Tamasaku, K., Ohashi, H., Goto, S., and Ishikawa, T. (2014). "Optics for coherent X-ray applications". In: *Journal of Synchrotron Radiation* **21**.5, pp. 976–985.

A

Publication list

Journal publications

Nash, B., Goldring , N., Edelen, J., Webb, S. and Celestre, R., (2021). Propagation of partially coherent radiation using Wigner functions. *Physical Review Accelerators and Beams*, **24**(1), 010702.

Qiao, Z., Shi, X., Celestre, R. and Assoufid, L. (2020). Wavelet-transform-based speckle vector tracking method for X-ray phase imaging. *Optics Express*, **28**(20), 1094.

Celestre, R., Berujon, S., Roth, T., Sanchez del Rio, M. and Barrett, R. (2020). Modelling phase imperfections in compound refractive lenses. *Journal of Synchrotron Radiation*, **27**(2), 305–318.

Berujon, S., Cojocaru, R., Piault, P., Celestre, R., Roth, T., Barrett, R. and Ziegler, E. (2020). X-ray optics and beam characterization using random modulation: experiments. *Journal of Synchrotron Radiation*, **27**(2), 293–304.

Berujon, S., Cojocaru, R., Piault, P., Celestre, R., Roth, T., Barrett, R. and Ziegler, E. (2020). X-ray optics and beam characterization using random modulation: theory. *Journal of Synchrotron Radiation*, **27**(2), 284–292.

Sanchez del Rio, M., Celestre, R., Glass, M., Pirro, G., Herrera, J. R., Barrett, R., da Silva, J. C., Cloetens, P., Shi, X. and Rebuffi, L. (2019). A hierarchical approach for modeling X-ray beamlines: application to a coherent beamline. *Journal of Synchrotron Radiation*, **26**(6), 1887–1901.

Chubar, O. and Celestre, R. (2019). Memory and CPU efficient computation of the Fresnel free-space propagator in Fourier optics simulations. *Optics Express*, **27**(20), 28750.

Conference proceedings

Celestre, R., Chubar, O., Roth, T., Sanchez del Rio, M. and Barrett, R. (2020). Recent developments in x-ray lenses modelling with SRW. *Proc. SPIE 11493, Advances in Computational Methods for X-Ray Optics V*, 11493-17.

Chubar, O., Wiegart, L., Antipov, S., Celestre, R., Coles, R., Fluerasu, A. and Rakitin, M. (2020). Analysis of hard x-ray focusing by 2D diamond CRL. *Proc. SPIE 11493, Advances in Computational Methods for X-Ray Optics V*, 11493-20.

Nome, R., Giles, C., Celestre, R., Tasca, K., Dias, C., Vescovi, R., Faria, G. and Ferbonink, G. (2018). Compact arrangement for femtosecond laser induced generation of broadband hard x-ray pulses. *High-Brightness Sources and Light-Driven Interactions*, ET1B.3.

Titre: Étude de l'effet des imperfections optiques aux faisceaux de rayons X partiellement cohérents en combinant les simulations optiques avec les mesures du front d'onde

Mots clés: Simulations optiques, lentilles à rayons X, métrologie à la longueur d'onde, optique physique

Résumé: En optique physique, les éléments faiblement focalisés sont généralement simulés comme un seul élément mince. Alors qu'une seule lentille à rayons X dans des conditions de fonctionnement typiques peut souvent être représentée de cette manière, la simulation d'une pile de lentilles complète avec une approche similaire manque de polyvalence. Ce travail propose de décomposer un LCR en ses petites lentilles séparées par une propagation en espace libre, comme le font les techniques de découpage en plusieurs tranches déjà utilisées pour les simulations optiques. Une attention particulière est accordée à la modélisation de l'élément lentille unique en ajoutant des degrés de liberté supplémentaires permettant la modélisation des désalignements typiques et des erreurs de fabrication. Des polynômes orthonormaux pour les aberrations optiques ainsi que des données de métrologie obtenues avec le suivi vectoriel du speckle des rayons X (XSVT) sont également utilisés pour obtenir des résultats de simulation réalistes, qui sont présentés dans plusieurs simulations cohérentes et partiellement cohérentes tout au long de ce travail. La mise en œuvre d'un modèle de lentilles à rayons X utilisant des données de métrologie permet d'extraire les erreurs de chiffres accumulées et de calculer les corrections de phase. Enfin, cette thèse présente une méthodologie pour le calcul du profil des correcteurs de réfraction, qui est appliquée pour produire des plaques de phase ablationnées au diamant. Les premiers résultats expérimentaux montrent une amélioration du profil du faisceau. Ce projet a abordé des aspects importants du programme ESRF-EBS d'optique des rayons X R&D tel que défini dans le plan de mise à niveau stratégique (*Orange book*).

Title: Investigations of the effect of optical imperfections on partially coherent X-ray beam by combining optical simulations with wavefront sensing experiments

Keywords: Optical simulations, X-ray lenses, at-wavelengh metrology, physical optics

Abstract: In physical optics, weakly focusing elements are usually simulated as a single thin element. While a single X-ray lens at typical operation conditions can often be represented in this way, simulating a full lens stack with a similar approach lacks versatility. This work proposes decomposing a CRL into its lenslets separated by a free-space propagation, similar to the multi-slicing techniques already used for optical simulations. Attention is given to modelling the single lens element by adding additional degrees of freedom allowing the modelling of typical misalignments and fabrication errors. Orthonormal polynomials for optical aberrations as well as metrology data obtained with X-ray speckle vector tracking (XSVT) are also used to obtain realistic simulation results, which are presented in several coherent- and partially-coherent simulations throughout this work. Implementing a model of X-ray lenses using metrology data allows extraction of the accumulated figure errors and enables the calculation of phase corrections. Finally, this thesis presents a methodology for calculating the profile of refractive correctors, which is applied to produce phase plates ablated from diamond. Early experimental results show an improvement on the beam profile. This project addressed important aspects of the ESRF-EBS X-ray optics R&D programme as laid out in the strategic upgrade plan (Orange book).

Université Grenoble Alpes
621 avenue Centrale
38400 Saint-Martin-d'Hères, France